

Copyright
by
Kody Merlin Powell
2013

The Dissertation Committee for Kody Merlin Powell certifies that this is the approved version of the following dissertation:

Dynamic Optimization of Energy Systems with Thermal Energy Storage

Committee:

Thomas Edgar, Supervisor

Michael Baldea

Ross Baldick

Halil Berberoglu

Roger Bonnecaze

John Hedengren

Dynamic Optimization of Energy Systems with Thermal Energy Storage

by

Kody Merlin Powell, B.S.Ch.E.

Dissertation

Presented to the Faculty of the Graduate School of

The University of Texas at Austin

in Partial Fulfillment

of the Requirements

for the Degree of

Doctor of Philosophy

The University of Texas at Austin

August 2013

To my beautiful wife Elisabeth, who deserves this degree as much as I do.

Acknowledgements

I would first like to thank my family, who have been such a tremendous source of strength and support during graduate school. I could not have done this without my wife, Elisabeth. Raising children while attending graduate school is a challenge and having someone there to handle so many other important details so I could focus on my studies has been such a great blessing.

I am tremendously grateful for my adviser, Dr. Thomas Edgar, who has been extremely generous in terms of both support and opportunity. I have had a unique graduate experience, which I have thoroughly enjoyed. Most of those opportunities would not have been available without an adviser who trusts and cares about his students. I would also like to thank Sarah De Berry-Caperton for saving me countless hours and headaches during my time here.

I would like to thank my research group, both past and present. Those in the program before me were so patient in answering questions and helping me get my feet wet as a researcher. They have become my friends, not just my colleagues. My contemporaries also had a big impact on my graduate studies. Jong Kim, Kriti Kapoor, and I entered the program together and we have been united in our struggles and our laughter ever since. Wesley Cole has been an example of hard work, dedication, and integrity. Akshay Sriprisad has been a source of much laughter that really made many of my days in the lab go by much faster. The members of the Edgar and Baldea research groups have become my friends and I have learned so much from all of them.

John Hedengren and Michael Baldea have been great mentors to me. I consider them both friends who have been willing to make time in their busy schedules to guide me on both technical and non-technical issues. The Utilities and Energy Management staff at

UT Austin have been amazing. Ryan Thompson and Juan Ontiveros have been particularly helpful on so many occasions. Despite having no formal obligation to assist students, they have gone above and beyond to enhance my educational experience.

I would like to thank my parents, Kerry and Karla, my siblings, and my other immediate family members. My family has always been so supportive during my long schooling experience. Making them proud has always been a driving force in my life. My in-laws, Brigitte and Philippe, have also given so much support to our family during this challenging but exciting time.

Finally, I would like to thank the sponsors of my research: The National Science Foundation, The Cockrell School of Engineering at UT Austin, and The Office of Sustainability at UT Austin. Without the generous support of these donors, none of this would be possible.

Dynamic Optimization of Energy Systems with Thermal Energy Storage

Kody Merlin Powell, Ph.D.

The University of Texas at Austin, 2013

Supervisor: Thomas Edgar

Thermal energy storage (TES), the storage of heat or cooling, is a cost-effective energy storage technology that can greatly enhance the performance of the energy systems with which it interacts. TES acts as a buffer between transient supply and demand of energy. In solar thermal systems, TES enables the power output of the plant to be effectively regulated, despite fluctuating solar irradiance. In district energy systems, TES can be used to shift loads, allowing the system to avoid or take advantage of peak energy prices. The benefit of TES, however, can be significantly enhanced by dynamically optimizing the complete energy system. The ability of TES to shift loads gives the system newfound degrees of freedom which can be exploited to yield optimal performance. In the hybrid solar thermal/fossil fuel system explored in this work, the use of TES enables the system to extract nearly 50% more solar energy when the system is optimized. This requires relaxing some constraints, such as fixed temperature and power control, and dynamically optimizing the over a one-day time horizon. In a district cooling system, TES can help equipment to run more efficiently, by shifting cooling loads, not only between chillers, but temporally, allowing the system to take advantage of the most efficient times for running this equipment. This work also highlights the use of TES in a district energy system, where heat, cooling and electrical power are generated from central locations.

Shifting the cooling load frees up electrical generation capacity, which is used to sell power to the grid at peak prices. The combination of optimization, TES, and participation in the electricity market yields a 16% cost savings. The problems encountered in this work require modeling a diverse range of systems including the TES, the solar power plant, boilers, gas and steam turbines, heat recovery equipment, chillers, and pumps. These problems also require novel solution methods that are efficient and effective at obtaining workable solutions. A simultaneous solution method is used for optimizing the solar power plant, while a static/dynamic decoupling method is used for the district energy system.

Table of Contents

List of Tables	xiii
List of Figures	xiv
CHAPTER 1 : INTRODUCTION	1
CHAPTER 2 : MODELING AND CONTROL OF A PARABOLIC TROUGH SOLAR POWER PLANT WITH THERMAL ENERGY STORAGE	7
Introduction.....	7
Overview of the system	8
Model Formulation	9
Results.....	16
Conclusion	26
Nomenclature.....	28
CHAPTER 3 : DYNAMIC OPTIMIZATION OF A HYBRID SOLAR THERMAL SYSTEM WITH THERMAL ENERGY STORAGE	30
Introduction.....	30
Model Development.....	31
Optimization Problem Formulation	35
Solution Method.....	39
Results.....	40

Discussion of Results	46
Conclusions and Future Work	48
Nomenclature	50
CHAPTER 4 : INTEGRATING LOGIC IN SIMULTANEOUS AND SEQUENTIAL DYNAMIC OPTIMIZATION SOLUTION METHODS	52
Introduction.....	52
Sequential Solution Method.....	54
Embedding MPECs into Simultaneous Equations.....	58
MPEC Formulations to Represent Logical Statements	61
Continuous Logic in Dynamic Systems.....	65
Continuous Logic in an NMPC Problem	75
Conclusions and Future Work	82
Nomenclature	84
CHAPTER 5 : AN ADAPTIVE GRID MODEL FOR DYNAMIC MODELING OF THERMOCLINE THERMAL ENERGY STORAGE SYSTEMS	86
Introduction.....	86
Background	87
Model Description	94
Results and Discussion	100

Conclusions.....	104
Nomenclature.....	105
CHAPTER 6 : ELECTRICAL, HEATING, AND COOLING LOAD FORECASTING FOR A DISTRICT ENERGY SYSTEM	106
Introduction.....	106
Background.....	108
System Overview.....	109
Model Development.....	114
Results.....	118
Conclusions.....	126
Nomenclature.....	129
CHAPTER 7 : DYNAMIC OPTIMIZATION OF A DISTRICT COOLING SYSTEM WITH THERMAL ENERGY STORAGE	130
Introduction.....	130
Background.....	130
Chiller Modeling.....	133
Static Optimal Chiller Loading.....	136
Dynamic Optimal Chiller Loading with Thermal Energy Storage.....	140
Results.....	144

Conclusions.....	149
Nomenclature.....	151
CHAPTER 8 : DYNAMIC OPTIMIZATION OF A DISTRICT ENERGY SYSTEM WITH COMBINED HEAT AND POWER AND THERMAL ENERGY STORAGE	152
Introduction.....	152
System Overview	154
Model Development.....	156
Static Optimization Problem Formulation	166
Dynamic Optimization Problem Formulation	170
Results and Discussion	172
Conclusions.....	176
Nomenclature.....	178
CHAPTER 9 : CONCLUSIONS AND FUTURE WORK	181
WORKS CITED	185

List of Tables

Table 2.1: A summary of each simulation scenario.....	26
Table 4.1: Results from the sequential and simultaneous methods.	81
Table 5.1: Mass balances under different logic conditions.....	97
Table 5.2: Energy balances for each node in the tank.	99
Table 6.1: Summary of weather and load for one year.....	111
Table 6.2: A comparison of adjusted R^2 values.....	119
Table 7.1: Operating ranges and model fitting results.....	135
Table 7.2: A summary of results.....	148
Table 7.3: Daily cost for the three cases.	149
Table 8.1: Lower and upper bounds on chiller loads.....	167
Table 8.2: Summary of constraints for other decision variables.	168

List of Figures

Figure 1.1: Electrical load profile.	2
Figure 1.2: Level curves and constraints for power generation example.	3
Figure 2.1: The parabolic trough plant with storage and control system.....	9
Figure 2.2: A cross-sectional view of the parabolic mirror and absorber pipe assembly.	10
Figure 2.3: A side-view of the absorber pipe assembly.....	13
Figure 2.4: A diagram of the boiler.	14
Figure 2.5: Power for the system without storage.	17
Figure 2.6: HTF flow rate for a system with no storage.	17
Figure 2.7: HTF temperatures for a system with no storage.....	18
Figure 2.8: Power for the system with storage.	19
Figure 2.9: HTF flow rates for a system with thermal energy storage.	20
Figure 2.10: Temperatures for a system with thermal energy storage.....	20
Figure 2.11: HTF fluid volume in thermal storage tanks.....	21
Figure 2.12: Power for system without storage on a cloudy day.....	22
Figure 2.13: HTF flow rate for a system with no storage on a cloudy day.	22
Figure 2.14: HTF temperatures for a system with no storage.....	23
Figure 2.15: Power for a system with thermal storage on a cloudy day.	24
Figure 2.16: HTF flow rates for a system with storage on a cloudy day.....	24
Figure 2.17: Temperatures for a system with storage on a partly cloudy day.	25
Figure 2.18: Volume of HTF in the storage tanks for a partly cloudy day.....	25
Figure 3.1: A parabolic trough CSP plant with two tank direct TES system.	32
Figure 3.2: A cross-sectional view of the receiver assembly.....	33
Figure 3.3: DNI in W/m^2 for each of the three scenarios.	40
Figure 3.4: Solar power using standard control scheme.	41
Figure 3.5: Temperatures using a standard control scheme.....	42
Figure 3.6: Flow rates when using a standard control scheme.	42
Figure 3.7: Storage volume for standard control scheme.	43

Figure 3.8: Power for dynamic optimization scheme.	44
Figure 3.9: Temperatures for dynamic optimization scheme.	44
Figure 3.10: Storage tank volumes when using dynamic optimization.	45
Figure 3.11: Flow rates when using dynamic optimization.	45
Figure 3.12: Total solar energy collected in MW_{th} for each scenario.	47
Figure 3.13: Solar heat collection efficiency for each scenario.	47
Figure 4.1: A schematic illustrating the orthogonal collocation on finite elements.	57
Figure 4.2: A plot of the convergence of the greater than/equal to logic MPEC.	64
Figure 4.3: A plot of residuals when solving using Newton's Method.	65
Figure 4.4: A schematic showing how the dynamic equations for tank overflow.	67
Figure 4.5: Flow rates in and out of the tank overflow system.	68
Figure 4.6: Plot of tank volume.	69
Figure 4.7: Plot of the pseudo-binary variable.	69
Figure 4.8: Complementarity variables used in the tank overflow system.	70
Figure 4.9: Schematic for the power flow example.	71
Figure 4.10: Inputs to the power flow model.	73
Figure 4.11: Flows in the power network.	74
Figure 4.12: State of charge (kWh) of the battery.	74
Figure 4.13: Pseudo-binary variables indicating battery charge conditions.	75
Figure 4.14: A schematic of the MPC scheme of a CSTR and surge tank.	76
Figure 4.15: Results from the CSTR with surge tank nonlinear MPC problem.	80
Figure 4.16: Results of the CSTR MPC problem.	82
Figure 5.1: Two tank thermal storage configuration.	88
Figure 5.2: Single mixed tank thermal storage configuration.	89
Figure 5.3: Single tank thermocline configuration for thermal energy storage.	89
Figure 5.4: Spatial discretization in the thermocline tank.	90
Figure 5.5: A plot of temperature vs. tank height.	92
Figure 5.6: The effect of temperature inversion.	94
Figure 5.7: A diagram of the adaptive-grid thermocline model.	95

Figure 5.8: A diagram showing the movement of nodes for downward flow.	98
Figure 5.9: Normalized tank inlet temperature and flow.	101
Figure 5.10: Normalized tank temperature vs. tank height at hour 3.	101
Figure 5.11: Normalized tank temperature vs. tank height at hour 4.	102
Figure 5.12: Normalized tank temperature vs. tank height at hour 5.	103
Figure 6.1: A district energy system.	110
Figure 6.2: Campus loads during an August week.	112
Figure 6.3: Temperature and humidity for an August week.	112
Figure 6.4: Campus loads during a February week.	113
Figure 6.5: Temperature and humidity for a February week.	113
Figure 6.6: Correlation coefficients for loads and weather.	114
Figure 6.7: A diagram of the neural network structure.	116
Figure 6.8: Dry bulb temperature and relative humidity for July 31, 2012.	121
Figure 6.9: Forecasted electric load and actual data for July 31st, 2012.	121
Figure 6.10: Cooling load forecast and actual data for July 31st, 2012.	122
Figure 6.11: Heating load forecast and actual data for July 31st, 2012.	122
Figure 6.12: Dry bulb temperature and relative humidity for February 14 th , 2012.	123
Figure 6.13: Electric load forecast and actual data for February 14 th , 2012.	123
Figure 6.14: Cooling load forecast and actual data for February 14 th , 2012.	124
Figure 6.15: Heating load forecast and actual data for February 14 th , 2012.	124
Figure 7.1: A district cooling system with chilling stations and thermal storage.	131
Figure 7.2: Chiller performance curves.	134
Figure 7.3: Solutions to the static problem vs. load.	141
Figure 7.4: The hierarchical structure for the dynamic optimization problem.	142
Figure 7.5: Total cooling demand and wet bulb temperature.	144
Figure 7.6: Chiller loads for equal chiller loading.	145
Figure 7.7: Chiller loads for static optimization.	146
Figure 7.8: Chiller loads using dynamic optimization.	147
Figure 7.9: Storage using dynamic optimization.	147

Figure 8.1: Flows for the district energy system.....	156
Figure 8.2: Parity plot illustrating the quality of the fit for Chiller 6.1.	158
Figure 8.3: 1/COP vs. load for all chillers.	159
Figure 8.4: Chiller power consumption as a function of chiller load.	159
Figure 8.5: Parity plot for the auxiliary power consumption model.....	160
Figure 8.6: Schematic of the gas turbine configuration.....	162
Figure 8.7: Model validation for the gas turbine model.	163
Figure 8.8: Diagram of the HRSG.	164
Figure 8.9: Diagram of the extraction steam turbine.	165
Figure 8.10: A diagram outlining the optimization problem decoupling.	171
Figure 8.11: Total power production, net power sold, and electricity price.	173
Figure 8.12: Total power production, net power sold, and electricity price.	174
Figure 8.13: Summary of total operating costs for one year under various scenarios....	175
Figure 9.1: A block diagram for dynamic real-time optimization.	182

CHAPTER 1 : INTRODUCTION

Energy storage technologies are beneficial for managing the transient demands of the energy infrastructure. They are also crucial to integrating intermittent renewable sources of energy into that infrastructure. While energy storage technologies are generally developed to make a system more reliable, allowing it to better manage supply/demand mismatch, they also give the system more degrees of freedom. These degrees of freedom can be exploited to yield optimal performance. The introduction of large-scale storage technologies into energy systems provide opportunities for dynamic optimization, where the system can be optimized over a time interval, rather than at a single instance in time. This enhanced flexibility means that energy supply and/or demand can be shifted temporally, so that an optimal objective can be achieved over the course of a day.

The central goal of this work is to find ways to exploit the flexibility that energy storage provides a system. While energy storage provides more degrees of freedom, it also makes the corresponding optimization problems exponentially more challenging to solve. This work focuses on thermal energy storage (TES), which is the storage of energy as heat or cooling. TES integrates seamlessly into thermal systems. TES is critical for solar thermal energy systems, which are subject to the intermittent and diurnal nature of solar irradiance. Cold TES has also found widespread application in district cooling systems, where chilled water produced by industrial chillers can be stored to help shift electricity demand. District energy systems can also benefit greatly from TES.

When considered in the context of a larger system, TES has benefits that extend beyond shifting cooling or heating supply and demand. TES can impact the performance of combined heat and power (CHP) and distributed energy systems. These systems are complex and contain a diverse and interrelated set of operating equipment. In order to realize the full benefit of TES, the entire system operation must be considered. This work explores dynamic optimization of energy systems with TES in several contexts: as part of

a solar thermal system, in a district cooling system, and in a distributed energy system with onsite power generation.

The central idea of the work is embodied in the following idealized example. Consider a system with two electric power generators and the electric load profile in Figure 1.1. Generator 1 is more efficient, so it is used as much as possible to meet the demand. Generator 2 is considered to be a less efficient peaking unit, which is only turned on to meet peak demand.

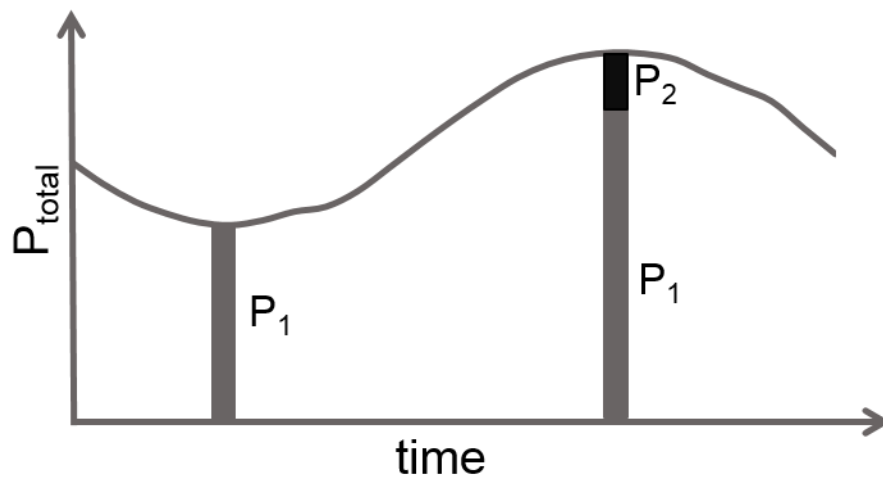


Figure 1.1: Electrical load profile.

Because there are two generators, the total load can be met by some combination of the two, with power denoted P_1 for Generator 1 and P_2 for Generator 2. Because there are two decision variables and only one constraint ($P_1 + P_2 = P_{total}$), the system has one degree of freedom, which can be determined by solving a static optimization problem. The total system efficiency is plotted using level curves in Figure 1.2. With the constraint that the sum of the generators' power production equal the total power demand, optimal solutions for that demand appear as a straight line on the plot. The minimum power demand is shown using the leftmost (solid red) line in this figure. All feasible solutions will lie on this line with the optimal solution shown by the small black dot, indicating that only the more efficient Generator 1 is used at this time. At the peak demand, represented by the rightmost

(solid red) line, the peaking power plant is used and the optimal combination of power from the generators is indicated by the dot that lies on this line.

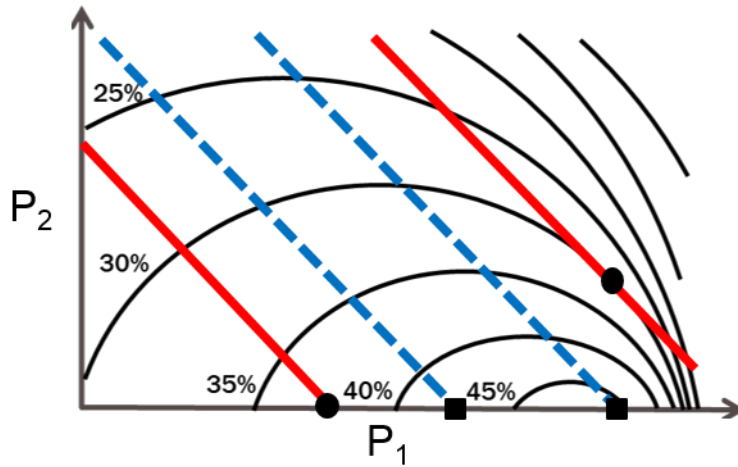


Figure 1.2: Level curves and constraints for power generation example.

When the ability to store energy is introduced to the system, new degrees of freedom become available for optimization. The system now has the ability to shift load from the peak time to the trough time, which is equivalent to shifting the entire constraint lines on Figure 1.2. If peak demand from Figure 1.1 is shifted to the minimum demand time, for example, total efficiency can be improved. The new load constraint lines for these time periods are the inner (dotted blue) lines. The optimal solutions for each of these periods are now represented by the squares. With this shift in load, electricity generation becomes more efficient at each time and overall efficiency is improved as a result. Because the peak has been reduced using storage, the inefficient Generator 2 is no longer necessary to meet the load.

While the preceding example is an abstraction, it highlights the benefit of storage. Storage gives a system newfound flexibility so that loads can be shifted in time. Dynamic optimization can be used to exploit this flexibility by determining optimal values for these new degrees of freedom. This work focuses on thermal energy storage, and covers several different systems which are analogous to the above example.

The work contains several chapters, each around this central theme, but designed to stand on its own. Because a wide range of systems are considered, the nomenclature differs for each chapter. In order to accommodate readers, a nomenclature table is added at the end of each chapter. The chapters are summarized as follows:

Chapter 2: Modeling and Control of a Parabolic Trough Solar Power Plant with Thermal Energy Storage

In Chapter 2, a dynamic, first principles model of a parabolic trough solar thermal power plant is developed. The model includes a two-tank TES system and a control system. The main contribution of this work is the demonstration of the value of TES for regulating a system. With TES, both solar field temperature and thermal power output can be effectively regulated. Additionally, TES enables the system to achieve higher solar shares with the same size solar field because excess energy can be harvested when it otherwise would be wasted.

Chapter 3: Dynamic Optimization of a Hybrid Solar Thermal System with Thermal Energy Storage

Chapter 3 uses the model developed in Chapter 2 and goes a step further. This chapter explores the benefit of using the degrees of freedom from TES and hybrid operation to maximize the amount of solar energy that can be collected, rather than only using the TES to improve system regulation. A 24-hour dynamic optimization problem is solved, where the plant's load can be met by a combination of solar or natural gas energy. When the system is given this flexibility, a remarkable improvement is observed. The dynamic optimization strategy highlights the synergy that can exist between different energy sources. By combining fossil energy with solar energy, more solar energy is harvested.

Chapter 4: Integrating Logic in Simultaneous and Sequential Dynamic Optimization Solution Methods

This chapter deals with the mathematical aspects involved in solving dynamic optimization problems, such as those discussed in Chapter 3. These problems must be solved in an efficient manner. Because the time horizons are so long, operating conditions

in the system can change dramatically. Often, the models require logical statements, which may disqualify the use of the efficient simultaneous solution method for solving dynamic optimization problems. This work attempts to integrate logical statements into a continuous model so that simultaneous solution methods can still be used. The methodology is compared to the corresponding formulation using a sequential method.

Chapter 5: An Adaptive Grid Model for Dynamic Modeling of Thermocline Thermal Energy Storage Systems

In Chapter 5, the focus of the work shifts to cool thermal storage using a single-tank-thermocline storage configuration. A novel adaptive-grid model is developed for modeling the dynamics of these storage systems. This model uses a high resolution grid to model the thermally stratified region of the tank (the thermocline) and variable volume nodes at each end of the tank. The thermocline section of the model moves with time using logical conditions to track the stratified area of the tank. Simulation times are reduced using this methodology compared to other models. More importantly, the model yields more accurate results because it prevents numerical diffusion and better represents temperature inversion in the tank.

Chapter 6: Electrical, Heating, and Cooling Load Forecasting for a District Energy System

District energy systems with TES provide an opportunity to apply a methodology similar to that of Chapter 3. The TES gives the system enhanced flexibility which can be exploited to yield optimal results over a 24-hour period. Solving these 24-hour dynamic optimization problems, however, require foreknowledge of the boundary conditions at each instance in time during that horizon. This chapter provides a proof of concept for load forecasting for a district energy system. The system explored in this work is the University of Texas at Austin campus, which supplies its own cooling, heating, and electricity, all from central locations. This work is unique in that it explores load forecasting for these three diverse loads for a large campus. The results are promising and indicate that the loads can be predicted with reasonable accuracy, using weather forecasts as inputs and a

nonlinear autoregressive model structure. The ability to forecast loads sets the stage for the dynamic optimization problems that will be solved in Chapter 7 and Chapter 8.

Chapter 7: Dynamic Optimization of a District Cooling System with Thermal Energy Storage

In this chapter, a district energy system with chilled water TES is considered for dynamic optimization. In addition to optimizing the loading on all the chillers in the system, TES gives the system degrees of freedom so that loads can be shifted temporally, rather than just from one piece of equipment to another. The complexity and non-convexity of this mixed-integer nonlinear program (MINLP) lead to the introduction of a novel solution method. The static problem of optimal chiller loading is decoupled from the dynamic problem of charging and discharging the storage tank, reducing the dynamic problem (originally formulated as a MINLP) to a nonlinear program (NLP) problem with far fewer variables. This allows the system to take advantage of the degrees of freedom of TES, while greatly reducing the complexity of the corresponding dynamic optimization problem. Both cost and energy savings are achieved by using the TES in this manner.

Chapter 8: Dynamic Optimization of a District Energy System with Combined Heat and Power and Thermal Energy Storage

The problem introduced in Chapter 7 is greatly expanded in this chapter, which explores a diverse and complex energy system with district heating, district cooling, TES, and a combined heat and power (CHP) system. This dynamic optimization problem must be solved so that electrical, heating, and cooling loads are met at every point in the time horizon. This work also explores the impact of TES in a system that interacts with the surrounding electric grid. The TES allows the system to shift cooling and therefore electric loads, which frees up electrical generation capacity so that the system's economics can be enhanced by selling excess power to the grid. This dynamic optimization problem is solved using a similar method as in the previous chapter. Results indicate that TES has the most benefit in an open-market scenario.

CHAPTER 2 : MODELING AND CONTROL OF A PARABOLIC TROUGH SOLAR POWER PLANT WITH THERMAL ENERGY STORAGE

Introduction

The intermittent nature of renewable energy resources, such as solar and wind, puts them at an inherent disadvantage when compared to fossil fuels. Fossil fuels essentially are stored energy, which can be dispatched on demand by combustion of the fuel. By contrast, solar and wind are available only when the sun is shining or the wind is blowing. In order to make these resources viable replacements for fossil fuels, economical energy storage technologies must be developed. Energy storage makes it possible to align energy production with consumer demand. Therefore, energy storage technologies will be vital for global energy sustainability [1]. Thermal energy storage (TES), or the storing of energy as heat or cooling, is a cost-effective technology with many potential applications [2].

Concentrating solar power (CSP) systems illustrate the value of TES technology [3]. CSP systems concentrate solar radiation using mirrors or lenses to heat a fluid for a power plant or other application [4]. Without storage, the power output from these systems is interrupted when a disturbance is introduced to the system. For example, when the sun goes behind a cloud, less energy is available, and the power output decreases accordingly [5]. Because CSP technologies are still being developed, few instances of TES with these systems have been studied. These instances are well-chronicled by Medrano et al. [6]. Because there are only few practical instances of TES with CSP systems, systems-level dynamic modeling of these systems is important to understand the complete system's behavior and to provide insights to help with further research, development, and design of such plants.

Many advanced control techniques have been applied to concentrating solar power systems to overcome the problems caused by the sporadic nature of solar radiation [7].

These techniques are generally focused on controlling the solar collector outlet temperature by varying the heat transfer fluid (HTF) flow rate (the manipulated variable) through the collector field [8]. If no energy storage is considered, the power output from the plant will vary as solar radiation varies. Conversely, modeling the solar collector with a two-tank-direct TES system creates an additional manipulated variable: the flow rate from the storage tank to the load heat exchanger or boiler. Thus, while the collector field outlet temperature can still be controlled, the power delivered to the load can be controlled independently, making it possible to sustain constant power output during cloud cover, or to shift power output to better meet variable consumer demand.

Because the TES system represents only part of the overall energy system, dynamic modeling of the complete system is necessary to gain understanding of how the storage components interact with the other components of the system. In this paper, the focus of the simulation is on the TES system and how it is used to improve control of the power output.

Overview of the system

The thermal energy storage system modeled in this work uses the two-tank-direct configuration where the heat transfer fluid also acts as the energy storage medium. This requires two separate tanks, but eliminates the need for an additional heat exchanger to transfer heat from the collection HTF to the storage medium. The fluid is stored at its lower temperature in a cold tank, heated in the solar collector field, and then stored at an elevated temperature in the hot tank [6].

A parabolic trough solar collector field with east-west, single-axis sun tracking is considered [9]. The solar collector uses parabolic mirrors to concentrate direct solar radiation onto an absorber pipe, through which the HTF flows while it absorbs heat. A feedback plus feedforward controller is used to control the outlet temperature using the mass flow rate of stream 1 (the total flow through the collector field) as the manipulated variable (see Figure 2.1).

The stored energy in the hot tank is delivered to the load by pumping the HTF through the boiler. In this model, it is assumed that saturated liquid water is fed to the boiler and it exits as saturated steam. In this exchange, the HTF returns to its lower temperature and is pumped back to the cold tank. The output power is represented by the flow rate of the saturated steam generated in the boiler. This flow rate is measured and a PID controller is used to control it using the flow of stream 2 (the flow from the hot tank to the cold tank) as a manipulated variable.

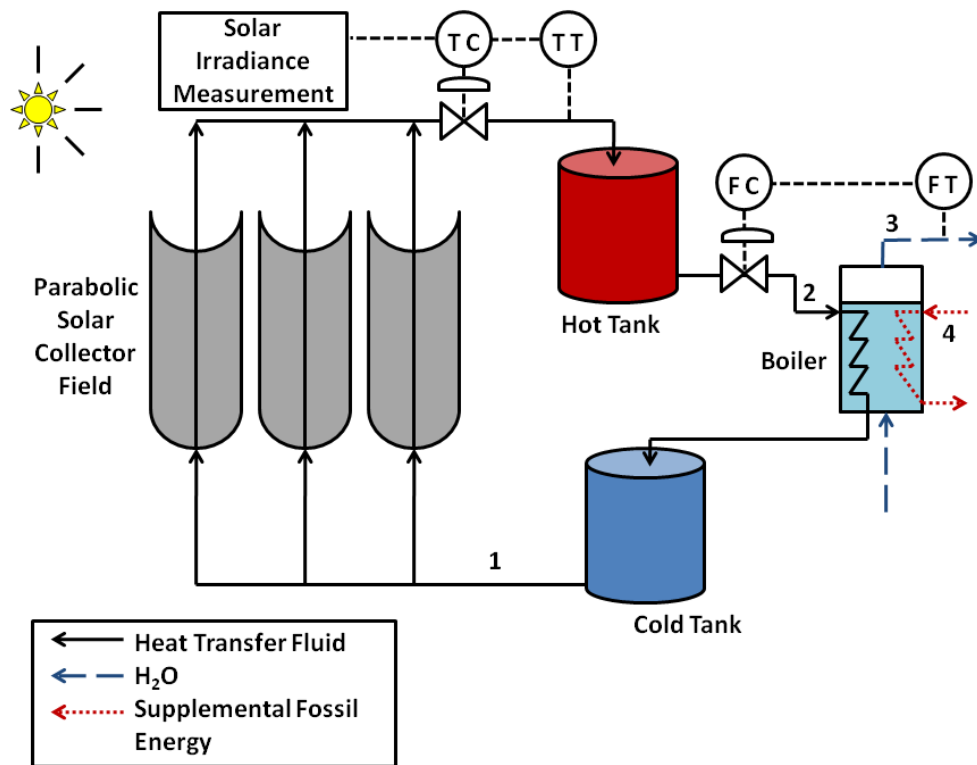


Figure 2.1: The parabolic trough plant with storage and control system.

Model Formulation

The solar collector consists of a parabolic mirror, which is used to focus solar radiation onto the absorber pipe. The absorber pipe runs along the focal point of the mirrors. It is enclosed in a glass envelope, which is mostly transparent to UV radiation, but opaque

to IR radiation. The absorber pipe is designed to have high absorptivity and low emissivity, so that it absorbs high amounts of radiation, while minimizing radiative heat losses. This is typically done by applying a selective coating to the outer surface of the pipe [10]. A cross-sectional view of the solar collector assembly is shown in Figure 2.2. As the figure shows, the parabolic mirror is used to concentrate solar irradiance by reflecting it onto a smaller surface, that of the absorber pipe.

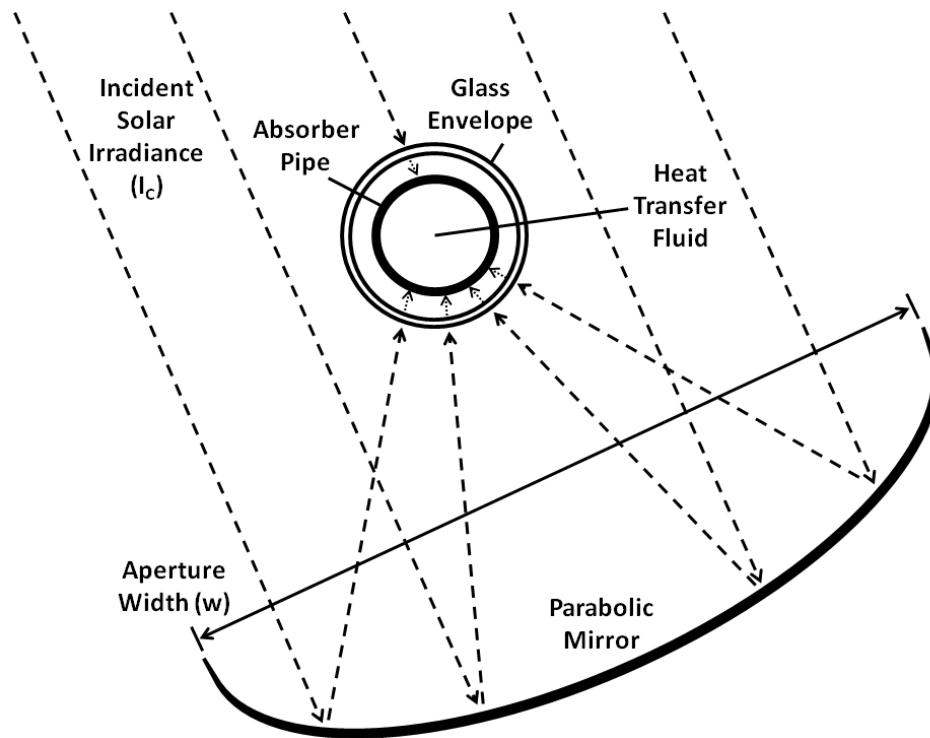


Figure 2.2: A cross-sectional view of the parabolic mirror and absorber pipe assembly.

Modeling of this system requires computing energy balances for the HTF, the absorber pipe, and the glass envelope. Neglecting radial temperature gradients and conductive heat transfer yields the following PDE, which represents the HTF energy balance:

$$\rho_F C_F A_{A,i} \frac{\partial T_F}{\partial t} = \dot{m} C_F \frac{\partial T_F}{\partial x} + h_p P_{A,i} (T_A - T_F) \quad (2.1)$$

where ρ represents the density, C , the heat capacity, A , the cross-sectional area, T , the temperature, \dot{m} , the mass flow rate of the HTF, x , the axial distance along the collector, h_p , the convective heat transfer coefficient inside the pipe, and P , the perimeter. The subscript F refers to the heat transfer fluid, A to the absorber, and A,i to the inner dimensions of the absorber pipe. The balance is derived assuming that convection is the dominant mode of heat transfer from the absorber pipe to the heat transfer fluid. The convective heat transfer coefficient, h_p , is calculated from the Dittus-Boelter correlation for the Nusselt number for turbulent flow in a circular pipe [11].

The energy balance is also computed on the absorber pipe:

$$\rho_A C_A A_A \frac{\partial T_A}{\partial t} = h_p P_{A,i} (T_F - T_A) - \frac{\sigma}{\frac{1}{\varepsilon_A} + \frac{1 - \varepsilon_E}{\varepsilon_E} \left(\frac{r_{A,o}}{r_{E,i}} \right)} P_{A,o} (T_A^4 - T_E^4) + I_C \eta_{optical} w \quad (2.2)$$

where ε represents emissivity, σ is the Stefan-Boltzmann constant, I_C is the direct solar irradiance incident on the collector surface, $\eta_{optical}$ is the optical efficiency (as calculated by Equation 2.19) which determines the fraction of radiative energy that is absorbed by the absorber pipe, r is the radius, and w is the solar collector width. The subscript A,o refers to the outer dimension of the absorber pipe, E refers to the glass envelope, and E,i refers to the inner dimension of the envelope. Convection between the absorber pipe and the glass envelope is neglected due to the vacuum between the two surfaces, leaving radiation as the dominant mode of heat transfer between these two surfaces. The radiative term includes a view factor between two concentric cylinders, as given by Incropera et al. [11]. This view factor is a function of the emissivity and radial dimensions of these surfaces. Variations of the emissivity of the absorber pipe and the glass envelope with temperature are neglected. The emissivity also represents an averaged value over all wavelengths, which are predominantly in the infrared portion of the spectrum.

Similarly, the energy balance on the glass envelope is computed:

$$\rho_E C_E A_E \frac{\partial T_E}{\partial t} = \frac{\sigma}{\frac{1}{\varepsilon_A} + \frac{1-\varepsilon_E}{\varepsilon_E} \left(\frac{r_{A,o}}{r_{E,i}} \right)} P_{A,i} (T_A^4 - T_E^4) - \sigma \varepsilon_E P_{E,o} (T_E^4 - T_{SKY}^4) - h_{AIR} P_{E,o} (T_E - T_{AIR}) \quad (2.3)$$

where the subscript, *AIR*, refers to the ambient air properties and *SKY* refers to the temperature of the sky to which the system radiates. No heat absorption term is added to this energy balance because the glass envelope is 96% transparent to radiation from the solar spectrum. It is not assumed transparent, however, to the longer wavelength infrared radiation emanating from the absorber tube. Hence, the radiative term in Equation (2.3) used describe heat transfer between the two properties. The infrared emissivity of the absorber tube is also assumed constant and a typical value for glass is used. It should be noted that, due to the differences between the radiative spectrum emanating from sunlight (predominantly ultraviolet, visible, and infrared) and the thermal radiation from the absorber pipe (mostly low frequency infrared), the glass envelope is assumed mostly transparent to the solar spectrum of radiation, but opaque to the thermal radiation emanating from the absorber tube. The transmittive losses in the envelope to solar radiation are accounted for, however, with a transmissivity term (see Equation 2.19). These assumptions are widely used in the literature [10], [12].

Solutions to the three partial differential equations (PDEs) resulting from the energy balance can be approximated by dividing the length of the collector into n discrete sections. This converts 3 PDEs into a set of 3n ordinary differential equations (ODEs). These spatial derivatives are then approximated using a backwards finite difference method as follows:

$$\frac{dT}{dx} \approx \frac{(T(i) - T(i-1))}{\Delta x} \quad (2.4)$$

The spatial discretization scheme is shown in Figure 2.3, where each cylindrical segment has a length of Δx . The system is solved in time using Runge-Kutta numerical integration to solve each segment with respect to time.

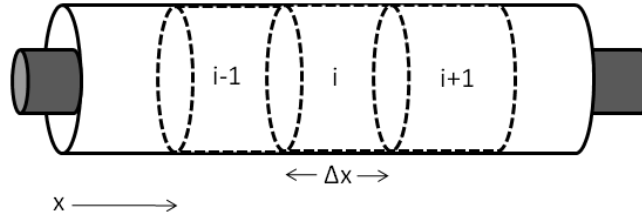


Figure 2.3: A side-view of the absorber pipe assembly.

The TES tanks are modeled by dynamic mass and energy balances for mixed tanks.

The mass balance for a tank is:

$$\rho_F \frac{dV}{dt} = \dot{m}_{in} - \dot{m}_{out} \quad (2.5)$$

where V is the total volume of HTF in the tank and the subscripts *in* and *out* refer to flow in and out of the tank, respectively.

The energy balance for each tank is:

$$\rho_F C_F \frac{d(VT)}{dt} = C_F (T_{in} \dot{m}_{in} - T \dot{m}_{out}) - UA_t (T - T_{AIR}) \quad (2.6)$$

where U is the overall heat transfer coefficient for the tank walls and A_t is the surface area of the tank subject to heat transfer. It is assumed that no heat transfer occurs from the top or bottom of either tank.

Because the volumes of HTF (V) in the tanks are not constant, the energy balances are solved for the product VT , which is then divided by V , the solution to the mass balance to obtain the tank temperature, T .

In order to prevent the tanks from violating volume constraints, the following logic is included in the tank models:

$$\text{If } V_{Tank} = V_{High} \text{ and } \dot{m}_{in,controlled} > \dot{m}_{out,controlled} \quad (2.7)$$

$$\text{Then } \dot{m}_{in} = \dot{m}_{out} = \dot{m}_{out,controlled} \quad (2.8)$$

$$\text{If } V = V_{Low} \text{ and } \dot{m}_{in,controlled} < \dot{m}_{out,controlled} \quad (2.9)$$

$$\text{Then } \dot{m}_{in} = \dot{m}_{out} = \dot{m}_{in,controlled} \quad (2.10)$$

Initially, it is assumed that the cold tank is full of HTF at a low temperature and the hot tank is at its lower-limit volume at some elevated temperature, leading to the initial conditions:

$$V_{Hot}(t=0) = V_{Low} \quad (2.11)$$

$$V_{Cold}(t=0) = V_{High} \quad (2.12)$$

$$T_{Hot}(t=0) = T_{Hot,0} \quad (2.13)$$

$$T_{Cold}(t=0) = T_{Cold,0} \quad (2.14)$$

The boiler model assumes the HTF enters a heating coil, which passes through a tank of saturated liquid water. The water side of the boiler is assumed to be at a constant temperature, while HTF inside the coil varies with time and distance along the coil. The energy balance on the HTF in the coil is as follows:

$$\rho_F C_F A_{p,i} \frac{\partial T_F}{\partial t} = \dot{m} C_F \frac{\partial T_F}{\partial z} + h_p P_{p,i} (T_B - T_F) \quad (2.15)$$

where z is the distance along the boiler coil and the subscripts p , i and B refer to the inner pipe and the boiler water temperature, respectively.

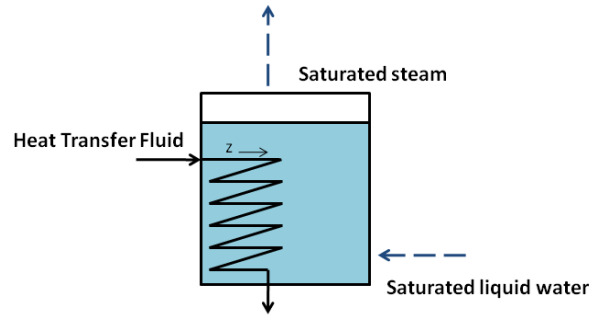


Figure 2.4: A diagram of the boiler.

The saturated steam flow rate is then computed from a steady-state energy balance on the boiler:

$$\dot{m}_F C_F (T_{F,in} - T_{F,out}) = \dot{m}_{steam} H_{fg} \quad (2.16)$$

where H_{fg} refers to the enthalpy of vaporization of the water at T_B .

The ASHRAE model was used to predict solar beam irradiance as a function of the incidence angle on the collector surface. The equation for predicting the irradiance in the direction of rays (I_N) is:

$$I_N = A \exp[-B / \cos(\theta_Z)] \quad (2.17)$$

where A and B are constants based on the month of the year and θ_Z is the solar zenith angle [13]. The amount of radiation incident on the reflector surface (I_C) is given by:

$$I_C = I_N \cos(\theta)(1 - F_C) \quad (2.18)$$

where θ is the incidence angle, which is a function of the location, the day of the year, and the time of day, and F_C is the cloud factor.

The optical efficiency is a function of ν_A (the absorptivity of the absorber pipe), τ_E (the envelope transmissivity), α_M (the mirror reflectivity), γ (the intercept factor), and K , the incidence angle modifier [14].

$$\eta_{optical} = K(\theta) \nu_A \tau_E \alpha_M \gamma \quad (2.19)$$

While parabolic trough collector systems experience several types of disturbances due to changes in ambient conditions (temperature, wind speed, etc.), cloud cover is the most critical disturbance. Cloud cover reduces the amount of solar radiation that is absorbed by the collector field. As a result, a system without thermal energy storage experiences large interruptions in power output. The cloud factor, F_C , is simulated using normally distributed random numbers, R_N , generated with mean, μ , and variance, Σ , each of which can be adjusted to represent varying degrees of cloud cover.

$$R_N \sim N(\mu, \Sigma) \quad (2.20)$$

where N represents a normal-random-number-generating function. F_C is kept between 0 and 1 by the following:

$$F_C = \begin{cases} 1 & \text{if } R_N > 1 \\ R_N & \text{if } 0 \leq R_N \leq 1 \\ 0 & \text{if } R_N < 0 \end{cases} \quad (2.21)$$

Because large disturbances greatly impact the operation of the system, automatic

control is essential to plant operation. The collector field temperature is controlled by a feedforward-plus-PID-feedback control scheme. This proactive control scheme uses measurements of direct normal irradiance (DNI) to anticipate changes in field outlet temperature. Feedback PID control is also added to reduce steady-state offsets and to account for additional disturbances (e.g. ambient temperature, wind speed, etc.). For a system with storage, the power output is controlled using a PID controller, which is activated after the hot storage tank begins charging. The PID controllers are tuned using IMC tuning relations [15]. For a system without TES, no power control is used.

In order to keep equipment well-maintained and running properly and for safety reasons, a minimum flow rate is applied to flow through the solar collector field and the rest of the system. This flow rate, 12 kg/min, contributes to heating losses, but this effect on the total performance of the system is minimal.

Results

A parabolic trough steam generation plant designed to produce 1 MW thermal with a total collector area of 3000 m² is considered. The control system is designed to control the collector outlet temperature to 390 °C. The boiler is assumed to operate at a constant temperature of 250 °C (40 bar pressure). It is assumed that a separate control system maintains the boiler temperature and pressure. Because there is no storage tank in this setup, the only manipulated variable is the HTF flow rate, which is the same through the collector field as it is through the boiler. The results of these simulations are shown in Figure 2.5 through Figure 2.7.

As Figure 2.7 indicates, the feedforward-plus-feedback controller works well to keep this temperature constant. Keeping the collector outlet temperature constant, however, causes the HTF flow rate to vary (Figure 2.6), which results in varying power output, as indicated by Figure 2.5.

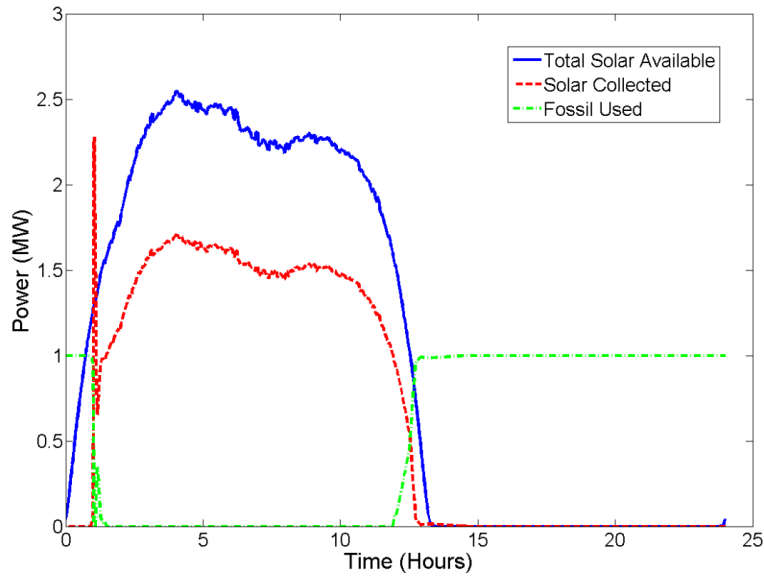


Figure 2.5: Power for the system without storage.

Because the plant is designed to produce 1 MW thermal, a backup fossil source of power (i.e. natural gas) must be used to account for any shortfall. As Figure 2.5 indicates, supplementary fossil fuel power is used whenever the solar portion of energy falls below the 1 MW threshold.

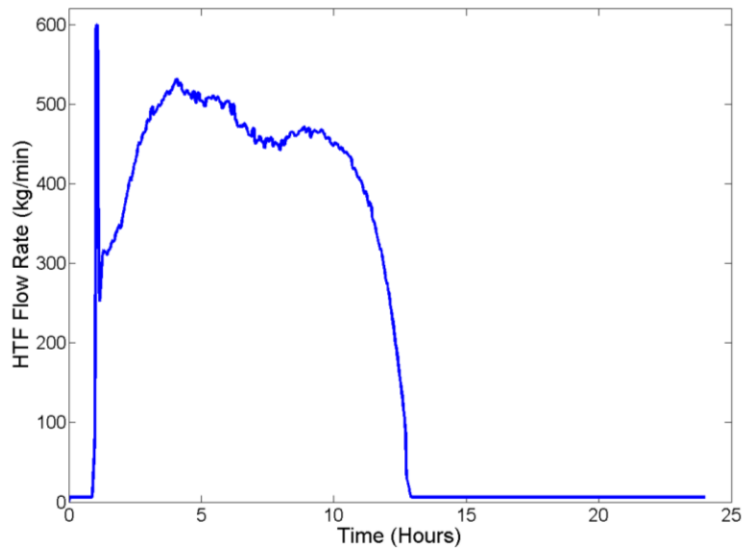


Figure 2.6: HTF flow rate for a system with no storage.

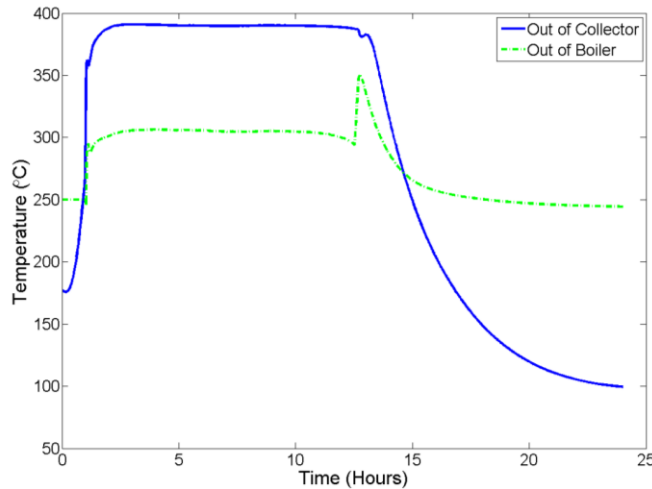


Figure 2.7: HTF temperatures for a system with no storage.

For a CSP system with no thermal storage, a control scheme designed to maintain a constant power output is not feasible, because the system can only produce power as it is available from the sun. With no storage, the system is unable to absorb excess energy when it is available and, as a result, there is no stored energy to draw upon when there is a shortage of solar radiation.

The same collector/boiler system is again considered, now with a thermal energy storage system. This setup makes it possible to control the power output and collector outlet temperature independently. The nominal thermal power output used here is 1 MW. The TES system used is the two-tank-direct system with two 150 m³ tanks, which results in 8 MWh (or 8 hours) of energy storage, given the nominal operating conditions.

The control scheme employed uses the HTF flow rate through the collector as a manipulated variable to keep the outlet temperature constant using feedforward plus feedback control. The HTF flow rate through the boiler is used to keep the power output (or equivalently, the steam generation rate) constant using a feedback controller. The results of this simulation are shown in Figure 2.8 through Figure 2.11.

As shown in Figure 2.8, the power controller keeps the power output constant at its set point. Early in the day, when more solar energy is available than the load requires, the energy is harvested by storing excess hot HTF in the hot storage tank. In Figure 2.9, all

points where the collector flow rate is greater than the boiler flow rate indicate charging of the system. When the opposite is true, the system is discharging. This allows the plant to continue to generate steam at a constant rate for several hours after sunset.

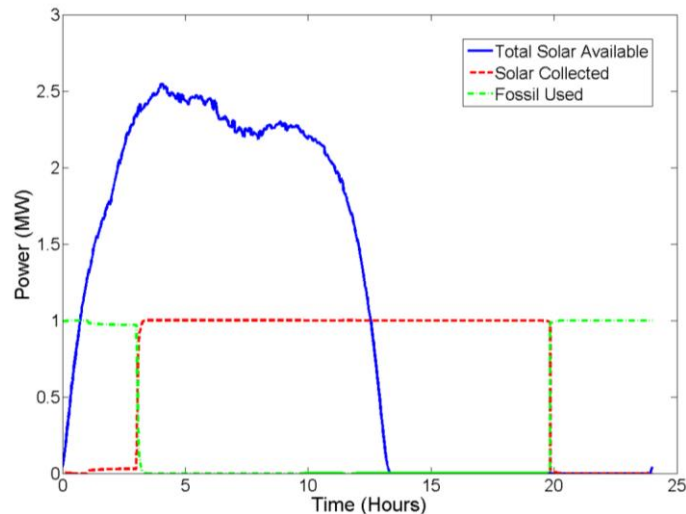


Figure 2.8: Power for the system with storage.

As indicated in Figure 2.9 through Figure 2.11, the system has completely charged at $t=11.3$ hours. However, because excess solar energy is still available, the system is allowed to overcharge. When this happens, the collector outlet temperature controller is disabled. The flow into the hot tank equals the flow out of the hot tank because the tank is full. This results in reduced flow rates through the collector field and higher temperatures out of the collector field. Additional energy is then harvested in the form of elevated temperatures. While it is beneficial to store more energy, the elevated temperatures result in larger heat losses from the collector field and thermal storage tanks. Additionally, excessive temperatures can cause damage to equipment or can lead to degradation of the HTF. When this occurs, parts of the solar field must be shut down to prevent the occurrence of excessively high temperatures.

Alternatively, more energy could be harvested by using larger tanks to keep the HTF flow rate through the collector high and the collector outlet temperature low. However, this additional capacity would only be utilized on days when conditions are ideal.

Therefore, the additional storage capacity may not be cost effective. The system, therefore, is sized to obtain an optimal combination of solar field area and storage capacity, based on minimizing the annualized costs of the plant. This analysis is done using average solar radiation data for the plant location.

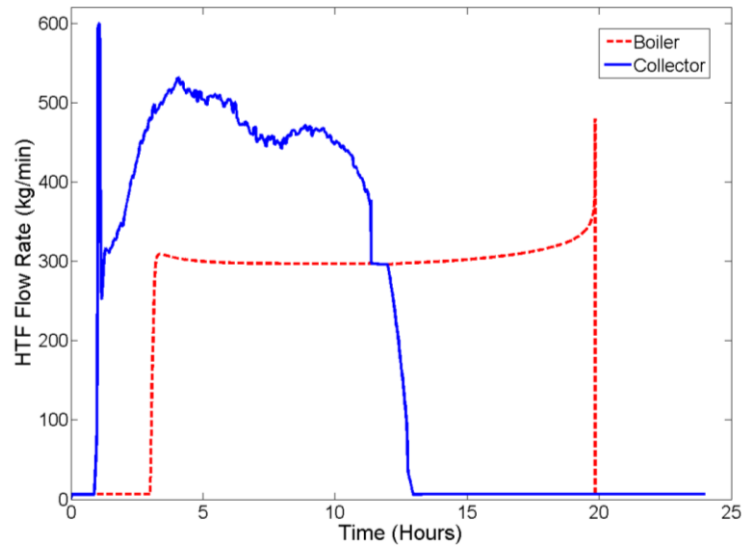


Figure 2.9: HTF flow rates for a system with thermal energy storage.

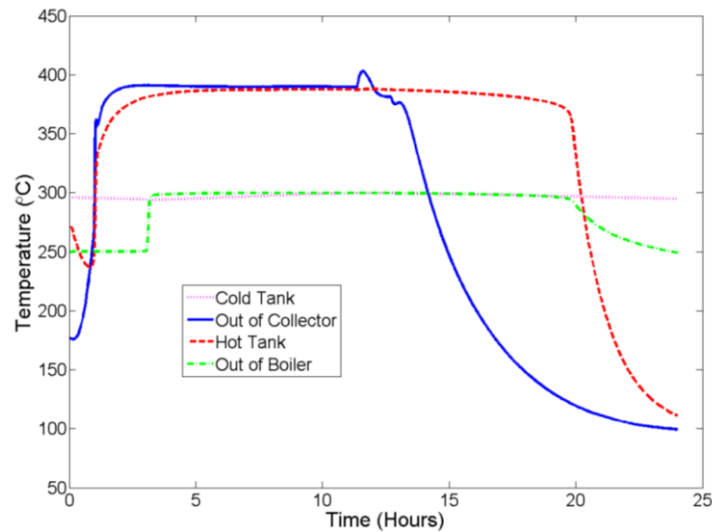


Figure 2.10: Temperatures for a system with thermal energy storage.

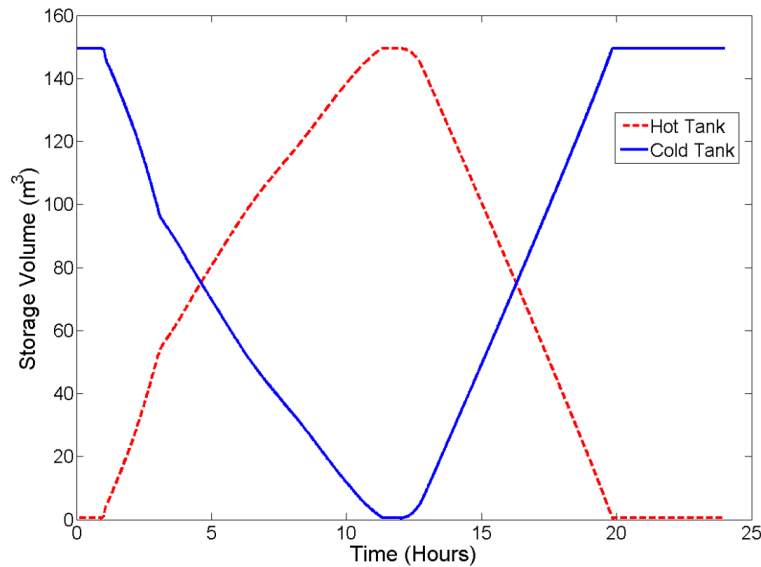


Figure 2.11: HTF fluid volume in thermal storage tanks.

When a cloudy day with larger variations in available solar energy is simulated, the system undergoes dramatic changes in power output. These results are shown in Figure 2.12 through Figure 2.14. As Figure 2.12 indicates, intermittent cloud cover causes the power delivered to the load to vary with the available solar radiation. These large fluctuations in output power put a large burden on the rest of the energy system, which may be required to meet specific loads. In this analysis, it is assumed that fossil backup fuel can be turned on and off quickly, but in actuality, the system may not have the ability to do this. For electric power generation in particular, this may cause other power plants to be required to ramp up and down quickly, which is not an efficient or ideal way to produce power.

The temperature control in this scenario is excellent, as Figure 2.14 illustrates. The temperature of the fluid exiting the boiler occasionally spikes as mass flow rates are suddenly reduced in effort to control the collector field outlet temperature. Despite accurate temperature control, the power output fluctuates dramatically.

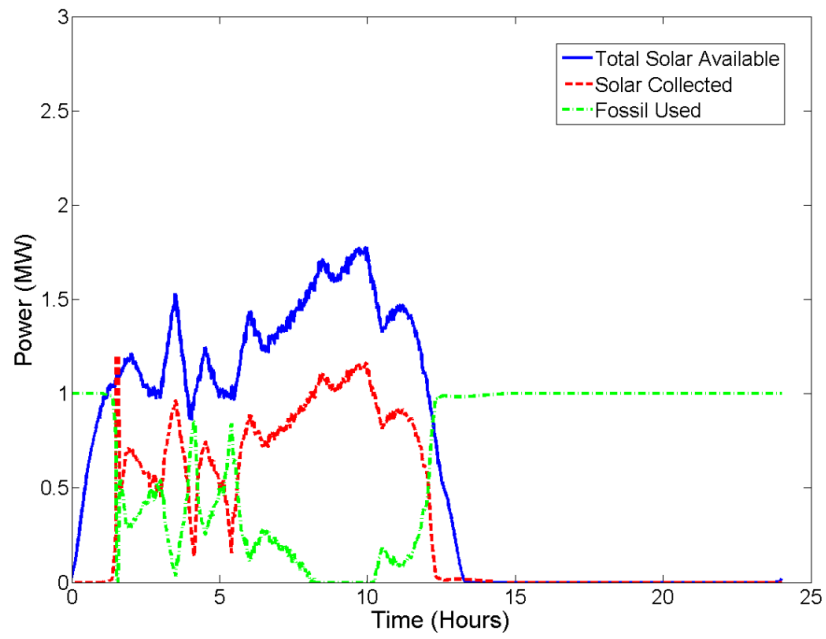


Figure 2.12: Power for system without storage on a cloudy day.

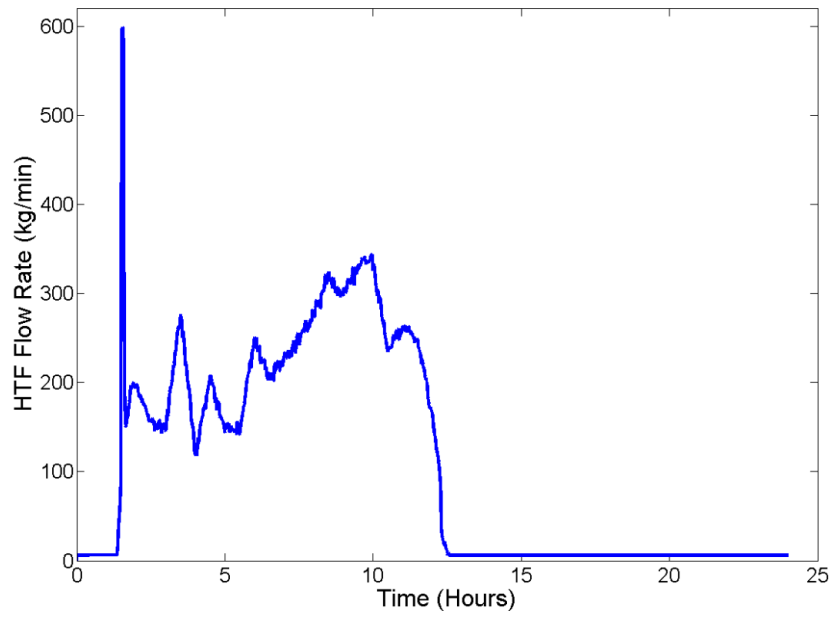


Figure 2.13: HTF flow rate for a system with no storage on a cloudy day.

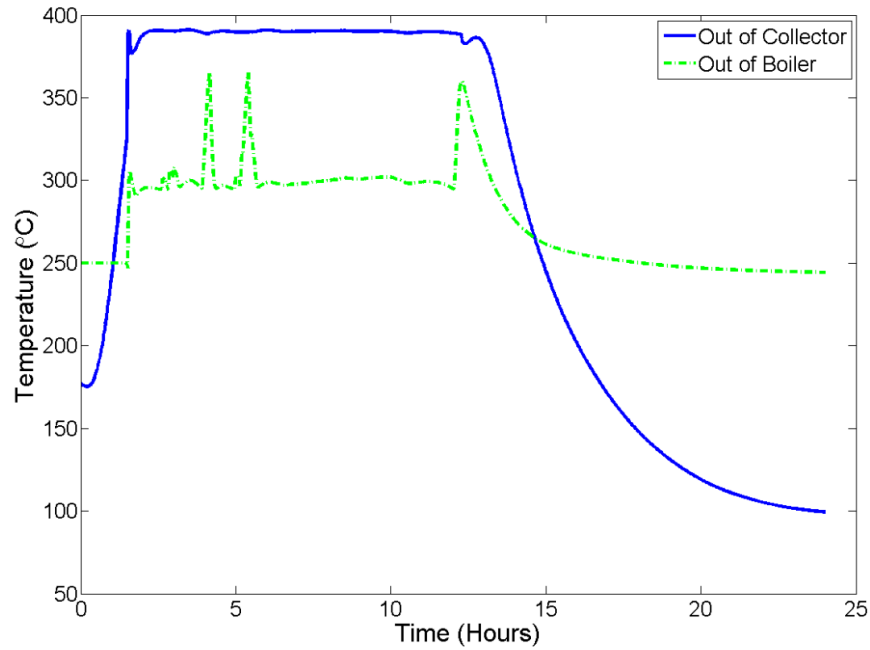


Figure 2.14: HTF temperatures for a system with no storage.

The value of thermal energy storage for control of the power output of a concentrating solar system is best seen on days when intermittent cloud cover persists. In contrast to the system with no storage, the system with storage maintains a constant power output, despite the fact that solar power is not continuously available. While it is important to control the collector outlet temperature to keep temperatures high enough to deliver heat to the load and low enough to prevent fluid degradation, it is not essential to perfectly control this outlet temperature at a constant value. Power output can still be well controlled despite small temperature fluctuations. Because the hot storage tank contains a store of energy, the boiler control system can draw upon this to maintain a constant power output.

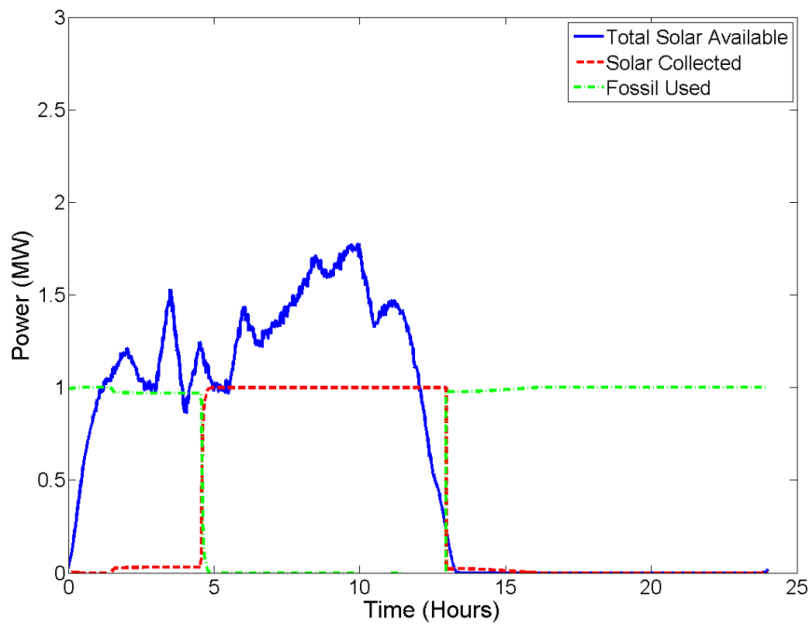


Figure 2.15: Power for a system with thermal storage on a cloudy day.

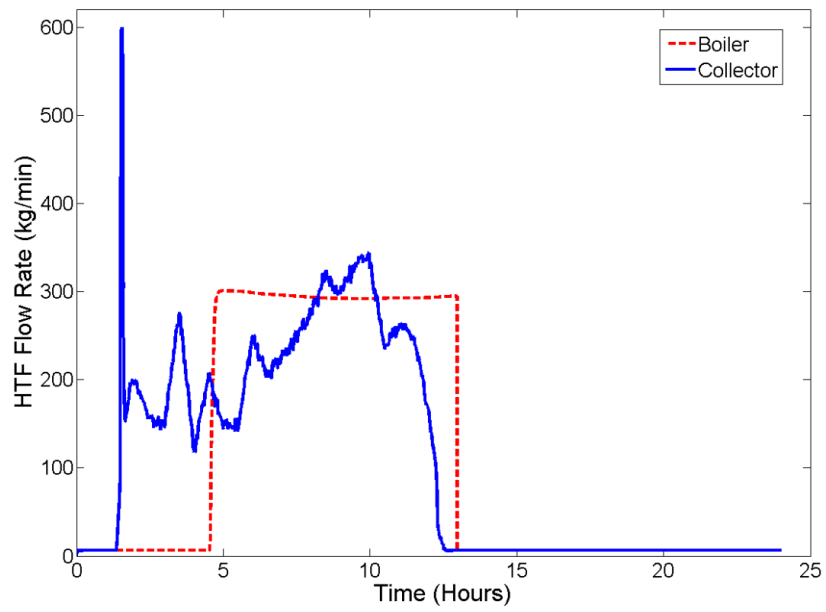


Figure 2.16: HTF flow rates for a system with storage on a cloudy day.

Because less total energy is available on a cloudy day, overcharging of the TES system does not occur in this case. The temperature of the hot storage tank, therefore, remains essentially constant at the collector outlet set point temperature of 390 °C.

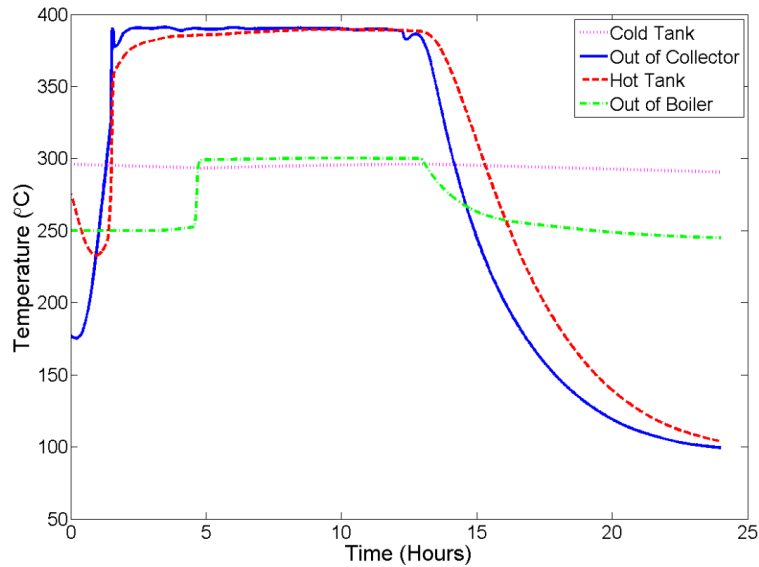


Figure 2.17: Temperatures for a system with storage on a partly cloudy day.

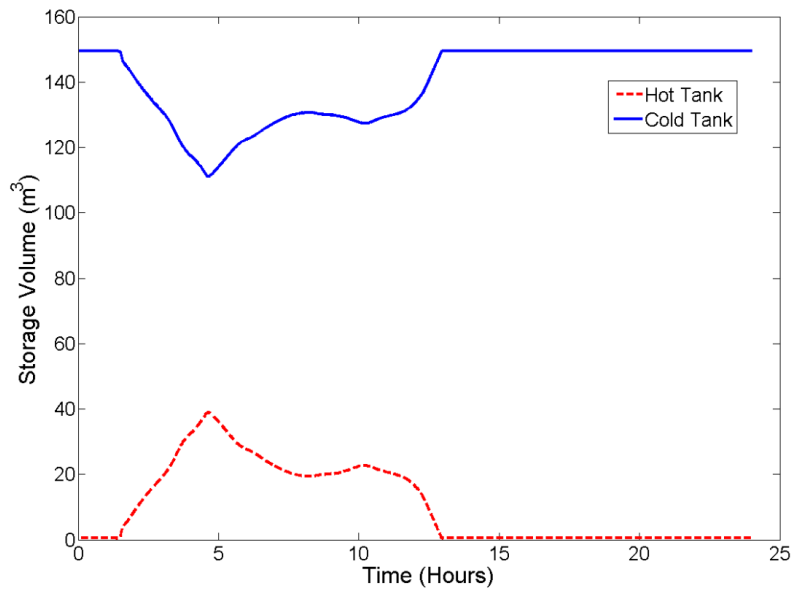


Figure 2.18: Volume of HTF in the storage tanks for a partly cloudy day.

Conclusion

A summary for each scenario considered is shown in Table 2.1. The results of these simulations show that, by adding 8 hours of storage capacity, the solar share (the fraction of energy provided by solar) of the power plant can be increased by as much as 47% to levels over 70% on a sunny day. The improvements in solar share are more meager on cloudy days. However, during intermittent cloud cover, the main benefit of thermal energy storage is the ability to maintain a constant power output by using the storage tank as a buffer between available energy and energy demand.

Table 2.1: A summary of each simulation scenario.

	Clear Day: System without Storage	Clear Day: System with Storage	Cloudy Day: System without Storage	Cloudy Day: System with Storage
Solar Energy Delivered to Load	16.48	16.82	8.40	8.49
Supplemental Fuel Required (MWh)	12.58	7.18	15.78	15.51
Solar Share	47.6%	70.1%	34.3%	35.4%

It has been shown that adding thermal energy storage to the energy system provides the important benefit of taking an intermittent energy source and converting it to a constant power source. A simple control scheme was proposed for doing this. However, more advanced control and optimization schemes can be pursued in order to more fully leverage the thermal energy storage. Optimal control schemes can be implemented to minimize operating costs or maximize the total benefit that solar energy provides to the system. For example, on cloudy days, it may be optimal to provide heat at lower temperatures and allow the system to rely partially on supplemental fossil fuel, thereby reducing the energy losses to the environment. When optimal control schemes are considered, energy storage provides the system with extra degrees of freedom that can be used to enhance the system's overall

performance.

Solar thermal power faces many economic and technical hurdles, which must be overcome to be truly competitive with fossil fuel energy. Thermal energy storage allows these systems to overcome many of the problems associated with solar power intermittency. Advanced control and optimization techniques are still needed to help these plants operate more efficiently, thereby making them more technically and economically viable.

Nomenclature

Symbol	Description	Units
A_A	Absorber pipe cross-sectional area	m^2
$A_{A,i}$	Inner pipe cross-sectional area for absorber pipe	m^2
A_E	Glass envelope cross-sectional area	m^2
$A_{P,i}$	Inner pipe cross-sectional area for boiler pipe	m^2
A_t	Tank area subject to heat transfer	m^2
C_A	Absorber pipe specific heat capacity	J/(kgK)
C_E	Glass envelope specific heat capacity	J/(kgK)
C_F	Heat transfer fluid specific heat capacity	J/(kgK)
F_C	Cloud factor	None
h_{air}	Ambient convective heat transfer coefficient	W/($m^2\text{°C}$)
H_{fg}	Heat of vaporization of water (@ 40 bar)	J/kg
h_p	Convective heat transfer coefficient for inner pipe	W/($m^2\text{°C}$)
I_C	Solar radiation incident on collector surface	W/ m^2
I_N	Solar irradiance in direction of rays	W/ m^2
K	Incidence angle modifier	None
L	Total solar collector length	m
\dot{m}	Mass flow rate	kg/s
n_{sc}	Number of solar collector assemblies	None
$P_{A,i}$	Inner absorber pipe perimeter	m
$P_{A,o}$	Outer absorber pipe perimeter	m
$r_{A,i}$	Inner absorber pipe radius	m
$r_{A,o}$	Outer absorber pipe radius	m
t	time	s
T_A	Temperature of fluid in absorber pipe	°C or K

T_{AIR}	Ambient air temperature	°C or K
T_{SKY}	Effective sky temperature for radiative heat transfer	°C or K
T_B	Boiler water temperature	°C or K
T_E	Temperature of glass envelope	°C or K
T_F	Temperature of heat transfer fluid	°C or K
U	Storage tank overall heat transfer coefficient	W/(m ² °C)
V	Volume of fluid in storage tank	m ³
w	Width of mirror aperture	m
x	Distance along solar collector length	m
z	Distance along boiler pipe length	m
α_m	Mirror reflectivity	None
γ	Intercept factor	None
ϵ_A	Absorber pipe emissivity	None
ϵ_E	Glass envelope emissivity	None
$\eta_{optical}$	Total optical efficiency	None
θ	Incidence angle on collector aperture	Radians
θ_z	Solar zenith angle	Radians
ρ_A	Absorber pipe density	Kg/m ³
ρ_E	Glass envelope density	Kg/m ³
ρ_F	Heat transfer fluid density	Kg/m ³
σ	Stefan-Boltzmann constant	W/(m ² K ⁴)
τ_E	Transmissivity of glass envelope	None
ν_A	Absorptivity of absorber pipe	None

CHAPTER 3 : DYNAMIC OPTIMIZATION OF A HYBRID SOLAR THERMAL SYSTEM WITH THERMAL ENERGY STORAGE

Introduction

Solar energy has tremendous potential to produce emission-free electricity [16]. With similarities to conventional power generation methods, solar thermal, or concentrated solar power (CSP), can be a low-cost alternative to fossil-fuel-based systems [17]. In order to provide reliable base load power, however, CSP systems must be equipped with large-scale thermal energy storage (TES) [18] and/or a backup energy source, such as natural gas or diesel fuel [16], [19].

Because of the intermittency of solar energy, it generally must rely on other energy technologies to ensure that consumer demand for power is always met. Hybrid systems, which combine solar thermal and other energy technologies, have been proposed as an alternative to solar-only power generation [20]. For instance, solar thermal power can be combined with conventional power generation technology so that solar energy is aided by proven power generation technology, such as gas and steam turbines [21]. When gas and steam turbines are used in tandem, solar energy can be used to supplement the steam cycle in an integrated solar and combined cycle (ISCC) power plant [22]. With concentrating solar collectors, solar heat can be delivered at higher temperatures to improve the Carnot efficiency of a solar gas turbine, where the air is heated by solar radiation before entering the gas turbine [23], [24].

Hybrid solar systems have also been proposed to include chemical processes, such as methane steam reforming as an intermediate step before combustion and delivery to a gas turbine [25] or chemical looping combustion [26]. Studies have also been done to determine how CSP can be coupled with other renewable technologies, such as wind, to better match consumer electricity demand [27].

Hybridization of CSP with other power production technologies represents a paradigm shift: rather than competing with other technologies as a sole power source, CSP can be used to complement these technologies. For instance, combining solar thermal systems with a fossil fuel, such as natural gas, gives the system operator more flexibility to determine how to run the system. While these fossil fuels are generally thought of as backup fuel sources to use during periods of cloud cover, dynamic optimization reveals that there are times when it is beneficial to use natural gas as a supplement while so that solar collectors can be run at lower temperatures. Optimizing the system so that the maximum amount of solar energy is harvested allows the solar and fossil components of the system to perform synergistically, resulting in more efficient performance. TES, when combined with CSP, provides additional flexibility, so that power can be produced on demand [28], [29], [30]. These degrees of freedom can also be exploited using optimization, so that an objective can be maximized or minimized over a time horizon [31], [32]. The goal of this work is to illustrate that the addition of fossil fuel to a CSP system can actually increase the total amount of solar energy that can be harnessed. This requires dynamic optimization, so that the degrees of freedom from both the backup fuel and the TES can be fully exploited to achieve an objective: maximizing the total solar energy collected over a 24 hour period.

Model Development

Parabolic troughs are the most prevalent and technologically mature CSP receiver technology [33], and therefore, provide an ideal demonstration of how optimization can improve CSP systems. This work uses the model developed by Powell and Edgar of a 1 MW_{th} parabolic trough CSP plant [29]. A simplified plant schematic is shown in Figure 3.1. This system uses a two-tank direct method for TES, where the heat transfer fluid, a synthetic oil in this case, flows from the cold tank, is heated in the solar field, and is delivered to the hot tank. The fluid flows from the hot tank, as heat is delivered to the steam generator (labeled heat sink) and the (now cooled) fluid returns to the cold storage tank. In

a CSP system, this would represent the steam generator, which produces steam for a turbine, but it can also represent an industrial heating load. The load is held constant using a combination of solar and gas energy, so modeling the power block was out of the scope of this study.

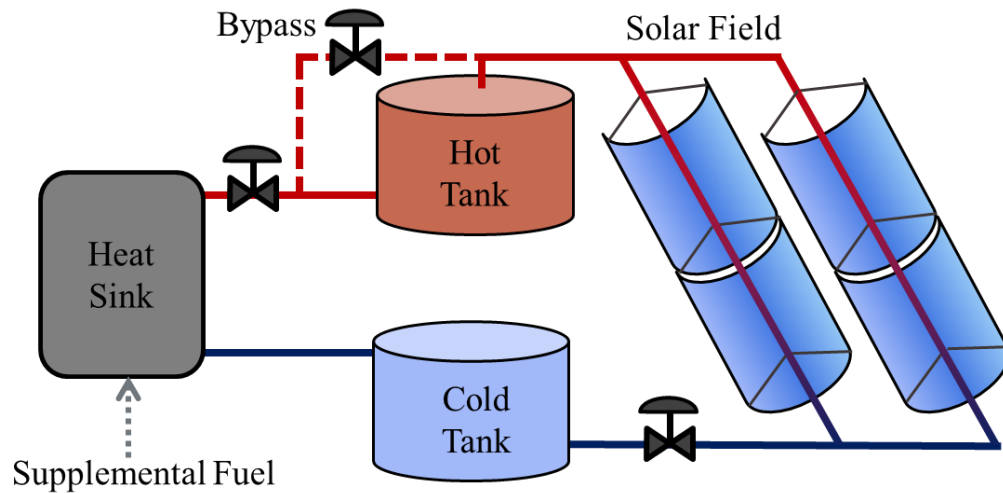


Figure 3.1: A parabolic trough CSP plant with two tank direct TES system.

As demonstrated in [29], the solar field is modeled by computing spatially-dependent energy balances on the heat transfer fluid, receiver tube, and glass envelope. Direct normal irradiance (DNI) is reflected off the parabolic mirrors and focused onto the receiver assembly, as shown in Figure 3.2. These energy balances are used to compute temperature as a function of distance down the collector assembly as a Partial Differential Equation (PDE). The heat transfer fluid exchanges heat by convection with the absorber pipe. Its energy balance is shown in (3.1).

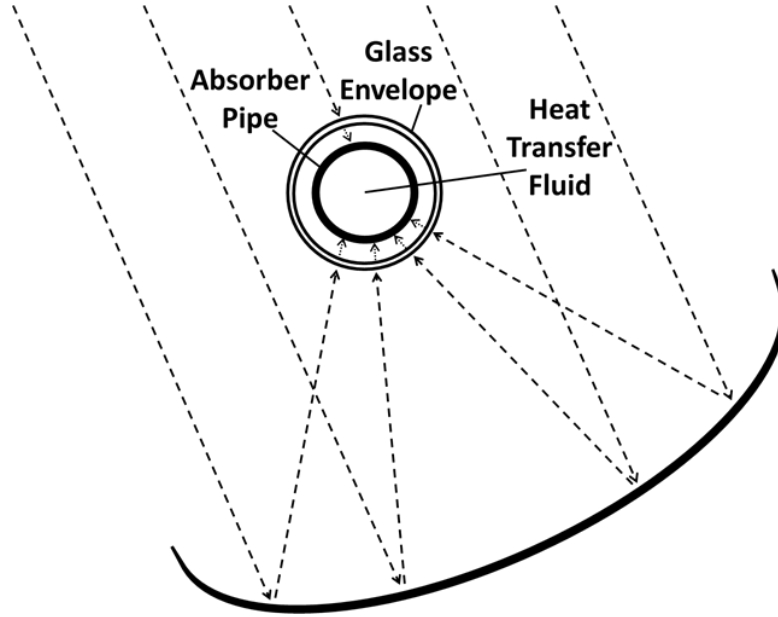


Figure 3.2: A cross-sectional view of the receiver assembly.

$$\rho_F C_F A_{A,i} \frac{\partial T_F}{\partial t} = \dot{m} C_F \frac{\partial T_F}{\partial x} + h_p P_{A,i} (T_A - T_F) \quad (3.1)$$

The absorber pipe exchanges heat with the heat transfer fluid as well as with the glass envelope by radiation. Convection between these surfaces is assumed negligible because of the vacuum between them. The absorber pipe also has a source term (I_C) as it absorbs the solar flux after it is reflected off of the mirrors. The absorber pipe energy balance is shown in (3.2).

$$\rho_A C_A A_A \frac{\partial T_A}{\partial t} = h_p P_{A,i} (T_F - T_A) - \frac{\sigma}{\frac{1}{\varepsilon_A} + \frac{1 - \varepsilon_E}{\varepsilon_E} \left(\frac{r_{A,o}}{r_{E,i}} \right)} P_{A,o} (T_A^4 - T_E^4) + I_C \eta_{optical} w \quad (3.2)$$

In addition to exchanging heat with the absorber pipe loses heat by radiation to the environment by convection and radiation. The absorber pipe energy balance is shown in (3.3).

$$\rho_E C_E A_E \frac{\partial T_E}{\partial t} = \frac{\sigma}{\frac{1}{\varepsilon_A} + \frac{1 - \varepsilon_E}{\varepsilon_E} \left(\frac{r_{A,o}}{r_{E,i}} \right)} P_{A,i} (T_A^4 - T_E^4) - \sigma \varepsilon_E P_{E,o} (T_E^4 - T_{SKY}^4) - h_{AIR} P_{E,o} (T_E - T_{AIR}) \quad (3.3)$$

This set of PDEs can be approximated as a set of Ordinary Differential Equations (ODEs) by spatial discretization of the receiver assembly. See Chapter 2 and [29] for more detailed information about the model development and the assumptions made in this model.

Because radiative heat losses are proportional to T^4 , they can be significant at high temperatures, making it critical to consider these losses when determining optimal operating conditions. Increased flow rates through the solar field reduce the operating temperature of the field and therefore, the heat losses. Increased flow rates, however, also mean more power consumed by pumping and reduced Carnot efficiency in the power block. The efficiency also changes with the solar flux level, making it important to consider optimizing in real-time [34]. If a dispatchable energy source, such as natural gas, is available, high power cycle efficiencies can still be achieved while minimizing radiative heat losses. Temperature in the solar field can be adjusted so that efficiency is maximized, while the system relies on the backup heat source to reach the appropriate temperature for the power cycle.

Mass and energy balances are used to describe the thermal storage tanks, with the mass balance given in (3.4) and the energy balance in (3.5).

$$\rho_F \frac{dV}{dt} = \dot{m}_{in} - \dot{m}_{out} \quad (3.4)$$

$$\rho_F C_F \frac{d(VT)}{dt} = C_F (T_{in} \dot{m}_{in} - T \dot{m}_{out}) - UA_t (T - T_{AIR}) \quad (3.5)$$

The model used in this work deviates from Powell and Edgar's work in that a storage bypass (shown in Figure 3.1) is added. The ability to bypass the storage tank can be used to prevent mixing fluids at different temperatures, which leads to destruction of exergy. This was not an issue in the previous work because the solar field outlet temperature was maintained at a constant level, so tank temperature fluctuated very little

[29]. Adding a bypass gives the system an additional mode of operation to use in optimization.

The model for the steam generator is based on an energy balance between the heat transfer fluid in the boiler tubes and the steam/water mixture (assumed saturated) on the shell side of the boiler. This simple model, also from [29] is given in (3.6).

$$\rho_F C_F A_{p,i} \frac{\partial T_F}{\partial t} = \dot{m} C_F \frac{\partial T_F}{\partial z} + h_p P_{B,i} (T_B - T_F) \quad (3.6)$$

The CSP plant produces thermal power at a constant rate, by a combination of solar heat and supplemental heat. This power output is held fixed at 1 MW_{th}, therefore, when the solar power is below this level, the supplemental fuel is burned to bring the system up to the set point of 1 MW_{th}. The solar heat output is represented by a steady state relationship, given in (3.7), where thermal power is calculated from the rate of heat transfer in the boiler.

$$\dot{q}_{solar} = \dot{m} C_F (T_{B,in} - T_{B,out}) \quad (3.7)$$

The supplemental heat is used whenever solar heat is below the 1 MW_{th} set point, as given in (3.8).

$$\dot{q}_{supp} = \begin{cases} 1 - \dot{q}_{solar}, & \text{if } \dot{q}_{solar} < 1 \text{ MW}_{th} \\ 0, & \text{otherwise} \end{cases} \quad (3.8)$$

Optimization Problem Formulation

Because of the intermittency of solar irradiance and the nonlinearities of the system, controlling the temperature in the solar field is not a trivial task [7], [35]. Often, model-based control techniques are recommended. In general, these techniques use a predictive model of the system to solve for optimal performance in terms of tracking a set-point or rejecting disturbances [36], [37]. A model predictive control (MPC) strategy can be very effective in regulating the system's faster dynamics, i.e. those of the solar collectors.

The addition of TES introduces slower dynamics to the system and additional opportunities for optimizing over a longer time horizon while leveraging the degrees of freedom that TES provides. Using storage, solar heat can be collected and stored/delivered at different temperatures, depending on the optimal solution, which is a function of ambient conditions over the course of the time horizon. Because these conditions fluctuate, dynamic optimization requires the incorporation of weather forecast data where the problem can be resolved at a later time step to account for any changes that occur in the forecast or the plant itself [38]. CSP plants are particularly dependent on DNI, so dynamic optimization requires a DNI forecast. While this is beyond the scope of this work, it is assumed that a reliable DNI forecast is available using methods similar to those found in [39], [40].

With TES, a backup fuel source, and a reliable DNI forecast, the CSP system can be optimized so that the solar energy collected and delivered to the heat sink over the time horizon is maximized. Alternatively, the backup fuel used can be minimized, while maintaining a specific thermal power output to the heat sink. The objective function (3.9) is designed to minimize the total supplemental and pumping energy needed, while maintaining a constant total heat output.

$$\min_u \int_{t_0}^{t_f} (\dot{q}_{supp} + \beta \dot{p}_{pump}) dt \quad (3.9)$$

The decision variables in this system are the heat transfer fluid flow rates through the solar field, through the bypass loop, and from the hot tank. While there are a total of five flow rates, only three are independent because of the mass flow relationships that exist for the splitter before the hot tank and the junction immediately after the hot tank. These relationships are shown in (3.10) and (3.11).

$$\dot{m}_{bypass} + \dot{m}_{hot,out} = \dot{m}_{sink} \quad (3.10)$$

$$\dot{m}_{field} + \dot{m}_{hot,in} = \dot{m}_{bypass} \quad (3.11)$$

Additionally, a steady state energy balance around the junction that combines bypass flow and flow from the hot tank is used to determine the temperature of the fluid before it enters the heat sink. This relationship is shown in (3.12).

$$C_{HTF} \left(\dot{m}_{bypass} T_{field,out} + \dot{m}_{hot,out} T_{hot} \right) = \dot{m}_{sink} C_{HTF} T_{B,in} \quad (3.12)$$

Inequality constraints are also added to the system to ensure that only physically implementable solutions are obtained. These constraints include non-negativity and upper limits for flow rates (3.13), upper and lower limits for storage volumes of both tanks (3.14), and upper limits on field outlet temperature (3.15). The flow limits in (3.13) apply for all flow rates in the system.

$$0 \leq \dot{m} \leq \dot{m}_{max} \quad (3.13)$$

$$V_{min} \leq V_{tank} \leq V_{max} \quad (3.14)$$

$$T_{field,out} \leq T_{max} \quad (3.15)$$

Because it is desirable to represent the system as a continuous set of equations so that efficient solution methods can be implemented, the logical relationship in (3.8) requires re-formulation. A mathematical program of equilibrium constraints (MPEC) is introduced. This set of equations, shown in (3.16)-(3.19), uses complementarity constraints to enforce some logical conditions.

$$\dot{q}_{solar} - \dot{q}_d = v_p - v_n \quad (3.16)$$

$$\dot{q}_{supp} = \dot{q}_d - \dot{q}_{solar} + v_p \quad (3.17)$$

$$v_p v_n \leq 0 \quad (3.18)$$

$$v_p, v_n \geq 0 \quad (3.19)$$

The inequality in (3.19) ensures that each of these slack variables (v_n and v_p) are nonnegative, while the inequality in (3.18) ensures that at least one of them must always be zero. When the left hand side of (3.16) is negative (meaning that the solar heat falls short of the demand), v_p must equal zero. Equation (3.17) then determines the supplemental power needed to reach the set point. When the left hand side of (3.16) is greater than or equal to zero (meaning that the solar heat meets or exceeds demand), the supplemental heat required is zero by (3.16) and (3.17). See [41], [42], [43] for more information on MPEC formulations.

With all of the constraints developed, the dynamic optimization problem becomes the total supplemental and pumping energy subject to the system model (see Equation 2.20). Each of the constraints shown in (3.10)-(3.19) must be satisfied at every point in the time horizon.

$$\min_{\dot{m}_{field}, \dot{m}_{bypass}, \dot{m}_{hot,out}} \int_{t_0}^{t_f} \left(\dot{q}_{supp} + \beta \dot{p}_{pump} \right) dt + \phi \quad (3.20)$$

s.t. (3.10)-(3.19)

In order to prevent excessive control moves and ensure an optimal solution that could be reasonably implemented, the problem is carefully tuned using the extra term (ϕ) in the objective function. This term adds a small penalty to the objective function to prevent the decision variables from changing too drastically from one time step to another, resulting

in operational wear and tear due to cycling of valves, pumps, and thermal cycling. When properly tuned, this ensures that the system yields a smoother optimal solution that would be more easily executed in an actual system. A quadratic penalty term is used in this work and is shown in (3.21). This function penalizes the square of changes in the control moves (u) from one time step ($i-1$) to the next (i), including the most recent past control move (u_0). The variable ε determines the magnitude of this penalty term in the objective function and is determined through trial and error that balances energy use with excessive movement of the process. While adding the penalty term yields more smooth solutions, it also negatively impacts the objective function, so this term must be carefully tuned so that significant energy savings are still achieved.

$$\phi = \sum_{i=1}^N \chi (u_i - u_{i-1})^2 \quad (3.21)$$

Solution Method

The system represented in (3.10)-(3.19) contains both differential and algebraic equations, making it a system of Partial Differential Algebraic Equations (PDAEs). Optimizing while ensuring that all PDAEs are satisfied, can be numerically challenging due to the large number of variables and equations from the discretized system. While three degrees of freedom are identified at each time instance, these variables must be chosen continuously over a time horizon, making a large set of feasible potential solutions. To reduce the dimensionality of the problem, the time horizon is discretized into smaller increments so that the solution has a finite number of decision variables. Using a sequential method, the decision variables for each time interval are specified pre-simulation. Given these inputs, the simulation is then carried out to compute the value of the objective function. This is repeated multiple times until the gradient of the objective function can be approximated using finite differences. Because the sequential method requires simulating the system repeatedly, it is generally inefficient for problems with many decision variables.

The more efficient simultaneous method is employed in this work. This method approximates differential equations as algebraic equations using orthogonal collocation on finite elements transforming the set of equations into a purely algebraic representation. The optimization problem can then be solved using standard Nonlinear Programming (NLP) solvers. For more information about simultaneous solution strategies for dynamic optimization, see [44]. The dynamic optimization problem is formulated and solved using APMonitor, an advanced modeling language, which specializes in solving and optimizing DAE systems using the simultaneous method [45].

Results

The dynamic optimization scheme formulated above is evaluated under three different scenarios: (1) a sunny day with no cloud cover, (2) a day with partial cloud cover in the morning, then clear skies in the afternoon, and (3) a day with intermittent sunshine throughout the day. The DNI values (accounting for tracking and optical losses) shown for each scenario are shown in Figure 3.3.

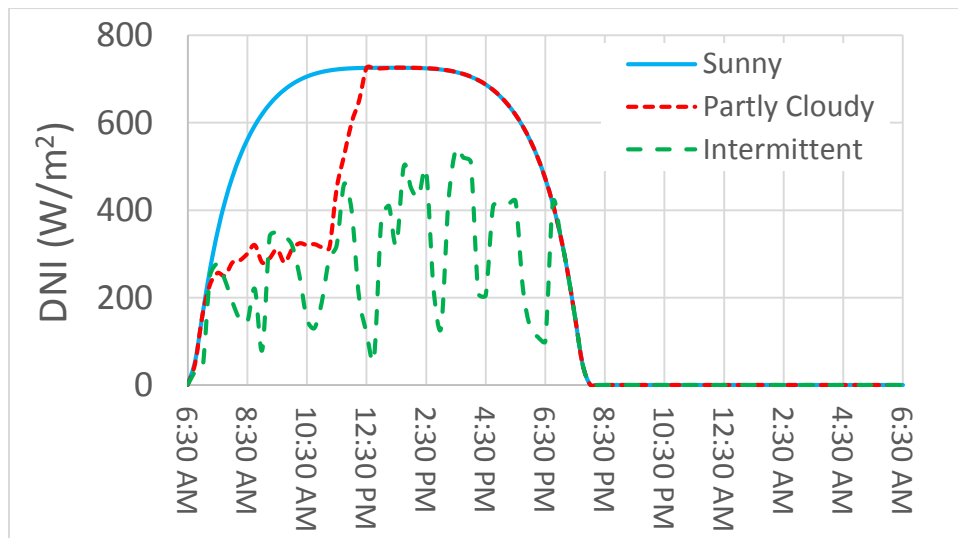


Figure 3.3: DNI in W/m^2 for each of the three scenarios.

The simulation is first run using the control scheme from [29], where the solar field outlet temperature is controlled to a constant level using the solar field flow rate as a

manipulated variable. Once sufficient storage is available, the thermal power output is controlled using the flow through the heat sink as a manipulated variable. The results for the scenario with a partly cloudy morning are shown in Figure 3.4 through Figure 3.7. As Figure 3.4 indicates, the power can be controlled very effectively using the stored energy in the hot tank. The solar field outlet temperature, shown in Figure 3.5, is also maintained easily. The two tank storage system serves as a buffer between the supply side (the solar field) and the demand side (the heat sink) of the system. As Figure 3.6 indicates, the flow rates in each of these sections can be altered individually, leading to the conclusion that, given sufficient storage, the temperature and power of the CSP plant can be controlled independent of each other. The storage system also allows the CSP plant to continue producing thermal power for several hours beyond sunset, as there is stored energy in the tanks until roughly 11:00 PM, as Figure 3.7 shows.

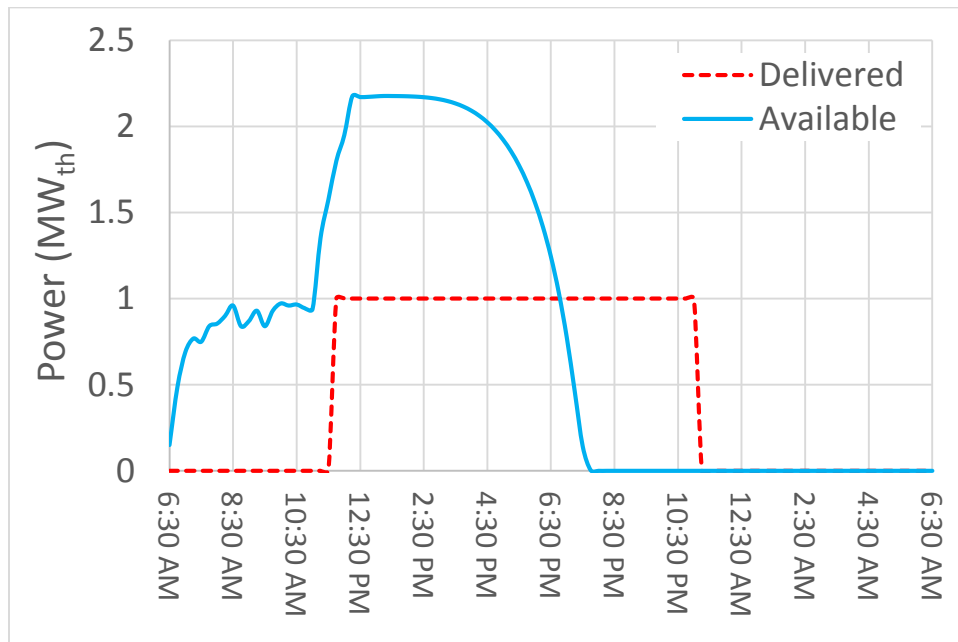


Figure 3.4: Solar power using standard control scheme.

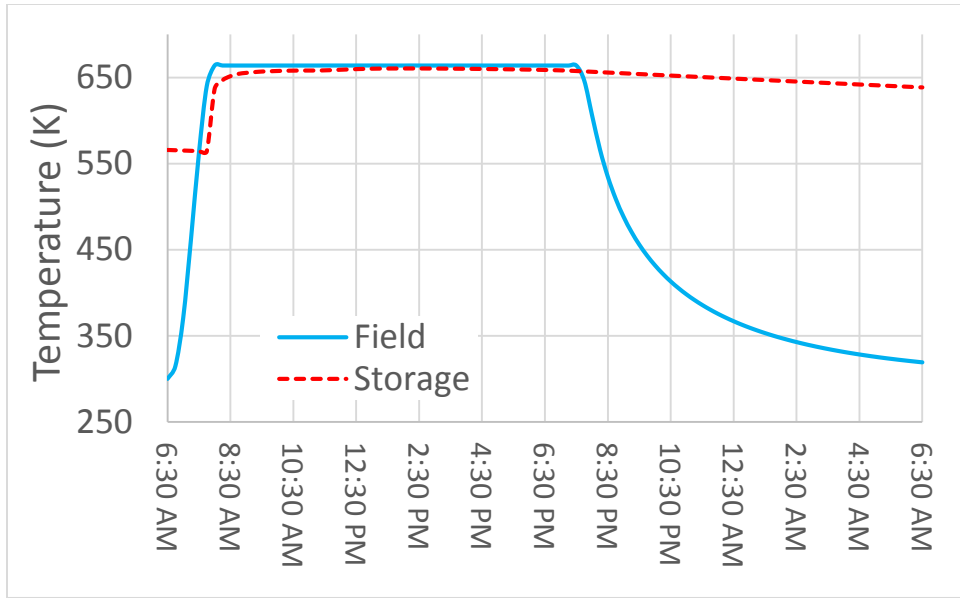


Figure 3.5: Temperatures using a standard control scheme.

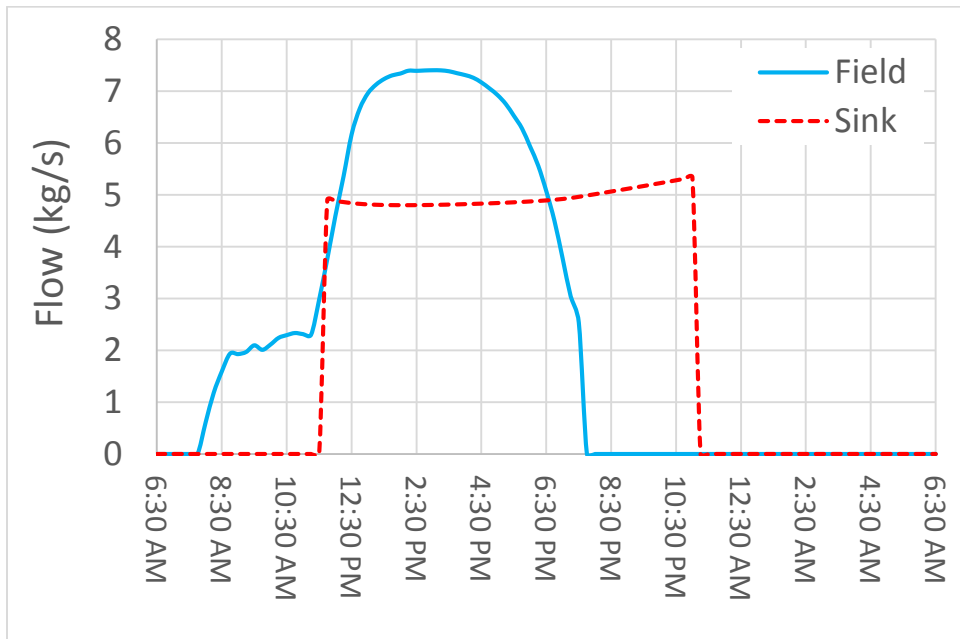


Figure 3.6: Flow rates when using a standard control scheme.

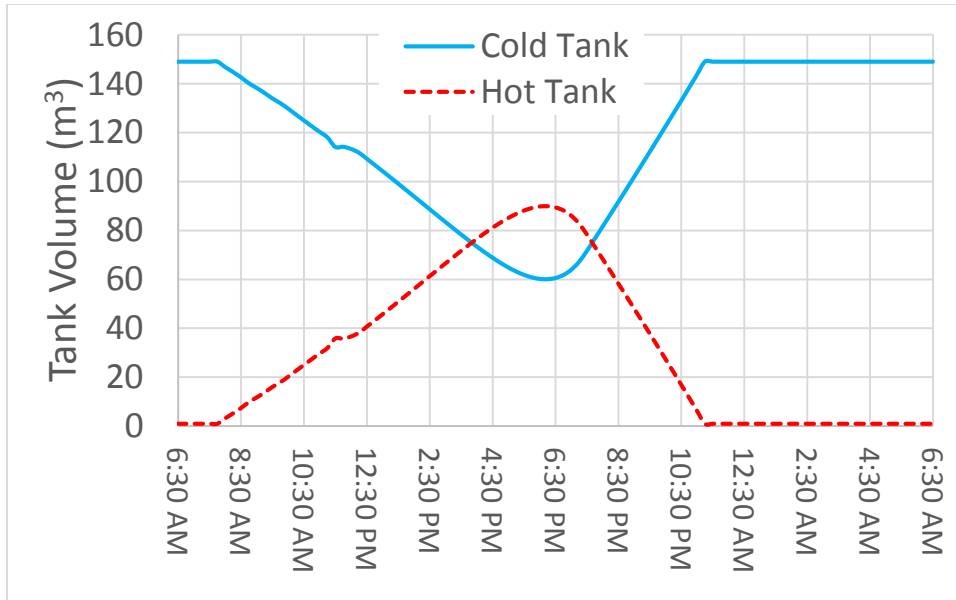


Figure 3.7: Storage volume for standard control scheme.

These simulation results highlight the value of TES in rejecting disturbances and extending the operating hours of a CSP system. The TES decouples supply and demand of energy so that power can be regulated to meet demand, despite fluctuating solar irradiance, provided that stored energy is available in the TES system. When the power delivered by solar falls short of the 1 MW_{th} set point, the backup source of energy can be activated so that the system delivers a constant supply of heat.

As demonstrated in the above results, TES gives a CSP system enhanced operational ability so that both power and temperature can be regulated effectively with a relatively simple control scheme. TES also gives the CSP system additional degrees of freedom which can be exploited through optimization. This allows the solar component of the system to perform synergistically with the supplemental fuel so that optimal performance is achieved, in this case, minimizing the total amount of supplemental fuel that must be consumed while meeting a constant 1 MW_{th} demand for 24 hours. In order to achieve this, the 24 hour time horizon is discretized into 15 minute increments, during

which, each decision variable (flow rate) is held constant. The optimal results are shown in Figure 3.8 through Figure 3.11.

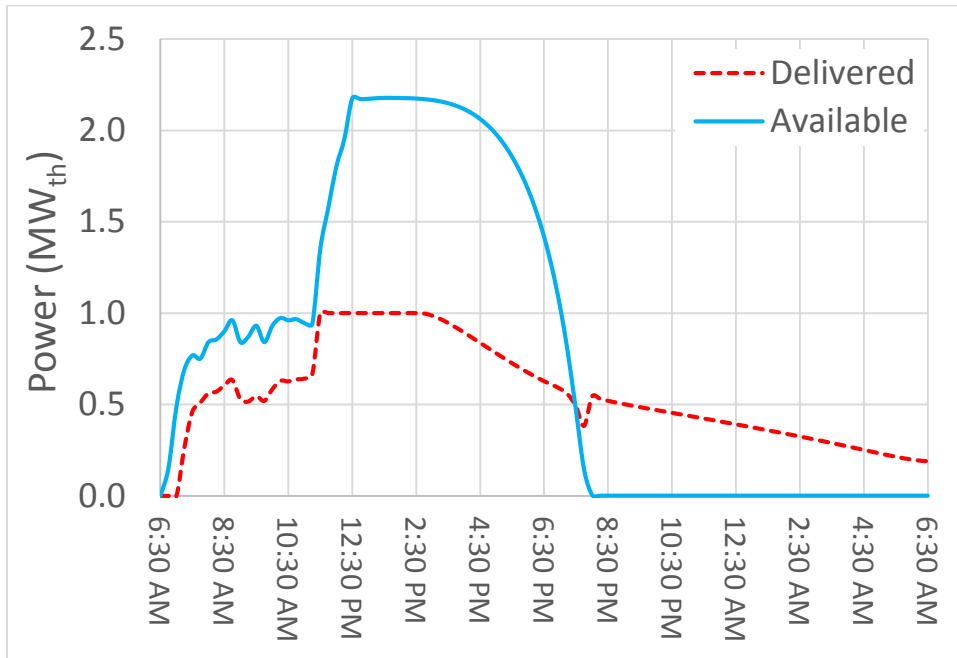


Figure 3.8: Power for dynamic optimization scheme.

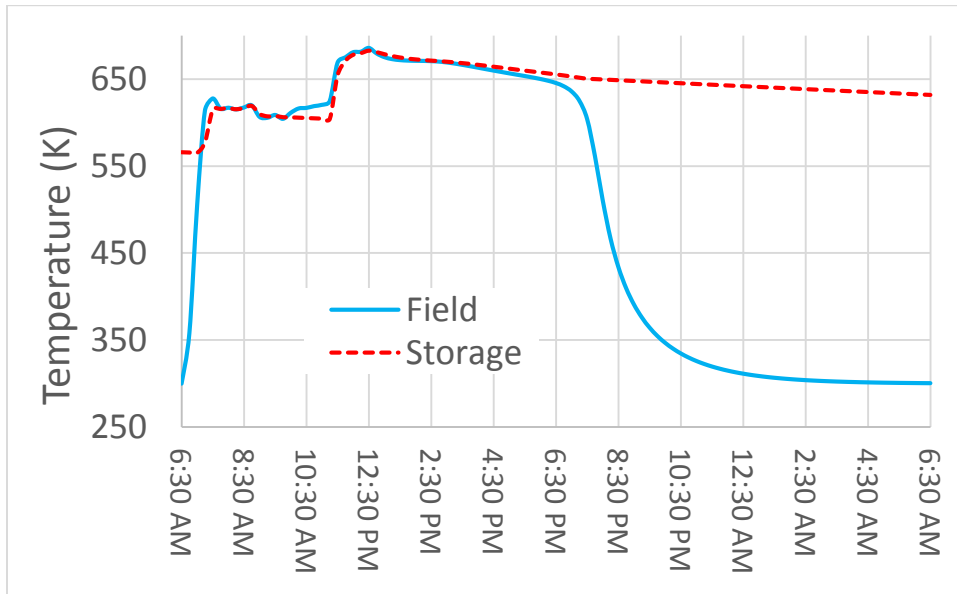


Figure 3.9: Temperatures for dynamic optimization scheme.

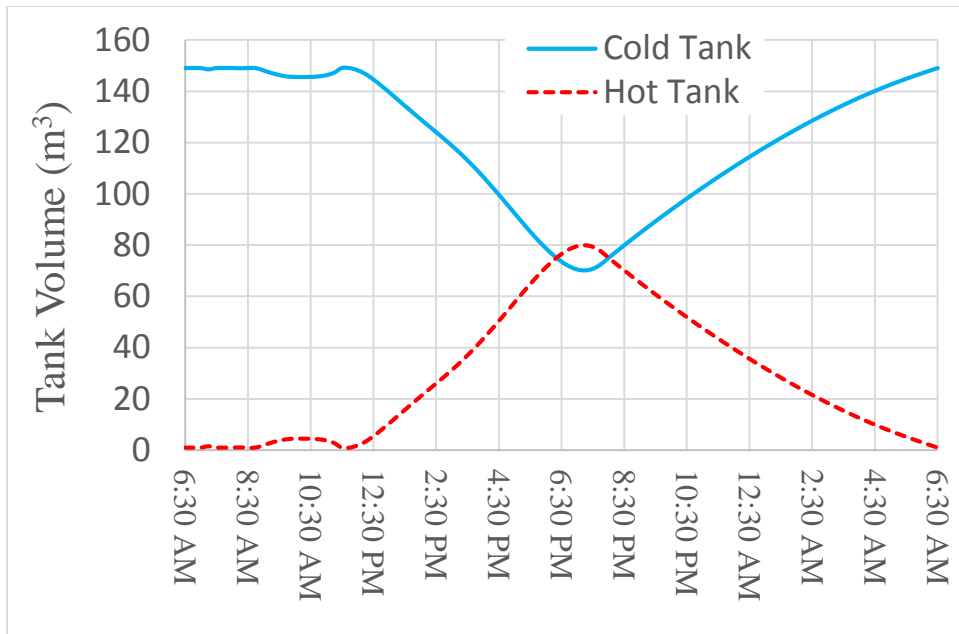


Figure 3.10: Storage tank volumes when using dynamic optimization.

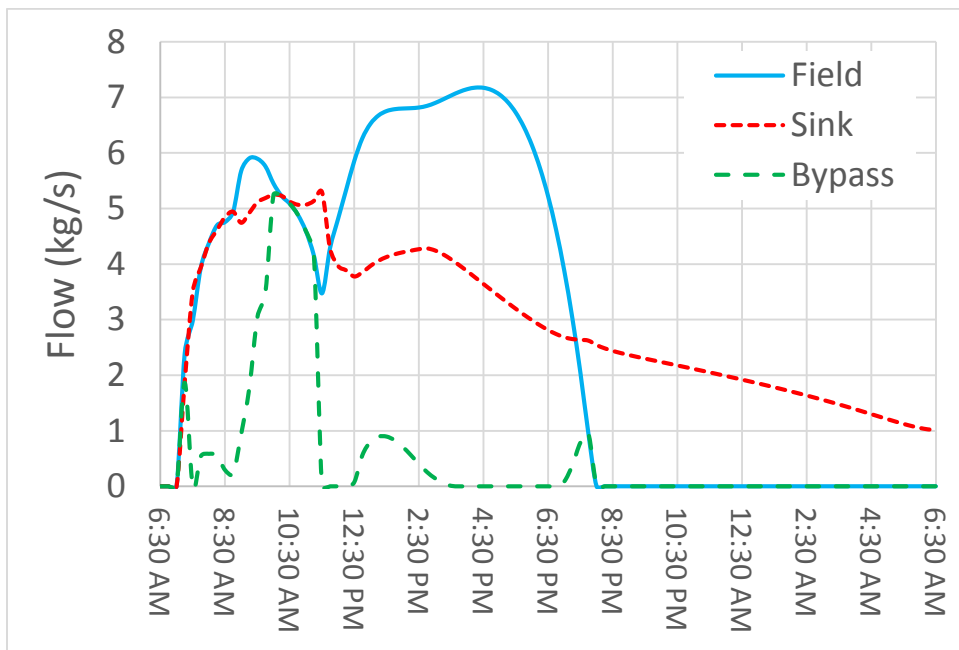


Figure 3.11: Flow rates when using dynamic optimization.

As Figure 3.8 shows, the system is operated in hybrid mode when using dynamic optimization. During the morning, when there is less solar energy available, the only a

portion of the 1 MW_{th} is delivered by solar with the rest being made up by the supplemental fuel. During this same period, the heat is collected at a lower temperature, just over 600 K, as Figure 3.9 shows. Because there is less energy being absorbed the solar field, reaching temperatures in excess of 650 K requires low solar field flow rates (as in Figure 3.6), which mean longer residence times and more heat loss due to radiation. The optimal solution avoids much of this heat loss as it keeps the field flow rate high (Figure 3.11) and the temperature lower. The system does not store energy during this period (Figure 3.10).

When the cloud cover dissipates and more solar energy is available, the solar field temperature increases and the corresponding flow rate decreases. The system begins storing the higher temperature fluid and meeting the entire load with solar heat. As the solar energy begins decreasing in the late afternoon, the system goes back into hybrid operation with the solar heat gradually tailing off. Correspondingly, the supplemental fuel usage gradually increases to keep the system at a constant power output of 1 MW_{th} .

Discussion of Results

While only the optimal results for the scenario with the partly cloudy morning are shown (for brevity), similar results are observed in the other two scenarios. The results are summarized in Figure 3.12 and Figure 3.13. Figure 3.12 shows the total solar energy collected in each scenario for each control scheme. Figure 3.13 shows the total solar efficiencies defined as the total amount of solar energy delivered to the heat sink over the total amount of solar energy available (not accounting for optical losses). As the figures indicate, the optimal results show a significant improvement in every case. This is largely due to the heat loss avoided by operating at lower temperatures. On the sunny day, only marginal improvements are shown because the optimal temperature is very near the controlled temperature in the standard control case. However, on the days when less solar energy is available, operating at lower temperatures provides more dramatic improvement. On the day with intermittent cloud cover throughout the day, the efficiency improvement is significant. This is largely due to the fact that heat is collected at lower temperatures.

This can only be done when the plant is operated in “hybrid” mode, with the supplemental fuel being used to provide a significant portion of the load. Operating in this manner allows the system to get the most benefit from solar energy, which means minimizing heat losses in the solar field and the total supplemental fuel when considering the entire 24-hour period.

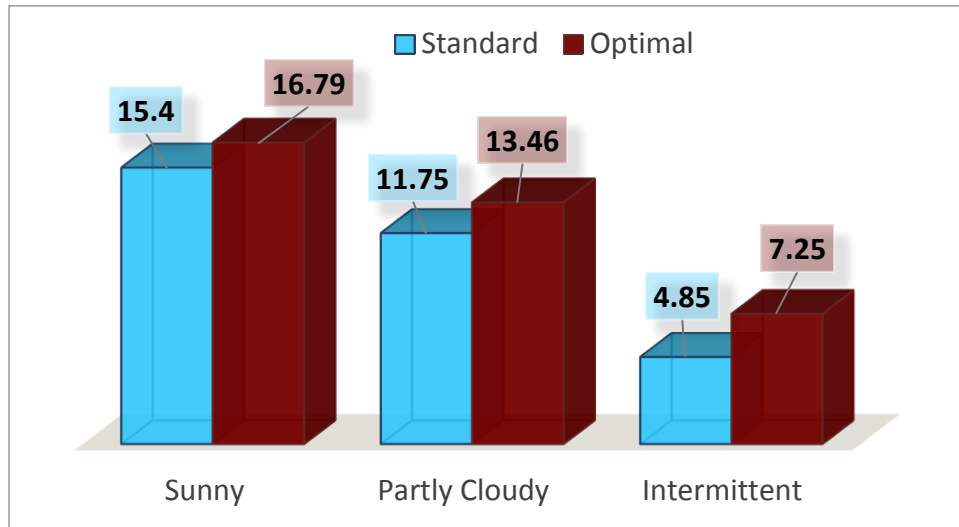


Figure 3.12: Total solar energy collected in MW_{th} for each scenario.

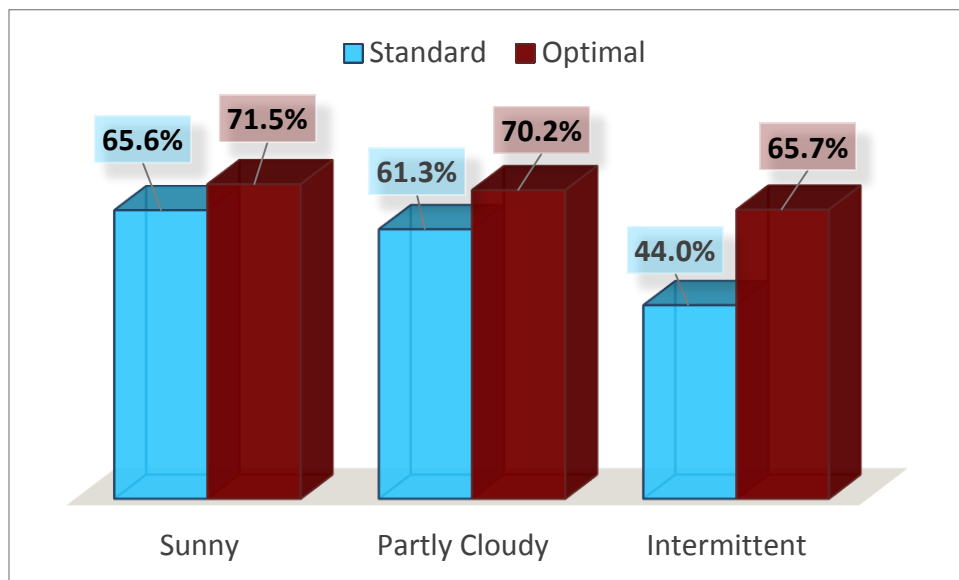


Figure 3.13: Solar heat collection efficiency for each scenario.

Dynamic optimization of hybrid CSP systems with TES requires adjustment of several operational conditions to yield optimal results. TES gives the system flexibility to collect and deliver heat at different temperatures and with different flow rates. When temperatures are allowed to vary, heat losses can be minimized. This requires relaxing the constant solar power condition and allowing the system to be supplemented with a fossil fuel. Dynamic optimization exploits these degrees of freedom so that solar energy and the fossil fuel can be synergistic in a manner that results in maximum benefit of solar energy.

This operating scheme requires accurate forecasts of the operating conditions, most notably DNI, for the upcoming day. While these forecasts will not always be accurate, the optimization scheme can be implemented on a dynamic basis, similar to model predictive control, where a control move is implemented for a single time step. At the next time step, the state variables are measured and the problem is re-solved using the most recent forecast information. Stability of the system can also be enhanced by introducing a hierarchical control scheme, where temperature set points are determined from the dynamic optimization. These set points can then be fed to lower-level controllers, which adjust flow rates to ensure that these temperature set points are maintained.

Conclusions and Future Work

This work illustrates that solar energy can actually be enhanced using fossil fuels. This requires additional degrees of freedom and solving an optimization problem to exploit the operational flexibility. TES is beneficial because it provides additional flexibility so that the system can shift loads to different times. The addition of TES makes the problem a dynamic optimization problem, which can be solved with an efficient simultaneous method.

Operating the plant in “hybrid” mode with optimization shows that some synergy exists between a solar thermal system and a fossil fuel system. This suggests that perhaps the best paradigm to adopt is that solar and fossil energy should complement each other, rather than compete with each other. Using this methodology, the system takes much

greater advantage of “lower grade” solar energy. While CSP plants are most prevalent in desert climates with high annual amounts of DNI, adopting a “hybrid” paradigm can expand the geographical areas where CSP systems may be technologically and economically viable.

The system modeled is a small scale (1 MW_{th}) system, which relies on parabolic trough technology. As larger, more efficient, and higher temperature CSP systems become more prominent, some of the ideas from this study can be incorporated into the design. This will likely require novel TES systems and materials. As research on solar thermal energy continues, it will be beneficial to consider hybrid operation in the design of these plants.

Nomenclature

Symbol	Description	Units
A_A	Absorber pipe cross-sectional area	m^2
$A_{A,i}$	Inner pipe cross-sectional area for absorber pipe	m^2
A_E	Glass envelope cross-sectional area	m^2
$A_{P,i}$	Inner pipe cross-sectional area for boiler pipe	m^2
A_t	Tank area subject to heat transfer	m^2
C_A	Absorber pipe specific heat capacity	$J/(kgK)$
C_E	Glass envelope specific heat capacity	$J/(kgK)$
C_F	Heat transfer fluid specific heat capacity	$J/(kgK)$
h_{air}	Ambient convective heat transfer coefficient	$W/(m^2K)$
h_p	Convective heat transfer coefficient for inner pipe	$W/(m^2K)$
I_C	Solar radiation incident on collector surface	W/m^2
I_N	Solar irradiance in direction of rays	W/m^2
\dot{m}	Mass flow rate	kg/s
$P_{A,i}$	Inner absorber pipe perimeter	m
$P_{A,o}$	Outer absorber pipe perimeter	m
$P_{E,o}$	Outer glass envelope perimeter	m
$P_{B,i}$	Outer boiler pipe perimeter	m
\dot{P}_{pump}	Pumping power	MW_e
\dot{Q}_{solar}	Solar thermal power	MW_{th}
\dot{Q}_{supp}	Supplemental thermal power	MW_{th}
$r_{E,i}$	Inner glass envelope radius	m
$r_{A,o}$	Outer absorber pipe radius	m
t	Time	s

T_A	Temperature of absorber pipe	K
T_{AIR}	Ambient air temperature	K
T_{SKY}	Effective sky temperature for radiative heat transfer	K
T_B	Boiler water temperature	K
T_E	Temperature of glass envelope	K
T_F	Temperature of heat transfer fluid	K
U	Storage tank overall heat transfer coefficient	W/(m ² K)
V	Volume of fluid in storage tank	m ³
w	Width of mirror aperture	m
x	Distance along solar collector length	m
z	Distance along boiler pipe length	m
β	Conversion factor for pumping power to thermal power	MW _{th} /MW _e
χ	Control move penalty coefficient	None
ϵ_A	Absorber pipe emissivity	None
ϵ_E	Glass envelope emissivity	None
$\eta_{optical}$	Total optical efficiency	None
ρ_A	Absorber pipe density	Kg/m ³
ρ_E	Glass envelope density	Kg/m ³
ρ_F	Heat transfer fluid density	Kg/m ³
σ	Stefan-Boltzmann constant	W/(m ² K ⁴)

CHAPTER 4 : INTEGRATING LOGIC IN SIMULTANEOUS AND SEQUENTIAL DYNAMIC OPTIMIZATION SOLUTION METHODS

Introduction

In the field of simulation, optimization, and control, models are ideally formulated as a set of continuous equations with continuous derivatives, so that solutions can be efficiently obtained using gradient-based solution algorithms, such as Newton's method. However, in many systems, the need frequently arises to include operators that may be discontinuous (such as the signum operator) or have discontinuous first derivatives (such as the absolute value operator). The introduction of such discontinuities into a model can have adverse impacts on the solver's ability to efficiently obtain an accurate solution due to the introduction of non-smooth gradients. Such problems have to be re-formulated and solved using a less desirable method.

In the field of dynamic optimization and control, optimization problems are particularly difficult, due to the high dimensionality of time-dependent problems, as model predictions and control actions for every time step must be prescribed by the solver. Furthermore, online applications require fast solution times so that control actions can be calculated and recommended within some pre-determined sampling period. The introduction of discontinuities further complicates matters, as some practitioners may resort to computationally expensive solution methods, such as Mixed Integer Nonlinear Programming (MINLP), in order to implement such disjunctive constraints.

Mathematical programs of equilibrium constraints (MPECs) have been proposed as a way to integrate non-smooth behavior into a set of simultaneous algebraic equations by the inclusion of complementarity conditions [46], [47]. Complementarity, the requirement that at least one of a pair of variables be at some limit, provides a framework for representing disjunctive behavior using a set of continuous equations. MPECs using complementarity constraints have found use in optimization problems in the fields of

structural mechanics [48], [49], chemical and process engineering [42], [43], [50], electric power generation [51], and other fields [41], [52].

Mathematical programs of complementarity constraints (MPCCs) are a subset of MPECs and can be used to represent non-smooth or discontinuous operators, such as absolute value, sgn, and min/max. This work presents the formulation of a greater than or equal to (\geq) and a less than or equal to (\leq) operator, which can be used for if/then logic in a process model. The formulation is presented as a set of continuous algebraic equations. The equations are formulated in such a way, however, that only binary (0 or 1) solutions are obtained for certain variables. These pseudo-binary variables are then used to represent logical conditions within the model. This work does not present a detailed explanation of the convergence properties of MPECs, but rather puts forward a novel formulation that can be used by practitioners to represent logical statements within a continuous process model.

Logical Disjunctions in Optimization

Logical expressions, such as the less than/equal to (\leq) operator are typically introduced into optimization problems through the use of mixed integer programming, where certain variables are constrained at integer values. A general disjunctive program can be converted to an equivalent MINLP [53], [54] and solved using various MINLP algorithms [55], [56], [57]. However, one drawback to MINLP formulations is that solution times grow exponentially with an increased number of discrete decisions [42]. When considering dynamic optimization problems, where the time domain is typically discretized and a set of decisions is required for each time, optimization problems can become especially large. When rapid solution is required, converting a large dynamic optimization problem with disjunctions to an MINLP problem may not be a tractable option. Therefore, the ability to embed logical statements or other disjunctive operators as sets of algebraic equations (or MPECs) while maintaining mathematical continuity, allows the problems to be posed as standard nonlinear programming (NLP) problems, for which many efficient real-time solvers exist.

Sequential Solution Method

When converting a dynamic optimization problem into an NLP, two basic methodologies exist: sequential methods and simultaneous methods [44]. A sequential method employs a forward-stepping differential algebraic equation (DAE) or ordinary differential equation (ODE) solver, using a Runge-Kutta or similar numerical integration technique. Using this method, inputs at every time step are specified. The DAE solver then integrates forward one step at a time using the pre-specified inputs. The sequential method ensures that the state equations are satisfied at all times, as they are enforced by the DAE solver as integration progresses. Logical statements and other disjunctions are fairly easy to implement when using sequential methods, as the state equations can be altered at any point during the integration. For example, when a state variable reaches some limit that triggers a disjunction, a logical statement can be embedded into the DAE model ensuring that the change will be applied to future output from the model while that particular condition holds.

Sequential methods for solving DAE systems certainly have some advantages. When used to solve dynamic optimization problems, however, the disadvantages of sequential methods far outweigh these advantages. These methods are inefficient for large-scale optimization problems because they require simulating the model many times with different values of inputs (at every time step) in order to compute numerical approximations to gradient matrices so that new guesses can be calculated. The simulated solutions are continuously converged from initial values that are not optimal, leading to excessive CPU time that is devoted to intermediate solutions. The requirement to converge the model equations at every iteration also leads to a challenge for unstable systems. If the specified decision variables produce an unstable response, the iteration may fail to find an adequate search direction for the next iteration [58]. It is also difficult to enforce inequality constraints on state (or dependent) variables because the values of these variables at each

time step are only obtained by forward integration using a set of pre-determined inputs, therefore, constraints cannot be directly imposed on these variables.

Simultaneous Solution Method

Simultaneous solution methods are frequently used in industry for dynamic optimization and real-time control problems because they help to overcome many of the computational inefficiencies associated with sequential solution methods [59], [60], [61]. Simultaneous solution methods use collocation (more specifically, orthogonal collocation on finite elements [62], [63]) to convert a DAE-constrained dynamic optimization problem to an NLP where the objective function is minimized and the constraint equations are solved simultaneously, making the algorithm much more computationally efficient. By comparison, a sequential method requires simulating through the differential constraint equations many times for every set of inputs [64].

The crux of a simultaneous solution method is the conversion of the DAE system to a system of purely algebraic equations using a collocation method. The differential equations are specified in (4.1) with time derivatives given as a function (f) of differential state variables (x), algebraic state variables (y), user-controlled inputs (u), and external inputs (p), each of which is a function of τ , a variable representing time, normalized to the range $[0,1]$ over the time interval.

$$\dot{x}(\tau) = f(x(\tau), y(\tau), u(\tau), p(\tau)) \quad (4.1)$$

Conversion of these differential equations is done by representing differential state profiles in time by polynomial approximations, which are generated using Lagrange interpolation polynomials (Ω). These polynomials are formulated to exactly match the value of the derivatives when evaluated at the collocation points (τ_i). This relationship, assuming constant inputs over the time interval, is shown in (4.2), where the derivatives are approximated as the summation of f evaluated at each collocation point (τ_j) multiplied by the corresponding interpolation polynomial (Ω_j).

$$\dot{x}(\tau_i) = \sum_{j=1}^{N_C} \Omega_j(\tau_i) f(x(\tau_j), y(\tau_j), u(\tau_j), p(\tau_j)) \quad (4.2)$$

The Lagrange polynomials are formulated as shown in (4.3) and are of order N_C-1 , where N_C is the number of collocation points used in the approximation over the time interval [65].

$$\Omega_j(\tau) = \prod_{k=1, k \neq j}^{N_C} \frac{\tau - \tau_k}{\tau_j - \tau_k} = \frac{\tau - \tau_1}{\tau_j - \tau_1} \frac{\tau - \tau_2}{\tau_j - \tau_2} \dots \frac{\tau - \tau_{N_C}}{\tau_j - \tau_{N_C}} \quad (4.3)$$

The relationship in (4.2) holds exactly at the collocation points because each polynomial (Ω_j) in (4.3) is formulated to have a value of unity at the corresponding collocation point (τ_j) and a value of zero at all the other collocation points [65].

$$\Omega_j(\tau_i) = \begin{cases} 1, & \tau_i = \tau_j \\ 0, & \tau_i \neq \tau_j \end{cases} \quad (4.4)$$

With state derivatives guaranteed to exactly match at the collocation points, the state variables themselves are approximated by integrating (4.2).

$$\hat{\Omega}(\tau) = \int_0^1 \Omega(\tau) d\tau \quad (4.5)$$

This allows for the state values themselves to be approximated.

$$x(\tau_i) = x_0 + w \sum_{j=1}^{N_C} \hat{\Omega}_j(\tau_i) f(x(\tau_j), y(\tau_j), u(\tau_j), p(\tau_j)) \quad (4.6)$$

where $\hat{\Omega}_j$ is the integral of Ω_j , which is a polynomial of order N_C , x_0 is the value of the state variable at the beginning of the time interval, and h is the width of the time interval.

In order to ensure integration accuracy and that Ω is explicitly defined at the right end of the time interval ($\tau=1$), Radau collocation points are used. The Radau collocation points are derived from Radau quadrature, which is similar to Gaussian quadrature, except that one collocation point is defined explicitly at one end (rather than having all points exclusively in the interior) of the time interval [66]. For dynamic optimization applications,

the interval is 0 to 1, with the state values at 0 obtained from the previous interval, and with a collocation point set exactly at 1.

With an approximation for a single time interval defined, multiple time intervals can be joined together, with a separate polynomial representing each interval, or finite element. The initial condition for each time interval is given as the final condition of the previous time interval (C^0 -continuity). Other quadrature methods propagate first derivatives (C^1 -continuity) or higher p -order derivative information (C^p -continuity) across the interval boundaries [67] to achieve higher accuracy across intervals. Figure 4.1 illustrates the orthogonal collocation on finite elements discretization scheme. Each time interval (k) of length w contains N_C collocation points. The example in the figure uses $N_C=3$, but higher or lower orders of approximation also exist. The approximation from finite element k would use the state value from the last collocation point ($i=N_C$) of element $k-1$ as its initial condition, as shown in (4.7). In (4.7), the subscripts (i and j) refer to the collocation point and the superscript (k) refers to the finite element number.

$$x_i^k(\tau_i) = x_{N_C}^{k-1} + w \sum_{j=1}^{N_C} \hat{\Omega}_j(\tau_i) f(x_j^k, y_j^k, u_j^k, p_j^k) \quad (4.7)$$

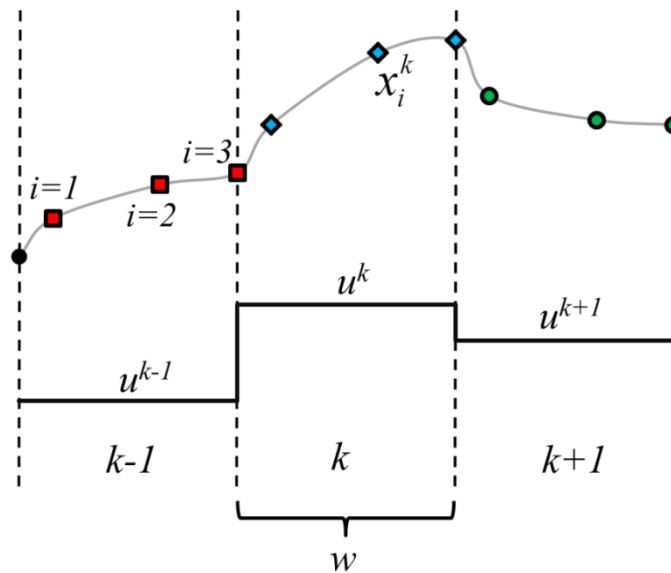


Figure 4.1: A schematic illustrating the orthogonal collocation on finite elements.

With the approximation in (4.7) completed, the differential equations are converted into algebraic equations, which can be solved by a nonlinear algebraic equation solver. Therefore, enforcing additional algebraic equality constraints (g) becomes possible, as these equations (4.8) can be included with the algebraic equations in (4.7).

$$g(x_j^k, y_j^k, u_j^k, p_j^k) = 0 \quad (4.8)$$

Nonlinear inequality constraints can also be included, as can upper and lower bounds on the variables themselves.

$$h(x_j^k, y_j^k, u_j^k, p_j^k) \leq 0 \quad (4.9)$$

$$u_l \leq u \leq u_u \quad (4.10)$$

$$x_l \leq x \leq x_u \quad (4.11)$$

$$y_l \leq y \leq y_u \quad (4.12)$$

The ability to directly impose constraints on state variables is one of the advantages of a simultaneous solution method, as opposed to sequential method. The algebraic formulation of (4.6)-(4.12) lends itself quite well to inclusion in an optimization problem which can be converged by an NLP solver.

Embedding MPECs into Simultaneous Equations

One of the disadvantages of a simultaneous solution method compared to a sequential method is that it is much more difficult to embed disjunctive constraints or logical conditions. Because the model is solved as a set of simultaneous algebraic equations, the introduction of disjunctions would make it difficult to solve the equations by standard methods. However, with the ability to enforce algebraic constraints within a differential model, MPECs, which are formulated as sets of algebraic equations, can be embedded into the model to represent disjunctions. These MPECs take advantage of a complementarity condition that at least one of two constraints be active, as shown in (4.13),

where \perp is the complementarity operator, enforcing at least one of these constraints at all times [42], [52].

$$0 \leq v_+ \perp v_- \geq 0 \quad (4.13)$$

In this work, v_+ and v_- are referred to as complementarity variables. The condition in (4.13) can be maintained by using a number of different formulations, and the performance of each may depend on the solution algorithm used. The first option is to represent the complementarity as an equality constraint as in (4.14).

$$v_+ v_- = 0 \quad (4.14)$$

This equation requires that at least one of the pair v_+ and v_- be equal to zero. Alternatively, inequality constraints may also be used.

$$v_+ v_- \leq 0 \quad (4.15)$$

or

$$v_+ v_- \leq \varepsilon \quad (4.16)$$

where ε is a very small positive number, indicating that some error in this relationship may be tolerated in order to enhance the convergence properties of interior point NLP methods [42].

Using the complementarity condition, several different MPECs can be formulated to represent some commonly used functions. These sets of equations can be embedded into a DAE model and keep the model continuous and smooth, despite the fact that these operators represent non-smooth or discontinuous operators in standard practice.

The absolute value operator

$$y = |x| \quad (4.17)$$

can be alternatively represented in a continuous optimization problem by embedding the following equations into the DAE or algebraic model:

$$x = v_+ - v_- \quad (4.18a)$$

$$\nu_+, \nu_- \geq 0 \quad (4.18b)$$

$$\nu_+ \nu_- = 0 \quad (4.18c)$$

$$y = \nu_+ + \nu_- \quad (4.18d)$$

In (4.18b), the complementarity variables are restricted to be nonnegative. Because the complementarity condition (4.18c) requires that at least one of these variables be zero, (4.18a) represents the difference between two nonnegative values. When x is positive, ν_- must be zero in order to satisfy (4.18c). ν_+ is therefore positive and equal to x . Thus, the summation of ν_+ and ν_- in (4.18d) becomes equal to the absolute value of x . Similarly, for negative x , ν_- must be positive and ν_+ must be zero. The summation of these two nonnegative values (4.18d), therefore, will always be a positive number equal in magnitude to x [42].

The min and max operators, which select the minimum and maximum value, respectively, of two inputs (x_1 and x_2)

$$y = \min(x_1, x_2), \quad z = \max(x_1, x_2) \quad (4.19)$$

can also be represented using MPEC formulations.

$$x_1 - x_2 = \nu_+ - \nu_- \quad (4.20a)$$

$$\nu_+, \nu_- \geq 0 \quad (4.20b)$$

$$\nu_+ \nu_- = 0 \quad (4.20c)$$

$$y = x_1 - \nu_+ \quad (4.20d)$$

$$z = x_1 + \nu_- \quad (4.20e)$$

In this formulation, if x_1 is greater than x_2 , ν_+ will assume the difference between these values. ν_- will be zero in order to satisfy the complementarity condition (4.20c). The lesser of x_1 and x_2 will therefore be the higher number (x_1) minus the difference (ν_+) leaving y to be equal to the min of the two as specified in (4.20d). The greater number will

be the higher number plus v_- , which is zero in this case. Therefore, z will represent the max of the two numbers, as (4.20e) indicates [42].

The signum operator gives an output of +1 for positive input and -1 for negative input.

$$y = \text{sgn}(x) \quad (4.21)$$

This binary behavior can also take on a continuous representation by using an MPEC formulation.

$$x = v_+ - v_- \quad (4.22a)$$

$$v_+, v_- \geq 0 \quad (4.22b)$$

$$v_+ v_- = 0 \quad (4.22c)$$

$$v_+(1-y) + v_-(1+y) = 0 \quad (4.22d)$$

As (4.22) indicates, when x is positive, v_+ will also be positive and equal in magnitude to x . Because v_- will be zero, y will have to equal +1 in order to satisfy (4.22d). Similarly, when x is negative, y will be equal to -1, as a positive value of v_- and a zero value of v_+ will enforce this in (4.22d) [42].

MPEC Formulations to Represent Logical Statements

Because MPECs provide a continuous formulation to represent some disjunctive relationships, it is possible to represent some logical behavior within a model using similarly constructed MPECs which take advantage of the complementarity relationships described above. For instance an MPEC can be used to represent a binary variable, which is 1 when some condition is true and 0 otherwise. This binary variable can then be integrated into the model equations such that certain equations only hold true under the logical conditions dictated by the MPEC. The remainder of this section discusses the development of a greater than/equal to (\geq) and a less than/equal to (\leq) operator. Section 4 will then discuss the methodology for implementing such logic into a set of DAEs.

With only a slight modification of (4.22), the MPEC can be constructed so as to produce a 1 for a positive input (x) and a 0 for a negative input. Here, the variable δ is introduced to represent the binary output of this MPEC.

$$\delta = \begin{cases} 1 & \text{if } x > 0 \\ 0 & \text{if } x < 0 \end{cases} \quad (4.23)$$

The MPEC formulation is very similar to the signum operator, with only a slight modification made in the fourth equation. As (4.24d) indicates, the output of this MPEC can be customized to yield various constants, depending on the terms added to or subtracted from δ .

$$x = \nu_+ - \nu_- \quad (4.24a)$$

$$\nu_+, \nu_- \geq 0 \quad (4.24b)$$

$$\nu_+ \nu_- = 0 \quad (4.24c)$$

$$\nu_+ (1 - \delta) + \nu_- (\delta) = 0 \quad (4.24d)$$

Using the formulation in (4.24), δ becomes a pseudo-binary variable, one which is continuous, but can only assume values of zero or one at the solution for negative or positive values of x , respectively.

Careful inspection of (4.24) reveals a major shortcoming. When $x=0$, both complementarity variables are simultaneously equal to zero. This means that (4.24d) will be satisfied by any value of δ , as the system has an infinite number of solutions in this case. The MPEC equations must therefore be modified in order to give the system the discrete switching behavior that is desired with no ambiguity for any value of x .

$$\delta = \begin{cases} 1 & \text{if } x \geq 0 \\ 0 & \text{if } x < 0 \end{cases} \quad (4.25)$$

Adding a second complementarity condition to the set of equations is proposed to overcome the issue of ambiguity when $x=0$. This equation (4.26d) contains a third complementarity variable, ν_0 , and is designed such that ν_0 will take on some finite (albeit

still ambiguous) value when v_+ and v_- are simultaneously zero, due to the input, x , being equal to zero.

$$x = v_+ - v_- \quad (4.26a)$$

$$v_+, v_- \geq 0 \quad (4.26b)$$

$$v_+ v_- = 0 \quad (4.26c)$$

$$(v_+^2 + v_-^2) v_0 = 0 \quad (4.26d)$$

$$v_+ (1 - \delta) + v_0 (1 - \delta) + v_- (\delta) = 0 \quad (4.26e)$$

In (4.26e) a third term is added for the case that only v_0 is nonzero (which occurs when $x=0$). However, some ambiguity still exists in this formulation, namely, that all complementarity variables may simultaneously be zero when x is zero, thereby satisfying (4.26e), regardless of the value of δ . In order to prevent this occurrence, v_+ and v_- are squared in (4.26d) order to ensure that these squared terms converge to zero at a faster rate, leaving v_0 at some nonzero value. With zero values for v_+ and v_- and a finite value for v_0 , the $(1-\delta)$ term multiplying v_0 must equal zero, giving δ a value of 1 when $x=0$. Changing the δ term in (4.26e) will obviously affect what δ converges to in this case, meaning that the MPEC can be formulated so that δ takes on some other, user-determined, value. The same holds true for the terms multiplying v_+ and v_- if other outputs are desired for positive and negative values for x , respectively.

An alternate formulation using only equality constraints is used for testing the convergence properties of this logical MPEC. The non-negativity constraints in (4.26b) are removed and these constraints are instead enforced by squaring the complementarity variables in the first equation (4.27a). Note that this is a system of four equations and four unknowns, with x being considered an external input to this system.

$$x = v_+^2 - v_-^2 \quad (4.27a)$$

$$v_+ v_- = 0 \quad (4.27b)$$

$$(v_+^2 + v_-^2) v_0 = 0 \quad (4.27c)$$

$$v_+ (1 - \delta) + v_0 (1 - \delta) + v_- (\delta) = 0 \quad (4.27d)$$

This system of equations is evaluated for convergence properties using Newton's method for solving systems of nonlinear equations. The system exhibits no issues with convergence for positive and negative values of x , with δ converging to 1 and 0, respectively, as desired. The predominant concern is obtaining a distinct desired solution when x is zero. Newton iterations for this scenario are shown in Figure 4.2 and Figure 4.3. As Figure 4.2 illustrates, v_+ and v_- converge to zero as expected. The other complementarity variable, v_0 , however, remains at its initial guess value, as the squared terms in (4.27c) converge to zero in order to satisfy (4.27a). This finite value for v_0 , however, forces δ to converge exactly to 1 in order to satisfy (4.27d), rather than leaving this value ambiguous, as the formulation in (4.24) would have.

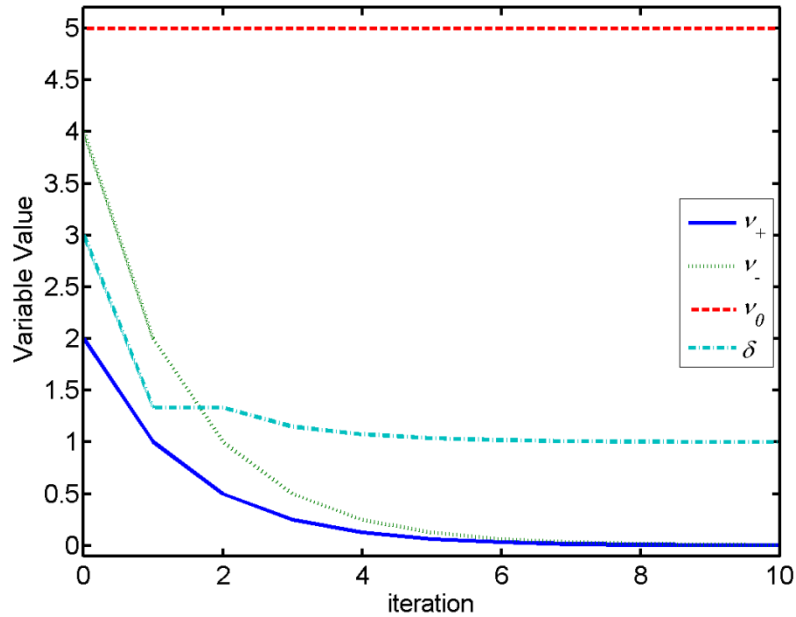


Figure 4.2: A plot of the convergence of the greater than/equal to logic MPEC.

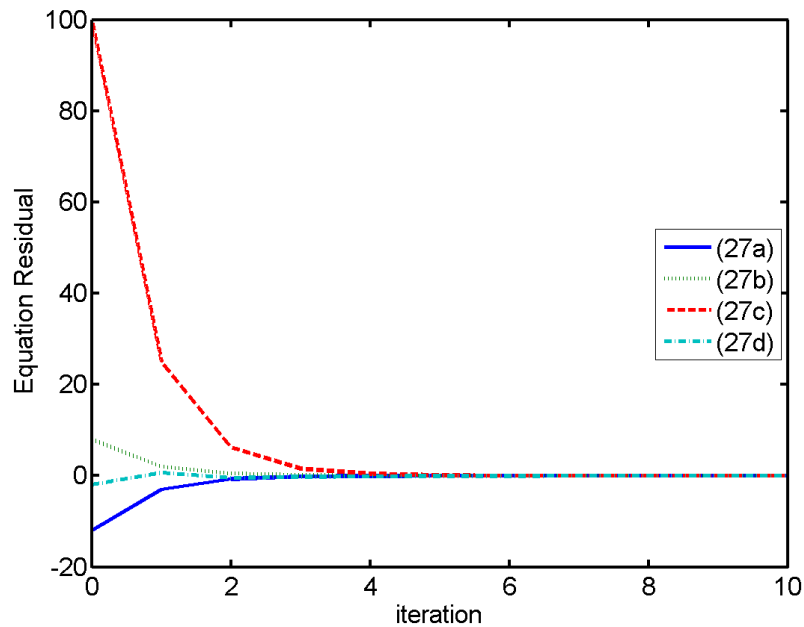


Figure 4.3: A plot of residuals when solving using Newton's Method.

Continuous Logic in Dynamic Systems

Using the collocation scheme combined with the logical MPEC framework developed in the previous section, dynamic systems of equations with logical conditions can be simulated using only a set of continuous algebraic equations. This is done by embedding a logical MPEC into the DAE system. The pseudo-binary variable, δ , from this MPEC can be multiplied with the model equations, meaning that some equations will hold only when $\delta=1$. Two simulation examples are used to illustrate how this is done.

A simple example to illustrate the need for representing logic in a DAE model is that of a simple tank with overflow, shown in Figure 4.4. While the dynamics of this system are trivial, the equations representing the dynamic behavior of the tank change dramatically when the tank reaches its overflow limit. The system, as posed in (4.28), can be represented as a simple ODE combined with a logical expression determining when the tank overflows.

$$\frac{dV}{dt} = Q_{in} - Q_{out} - Q_{over} \quad (4.28a)$$

$$Q_{over} = \begin{cases} Q_{in} - Q_{out} & \text{if } V \geq V_{max} \text{ \& } Q_{in} > Q_{out} \\ 0 & \text{otherwise} \end{cases} \quad (4.28b)$$

where V is the volume of fluid in the tank, Q_{in} is the flow into the tank, Q_{out} is the flow out of the tank, and Q_{over} is the flow exiting the tank as overflow, when the tank volume exceeds its capacity, V_{max} . While the system simple in (4.28) is very simple, the logical statement (4.28b) prevents it from being solved using a standard simultaneous solution method. However, by including the algebraic equations representing the greater than/equal to logic MPEC, this system can be solved using a simultaneous solution method. This DAE system translated into a continuous logic formulation using an MPEC with complementarity constraints is given in (4.29), where (4.29e)-(4.29h) represent the additional algebraic equations introduced by the logical MPEC.

$$\frac{dV}{dt} = Q_{in} - Q_{out} - Q_{over} \quad (4.29a)$$

$$(1 - \delta_{hi}) Q_{over} = 0 \quad (4.29b)$$

$$Q_{over} \geq 0 \quad (4.29c)$$

$$V \leq V_{max} \quad (4.29d)$$

$$V - V_{max} = v_+^2 - v_-^2 \quad (4.29e)$$

$$v_+ v_- = 0 \quad (4.29f)$$

$$(v_+^2 + v_-^2) v_0 = 0 \quad (4.29g)$$

$$v_+^2 (1 - \delta_{hi}) + v_-^2 (\delta_{hi}) + v_0 (1 - \delta_{hi}) = 0 \quad (4.29h)$$

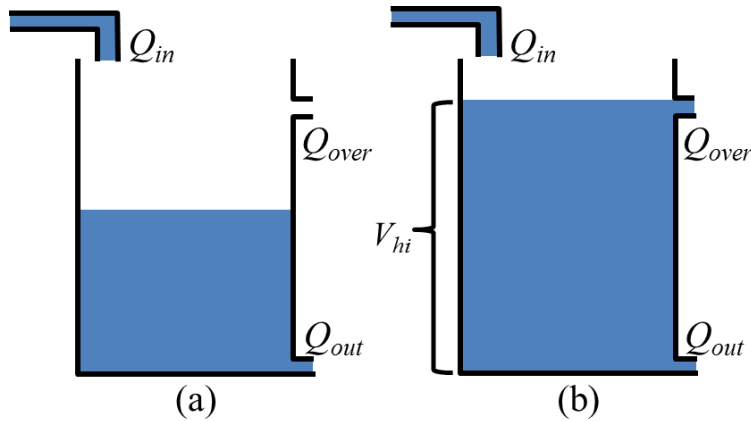


Figure 4.4: A schematic showing how the dynamic equations for tank overflow.

In this formulation, δ_{hi} is a pseudo-binary variable that is equal to one when the tank is full and zero when it is not full. When the tank is not full, (4.29b) will ensure that Q_{over} is zero. When the tank is full, Q_{over} will take on whatever value necessary to satisfy the material balance (4.29a). However, Q_{over} must be restricted to non-negative values in order to prevent negative values of Q_{over} from satisfying (4.29a) when the tank is not full. The MPEC tests whether the quantity $V - V_{max}$ is greater than or equal to zero. However, in order to enhance convergence properties, V is also restricted by (4.29d), so that V cannot exceed its limit. Alternatively, this constraint can be imposed solely by the MPEC equations. However, this may lead to poor convergence properties of the system. Convergence is also enhanced in this case by squaring v_+ and v_- in (4.29g) and (4.29h), forcing the squared terms to converge more quickly so that v_0 remains near its initial guess in the event that the system is at its volume limit.

In order to demonstrate the ability of (4.29) to accurately represent a logic-dependent dynamic system, the set of equations with pre-specified inputs (Q_{in} and Q_{out}) is solved using a DAE solution package known as Advanced Process Monitor, or APMonitor [45]. This software package allows a user to define a model using both differential and algebraic equations. The software performs the collocation to convert the differential equations to algebraic equations and the problem is converted to a set of nonlinear algebraic

equations. For optimization, an NLP problem would be solved. Because the system is still a continuous set of equations, APMonitor computes the gradient matrices with automatic differentiation, ensuring accuracy and fast solution times. The APOPT solver, which uses an active set method, demonstrates the best convergence as the problem is solved assuming some set of constraints to be active, which works well with inequality constraints such as (4.29c) and (4.29d).

The results of the simulation are shown in Figure 4.5 through Figure 4.8. As Figure 4.5 and Figure 4.6 illustrate, the overflow (Q_{over}) remains at zero until the tank fills. Once the tank fills, the logical condition that $Q_{over}=0$ is nullified as $\delta_{hi}=1$, allowing Q_{over} to take on whatever positive value is needed to satisfy (4.29a). The complementarity variables (Figure 4.8) are well behaved, with ν_- equaling zero when the tank is at the high limit and ν_0 equaling zero when the tank is not at the high limit. The positive complementarity variable (ν_+) is always zero as the system is prevented from exceeding the high limit by (4.29d).

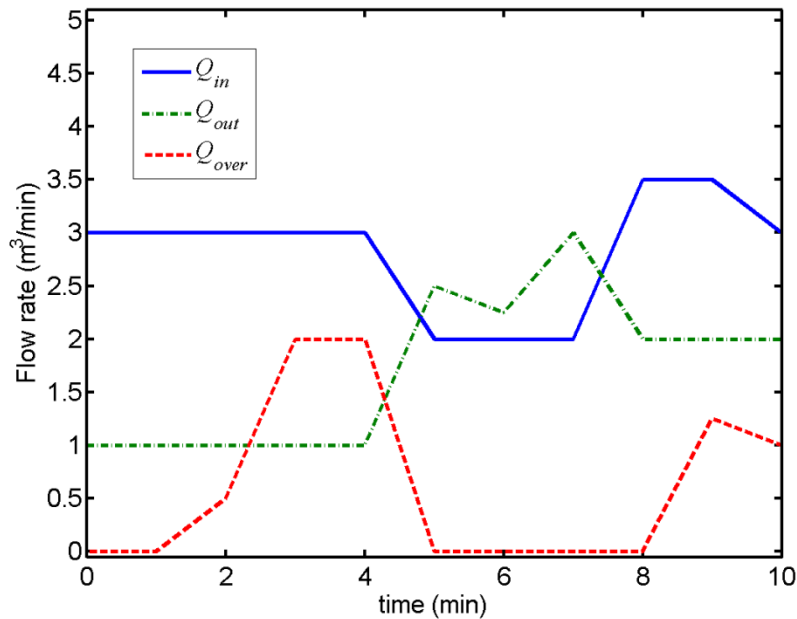


Figure 4.5: Flow rates in and out of the tank overflow system.

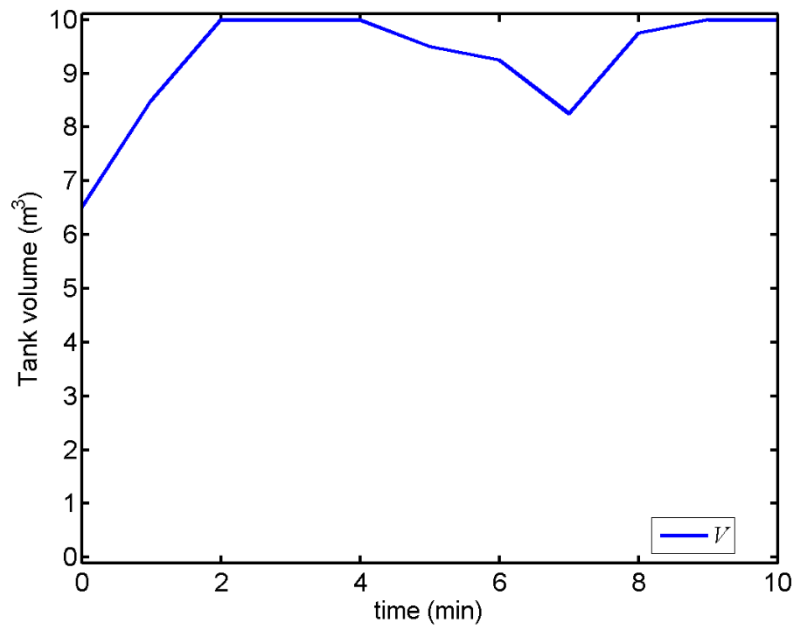


Figure 4.6: Plot of tank volume.

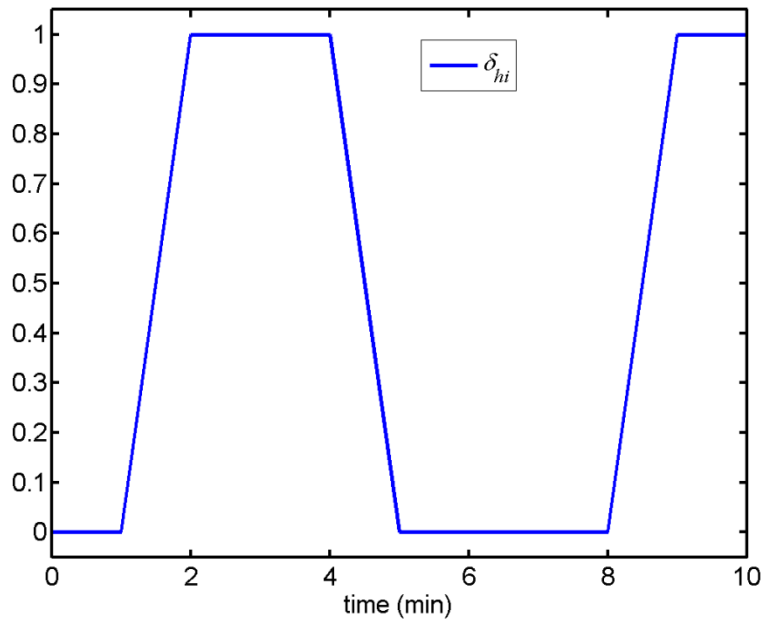


Figure 4.7: Plot of the pseudo-binary variable.

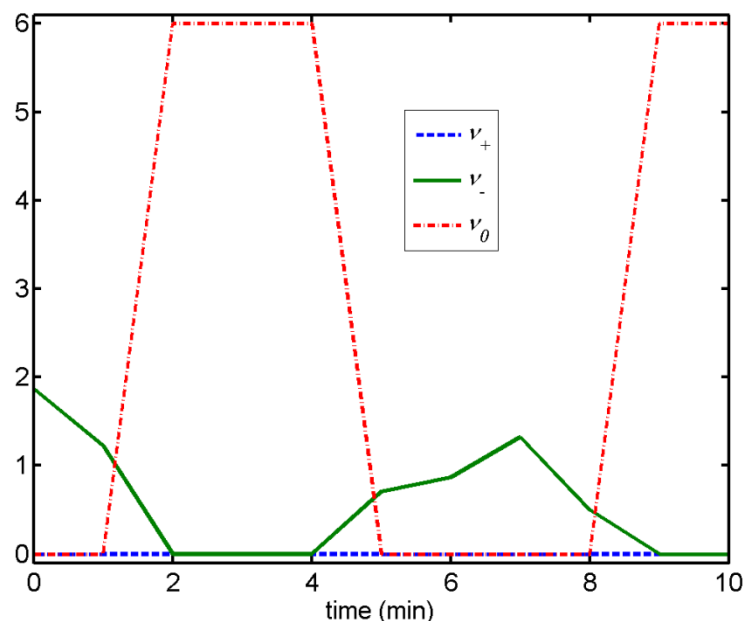


Figure 4.8: Complementarity variables used in the tank overflow system.

Remarkably, the results illustrate that logic can be embedded into a dynamic system using only continuous algebraic equations to model the system. While convergence for the formulation in (4.29) is obtained, there are many variations of the MPEC formulation, some of which do not display the same ability to converge consistently. When implementing similarly-formulated MPECs, it may be necessary to explore various formulations to determine which will be the most robust for the application and choice of solver.

The logical MPEC's performance is also tested in a microgrid (shown in Figure 4.9) with a photovoltaic solar panel, a battery, a load (represented by a building), and the electric grid. This system assumes simple dynamics for the battery (4.30a). Energy balances are computed around the photovoltaic panel and the load in order to obtain (4.30b) and (4.30c), respectively. A logic-based operating strategy is applied in order to specify the system's operation. Using this strategy, the maximum amount of solar power is delivered to the load by using the battery. When solar power available (q_{pv}) exceeds the demand (q_{load}), the battery (whose state of charge is represented by E_{batt}) is charged. When the battery reaches its capacity (E_{max}), the excess power is delivered to the grid with flow

q_3 . Conversely, when the battery is void of charge, power must be imported from the grid to the load with flow q_4 . This logic is specified in (4.30d) and (4.30e). The variables q_1 and q_2 represent the power delivered to and extracted from the battery, respectively.

$$\frac{dE_{batt}}{dt} = q_1 - q_2 \quad (4.30a)$$

$$0 = q_{PV} - q_1 - q_3 \quad (4.30b)$$

$$0 = q_{load} - q_2 - q_4 \quad (4.30c)$$

$$q_3 = \begin{cases} q_{PV} - q_1 & \text{if } E_{batt} \geq E_{max} \text{ \& } q_{PV} > q_1 \\ 0 & \text{otherwise} \end{cases} \quad (4.30d)$$

$$q_4 = \begin{cases} q_{load} - q_2 & \text{if } E_{batt} \leq 0 \text{ \& } q_{load} > q_2 \\ 0 & \text{otherwise} \end{cases} \quad (4.30e)$$

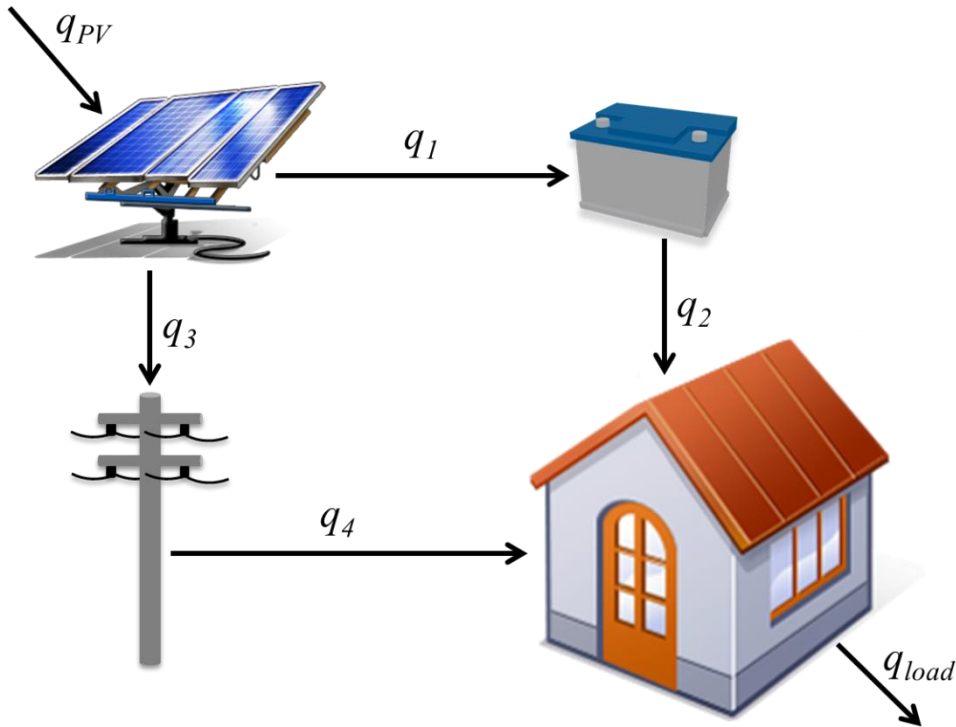


Figure 4.9: Schematic for the power flow example.

Conversion of the model to continuous form requires two sets of logical MPEC equations representing the logical decisions of (4.30d) and (4.30e). This requires two sets of pseudo-binary (δ) and complementarity variables (ν), which are assigned the subscripts hi and lo, corresponding to the full (4.30d) and empty (4.30e) battery charge conditions, respectively. When converted to continuous logic form, (4.30) becomes (4.31).

$$\frac{dE_{batt}}{dt} = q_1 - q_2 \quad (4.31a)$$

$$0 = q_{PV} - q_1 - q_3 \quad (4.31b)$$

$$0 = q_{load} - q_2 - q_4 \quad (4.31c)$$

$$E_{min} \leq E_{batt} \leq E_{max} \quad (4.31d)$$

High limit MPEC eqns corresponding to (4.30d)

$$(1 - \delta_{hi}) q_3 = 0 \quad (4.31e)$$

$$q_3 \geq 0 \quad (4.31f)$$

$$E_{max} - E_{batt} = \nu_{hi+}^2 - \nu_{hi-}^2 \quad (4.31g)$$

$$\nu_{hi+} \nu_{hi-} = 0 \quad (4.31h)$$

$$(\nu_{hi+}^2 + \nu_{hi-}^2) \nu_{hi,0} = 0 \quad (4.31i)$$

$$\nu_{hi+}^2 (1 - \delta_{hi}) + \nu_{hi-}^2 (\delta_{hi}) + \nu_{hi,0} (1 - \delta_{hi}) = 0 \quad (4.31j)$$

Low limit MPEC eqns corresponding to (4.30e)

$$(1 - \delta_{lo}) q_4 = 0 \quad (4.31k)$$

$$q_4 \geq 0 \quad (4.31l)$$

$$E_{min} - E_{batt} = \nu_{lo+}^2 - \nu_{lo-}^2 \quad (4.31m)$$

$$\nu_{lo+} \nu_{lo-} = 0 \quad (4.31n)$$

$$(\nu_{lo+}^2 + \nu_{lo-}^2) \nu_{lo,0} = 0 \quad (4.31o)$$

$$v_{lo+}^2 (1 - \delta_{lo}) + v_{lo-}^2 (\delta_{lo}) + v_{lo,0} (1 - \delta_{lo}) = 0 \quad (4.31p)$$

The continuous logic formulation for the microgrid is demonstrated using a simulation with pre-determined q_{pv} and q_{load} over a 24-hour time horizon, which is shown in Figure 4.10. Hourly time intervals are used in the simulation. As the figure shows, the supply (q_{pv}) and demand (q_{load}) do not perfectly coincide, with the available solar power peaking near midday and the demand peaking later in the afternoon, requiring the system to use battery energy storage in order to maximize the power delivered to the load from the solar panel. As Figure 4.11 through Figure 4.13 illustrate, at the beginning of the day, there is no charge in the battery (indicated by $\delta_{lo}=1$) and the demand exceeds the load, forcing power to be drawn from the grid. As the solar power picks up, the battery charges until it reaches its capacity (indicated by $\delta_{hi}=1$). When this occurs, the logic dictates that the excess power be exported from the solar panel to the grid, indicated by the positive values for q_3 in Figure 4.11. At the end of the day, the solar power is diminished, the battery completely discharges, and power is again imported from the grid.

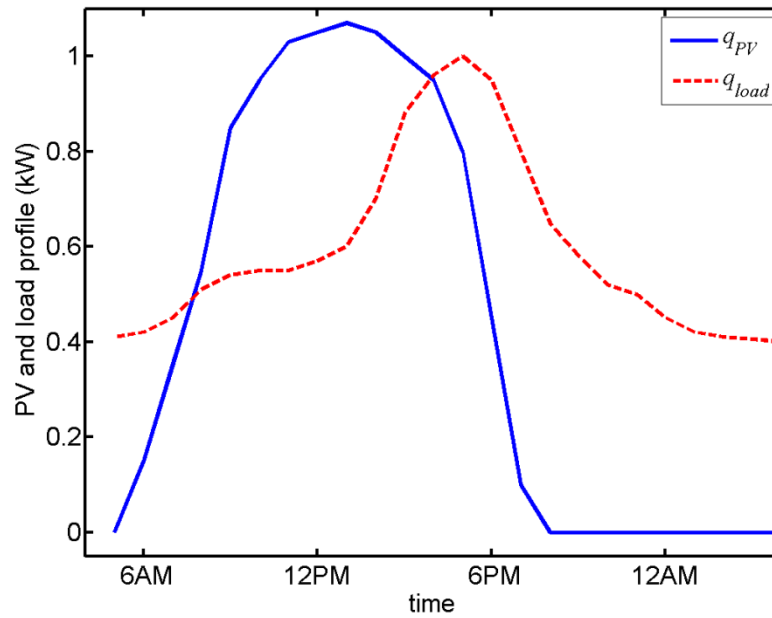


Figure 4.10: Inputs to the power flow model.

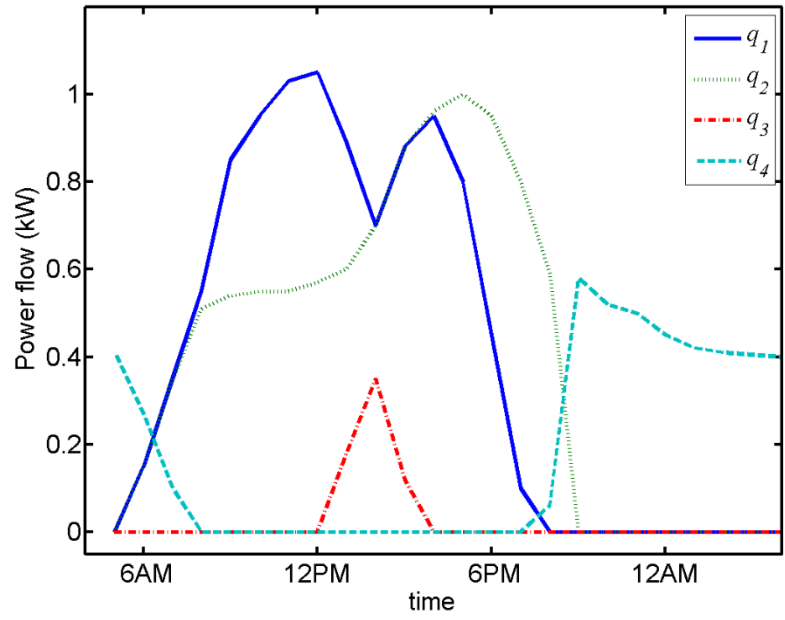


Figure 4.11: Flows in the power network.

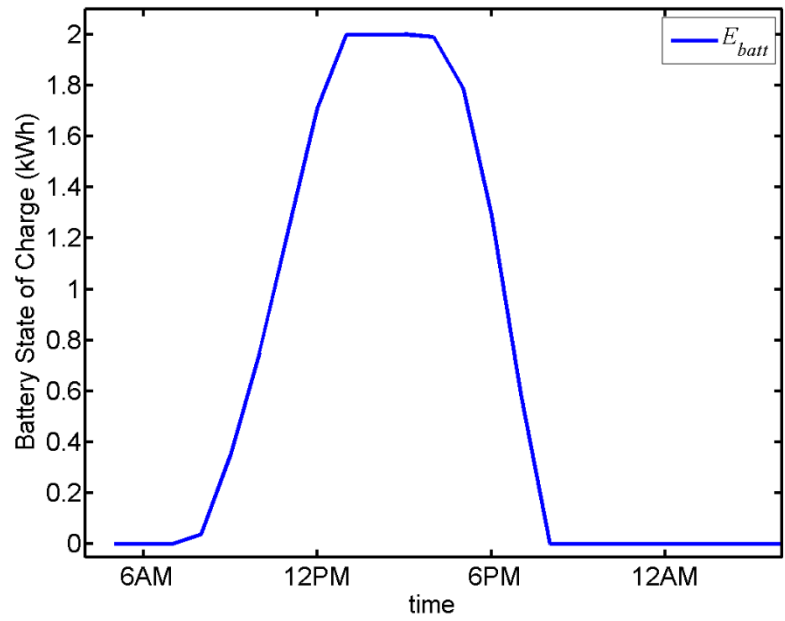


Figure 4.12: State of charge (kWh) of the battery.

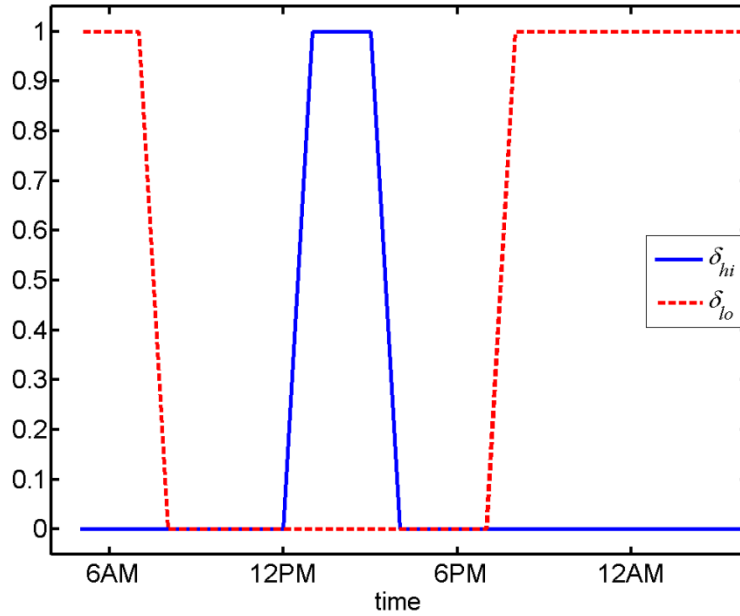


Figure 4.13: Pseudo-binary variables indicating battery charge conditions.

The power flow example again demonstrates the value of using MPECs to represent logical decisions in a DAE system. Embedding this logic in the form of continuous algebraic equations allows the system to be solved using the simultaneous method, which has been proven to significantly increase computational efficiency as compared to a sequential method.

Continuous Logic in an NMPC Problem

As a demonstration of the value of integrating logic into a simultaneous solution method, a nonlinear model predictive control (NMPC) problem is solved for a continuous stirred tank reactor (CSTR), which carries out the reaction:



The objective of the controller is to regulate the concentration of component C (C_C) using the heat input to the reactor (q_{heat}) and the flow rate of component B (Q_B) as manipulated variables. The system is subject to disturbances in the flow of component A ($Q_{A,in}$) and is

equipped with a surge tank to buffer out the effects of sudden increases in Q_A . However, in the case that the volume of fluid in the surge tank exceeds the tank capacity, the surge tank will overflow and a sudden increase in the flow of A will enter the CSTR as shown in Figure 4.14. NMPC in this scenario can monitor the level in the surge tank (h) and the flow of A coming into the surge tank so that sudden disturbances due to surge tank overflow can be anticipated and accounted for pre-emptively by the controller. The model requires a built-in logical statement as in (4.28) to represent the tank overflow condition.

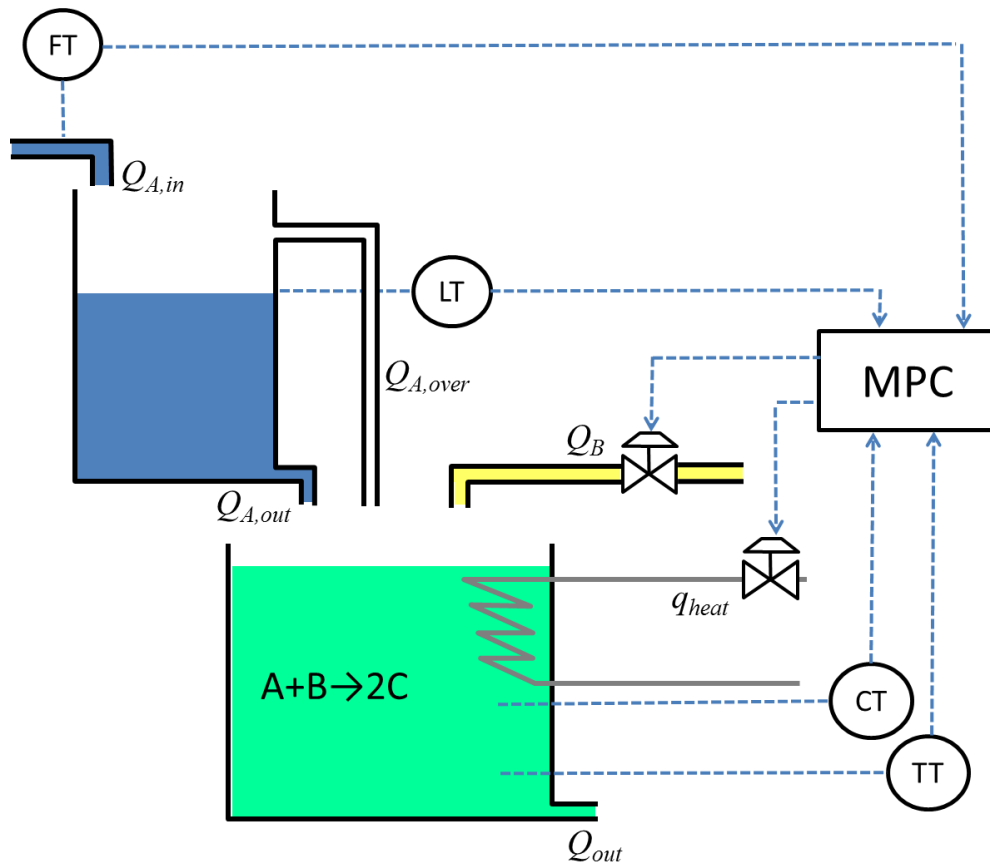


Figure 4.14: A schematic of the MPC scheme of a CSTR and surge tank.

In the MPC problem, the outflow from the bottom of the surge tank ($Q_{A,out}$) is proportional to the square root of the height (h) in the tank (4.34), with the dynamics of

the tank represented by a simple material balance (4.33). The model requires a built-in logical statement to represent the tank overflow condition (4.35).

$$A_{\text{tank}} \frac{dh}{dt} = Q_{A,\text{in}} - Q_{A,\text{out}} - Q_{A,\text{over}} \quad (4.33)$$

$$Q_{A,\text{out}} = C\sqrt{h} \quad (4.34)$$

$$Q_{A,\text{over}} = \begin{cases} Q_{A,\text{in}} - Q_{A,\text{out}} & \text{if } h \geq h_{\text{max}} \text{ \& } Q_A > Q_{A,\text{out}} \\ 0 & \text{otherwise} \end{cases} \quad (4.35)$$

The CSTR is assumed to be at constant volume so that the total inlet flow equals the flow out (Q_{out}) at all times (4.36).

$$Q_{\text{out}} = Q_{A,\text{out}} + Q_{A,\text{over}} + Q_B \quad (4.36)$$

The kinetics in the tank are first order in both A and B and the rate law (4.37) has temperature dependence subject to the Arrhenius equation, where R_A is the rate of reaction of component A, k_0 is the reaction rate constant, E_A is the activation energy, R is the ideal gas constant, T is the temperature in the tank, C_A and C_B are the concentrations of component A and B, respectively.

$$R_A = k_0 e^{\frac{-E_A}{RT}} C_A C_B \quad (4.37)$$

The tank temperature is determined by an energy balance on the tank (4.38), where q_{heat} is the rate that heat is delivered to the tank, V is the CSTR volume, ρ and C_P are the density and the heat capacity, respectively of the fluid in the system, and the subscript 0 refers to the fluid before it enters the tank. The components A, B, and C are all assumed dilute so that their concentrations do not affect the density, heat capacity, or overall material balances of the solution. This assumption also permits neglecting heat of reaction in the energy balance.

$$\rho V C_P \frac{dT}{dt} = \rho C_P Q_{\text{out}} (T_0 - T) + q_{\text{heat}} \quad (4.38)$$

Material balances on each component are also computed, giving three more differential equations (4.39)-(4.41), where C_C is the concentration of component C.

$$V \frac{dC_A}{dt} = (Q_{A,out} + Q_{A,over}) C_{A0} - Q_{out} C_A - R_A V \quad (4.39)$$

$$V \frac{dC_B}{dt} = Q_B C_{B0} - Q_{out} C_B - R_A V \quad (4.40)$$

$$V \frac{dC_C}{dt} = 2R_A V - Q_{out} C_C \quad (4.41)$$

The MPC problem seeks to minimize deviations from the set point for C_C subject to disturbances in $Q_{A,in}$ without making drastic control moves. To achieve this trade-off, a quadratic performance index is used where the squared deviations at the end of each time interval are weighted differently (10 for set point deviations and 1 for manipulated variable changes) and summed to create a performance index to be minimized. This yields the dynamic optimization problem in (4.42), which is subject to the system model in (4.33) through (4.41) and inequality constraints on the inputs.

$$\min_{Q_B, q_{heat}} \sum_{i=1}^{N_t} 10(C_{C,i} - C_{C,SP})^2 + \sum_{i=1}^{N_t} 1(Q_{B,i} - Q_{B,i-1})^2 + \sum_{i=1}^{N_t} 1(q_{heat,i} - q_{heat,i-1})^2 \quad (4.42a)$$

Subject to (4.33)-(4.41)

$$0 \leq Q_B \leq Q_{B,max} \quad (4.42b)$$

$$0 \leq q_{heat} \leq Q_{heat,max} \quad (4.42c)$$

A first order hold is used for the manipulated variables (MVs) where the value of these variables is held constant over each time interval. A total of N_t time intervals are used in the model prediction. As Figure 4.14 shows, the controller checks the most recent state measurements (concentrations and temperature in the CSTR and fluid height in the surge tank) and disturbance measurements (flow of A) at each time step in order to update the

model and ensure accurate future predictions. The model with built-in logic for surge tank overflow allows the controller to anticipate large influxes of flow and proactively account for this disturbance.

The optimization problem posed in (4.42) is solved using both a sequential and a simultaneous solution method. In this problem $N_r=30$ over 1 minute time intervals with a control horizon equal to the prediction horizon of 30 minutes. With two MVs, the optimization problem has 60 degrees of freedom in total. The sequential method version of the problem uses an optimization solver (FMINCON) in MATLAB [68], which takes pre-determined values of the inputs, simulates the system using an explicit ODE integrator (ODE45), computes the objective function and uses this information to construct numeric approximations to the gradient matrices to compute a new search direction for the next iteration. The sequential method also uses if/then logic as in (4.28b) to describe the changing dynamics of the surge tank. This methodology requires simulating through the entire time horizon of the system model thousands of times in order to generate the gradient matrices and iterate.

The simultaneous version of the problem is solved using APMonitor with the greater than/equal to MPEC described in (4.29), which, combined with the built-in orthogonal collocation scheme in APMonitor, allows the problem to be expressed entirely as a set of algebraic equations and inequality constraints, which can be solved using an NLP. The APOPT solver is again used to obtain a solution to this NLP. This method does not require multiple simulations of the system model as it solves the constraints of the system simultaneously subject to minimization of the objective function. As opposed to the sequential approach, the simultaneous method converges the equation residuals only once at the optimal solution.

It is important to note that the addition of a logical statement using this MPEC formulation cannot be applied to conditions that are a function of the decision variables. These conditions make the optimization problem severely non-convex, so that it converges to local solutions, if a solution can be obtained. The formulation in this problem is only

dependent on the disturbance variable, so that the logic portion is subject to solving a set of non-linear equations. It has does not directly impact the optimization problem, so a solution is obtained in this case.

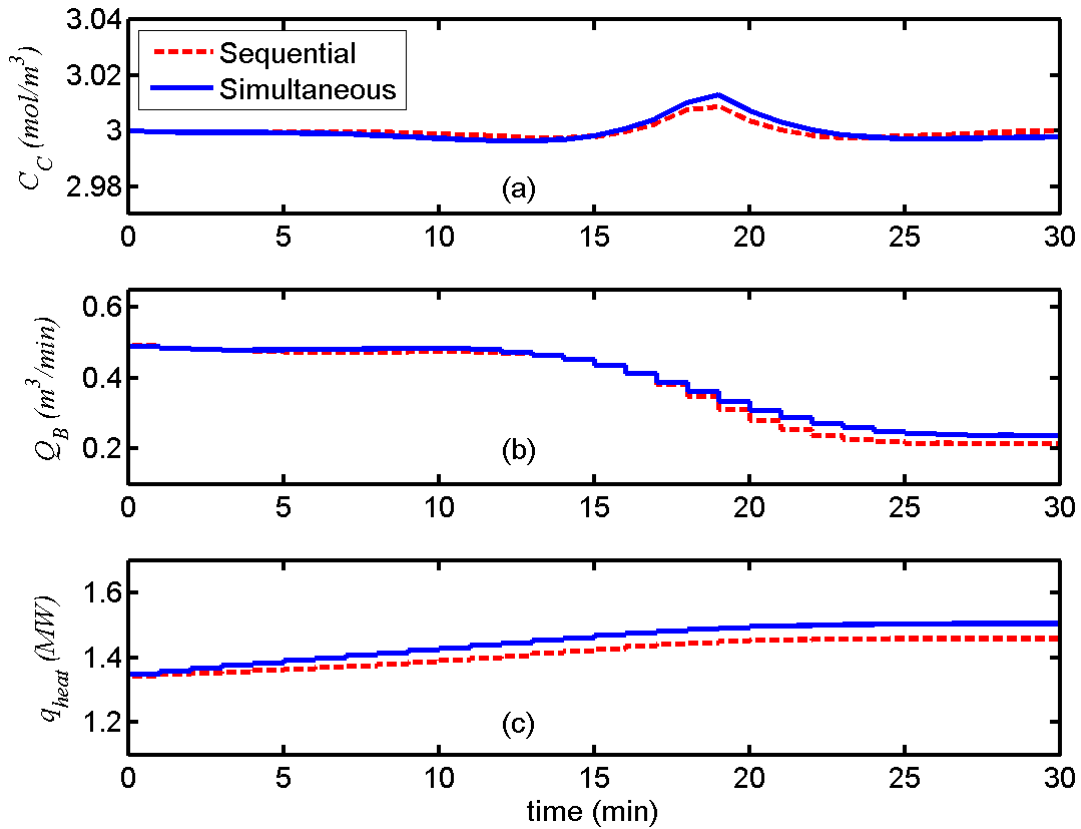


Figure 4.15: Results from the CSTR with surge tank nonlinear MPC problem.

The MPC problem is solved with the system initially at steady state with $Q_{A,in}=Q_{B,in}=0.5$ m³/min and C_C exactly on set point at 3 mol/m³. At time $t=0$, however, a step change disturbance is introduced, changing $Q_{A,in}$ to 0.8 m³/min. The results from each solution method showing the controlled variable (CV) and the MVs are shown in Figure 4.15. As the figure shows, despite the introduction of a large disturbance, the CV is maintained very near its set point in each case. There are slight differences in the solutions using the sequential method relying more heavily on Q_B control moves and the simultaneous method relying more heavily on q_{heat} control moves. The optimization results

of the two methods are compared in Table 4.1, which shows that the sequential method produces a slightly better objective function, but requires 300 times more computational effort. The simultaneous method has negligible computation time for an MPC problem with a one minute time interval, indicating that this MPC scheme could be implemented with no concerns on completing the solution within the required cycle time. In contrast, it would be difficult to implement a real-time MPC application with the sequential method due to the computation time exceeding the time interval in used in the MPC problem.

Table 4.1: Results from the sequential and simultaneous methods.

	Sequential	Simultaneous
Objective function value	0.0094	0.0108
System model evaluations	3,336	1
Computation time (s)	331.6	1.1

The profiles of some relevant state variables are shown in Figure 4.16 for the simultaneous solution method. As these plots indicate, the continuous logic formulation produces the desired switching behavior with no issues. As the surge tank reaches its overflow condition, the tank overflows but otherwise, $Q_{A,over}=0$. In this MPC application, it is invaluable to have the overflow condition represented in the model, as it allows the controller to anticipate large interruptions to the operation of the CSTR. While the disturbance it introduced at $t=0$, its major impact is not observed until $t=18$ min when the tank overflows. The model however, allows for this change to be predicted and control moves to be made pre-emptively. As Figure 4.15 shows, more drastic control moves are made several minutes before the tank overflows. Predicting this occurrence with a logic-embedded model allows the system to effectively maintain its set point despite the large change in operating conditions.

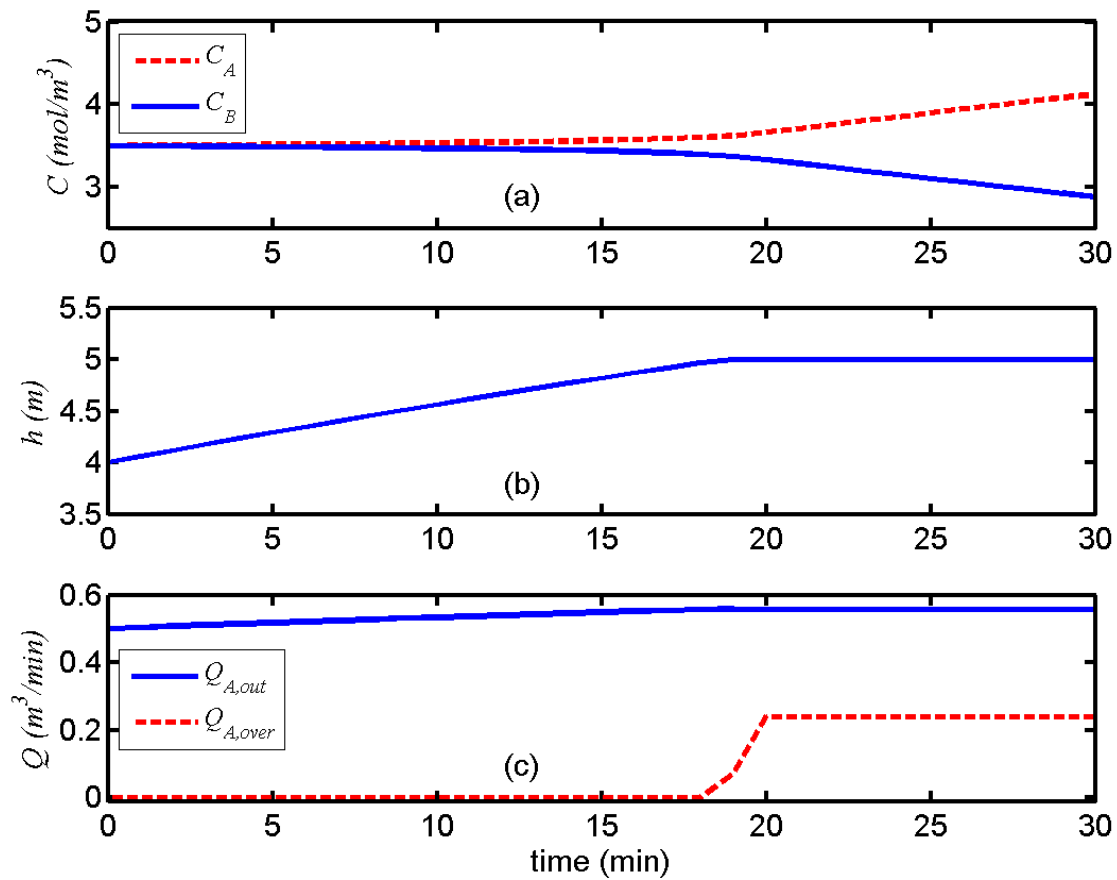


Figure 4.16: Results of the CSTR MPC problem.

Conclusions and Future Work

This work demonstrates how logical expressions based on a greater than/equal to (\geq) or less than/equal to (\leq) operator can be used in NMPC. As opposed to prior work, the new method is well-conditioned at the switching point, leading to a unique solution with improved convergence properties. These equations, known as MPECS, can be embedded into a DAE model using only continuous algebraic equations. The MPECS take advantage of complementarity conditions, requiring that at least one of a set of two inequality constraints be active at all times. Two simulation examples have been presented to demonstrate the viability of using MPECS to represent these logical decisions. The

examples, as presented, demonstrate rapid and accurate convergence, illustrating how a logical operating scheme can be simulated using an efficient simultaneous solution method.

In addition to simulation, an NMPC problem is also solved using the formulation developed in this work. The simultaneous solution method combined with the continuous logic formulation is compared to a sequential method using simple if/then logic. The results show that the methods produce nearly equivalent solutions. However, the simultaneous method with continuous logic is 300 times faster in obtaining a solution. The continuous logic formulations allow implementation of logical statements into a model without having to resort to the less efficient sequential method for real-time NMPC or dynamic optimization calculations. The model including the dynamics and the logical statements are implemented as a continuous system of algebraic equations, which can be solved with efficient NLP solvers.

While the examples posed in this work demonstrate the potential of using MPECs for logical decisions, this nascent topic requires much more research to be a viable method for solving optimization problems with such decisions. One of the key challenges to overcome is the non-convexity that is characteristic of many problems with logical decisions like this, which causes the optimizer to converge to local solutions. Furthermore, the mathematical properties of logical MPECs must be studied to provide a better understanding of how these problems are handled by various solvers and what can be done to further enhance performance. In particular, in the examples in this paper, the logical conditions are dependent on pre-determined inputs. Optimality is more difficult to obtain when the logical statements depend on the decision variables, with the optimizer typically finding a feasible solution and stopping, if it can find a feasible solution. This work presents the concept of using MPECs to represent logical decisions when using a simultaneous solution method so that this concept may be explored for other applications.

Nomenclature

Symbol	Description	Units
A_{tank}	Cross-sectional area of reactor tank	m^2
C	Valve constant	$m^{2.5}/min$
C_A	Concentration of component A	mol/m^3
C_B	Concentration of component B	mol/m^3
C_C	Concentration of component C	mol/m^3
C_P	Heat capacity	$kJ/(kgK)$
E_A	Activation energy	$kJ/(kmol)$
E_{batt}	Energy stored in battery	kWh
g	Equality constraint function	-
h	Inequality constraint function	-
h	Tank height	m
i	Collocation point index	-
j	Collocation point index	-
k	Time interval index	-
k_0	Reaction rate constant	$m^3/(mol*min)$
N_c	Number of collocation points	-
p	External model input	-
Q	Flow rate	m^3/min
q	Power flow	kW
q_{heat}	Heat flow	MW
R	Ideal gas constant	$kJ/(kmolK)$
R_A	Reaction rate of component A	$mol/(m^3min)$
t	time	min
T	Temperature	K
u	Decision variable	-

V	Tank volume	m^3
w	Width of time interval	-
x	Dynamic state variable	-
y	Algebraic state variable	-
δ	Pseudo-binary variable	-
ε	Non-zero constraint tolerance	-
ρ	Density	kg/m^3
τ	Dimensionless time variable	-
v	Complementarity variable	-
Ω	Interpolation polynomial function	-

CHAPTER 5 : AN ADAPTIVE GRID MODEL FOR DYNAMIC MODELING OF THERMOCLINE THERMAL ENERGY STORAGE SYSTEMS

Introduction

The introduction of intermittent renewable sources of energy and an ever-increasing push for more efficient operation of conventional power generation systems has led to the advent of a smart electric grid [69]. One of the key objectives for a smart grid is to maintain reliability and efficiency in the presence of transient supply and demand for energy [70], [71]. In order to achieve this objective, reliable, cost-effective energy storage technologies are required [72], [73]. Furthermore, because a smart grid embodies intelligent operation, accurate dynamic models of energy systems are required to adequately predict or optimize system performance.

Because thermal energy flows play a significant role in power generation and consumption, thermal energy storage is a promising solution to some of the grid's storage needs [74], [75]. In order to ensure effective and reliable integration of thermal energy storage technologies into a smart grid environment, accurate and computationally efficient models are required for simulation. A prevalent configuration for thermal energy storage technologies is the thermocline system using chilled or heated liquids as storage media, where thermal energy is stored under a temperature gradient. This system uses buoyancy forces to maintain the gradient, ensuring efficient operation by reducing mixing [76].

The use of thermocline systems creates a need for accurate models to represent this system. Because thermocline systems have spatial temperature dependence, modeling these systems is much more complicated than isothermal systems, which has led to the development of complex two- and three-dimensional dynamic models [77], [78]. However, for simulation and optimization of integrated energy systems, where the thermal energy storage is a small part of a much larger energy network, accurate, yet simplified models

are needed [79]. These models must be computationally efficient while accurately representing tank behavior under transient environmental conditions.

In this work, a novel one-dimensional adaptive-grid thermocline model is presented. This model reduces the number of states required for accurate temperature prediction in the tank by a factor of ten compared to standard fixed-grid one-dimensional model. The model equations can therefore be solved much more quickly and with greater accuracy than other one-dimensional models and are therefore much more amenable for use in a larger energy system model to be used for simulation or optimization in a smart grid environment.

Background

Thermal energy storage, or the storing of energy as heat or cooling, is a promising energy storage technology because of its simplicity. Thermal energy is stored by changing a material's temperature (sensible heat storage) or phase (latent heat storage), meaning that any material with significant thermal mass can become a storage medium, thus making thermal energy storage a low cost energy storage technology [80]. Thermal energy storage can be used in conjunction with solar thermal heating systems to help maximize the heat delivered from the sun to the heated space [81]. Thermal energy storage is critical in the field of concentrated solar power (CSP) because it allows these systems to continuously generate power during intermittent cloud cover or even after sunset [82]. Thermal energy storage can also be used for cooling applications as a demand-side energy management tool allowing for cooling loads to be shifted to off-peak hours, thereby reducing strain on grid power generation equipment during peak periods [83].

Thermal energy storage can use a wide variety of materials as storage media including liquids, solids, vapors, or combinations, as in pebble (or packed) bed thermal energy storage systems. Phase change materials, which store energy as latent heat, can greatly increase storage density [84]. Thermal energy storage systems employ a variety of configurations including direct (when the circulating fluid is also the storage medium) and

indirect (when the circulating fluid transfers heat to a separate medium for storage). For liquid systems, the means by which the warm and cold fluids are separated from each other is a critical issue as mixing of the two destroys exergy (the amount of useful energy) and reduces the effective storage capacity of the system [85]. A single well-mixed tank (Figure 5.2), for example, will be the least exergetically efficient, while a two-tank method is the most efficient because it achieves perfect separation of the warm and cold fluids (see Figure 5.1) [86]. A thermocline system (shown in Figure 5.3) uses density differences between the warm and cold fluid to achieve thermal stratification, where the less dense warm fluid is separated from the cold fluid by buoyancy forces, thus achieving temperature separation using a single tank [87]. In thermocline systems, the exergetic efficiency depends on the ability to keep the thermocline region as narrow as possible, thereby achieving the best possible temperature separation. This ability is a function of tank design factors, such as the design of the inlet flow diffusers (designed to evenly distribute inlet flow over the cross-sectional area of the tank) [88], [89], [90] and tank dimensions [91], as well as tank operating conditions, such as flow rate and inlet temperature [92], [93].

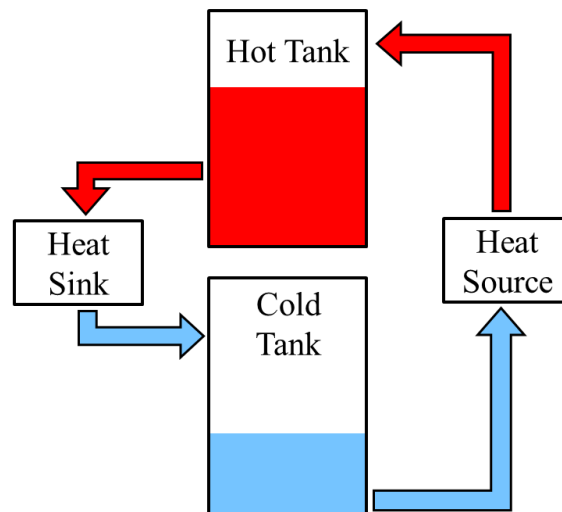


Figure 5.1: Two tank thermal storage configuration.

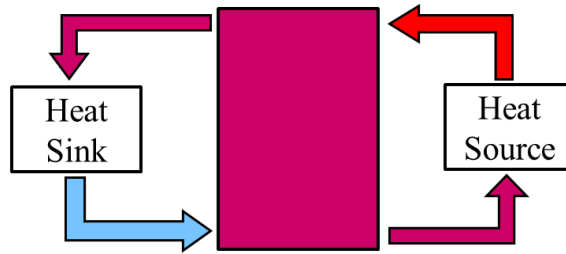


Figure 5.2: Single mixed tank thermal storage configuration.

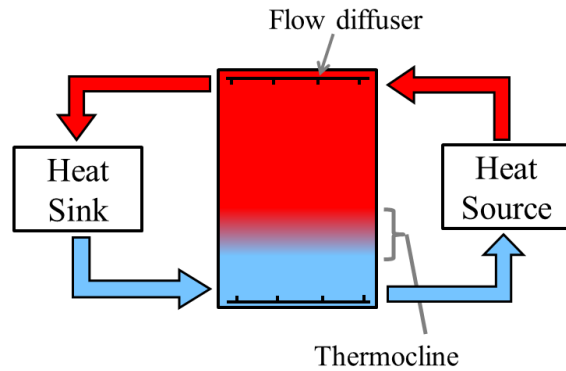


Figure 5.3: Single tank thermocline configuration for thermal energy storage.

Because thermocline systems are prevalent and the phenomenon of thermal stratification is complex, modeling of thermocline systems is an active research field. For tank and diffuser design, complex two- and three-dimensional models may be utilized to fully understand the dynamics of the system [77], [78]. Some of these models use computational fluid dynamics (CFD) codes and, while providing an understanding of the dynamic behavior of thermocline tanks, are computationally intensive and therefore not suitable for solving problems over long time horizons or for real-time applications. For these purposes, one-dimensional models which track temperature as a function of height in the tank are much more amenable.

A one-dimensional model can be represented as a single partial differential equation (PDE), which is generated from a spatially-dependent energy balance on the tank, shown in (5.1). Because the storage medium for thermocline systems are generally liquids

assumed to be incompressible and because thermocline tanks are maintained at constant volume, a mass balance is not required.

$$\frac{\partial T}{\partial t} = (\dot{m}_{source} - \dot{m}_{sink}) \frac{\partial T}{\partial x} - UP(T(t, x) - T_{amb}) + \frac{\varepsilon A_{xs}}{\rho C_p} \frac{\partial^2 T}{\partial x^2} \quad (5.1)$$

Because heat transfer from one node to another can occur by diffusion, conduction, or axial mixing due to turbulent flow, the term ε is used as a lumped parameter which represents the combined effect of these modes of heat transfer. Rather than using a complex two- or three-dimensional model to predict these phenomena, ε can be used as a fitting parameter in a one-dimensional model, ensuring that the model predictions align closely with measured data.

Analytical solutions to (5.1) are difficult to obtain, particularly under transient conditions (inlet temperature and flow rate). Therefore, in order to solve for spatial temperature dependencies, spatial derivatives are approximated by discretizing the tank into nodes vertically with a finite difference method used to describe energy flow between nodes. Figure 5.4 shows a spatial discretization scheme.

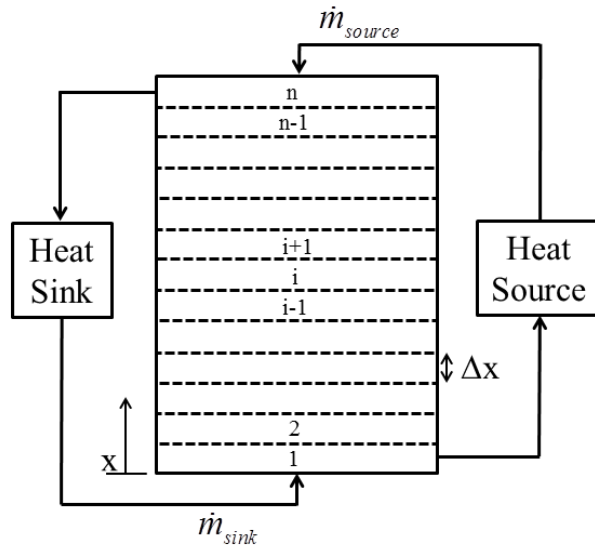


Figure 5.4: Spatial discretization in the thermocline tank.

Using the discretization scheme shown in Figure 5.4 and computing energy balances on each node, the single PDE is converted into a set of n ordinary differential equations (ODEs), where n is the total number of nodes used in the spatial approximation. The ODE for the i^{th} node is shown in (5.2). Because (5.2) represents an approximation, accuracy depends on the number of nodes used. Increasing n improves accuracy as the height of each node (Δx) decreases, making (5.2) a better approximation of (5.1). Integrating this set of equations yields an approximate dynamic temperature profile of the system.

$$\begin{aligned} \rho C_p A_{xs} \Delta x \frac{dT_i}{dt} = C_p \dot{m}_{sink} (T_{i-1} - T_i) + C_p \dot{m}_{source} (T_{i+1} - T_i) - \\ UP \Delta x (T_i - T_{amb}) + \frac{\varepsilon A_{xs}}{\Delta x} (T_{i+1} - 2T_i + T_{i-1}) \end{aligned} \quad (5.2)$$

The tank is used in conjunction with two different loops: one for flow through the heat source and the other for flow through the heat sink. During heating mode, the cold storage medium flows from the bottom of the tank, through the heat source, where its temperature increases, and then returns to the top of the tank. During cooling mode, warm fluid flows from the top of the tank, through the heat sink, where its temperature decreases and then returns to the bottom of the tank. While the two modes of operation generally take place at different times, it is possible to run them simultaneously. A model can be constructed to represent flow in either direction using two separate mass flow terms: \dot{m}_{source} (for flow through the heat source) and \dot{m}_{sink} (for flow through the heat sink). The net flow in the tank will be downward when source flow exceeds sink flow and upward when sink flow exceeds source flow.

A negative result of spatial discretization using a finite difference method for systems with flow is numerical diffusion, which causes the model to exhibit higher diffusivity than the true physical system [94], [95]. To minimize this effect, higher spatial resolution is typically used, which results in more nodes, and therefore more equations. Because of the spatial dependence of temperature in thermocline thermal energy storage

systems, the existence of numerical diffusion is an important consideration, as it affects the degree of stratification predicted by the model, which impacts the performance of the model [96]. Figure 5.5 shows the relationship between the number of nodes used in simulation and the degree of stratification which the model predicts. As the figure indicates, the use of more nodes reduces the effect of numerical diffusion. However, using more nodes means that more equations must be solved, making the problem more computationally intensive.

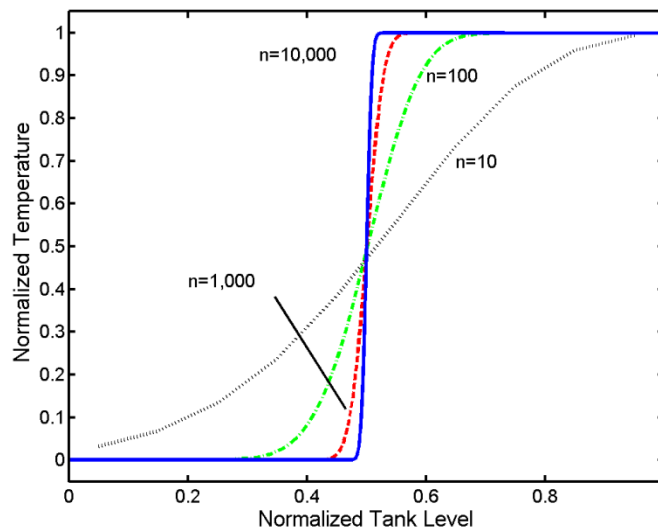


Figure 5.5: A plot of temperature vs. tank height.

A wide range of methods have been used in attempt to construct accurate, yet sufficiently simple one-dimensional models [97], [98], [99]. The energy balances represented in (5.1) and (5.2) are generally accurate (given a sufficiently high spatial resolution) when inlet temperature (at either the top or the bottom) to the tank is constant. However, because the phenomenon of thermal stratification is due to density gradients that arise as a result of temperature differences, when the density gradient is inverted, undesirable mixing occurs within the tank. Therefore, when the density of fluid entering the tank is higher than the fluid below it, buoyant forces will cause these layers of fluid to mix, a condition which is detrimental to efficiency due to entropy generation.

Several different approaches have been used in dynamic modeling to account for the possibility of variable temperature inlet flow, which results in unwanted density gradients. In a multimode approach, the tank is divided into discrete sections (as shown in Figure 5.4). A variable inlet position model adds incoming fluid to the node that most closely matches the inlet flow in density [2]. The result of this approach is the prediction of an ever widening thermocline or possibly the existence of multiple thermoclines in the tank. Another approach to this problem is to use a fixed inlet model, but to average the temperatures of adjacent nodes at the end of each time step whenever temperature inversions exist [98], [100]. Similarly, under the assumption that the lowest density node must always be at the top of the tank, a multimode inversion approach is used. At the end of each time step, any nodes exhibiting inverted temperatures are switched spatially until the nodes are properly ordered from highest temperature at the top of the tank to lowest at the bottom [101]. These approaches represent varying levels of accuracy. They are difficult, however, to incorporate as continuous-time ODE or PDE models because of the computations that must be completed at the end of each time step. Another approach that helps account for varying inlet conditions is a plume entrainment model where it is assumed that liquid jets persist at the tank inlet. Energy and mass balances are then computed separately on the jet stream and the surrounding fluid so that they interchange energy with each other [102]. These models help account for some of the effects of varying inlet temperature. However, with effective diffuser design, it can be reasonably assumed that the effects of jet streams are negligible.

Figure 5.6 illustrates the phenomenon of temperature inversion, as observed in operating thermocline systems. When colder fluid enters the top of the tank, buoyancy forces cause this denser fluid to mix with the layer below it. This mixing continues until equilibrium is reached with temperature monotonically increasing as a function of tank height. Delivering colder (warmer) than nominal fluid to the top (bottom) of the tank means that the energy storage system is being under-utilized as temperature differences in the heat

source or heat sink are not fully exploited. This condition represents destruction of exergy in the tank. Therefore, it is critical to model these effects properly in a dynamic system.

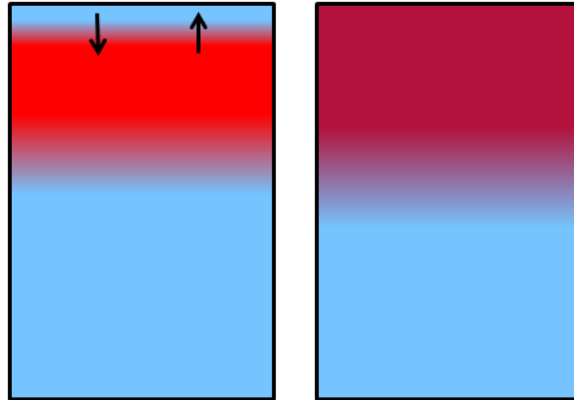


Figure 5.6: The effect of temperature inversion.

A particular class of transport problems involves situations in which an interface or boundary moves over time. These problems are known as Stefan problems and arise in a number of different fields [103], [104]. The boundary in these problems is commonly an interphase between two phases with the transport properties of each phase varying widely, making these problems difficult to solve. In fact, analytical solutions for such problems exist only for a limited number of cases [105], [106], making the use of numerical methods critical.

One numerical approach to solving problems of this type is to use an adaptive-grid, which tracks the moving front using a dynamically changing mesh [107]. While stratified thermal energy storage systems do not have distinct phase boundaries, they do have a relatively small region of varying temperature between two larger, constant temperature regions. Therefore, an adaptive-grid technique can be used to drastically reduce the number of states required to represent the system.

Model Description

Rather than using a fixed, equally-spaced grid as is typical in thermocline tank modeling, the adaptive-grid model uses a finely-spaced grid in the vicinity of the

temperature gradient. This section, referred to as the thermocline region, moves to track the temperature gradient as it moves through the tank. This movement is accommodated by two variable volume nodes at the ends of the tank. For downward flow, the top node (Node n) expands while the bottom node (Node 1) contracts (see Figure 5.7). The middle nodes (Node 2 through Node n-1) move with the flow so that the temperature gradient remains centered in the thermocline region of the grid. In certain situations, however, the grid will remain fixed. This occurs at the beginning and end of charge and discharge cycles, when the temperature gradient enters or exits at one end of the tank. This requires logic to be built into the material balances for the end nodes of the tank and determines when the nodes move or when they remain fixed. In order to accommodate this, the flows in and out of the tank (denoted \dot{m}_{sink} and \dot{m}_{source}) only enter and exit through the top and bottom control volumes. New flow rates (\dot{m}_{down} and \dot{m}_{up}) are defined as the net flow through the inner nodes of the tank. When the grid moves, \dot{m}_{down} and \dot{m}_{up} are set equal to zero as the inner nodes move with the flow, rather than the flow passing through them. These flows are illustrated in Figure 5.7.

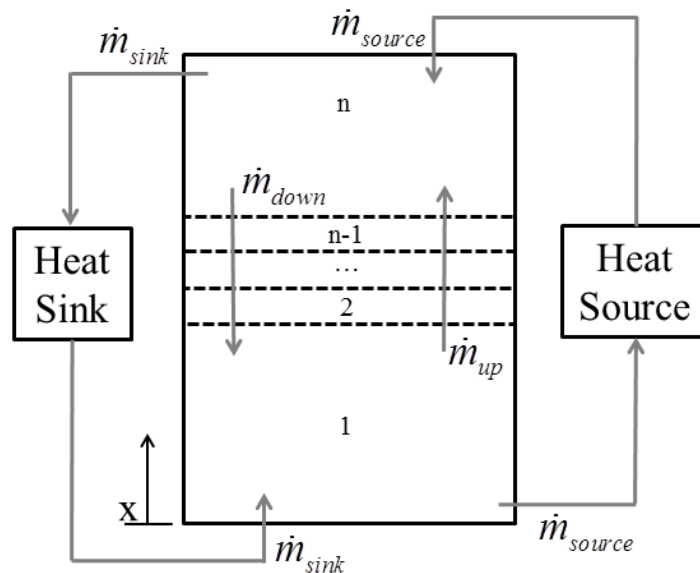


Figure 5.7: A diagram of the adaptive-grid thermocline model.

The logic that determines when the node boundaries move is shown in Table 5.1. The conditions that prevent the boundaries from moving when net flow is downward ($\dot{m}_{source} > \dot{m}_{sink}$) are when the center of the temperature gradient is located above the center node (determined by $T_{mid} < T_{avg}$) or when the volume of Node 1 has reached its minimal prescribed value ($V_1 \leq V_{min}$), indicating that the thermocline region has reached the bottom of the tank. When either of these conditions applies, the volumes of the end nodes will be fixed and net flow downward will be defined, as indicated in (5.3a). Similar conditions are used for upward flow as shown in (5.3b). When none of the restrictions in (5.3a) or (5.3b) apply, the nodes will move in order to track the temperature gradient, keeping its center aligned with the center node(s). This is dictated by (5.3c), where net flow through the thermocline region is defined to be zero. Note that material balances for the inner nodes are not shown because they are trivial, with flow in and out always being equal, resulting in no change in node volume.

Table 5.1: Mass balances under different logic conditions

$\left. \begin{aligned} \dot{m}_{source} > \dot{m}_{sink} \wedge V_1 \leq V_{min} \\ \vee \dot{m}_{source} > \dot{m}_{sink} \wedge T_{mid} < T_{avg} \end{aligned} \right\} \Rightarrow$ $\frac{dV_n}{dt} = \frac{dV_1}{dt} = 0,$ $\dot{m}_{down} = \dot{m}_{source} - \dot{m}_{sink},$ $\dot{m}_{up} = 0$	<p>If net flow through the tank is in the downward direction (i.e. $\dot{m}_{source} > \dot{m}_{sink}$) and either the thermocline is above center or the volume of node 1 is at or below a minimum value, the nodes remain stationary and net flow through the nodes is defined in the downward direction.</p>	(5.3a)
$\left. \begin{aligned} \dot{m}_{sink} > \dot{m}_{source} \wedge V_n \leq V_{min} \\ \vee \dot{m}_{sink} > \dot{m}_{source} \wedge T_{mid} > T_{avg} \end{aligned} \right\} \Rightarrow$ $\frac{dV_1}{dt} = \frac{dV_n}{dt} = 0,$ $\dot{m}_{up} = \dot{m}_{sink} - \dot{m}_{source},$ $\dot{m}_{down} = 0$	<p>If net flow through the tank is in the upward direction (i.e. $\dot{m}_{sink} > \dot{m}_{source}$) and either the thermocline is below center or the volume of node n is at or below a minimum value, the nodes remain stationary and net flow through the nodes is defined in the upward direction.</p>	(5.3b)
$\left. \begin{aligned} \dot{m}_{source} > \dot{m}_{sink} \wedge V_1 > V_{min} \\ \wedge T_{mid} \geq T_{avg} \\ \dot{m}_{sink} > \dot{m}_{source} \wedge V_n > V_{min} \\ \wedge T_{mid} \leq T_{avg} \end{aligned} \right\} \Rightarrow$ $\rho \frac{dV_1}{dt} = \dot{m}_{source} - \dot{m}_{sink},$ $\rho \frac{dV_n}{dt} = \dot{m}_{sink} - \dot{m}_{source},$ $\dot{m}_{up} = \dot{m}_{down} = 0$	<p>If none of the restrictions in (5.3a) or (5.3b) apply, there is no net flow through the nodes as the control volumes of Node 1 and Node n expand or contract.</p>	(5.3c)

The adaptation strategy is illustrated in Figure 5.8. With the tank starting at its cooler temperature, warm flow enters and the temperature gradient begins to develop as shown in Figure 5.8(a). The nodes remain stationary in this case because $\dot{m}_{source} > \dot{m}_{sink}$ and $T_{mid} < T_{avg}$, indicating that the temperature gradient is above the thermocline region specified in the model. As flow moves downward and $T_{mid} = T_{avg}$, the nodes begin to move

as indicated in Figure 5.8(b) and (c). Movement stops as the thermocline region of the model reaches the bottom of the tank as determined by the condition $V_1 \leq V_{min}$.

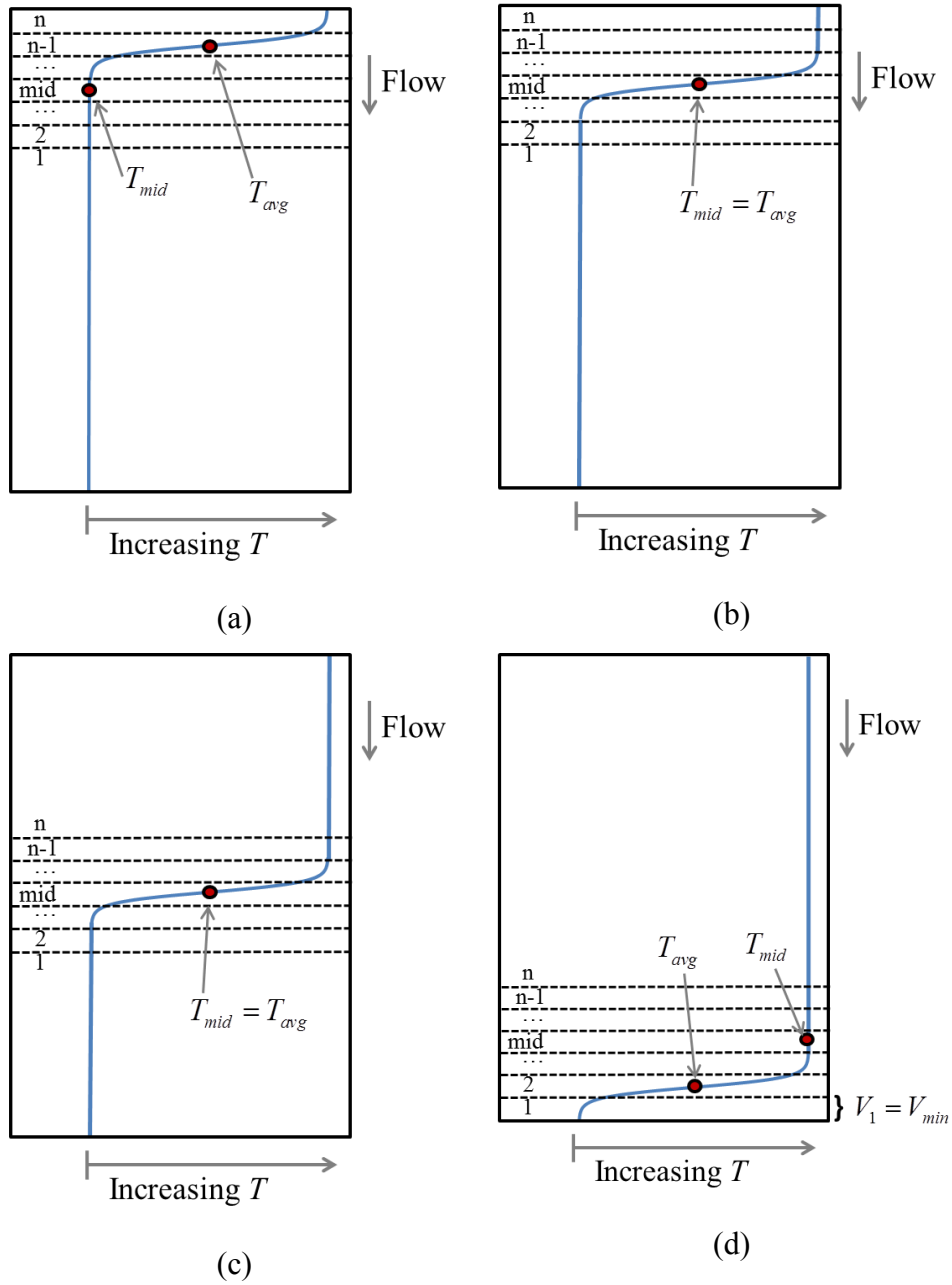


Figure 5.8: A diagram showing the movement of nodes for downward flow.

Energy balances are used to determine the temperature of each node and are shown in Table 5.2. The energy balance for the top node (Node n) is shown in (5.4a), which has volume included in the differential because the volume of this node is variable. Similarly, (5.4c) shows the energy balance for the bottom node (Node 1). The inner nodes (Nodes 2 through $n-1$) representing the thermocline region of the model have constant volume, so this term is removed from the differential in their energy balances (5.4b). When the nodes move according to (5.3c), there is no net flow through these nodes, which eliminates numerical diffusion.

Table 5.2: Energy balances for each node in the tank.

$\rho C_p \frac{d(V_n T_n)}{dt} =$ $C_p (\dot{m}_{source} T_{source} - \dot{m}_{sink} T_n - \dot{m}_{down} T_n + \dot{m}_{up} T_{n-1})$ $-UP\Delta x_n (T_n - T_{amb}) + \frac{\varepsilon A_{xs}}{\Delta x} (T_{n-1} - T_n)$	Energy balance on Node n	(5.4a)
$\rho C_p V_i \frac{dT_i}{dt} = C_p (\dot{m}_{up} (T_{i-1} - T_i) + \dot{m}_{down} (T_{i+1} - T_i))$ $-UP\Delta x (T_i - T_{amb}) + \frac{\varepsilon A_{xs}}{\Delta x} (T_{i+1} - 2T_i + T_{i-1})$	Energy balance for Node 2 through Node $n-1$	(5.4b)
$\rho C_p \frac{d(V_n T_n)}{dt} =$ $C_p (\dot{m}_{source} T_{source} - \dot{m}_{sink} T_n - \dot{m}_{down} T_n + \dot{m}_{up} T_{n-1})$ $-UP\Delta x_n (T_n - T_{amb}) + \frac{\varepsilon A_{xs}}{\Delta x} (T_{n-1} - T_n)$	Energy balance for Node 1	(5.4c)

In order to account for the mixing that occurs under temperature inversion due to variable inlet temperature, the model can be enhanced to include temperature-gradient dependence on the mixing parameter (ε). When the temperature of a node is higher than the node above it, buoyant mixing would ensue. This can be represented mathematically by using a much higher mixing parameter (ε_{hi}) when this condition exists, as indicated by (5.5). This term should be several orders of magnitude higher than the standard mixing parameter (ε), although both can be used as fitting parameters in the model.

$$\varepsilon_{i \text{ to } i+1} = \begin{cases} \varepsilon_{hi} & \text{for } T_i > T_{i+1} \\ \varepsilon & \text{otherwise} \end{cases} \quad (5.5)$$

The adaptive-grid thermocline model is represented by n+2 dynamic states: temperature for each node and volume for the end nodes. Using this model, n can be much smaller than in a standard model because high resolution nodes are only used in the thermocline region. Because of the elimination of numerical diffusion, these nodes can also have larger spacing than in a standard model, where very high resolution must be used to reduce this effect. As a result, the adaptive-grid model can generally have a fraction of the number of variables and equations as a standard model. Although somewhat counterintuitive, this reduced model is actually more accurate than a standard model because it prevents numerical diffusion and properly handles variable inlet temperature in the general case.

Results and Discussion

The adaptive-grid model is validated using operational data from an industrial scale chilled water thermal energy storage tank. The tank is designed to store approximately 8,000 ton-hours of cooling over a roughly 10°C temperature gradient. The tank is used in a district cooling loop, where a system of industrial-sized electrical and thermal chillers is considered to be the heat sink. The heat source for this system is a set of commercial buildings that use the chilled water to cool building air. The tank used is 56 feet in height and 50 feet in diameter.

The model results are presented under discharge conditions, with warm water entering the top of the tank and colder water exiting at the bottom. Figure 5.9 shows the inputs for the tank during one day of operation. As the figure indicates, flow and temperature are kept fairly constant during the first three and a half hours of operation. Three hours and forty minutes into the discharge period, the source flow spikes, causing a drastic decrease in tank inlet temperature several minutes later.

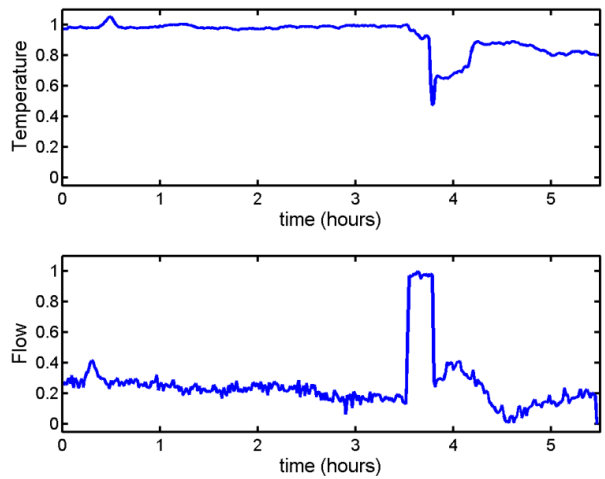


Figure 5.9: Normalized tank inlet temperature and flow.

Figure 5.10 shows the predicted temperature profile in the tank at 3 hours. The results from the standard and variable inlet position model using 600 nodes are also shown. This high spatial resolution is required to prevent excessive numerical diffusion and to ensure that the model remains sufficiently accurate. In comparison, the adaptive-grid model requires only 60 nodes to produce similar and, in fact, more accurate results. Because the inlet temperature has been essentially constant up to this time, all three models perform reasonably well in comparison to the actual measured temperatures.

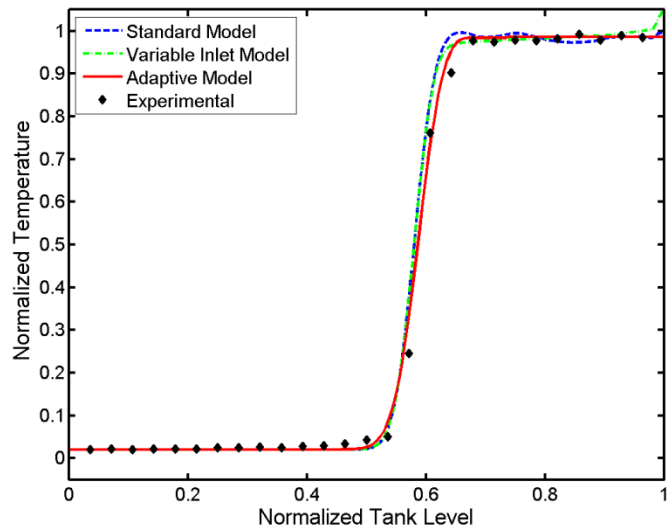


Figure 5.10: Normalized tank temperature vs. tank height at hour 3.

After hour three of discharging, when cooler water enters the top of the tank, temperature inversion occurs. The experimental data at hour four (Figure 5.11) and hour five (Figure 5.12) clearly show that temperature inversion is not maintained. Instead, the cold water at the top of the tank diffuses down and mixes with the warmer layers below. This occurs until the tank equilibrates and a monotonically increasing temperature profile is achieved. The figures show that the standard model does not adequately represent the effect of temperature inversion, with the results showing that the inversion persists, rather than dissipates. The variable inlet position model also inaccurately describes the tank's dynamic response to temperature inversion by predicting an ever-widening thermocline region. The adaptive-grid model, however, approximates the regions above and below the thermocline being at a constant temperature, which is much more consistent with the data.

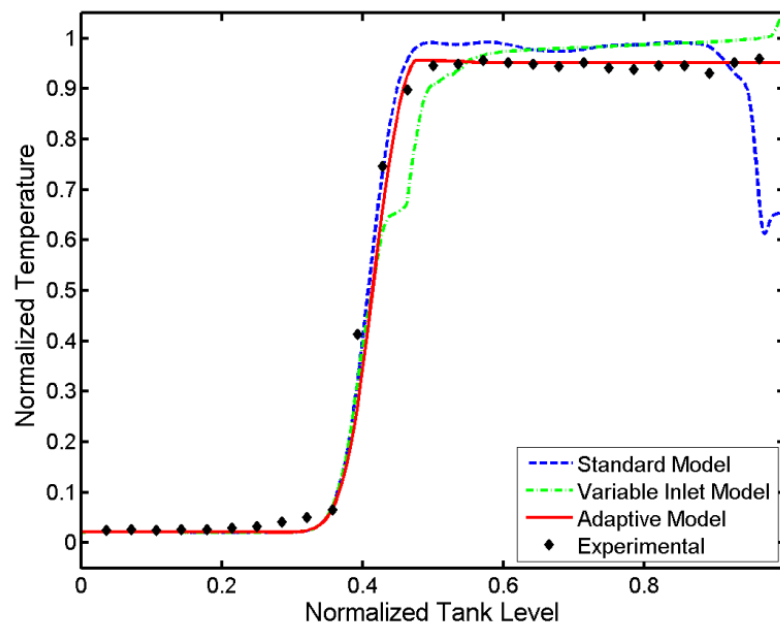


Figure 5.11: Normalized tank temperature vs. tank height at hour 4.

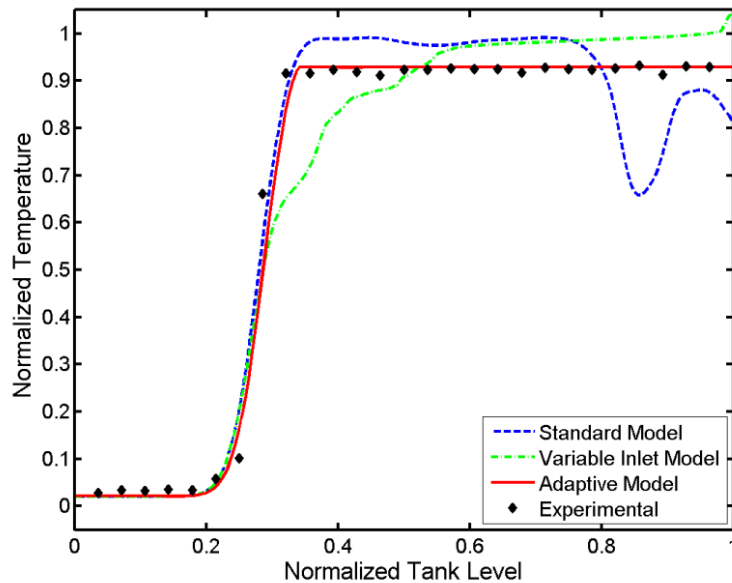


Figure 5.12: Normalized tank temperature vs. tank height at hour 5.

The adaptive-grid model has several advantages over a standard model. It is more accurate under the condition of temperature inversion. It also requires a significantly reduced number of state variables and equations, so it is less computationally intensive. The major reason for these phenomena is that the model prevents excessive numerical diffusion as the control volumes move with the flow. The adaptive-grid model does have disadvantages however. For example, if higher temperature fluid is introduced to the tank after several hours of downward flow, theoretically, a second thermocline could form. Because the adaptive-grid model approximates the ends of the tank as constant temperature regions, this model would not accurately represent this phenomenon. However, it can safely be assumed that the occurrence of a second thermocline would be rare under general operating conditions. For circumstances where this may be a key issue, the inclusion of a temperature-gradient-dependent ε term into a standard model produces accurate results. However, the large magnitude of ε under temperature inversion conditions creates a very stiff model that is extremely computationally intensive when a large number of states are used. The adaptive-grid model, therefore, presents a high accuracy and high computational

efficiency solution to simulating thermocline thermal energy storage systems under most conditions.

Conclusions

The implementation of the smart grid requires reliable and economical energy storage technologies. Thermocline thermal energy storage systems have proven to be cost effective as they require minimal capital investment, but can shift a significant portion of the thermal load for a system. These systems can be used in lieu of electrical storage due to the fact that thermal loads are a significant contributor to electricity consumption. They have found application in HVAC applications for space cooling and space heating and in concentrated solar power generation.

In addition to energy storage, the smart grid will require accurate and efficient modeling, so that simulation can be used to predict performance or for real-time optimization. Because thermocline systems have a spatial dependence on temperature, modeling of these systems becomes more complex than for isothermal systems. Two of the key issues encountered in modeling thermocline systems are numerical diffusion and temperature inversion. By employing an adaptive-grid methodology, where the control volumes representing the thermocline region of the tank move with the flow, the effect of numerical diffusion is minimized, meaning that more accurate models can be produced using far fewer state variables and equations. Because larger nodes at the ends of the tank are used to represent constant temperature regions, this model also better represents scenarios where temperature inversion occurs. The model is enhanced by adding a temperature-gradient-dependent mixing parameter to represent buoyancy mixing, which occurs when temperature inversion persists.

Nomenclature

Symbol	Description
A_{xs}	Tank cross sectional area
C_P	Storage fluid heat capacity
\dot{m}	Mass flow rate
P	Tank perimeter
T	Temperature
t	Time
U	Tank fluid to ambient overall heat transfer coefficient
V	Node volume
V_{min}	Minimum desired node volume
x	Tank height from bottom of tank
Δx	Length of node
ε	Lumped mixing term representing diffusion, conduction, and axial mixing
ε_{hi}	Higher-valued mixing term under conditions of temperature inversion
ρ	Storage fluid density
Subscripts	
amb	Ambient conditions
avg	Average temperature of node 1 and node n
$down$	Net flow downward through inner nodes
i	Node number
mid	Temperature of middle node (for odd n) or average temperature of two middle nodes (for even n)
n	Total number of nodes used in spatial discretization of the tank
$sink$	Flow through heat sink
$source$	Flow through heat source
up	Net flow upward through inner nodes

CHAPTER 6 : ELECTRICAL, HEATING, AND COOLING LOAD FORECASTING FOR A DISTRICT ENERGY SYSTEM

Introduction

District energy systems offer many economic and environmental benefits, such as: the ability to recycle waste heat with combined heat and power (CHP), economies of scale in district heating and cooling applications, and the ability to integrate large scale energy storage [108]. CHP systems are distributed electricity generation resources where smaller-scale power plants are used to provide electricity for the geographical area immediately adjacent to the power plant. Because they are located near commercial or residential buildings, the effluent heat from the turbine can be readily recovered and used to heat the neighboring buildings [109]. This is typically done in a district heating loop, where hot water, steam, or another fluid is used to transport the heat to the network of buildings [110]. Similarly, district cooling systems use centrally-located chilling equipment to generate cooling in the form of chilled water or another medium so that it can be distributed to the nearby buildings for air conditioning [111]. This enhances the economics of cooling a large campus because cooling can be done on a large scale using industrial size chillers. Distributed electricity generation systems, such as CHP, can also substantially reduce transmission costs and efficiency losses as the power does not have to be transported using high-voltage power lines over long distances as compared to larger, centralized power plants [112].

While producing electricity, heat, and cooling on a district level has many advantages, it also requires intelligent operation. Because energy demand fluctuates, district energy systems must continually adjust their operation so that demand is met at all times [113]. Because each of these loads may vary somewhat autonomously, regulating the system so that each load is met in real time can be difficult. Optimizing the system's operation so that efficiency is maximized or cost is minimized can also be problematic as

the demand continually changes. Optimizing over a time horizon of several hours or days, for example, requires prior knowledge of the conditions under which the system will operate at each instance in time during that span, i.e., a load forecast.

Load forecasting is crucial in electrical power production, as it is used to determine day-ahead prices for the electricity market and which units should be committed for economic dispatch [114], [115], [116]. An electric grid may encompass hundreds of power plants and serve populations of millions of people, so accurate forecasting is critical so that reliable and economical electric power can be produced and delivered. On a smaller scale, load forecasting is also critical for the regulation of microgrids [117] to ensure that demand is always met.

Although less predominant than electric load forecasting, cooling [118], [119], [120] and heating [121], [122] load forecasting are also important for advanced decision making in district energy systems. Optimizing the system so that each load can be met in the most efficient and cost-effective manner requires the incorporation of a load forecast, particularly when the dynamics of the system are on the order of several hours, such as when energy storage systems are involved. Energy storage gives the system flexibility to shift loads from one time to another. These degrees of freedom can be exploited through dynamic optimization [123]. However, this requires advanced knowledge of the loads over the time horizon under consideration.

The following study is unique because it covers a large-scale district energy system that simultaneously produces electricity, heating, and cooling for a large campus. Each of these utilities is produced centrally and distributed to hundreds of buildings. Forecasting each of these loads based on meteorological and time (hour, day of the week, etc.) variables is challenging, but critical to optimization of the system, which includes CHP, chilled water thermal energy storage (TES), gas turbines, steam turbines, heat recovery steam generators (HRSGs), and auxiliary boilers. This work includes detailed analysis of each of these loads as well as the development of models to accurately forecast them 24+ hours in advance.

Background

Energy load forecasting models are utilized for a number of applications including cooling loads [118], heating loads [122], and electrical loads [124]. A review of the literature has found that early investigations into energy load forecasting relied heavily on the artificial neural network (ANN), a computational nonlinear model [125], [126], [127], [128], [129], and similar approaches such as genetic algorithms [130], [131]. An empirical “black-box” approach to forecasting, ANN models are straightforward to develop and produce models that are typically as reliable as the data used to train them. However, due to their simplicity, ANNs have drawn a number of critics that suggest that there may be better-suited methods to the problem of forecasting energy loads [132], [133].

Time series analysis models are an improvement upon ANNs when data points possess inherent temporal ordering. This is often the case in energy load forecasting where current states are related to past events such as HVAC cycling and time series analysis accounts for these trends and transient states. Time series analysis methods are categorized into two main groups, time-domain and frequency-domain. Time-domain models include autoregressive, integrated, and moving average models. Variants such as autoregressive moving average (ARMA) and autoregressive integrated moving average (ARIMA) models are especially prevalent in the literature and have been investigated extensively with relation to energy load forecasting [133], [134], [135], [136], [137]. The concentration of studies focusing on nonlinear specific variants of ARMA and ARIMA models with respect to load forecasting is quite low, with only a few groups pursuing this body of work [138]. Frequency-domain methods have also been applied to energy load forecasting applications in the literature [139], [140], [141], [142].

With specific application to forecasting building energy loads, ANN is still the dominant methodology used in the literature, due to ease of model development and acceptable model accuracy. Kusiak et al., for example, utilized ANNs with humidity and temperature inputs to perform steam load forecasting for buildings [143]. Results returned

from their ANN models were satisfactory (mean absolute percentage error for the model typically >10% in most tested months) but could be improved by time series analysis. Neural network variants have been used similarly for building load forecasting by Kwok, Ben-Nakhi, and Li, [144], [145], [146]. Novel techniques have also been utilized with respect to building load forecasting. Duanmu et al. developed a simplified prediction model, the Hourly Cooling Load Factor Model (HCLFM) that produced quick and fair estimates of cooling load forecasts in buildings [147].

System Overview

The main campus at the University of Texas at Austin serves over 70,000 students, faculty, and staff. The campus also includes over 160 buildings with approximately 17 million square feet (1.6 million m²) of space. The Hal C. Weaver power plant and associated facilities are responsible for providing all the cooling, heating, and electrical needs for the campus. Ties to the city grid exist, but they are for emergency purposes only. Because the campus is research-oriented, operating 24 hours per day year-round, the utilities must be both flexible to meet the variability and reliable to ensure that campus needs are not interrupted. The power plant includes 137 MW of onsite combined heat and power (CHP) generation, 1.2 million lb/hr (151 kg/s) of steam generation, and 46,000 tons (162 MW) of chilled water capacity. A district heating and cooling network runs throughout campus in over 6 miles of distribution tunnels. The system also includes a 4 million gallon (15,100 m³) thermal energy storage tank with a capacity of 39,000 ton-hr (137 MWh).

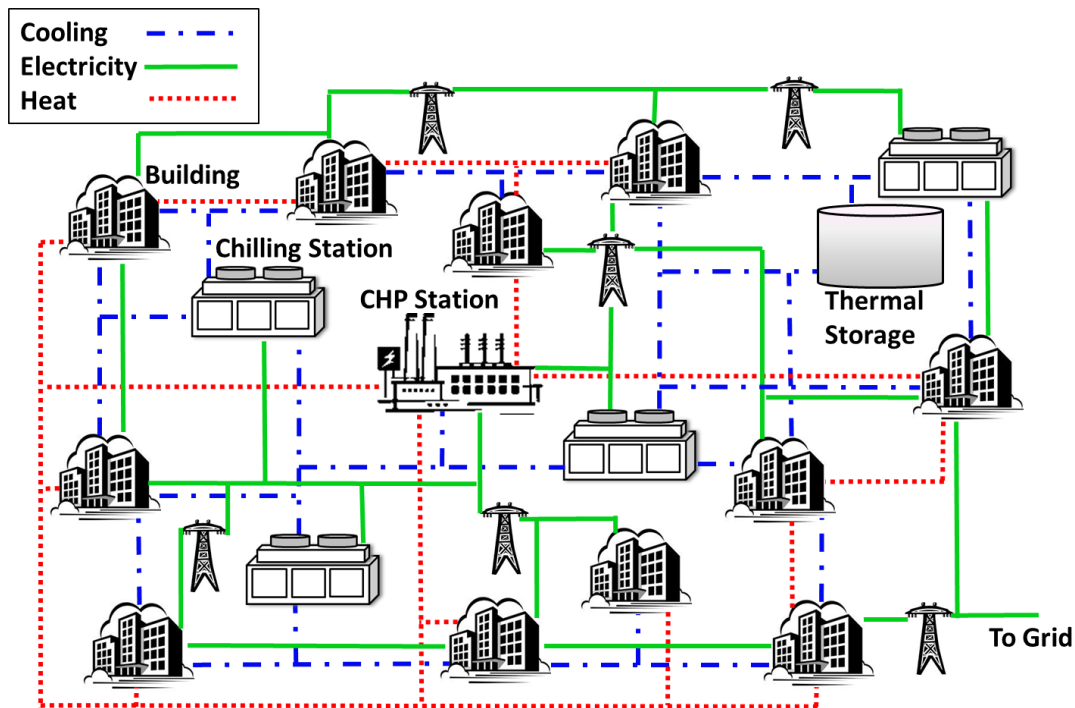


Figure 6.1: A district energy system.

A simplified schematic of the system is shown in Figure 6.1, which illustrates the CHP plant, the buildings, the TES unit, and the chilling stations. The chilling stations are electric-powered centrifugal chillers that produce chilled water, which is then pumped around campus to meet building cooling needs. The chilled water can also be stored in the TES tank so that the cooling load can be offset if needed. Information about the loads is summarized in

Table 6.1. Located in Austin, TX, USA, the heating, ventilation, and air conditioning (HVAC) needs for the system are dominated by cooling, which, in turn, contributes significantly to the electric load, as all cooling is met by the electric-powered chillers. As the table shows, ambient temperatures can be quite high, exceeding 40 °C. Relative humidity can also reach 100%, although this is typically only observed during cooler periods.

Table 6.1: Summary of weather and load for one year.

	Minimum	Average	Maximum
Cooling Load (MW)	16.5	58.7	116.3
Heating Load (MW)	17.2	28.8	67.8
Electrical Load (MW)	26.1	40.3	61.9
Dry Bulb Temp. (°C)	-5.0	20.8	40.6
Wet Bulb Temp. (°C)	-6.1	16.5	26.1
Relative Humidity (%)	12.3	60.2	99.9

Figure 6.2 illustrates how loads vary over a typical week and how temperature and humidity (shown in Figure 6.3) impact the loads. These figures represent loads for a week in early August 2012 during which temperatures get high during mid-day. Corresponding to the changing temperatures, the cooling and electrical loads fluctuate significantly. Careful observation of Figure 6.2 reveals that building/campus occupancy plays a significant role in the cooling and electrical loads. This is illustrated by the more constant loads observed during the weekend (Saturday and Sunday). This highlights the importance of inputs beyond meteorological variables. Because the plot shows summer-time conditions, heating loads are low and fluctuate very little. Although direct heating of building space is not typically done during summer months, steam is used for lab equipment and other purposes on campus. Steam is also used for building dehumidification as air may be sub-cooled to remove moisture and re-heated to reach the appropriate temperature.

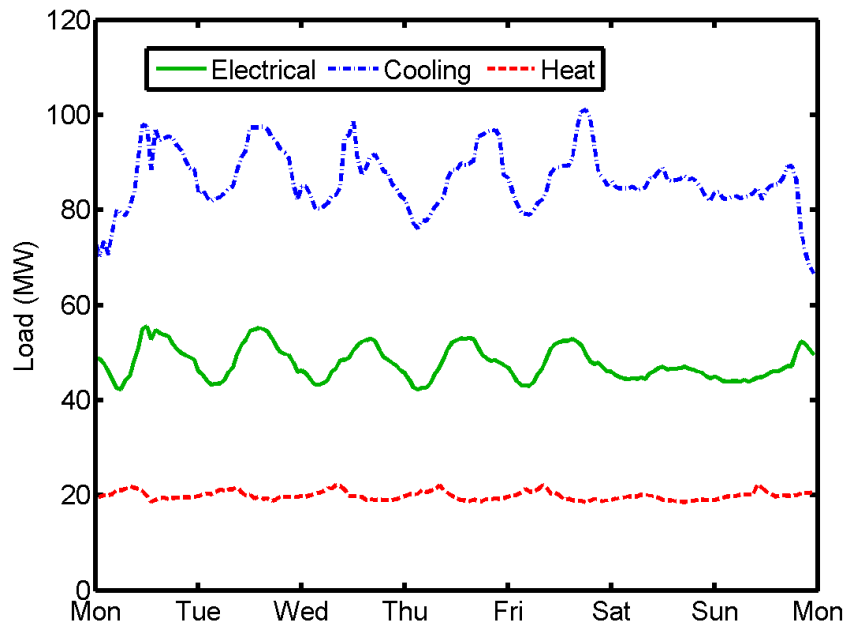


Figure 6.2: Campus loads during an August week.

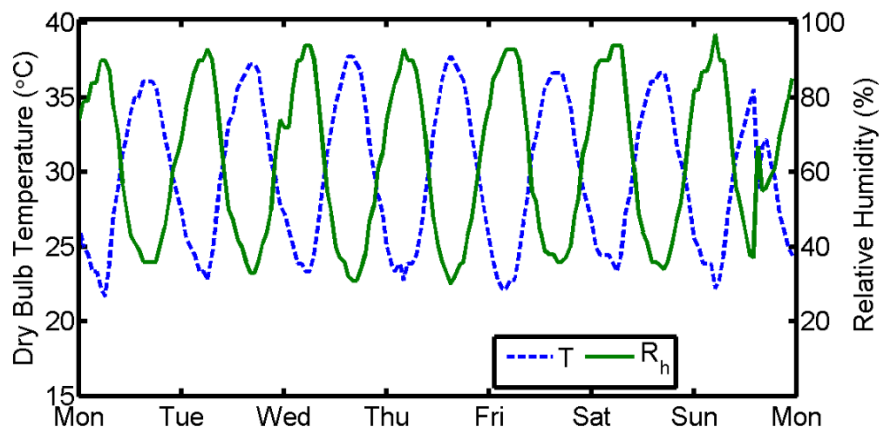


Figure 6.3: Temperature and humidity for an August week.

Winter loads look significantly different than summer loads with a representative week (in February 2012) shown in Figure 6.4 and ambient conditions in Figure 6.5. As Figure 6.5 shows, the conditions during this particular week are much less regular than those in Figure 6.3. Accordingly, the loads in Figure 6.4 show much more sporadic behavior. As expected, cooling loads are much lower and heating loads much higher than in the summer months. The heating loads also fluctuate much more, making them more

difficult to accurately forecast. These figures highlight both the difficulty and the importance of developing accurate forecasting models to represent loads which are heavily dependent on meteorological variables, but also vary with respect to season and building occupancy.

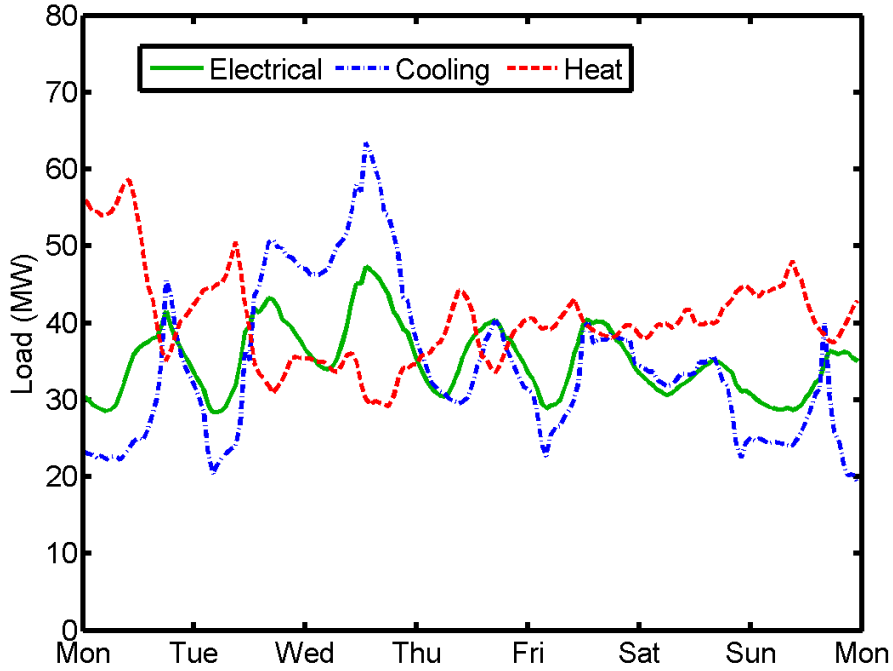


Figure 6.4: Campus loads during a February week.

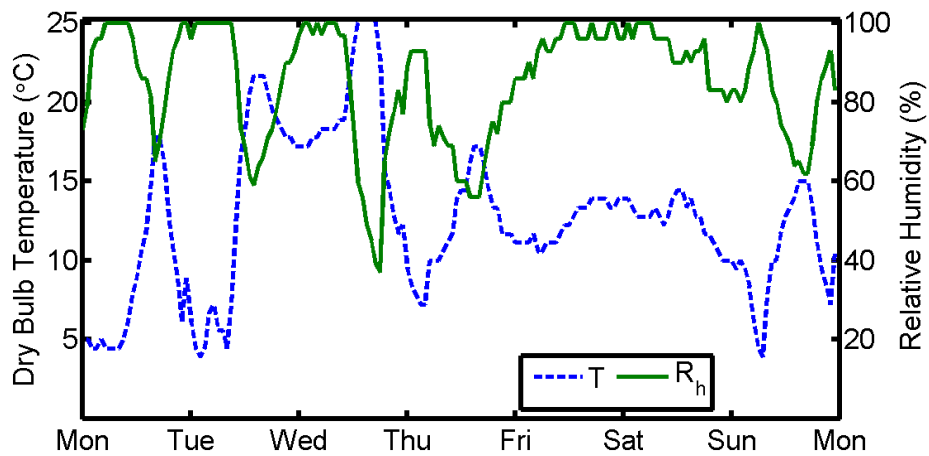


Figure 6.5: Temperature and humidity for a February week.

Correlation analysis also provides some insight into the impact of meteorological variables on the loads as well as the correlation of the loads with each other. The correlation coefficients of hourly data over the year-long period are shown in Figure 6.6. As the figure shows, all the loads are highly correlated with each other, which indicates that they undergo similar variations. The cooling and electric loads are positively correlated, while they are both negatively correlated with heating load. Each load is strongly correlated with ambient dry bulb temperature and less so with ambient relative humidity. Cooling and electrical energy usage are positively correlated to temperature and negatively correlated to humidity, while the reverse holds true for heating. Because of the strong correlation of loads with meteorological variables, it is clear that these variables, particularly temperature, would be important inputs for a load prediction model.

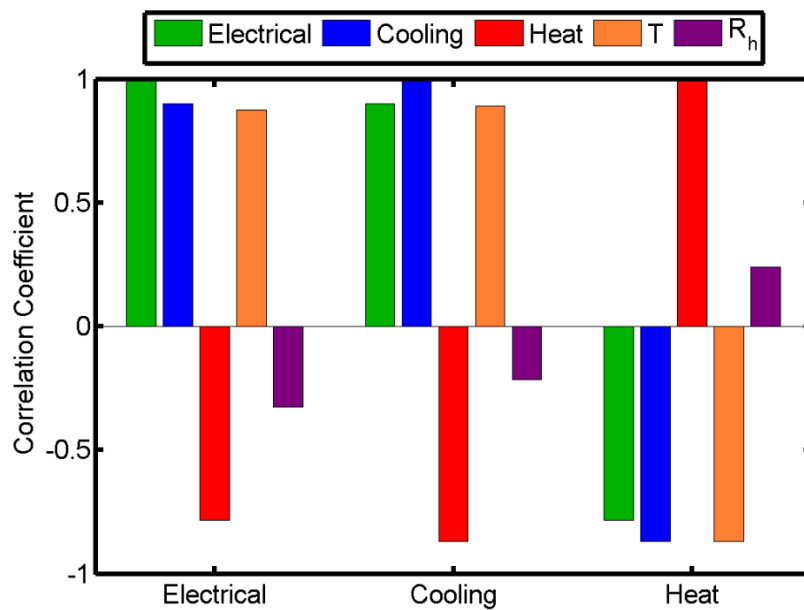


Figure 6.6: Correlation coefficients for loads and weather.

Model Development

Load forecasting for large-scale energy systems, such as a campus with many buildings, requires models that represent complex relationships between inputs (such as weather or occupancy) and the output (the load). First-principles models are generally not

practical for this task as they require detailed models of each building and component in the system. Alternatively, data-driven, empirical models can capture these complex relationships with comparatively little information about the system. Because empirical models do not represent the physics in the system, the model structure and the proper inputs must be carefully selected. The model parameters must also be appropriately identified using an adequate amount of historical data from the system.

A linear model is the most basic empirical model to use for load forecasting. A linear model can be identified using inputs such as weather, previous loads, and time variables to represent the hour of the day, day of the week, month, etc. These time variables serve as a proxy for occupancy, which is generally difficult to quantify and predict. Because of the regularity of work schedules and seasonal load variations, occupancy can be represented using different model parameters corresponding to different hours, days, or months. The linear load-forecasting model takes on the form shown in (6.1), where a , b , and c are the model fitting coefficients, L_k is the load at time k , N is the model order (i.e. the number of time steps back to retrieve inputs), and θ represents the values of weather variables. The subscripts h , d , and m refer to the hour of the day, day of the week, and month of the year, respectively. Therefore, there are different additive constants (c_h , c_d , and c_m) for each time period.

$$L_k = \sum_{i=1}^N a_i L_{k-i} + \sum_{i=0}^N b_i \theta_{k-i} + c_{h,k} + c_{d,k} + c_{m,k} + d \quad (6.1)$$

The relationship in (1) is an autoregressive model with exogenous inputs (ARX model) and uses past load information to predict future loads, making it recursive in nature. Exogenous inputs such as weather or time can be added to improve model accuracy by representing the dependence of the load on these additional inputs. The model order, N , can be adjusted so that more (or fewer) past states and inputs are used. A zero-order model ($N=0$) does not include any past state information and reduces to a steady-state model representing the load as a linear function of exogenous inputs only.

For representing the nonlinearity in the relationships between inputs and loads, neural networks are a viable option. ANNs are a class of empirical models with the ability to represent complex input/output relationships. They combine many functions into a single model with the option to select the basic functional form(s) as well as the number of functions used in the model. This provides flexibility to add complexity as needed, with more functions being used to represent increasingly complex behavior. A three-layer perceptron is a type of neural network that uses linear combinations of activation functions (ϕ) to map outputs to inputs. Figure 6.7 shows a three-layer perceptron with multiple inputs (u_i) and a single output (y). The weights ($w_{i,j}$ and W_j) are fitting parameters, which are adjusted using optimization to obtain optimal model performance. As more nodes in the middle (or hidden) layer are added (which means more activation functions), the model gains more fitting parameters, which leads to an enhanced ability to represent complex input/output behavior. Increasing the size of the model also leads to increased complexity and the tendency for over-fitting. Therefore, it is important to select a model with enough parameters to represent the data well, but not so many as to over-complicate the problem.

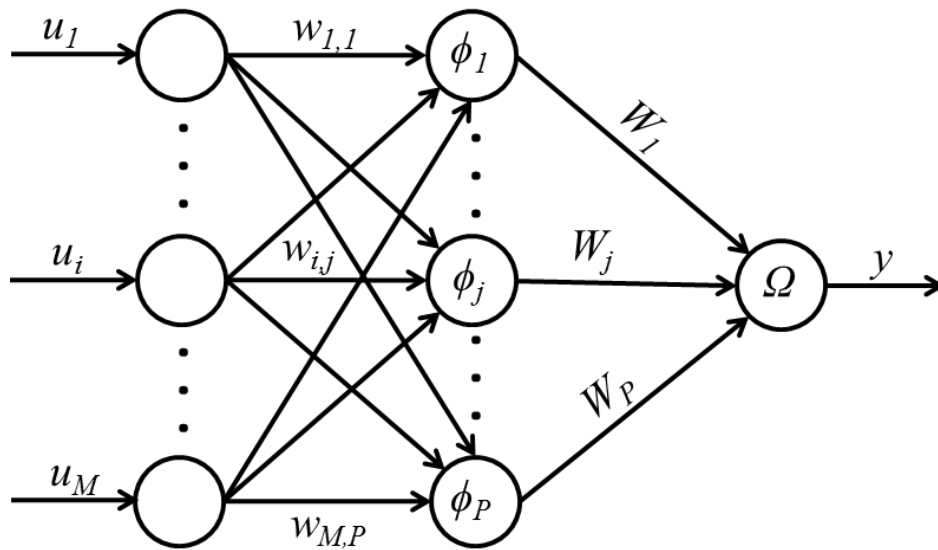


Figure 6.7: A diagram of the neural network structure.

The neural networks used in this work use sigmoidal (hyperbolic tangent) activation functions. For load forecasting, these functions are advantageous because they represent continuous behavior, but the fact that they saturate at high and low input values also allows them to approximate on/off behavior for certain phenomena. Using these activation functions, the model equations are shown in (6.2) and (6.3) where Q and q represent constant bias terms (also used as fitting parameters) and P and M represent the number of hidden nodes (or activation functions) and inputs, respectively.

$$\Omega(\varphi_j) = \sum_{j=1}^P W_j \varphi_j + Q \quad (6.2)$$

Here, φ represents the activation functions that are a direct function of model inputs (u).

$$\varphi_j(u_i) = \tanh\left(\sum_{i=1}^M w_{i,j} u_i + q_j\right) \quad (6.3)$$

Combining (6.2) and (6.3) to obtain the model function (f) explicitly in terms of u yields (6.4).

$$f(u_i) = \sum_{j=1}^P W_j \tanh\left(\sum_{i=1}^M w_{i,j} u_i + q_j\right) + Q \quad (6.4)$$

Using the three-layer perceptron described in (6.4) to represent the relationship between inputs and the load at a given time (k), the forecast model takes on the form shown in (6.5), where N again represents the model order. Using a neural network model, the hour, day, and month time variables can be represented using their integer values (i.e., 1-24, 1-7, and 1-12). In (6.5), Ω represents the collection of time variables.

$$L_k = f\left(L_{k-1}, \dots, L_{k-i}, \dots, L_{k-N}, \theta_k, \dots, \theta_{k-i}, \dots, \theta_{k-N}, \Omega_k\right) \quad (6.5)$$

The nonlinear model is also recursive and is classified as a nonlinear autoregressive model with exogenous inputs (NARX). The neural network is used to make a one-step ahead prediction of the load using readily available data (past loads, past weather

measurements, forecasted weather, and time). Using this prediction, the load value can be used to recursively predict loads further into the future. The use of previously measured loads also allows the model to self-correct as newly-acquired information (i.e., new measurements or a new weather forecast) becomes available. Measured loads also provide a reference point so that future predictions can be more accurate. When the model order is zero ($N=0$), no past load data is used and the model reduces to a static model.

Results

Using a year of hourly-averaged load data for electrical, heating, and cooling, models of various neural network sizes and orders are fit to minimize the sum-squared error between the model and the measured data. Corresponding weather data obtained from the National Weather Database are used as model inputs. Various model orders and neural network sizes are used to obtain the appropriate balance between model accuracy and simplicity. Adjusted R^2 is used as a metric to compare models against each other.

Fitting the linear ARX models is relatively straight-forward as model parameters can be determined using matrix algebra to determine the global solution for the best fit. The NARX models are nonlinear in the fitting parameters (W , w , Q , and q) and therefore require a more complex nonlinear optimization algorithm to determine an adequate solution. The Levenberg-Marquardt algorithm is used to solve for these parameters using the MATLAB Neural Network Toolbox. Because the fitting problem is non-convex, this algorithm does not guarantee a global solution. Model parameters are randomly initialized and sometimes require several initial guesses to converge on a good model fit. This is done several times and only the best model fit is kept. Both the linear ARX and NARX models are fit to a one-step ahead prediction. To make longer predictions, the model outputs can be used recursively to generate a prediction for as many time steps into the future as necessary, provided that the corresponding forecasted weather information is available.

While a statistical analysis using an F-test to find the appropriate model order determines that inputs for load data from up to six previous time steps are statistically

significant, the model fits improve only marginally for orders high than two. This is true for the load forecasting model for all loads (cooling, electrical, and heating). Therefore, a second order model is selected in all cases. The number of hidden nodes selected for the neural networks is 10, as model fits do not improve significantly beyond this point.

Although the dynamic models are fit using only a one-step-ahead prediction, they are evaluated on their ability to predict 24 hours into the future. Because of the recursive nature of the model, it is critical that the one-step-ahead be especially accurate as the outputs are used recursively to make predictions further in advance. Any error, therefore, will be compounded. As will be demonstrated, this is not problematic, as the steady-state relationships dominate when the prediction is extended out to long time horizons (greater than about ten hours). In order to evaluate the models' ability to predict loads 24 hours in advance, the dynamic models are run recursively by looping the model-predicted loads and using them as inputs for future predictions. At a given time k , the only information available to the model are the previously measured loads (at times $k-1$ and $k-2$), measured and forecasted weather data (from time $k-2$ to time $k+23$), and the corresponding time variables at time k . Adjusted R^2 , which includes a penalty for model complexity) is used as the metric to evaluate the fits. These values are shown in Table 6.2.

Table 6.2: A comparison of adjusted R^2 values.

	Cooling	Heating	Electrical
Static Neural Network (weather only)	0.906	0.820	0.808
Static Neural Network (weather and time)	0.945	0.942	0.910
Linear ARX (weather only)	0.911	0.932	0.749
Linear ARX (weather and time)	0.936	0.948	0.850
NARX (weather only)	0.948	0.977	0.784
NARX (weather and time)	0.964	0.986	0.933

Several conclusions can be drawn from the data in Table 6.2. By comparing the weather-only models to the weather and time models, conclusions can be made about how much campus occupancy impacts the load. For the electrical load, for example, there is a substantial improvement in the model fit if occupancy is added as a model input. The cooling load, by contrast, appears to have much less dependency on occupancy, which is indicative of the thermal inertia that large buildings have and is also reflective of the lack of an occupancy-dependent building control scheme, which is characteristic of older campus buildings. Similarly, heating loads also appear to have little dependency on occupancy when looking at the NARX models. However, the static models indicate a significant improvement when including occupancy. This is due to the large impact that the month of the year has on the output, as the loads change significantly on a seasonal basis. The linear ARX models are reasonably accurate for predicting cooling and heating loads, although the NARX models prove to be even more so. For electrical loads, however, the linear ARX models are much less accurate, with an adjusted R^2 value of only 0.85. In all cases, the NARX models with time variables as inputs yield the most accurate results, indicating that the relationships are nonlinear in general. Based on this analysis, the second order NARX models with weather and time inputs are recommended for use in a 24-hour forecast prediction.

The results of the second order NARX models are shown for a summer day (July 31st), shown in Figure 6.9 through Figure 6.11, and a winter day (February 14th), shown in Figure 6.13 through Figure 6.15. Figure 6.8 and Figure 6.12 show the corresponding weather information for the same days. The predictions are made before the first hour of each day, using the forecasted weather inputs and time data for each hour of the following day. Using the NARX models, the loads are then predicted recursively. The model-forecasted loads are indicated by the dashed lines, while the actual measured values are represented by the solid lines. 95% confidence bounds are also computed using the standard deviation of the fitting error.

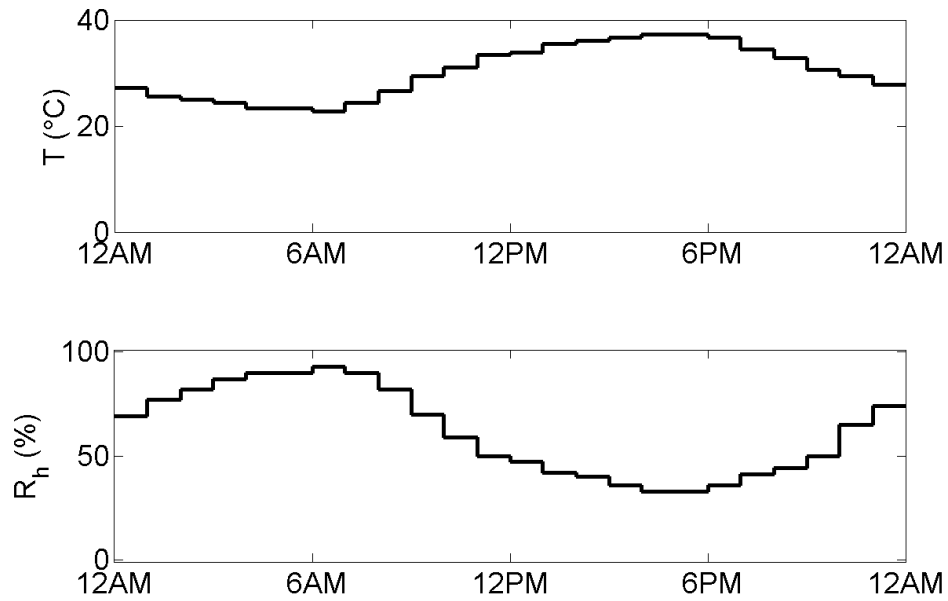


Figure 6.8: Dry bulb temperature and relative humidity for July 31, 2012.

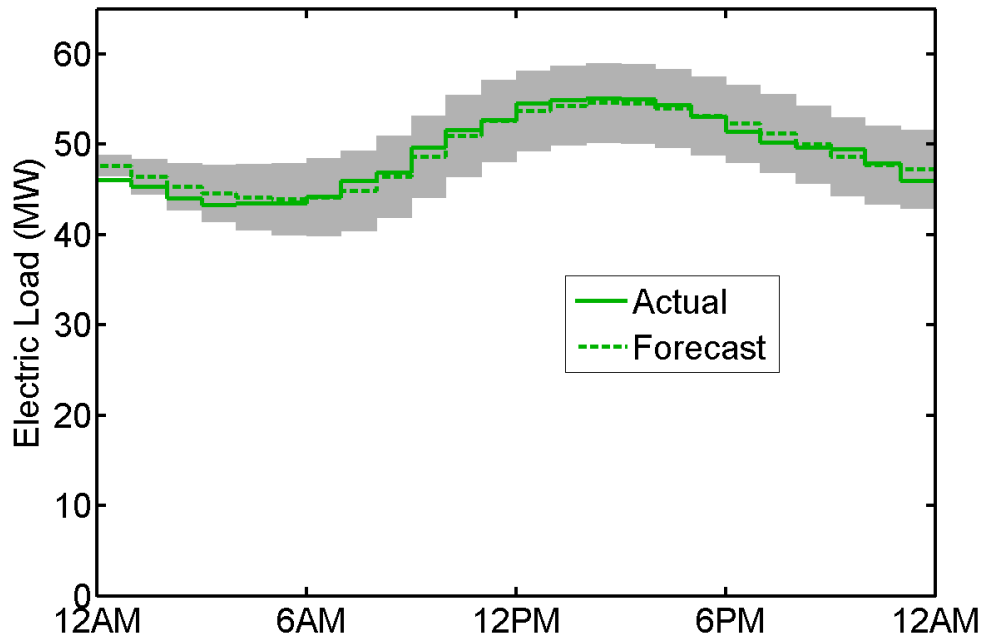


Figure 6.9: Forecasted electric load and actual data for July 31st, 2012.

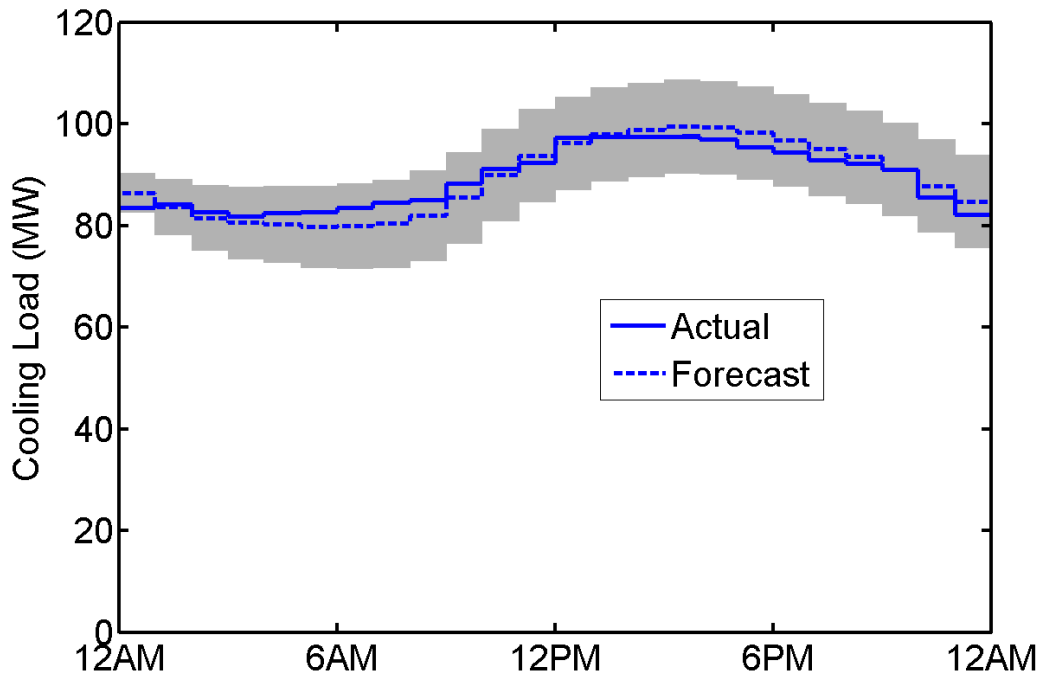


Figure 6.10: Cooling load forecast and actual data for July 31st, 2012.

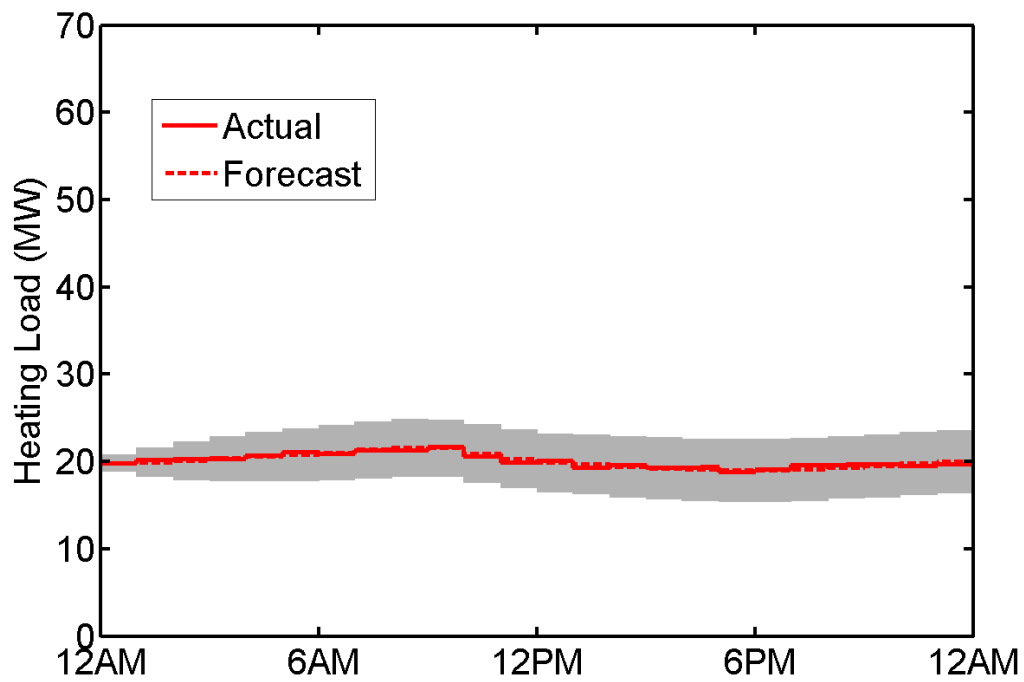


Figure 6.11: Heating load forecast and actual data for July 31st, 2012.

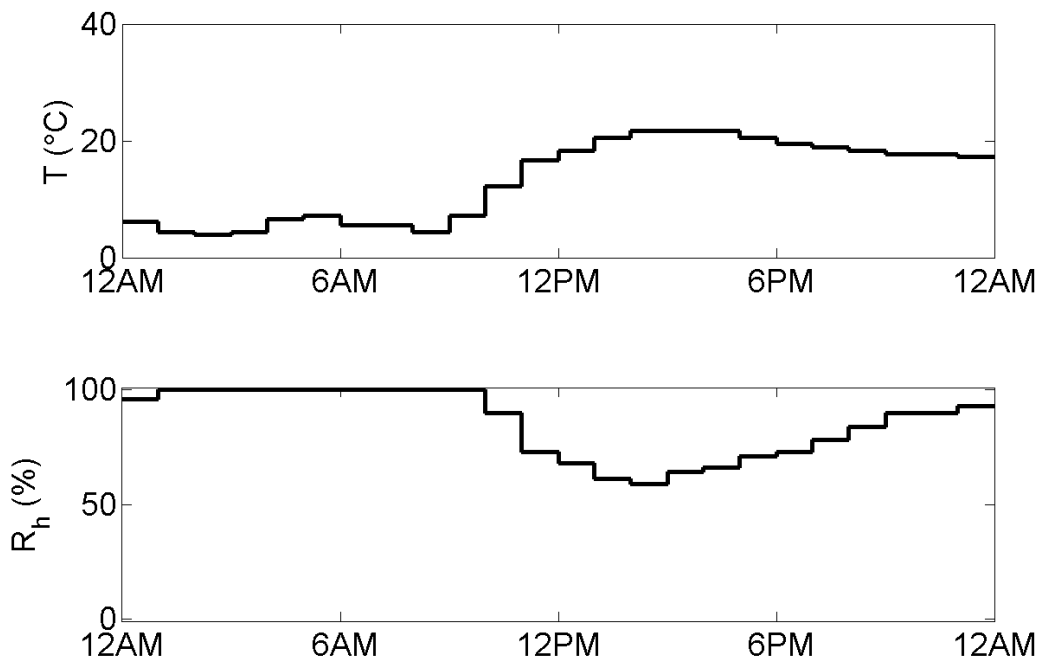


Figure 6.12: Dry bulb temperature and relative humidity for February 14th, 2012.

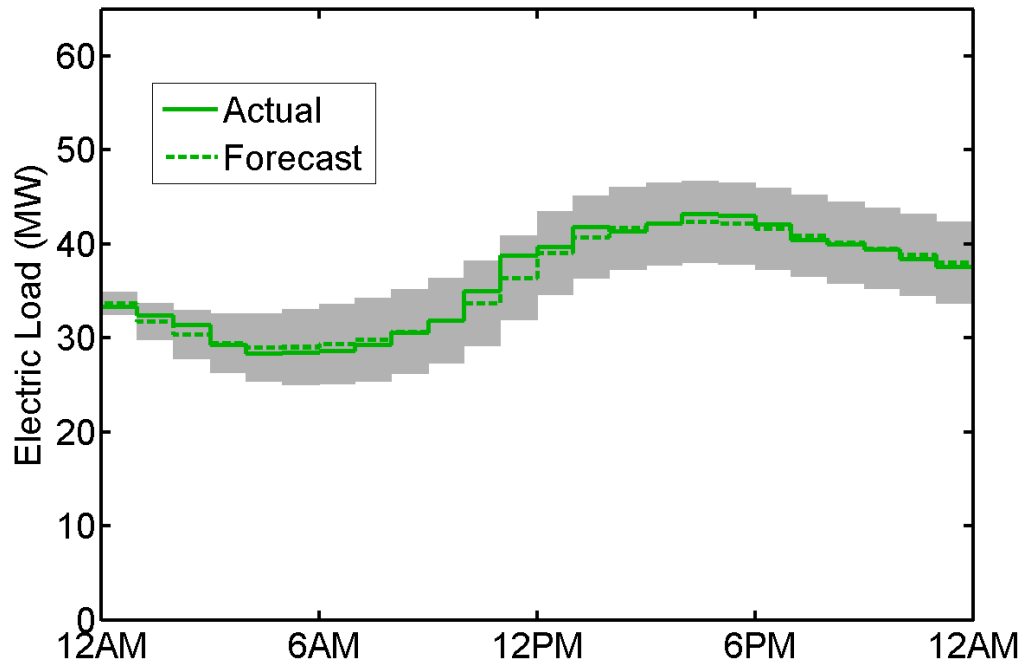


Figure 6.13: Electric load forecast and actual data for February 14th, 2012.

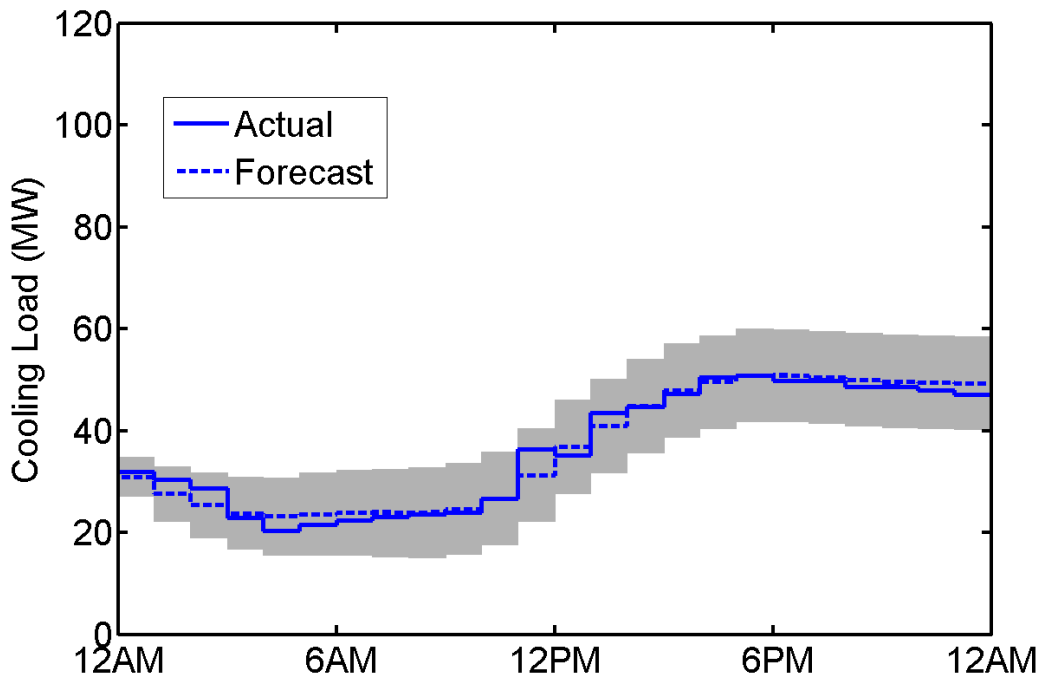


Figure 6.14: Cooling load forecast and actual data for February 14th, 2012.

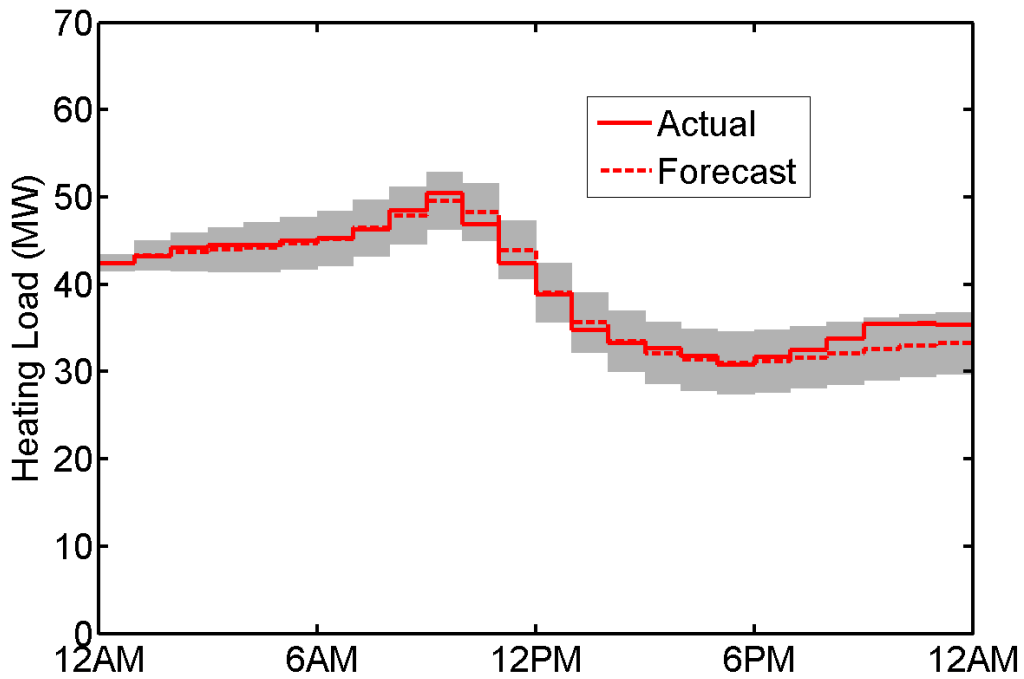


Figure 6.15: Heating load forecast and actual data for February 14th, 2012.

As each of the load forecasting figures shows, the confidence intervals are small in the first few hours of the forecast. This is due primarily to the fact that the actual measured loads for the two hours prior to the prediction are used as inputs. These measured loads provide a reference point so that the predictions in the hours that immediately follow are generally more accurate. The use of a second order model also means that an initial slope is provided and can help indicate whether the load is increasing, decreasing, or remaining relatively constant. The confidence intervals gradually increase, however, over the first several hours of the prediction and the previously-measured loads become less and less relevant. After roughly ten hours, the magnitude of the range of the confidence bounds remain fairly constant. This indicates that, while the dynamics of the system are important, the static relationships between loads and the exogenous inputs (temperature, relative humidity, and time variables) are reasonable predictors of the loads by themselves. Therefore, the confidence bounds do not continue to grow, but rather stabilize, as these static relationships provide an accurate forecast independent of previous measured loads, which are less meaningful for forecasting further out. The fitting results highlighted in Table 6.2 confirm this, as the static neural network models still produce accurate predictions, with adjusted R^2 values above 0.9 for all of the models.

In order to ensure that results are always as accurate as possible, predictions can be made on an ongoing basis. For instance, if predictions are made every hour using the most recent measured load data and weather forecast, the forecast error for the hours that immediately follow will generally be reduced compared to the previous hour's prediction. Implementing this strategy ensures that forecasts stay accurate and gives the models a self-correcting nature. When observed data differs from the predicted result, the measured load is then used as an input, and the model can account for it and make better predictions during the following forecast.

The heating loads for summer are fairly flat and the forecasts are generally very accurate on summer days, as Figure 6.11 indicates. During winter time, when space heating of campus buildings ramps up, heating loads vary much more significantly. The forecasting

model is still able to accurately predict these fluctuations, as shown in Figure 6.15. The heating load forecasting model demonstrates the best fit. Part of the reason for this is that summer loads fluctuate very little and the forecasts are generally very accurate during this period.

The cooling load forecasting model is next in accuracy, although there can occasionally be significant errors in the forecasts. Forecasting the cooling load for this particular system is more difficult because the cooling system relies on a collection of eleven different chillers to meet the cooling load. Chillers can be switched on and off at an operator's discretion, which introduces a human element into the load forecasting. While the cooling load must be met in real time, there are occasionally sudden jumps in the data, indicating that a chiller has just been switched on or off.

The electric load is fundamentally different from the HVAC loads in that changes can be more instantaneous, as there is less of an inertia element. Equipment that consumes a lot of electric power, for instance, can be switched on or off and the change in load will be observed on a much faster time scale than with cooling or heating. Although these changes in individual pieces of equipment are generally small compared to the total load, they are unpredictable. Electric load is also much less dependent on weather conditions than cooling and heating. As Table 6.2 indicates, the weather-only models for predicting electric load produce comparably poor results. When time variables are introduced to the model, however, the fits improve dramatically. This indicates that electric loads are very reliant on campus occupancy as the model is able to identify that electricity usage varies with time of day or day of the week. The electric load forecasting model is the least accurate of the three. However, its results are generally reliable and can be quite valuable when used to make decisions about plant operation.

Conclusions

The ability to forecast loads in advance for central utilities generation can be a valuable tool. It allows the plant to be operated proactively so that large equipment can be

ramped up or down in anticipation of changing loads. It can also be used to solve for optimal operation to help determine how to run the equipment while meeting the predicted loads. When considering the use of energy storage, such as TES, the optimization can be done dynamically, and the storage can be used to shift times of generation or consumption of a resource so that energy consumption is minimized over a set time horizon. The ability to leverage this flexibility requires the ability to adequately forecast the load requirements for the system.

The relationships between exogenous variables (such as weather or occupancy) and energy consumption are quite complex, particularly when many buildings are considered as is the case for large campuses with central utilities generation. This generally prohibits first principles modeling as it would require accurate, detailed models of each building. However, when aggregate behavior of a campus is considered, the effect of an individual building is marginal compared to the complete system's behavior, which tends to dampen any irregularities caused by a single building. The results of this study indicate that this aggregate behavior can be accurately represented by an empirical model. Neural networks using sigmoidal activation functions have proven to be a good candidate for representing the complex relationships as they have aspects of both continuous and discontinuous relationships. Furthermore, they provide a flexible number of fitting parameters so that more or less complexity can be added to the model, depending on the behavior observed. By making the model autoregressive (i.e., a NARX model), accuracy can be improved by using recent measured loads as a reference point for future predictions. With this recurrent behavior built into the model, the forecast can be updated at each time step, taking into account the most recent measurements for the loads and the most up-to-date weather forecast information. Thus, a reasonably simple tool can have a profound impact on plant operation, giving the plant operators the ability to plan ahead.

Distributed energy systems will likely have a very important role in the future energy economy, particularly as smaller-scale renewable technologies become more prominent. While the distributed generation model presents many advantages, there are

also challenges. One of these challenges is providing efficient and reliable energy on demand for consumers. Both efficiency and reliability can be enhanced by proactive operation of the system, which requires foreknowledge of the demand that must be met. Therefore, energy demand forecasting can be an important tool for maintaining effective and reliable energy infrastructure.

Nomenclature

Symbol	Description
a	Linear model fitting parameter
b	Linear model fitting parameter
c	Linear model fitting parameter
d	Linear model fitting parameter
f	Neural network function
i	Summation index
j	Summation index
k	Index for time step
L	Load
M	Number of inputs in neural network
P	Number of nodes in neural network
Q, q	Neural network bias terms
u	Vector representing model inputs for neural network model
W, w	Neural network fitting parameter
y	Output from neural network model
θ	Vector containing weather-related inputs
φ	Neural network activation function
ψ	Vector containing time-related inputs
Ω	Output function in neural network

CHAPTER 7 : DYNAMIC OPTIMIZATION OF A DISTRICT COOLING SYSTEM WITH THERMAL ENERGY STORAGE

Introduction

A smart energy grid designed to deliver energy to consumers in the most efficient and reliable manner possible will rely heavily on energy storage and optimization. Energy storage technologies are key enabling technologies for renewable energy resources, such as solar [29], [148], [149] and wind [150], [151]. Storage allows these intermittent renewables to be dispatched on demand, making them more reliable and therefore more competitive with traditional fossil resources. Energy storage can also be a valuable technology for traditional energy systems, providing reduced capital costs, increased power capacity, increased efficiency, and the ability to reduce peak energy demand by shifting load to off-peak times [152].

Because thermal loads account for a significant portion of peak energy consumption, thermal energy storage has proven to be a cost-effective peak reduction technology [153], [154]. Thermal energy storage gives a system the ability to shift loads temporally by providing system operators more degrees of freedom in operating the system. Optimization can then be applied to help operators use the system most effectively in terms of energy or cost minimization [80]. This methodology is applied to a district cooling system with chilled water thermal energy storage (see Figure 7.1).

Background

In warm climates, cooling demand is typically a significant contributor to total energy demand in buildings. Cooling loads are most frequently met by running electrically-powered air conditioners or chillers. For large-scale systems, such as campuses with many buildings, performance improvement of chilling equipment through optimization is a viable cost and energy saving approach. In order to meet cooling loads and also to have

redundancy for reliability purposes, large-scale systems on a district cooling loop typically have multiple chillers. From an optimization point of view, this gives the system more degrees of freedom, as different combinations of cooling load can be placed on each chiller, while still meeting the total cooling demand for the system. Optimization leads to improved energy efficiency compared to using simple rules, such as equal ratio chiller loading, where the part load ratios (the load on a chiller divided by its capacity) for each chiller are set to be equal [155]. When chiller efficiency varies widely with load and ambient conditions (most notably wet bulb temperature), an optimization-based approach to chiller loading can have a significant impact on energy savings [156].

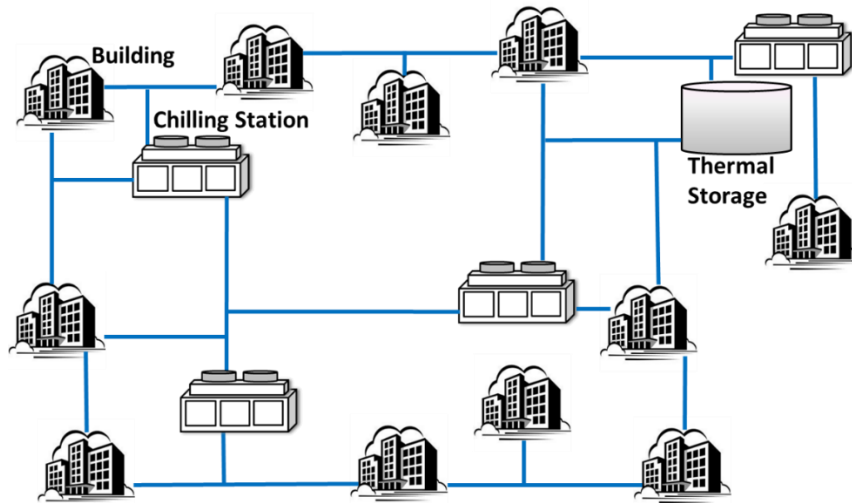


Figure 7.1: A district cooling system with chilling stations and thermal storage.

While multiple chillers in a system give it degrees of freedom which can be exploited through optimization, the addition of thermal energy storage significantly increases this flexibility. The ability to store energy means that cooling loads do not have to be exactly met by chilling equipment at all points in time. Instead, cooling can be generated in excess of the real-time demand and stored. If stored cooling (typically in the form of chilled water or ice) is available, chilling equipment can run at loads less than the real-time demand using the stored energy to make up the difference [157]. This enhanced flexibility allows chillers to shift cooling loads to periods where ambient conditions may

allow them to operate more efficiently and to optimally distribute these loads in time and over the range of available chillers. Under a time-of-use electricity pricing structure, significant cost savings will also be achieved.

While thermal energy storage can greatly enhance a system's ability to operate more efficiently for the reasons previously explained, the addition of energy storage translates the optimal chiller loading problem from a static optimization problem to a dynamic optimization problem. This increases the size of the optimization problem as chiller loading must be solved at every step in the time horizon. Another complicating factor is that, for the static problem, the only load of concern is the instantaneous load, while for the dynamic problem chiller loading must be determined for some period into the future, where exact loads as well as ambient conditions are largely unknown. Therefore, solving the dynamic optimization problem typically requires incorporating a forecast of weather and of cooling load for the duration of the prediction horizon. While weather forecasts are readily available, forecasting cooling demand is a field of its own. To this end, several techniques have been developed that use weather forecast information and modeling techniques (such as neural networks or support vector regression) to predict cooling loads in advance [144], [145], [146].

Another complicating factor in optimal chiller loading is the mixed-integer nature of the problems, where the feasible region for a chiller covers the "off" position and a range from its minimum to its maximum operating load, with no feasible solution between "off" and the minimum load. This fact has led researchers to use non-derivative-based optimization methods such as genetic algorithms [158], [159] or particle swarm algorithms [160]. The problem can also be formulated as a mixed-integer non-linear programming problem where branch and bound techniques are applicable [161]. Generally speaking, these problems are more difficult to solve than continuous optimization problems due to the combinatorial complexities of integer-constrained problems. These complexities are compounded when storage is added to the system and the problem becomes a dynamic optimization problem. Dynamic programming, which seeks to avoid complete

enumeration, has been proposed as a solution to these types of problems [162], [163]. Dynamic programming (and enumeration) can ensure global optimality, but only when using discretized versions of otherwise continuous decision variables, so that the optimization problem becomes finding the best of a series of finite choices. Therefore, this approach may be advantageous in some circumstances. However, it is desirable to maintain the continuous nature of the decision variables so that true optimality of the system can be ensured.

Chiller Modeling

Industrial sized chillers are large, complex pieces of equipment, making accurate first principles modeling a difficult task. Empirical, or black box, models can be relatively easily developed. These models use equations with a particular structure (e.g. polynomial, neural network, etc.) to describe the chiller performance. The models are generally equipped with a number of parameters, which can be fit to the given model structure through regression techniques [164]. Because there is generally no physical basis for the equations and parameters, these models can be accurate over the range of data to which they are fit because of the high number of parameters available for fitting [165], [166], [167], [168], but they are generally inaccurate outside that range.

A reasonable compromise between a first principles model and a purely empirical model is a semi-empirical model, which provides the structure to the model equations, based on the physics of the actual system, but allows for some unmeasured constants to be varied in order for the model to provide a good fit to the data. A thermodynamic chiller performance model, which has proven to be accurate, yet sufficiently simple, is that developed by Gordon and Ng [169]. This model can be used to evaluate a chiller's coefficient of performance (COP) as a function of the cooling load on the chiller, the condenser inlet temperature (which is a strong function of the ambient wet bulb temperature), and the chilled water temperature exiting the evaporator. The COP is then used to determine the power consumption by the chiller. The model is well formulated in

that it provides several terms that can be used as fitting parameters, while still possessing a structure that allows the model to be extrapolated beyond the range of the data over which it is fit [170]. The relationship for COP can be found in (7.1).

$$\frac{1}{COP} = -1 + \left(\frac{T_c^{in}}{T_e^{out}}\right) + \left(\frac{1}{Q}\right)\left(\frac{q_e T_c^{in}}{T_e^{out}} - q_c\right) + \left(\frac{1}{Q}\right)\left(\frac{q_e}{M_c T_e^{out}}\right)\left(\frac{q_e T_c^{in}}{T_e^{out}} - q_c\right) + \left(\frac{Q}{T_e^{out}}\right)\left(\frac{T_c^{in}}{T_e^{out}}\right)\left(\frac{1}{M_c} + \frac{1}{M_e}\right) + \frac{q_c}{M_e} + \frac{q_e T_c^{in}}{T_e^{out} M_c} + \left(\frac{T_c^{in} q_e}{T_e^{out}} - q_c\right)\left(\frac{1}{M_c} + \frac{1}{M_e}\right) \quad (7.1)$$

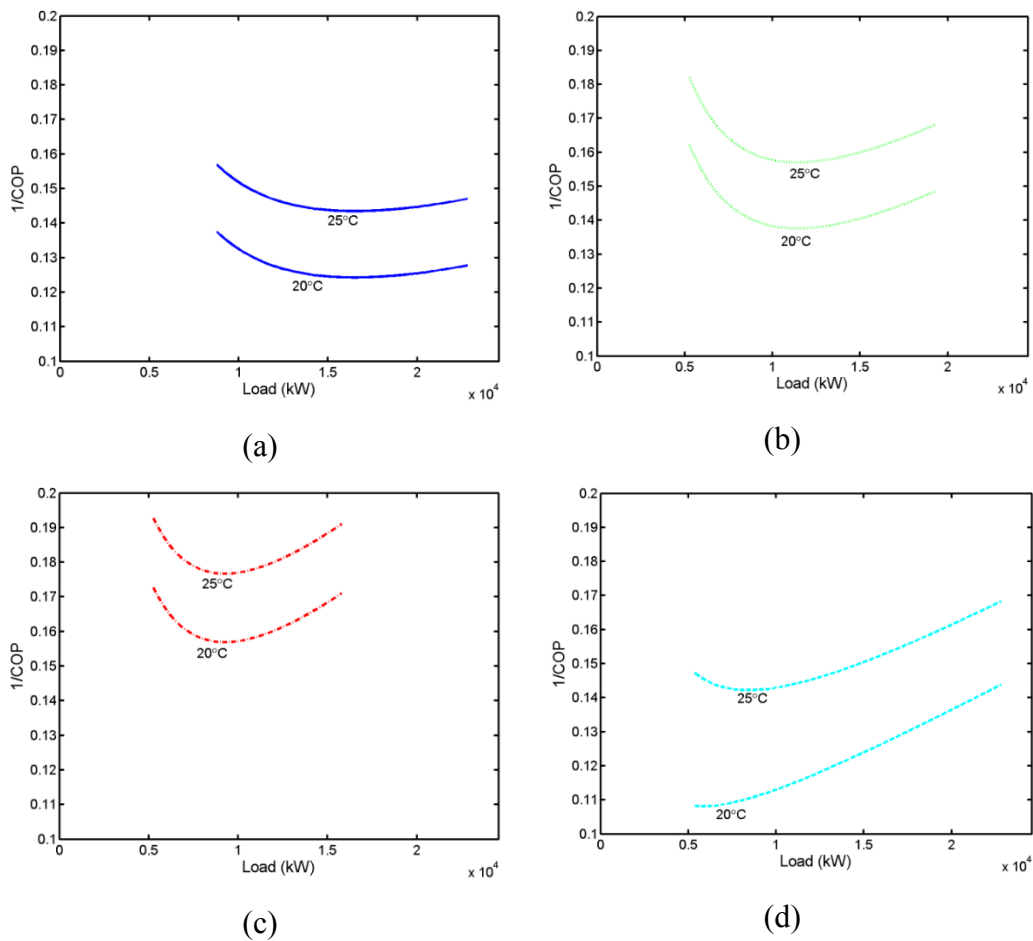


Figure 7.2: Chiller performance curves.

This thermodynamic chiller model can be fit to data for chillers using some of the constants in the model as fitting parameters and employing a least-squares model fitting

algorithm. The parameters used for fitting in this work are q_e and q_c (the heat losses at the evaporator and condenser, respectively) and M_e and M_c (the product of overall heat transfer coefficient and heat transfer area for the evaporator and condenser, respectively). The performance curves for a chilling network consisting of four chillers of various designs and operating ranges are shown in Figure 7.2. These curves are generated using (7.1) and fitting the above-specified parameters for a four chiller system in Austin, TX. The parameters are identified by solving a least-squares optimization problem with an objective to minimize the total squared error of the model predictions compared to actual operating data. In order to obtain accurate models over the entire range of operating conditions, each model is fit to a year's worth of hourly operating data, creating 8,760 data points for each chiller model. The models generated from these fits are used for subsequent analysis in this paper. Table 7.1 summarizes the model fitting analysis and indicates that reasonable model fits are found for each of the chillers, with high R^2 values and average error not exceeding 2.44%. The chiller operating ranges are also shown, indicating the minimum and maximum loads for which each chiller can be run. These ranges are used as constraints in the energy and cost minimization problems described later.

Table 7.1: Operating ranges and model fitting results.

	Min Load (kW)	Max Load (kW)	R^2	Avg. Error
Chiller 1	8,800	22,800	0.936	2.44%
Chiller 2	5,300	19,300	0.958	2.41%
Chiller 3	5,300	15,800	0.930	2.30%
Chiller 4	5,300	22,800	0.991	1.53%

As Figure 7.2 indicates, chiller efficiency strongly depends on the load placed on each chiller and varies considerably from one chiller to another. Furthermore, chillers

operate much more efficiently at a lower ambient wet bulb temperature because heat is rejected by the condenser at a lower temperature.

Static Optimal Chiller Loading

In order to enhance the steady-state operation of a chilling system by optimal chiller loading, a static optimization problem must be solved, with the objective of minimizing total power consumption by optimally distributing the cooling load across the available chillers. This problem has been attempted in a number of ways [158], [161], [171], and the decision for choosing an optimization method ultimately depends on the model used to represent the system and the optimization resources that are available. Close examination of (7.1) reveals that, upon multiplying through by Q , the cooling load, to get power consumption (P) as a function of Q , the model is quadratic with respect to Q , as (7.2) indicates.

$$\begin{aligned}
 P = \frac{Q}{COP} = & -Q + \left(\frac{T_c^{in}}{T_e^{out}} \right) Q + \left(\frac{q_e T_c^{in}}{T_e^{out}} - q_c \right) \\
 & + \left(\frac{q_e}{M_c T_e^{out}} \right) \left(\frac{q_e T_c^{in}}{T_e^{out}} - q_c \right) + \left(\frac{Q^2}{T_e^{out}} \right) \left(\frac{T_c^{in}}{T_e^{out}} \right) \left(\frac{1}{M_c} + \frac{1}{M_e} \right) \\
 & + Q \frac{\frac{q_c}{M_e} + \frac{q_e T_c^{in}}{T_e^{out} M_c} + \left(\frac{T_c^{in} q_e}{T_e^{out}} - q_c \right) \left(\frac{1}{M_c} + \frac{1}{M_e} \right)}{T_e^{out}}
 \end{aligned} \tag{7.2}$$

For convenience, the terms in (7.2) can be grouped based on their dependence on Q , yielding (7.3), where the parameters α , β , and γ are assumed to be independent of Q . This assumption is justified by the fact that T_e^{out} , the temperature of the chilled water exiting the evaporator maintained at a constant set-point and T_c^{in} , the cooling water temperature entering the condenser, is predominantly a function of the cooling tower performance and the ambient conditions, primarily the wet bulb temperature.

$$P = \alpha + \beta Q + \gamma Q^2 \tag{7.3a}$$

$$\alpha = \left(\frac{q_e T_c^{in}}{T_e^{out}} - q_c \right) + \left(\frac{q_e}{M_c T_e^{out}} \right) \left(\frac{q_e T_c^{in}}{T_e^{out}} - q_c \right) \quad (7.3b)$$

$$\beta = -1 + \left(\frac{T_c^{in}}{T_e^{out}} \right) + \frac{q_c + \frac{q_e T_c^{in}}{T_e^{out}} + \left(\frac{T_c^{in} q_e}{T_e^{out}} - q_c \right) \left(\frac{1}{M_c} + \frac{1}{M_e} \right)}{T_e^{out}} \quad (7.3c)$$

$$\gamma = \left(\frac{1}{T_e^{out}} \right) \left(\frac{T_c^{in}}{T_e^{out}} \right) \left(\frac{1}{M_c} + \frac{1}{M_e} \right) \quad (7.3d)$$

The objective of minimizing the total power consumption for a set of N_c chillers while meeting or exceeding a total cooling demand (Q_{tot}) at a given instant in time yields the optimization problem in (7.4). Because it may be optimal to turn some chillers off, the binary decision variable δ is added to the formulation, taking on a zero value when chiller i is off and one when it is on. This makes the problem a mixed integer nonlinear programming (MINLP) problem, which is typically solved using a branch and bound or another MINLP solution algorithm [172].

$$\min_{Q_i, \delta_i} \sum_{i=1}^{N_c} (\alpha_i + \beta_i Q_i + \gamma_i Q_i^2) \delta_i \quad (7.4a)$$

subject to

$$\sum_{i=1}^{N_c} Q_i \delta_i \geq Q_{tot} \quad (7.4b)$$

$$Q_{min,i} \leq Q_i \leq Q_{max,i} \quad (7.4c)$$

$$\delta_i \in [0,1] \quad (7.4d)$$

If a known subset of chillers is anticipated to be on, however, the problem is reduced to a simple quadratic programming (QP) problem, which takes on the form:

$$\min_x \mathbf{x}^T \mathbf{H} \mathbf{x} + \mathbf{F}^T \mathbf{x} \quad (7.5a)$$

subject to

$$\mathbf{A} \mathbf{x} \leq \mathbf{B} \quad (7.5b)$$

$$\mathbf{x}_{min} \leq \mathbf{x} \leq \mathbf{x}_{max} \quad (7.5c)$$

where x is a vector containing the load placed on each chiller, with N_{AC} referring to the total number of chillers assumed to be active,

$$\mathbf{x} = \begin{bmatrix} Q_1 \\ \vdots \\ Q_i \\ \vdots \\ Q_{N_{AC}} \end{bmatrix} \quad (7.5d)$$

H is a diagonal matrix containing the quadratic terms from each chiller model,

$$\mathbf{H} = \begin{bmatrix} \gamma_1 & 0 & \cdots & 0 \\ 0 & \ddots & & \\ \vdots & & \gamma_i & \vdots \\ & & & \ddots & 0 \\ 0 & \cdots & 0 & \gamma_{N_{AC}} \end{bmatrix} \quad (7.5e)$$

and F is a vector containing the linear terms from the chiller model.

$$F = \begin{bmatrix} \beta_1 \\ \vdots \\ \beta_i \\ \vdots \\ \beta_{N_{AC}} \end{bmatrix} \quad (7.5f)$$

The constraint that the total demand must be met is enforced using the A and B terms, which are a vector and a scalar, respectively. In this case A is a horizontal N_{AC} -vector of ones and B is the negative of the total cooling demand.

$$A = [1 \quad \dots \quad 1] \quad (7.5g)$$

$$B = -Q_{tot} \quad (7.5h)$$

Formulating the problem as a QP has several advantages. First, the problem can be solved quickly using an off-the-shelf QP solver. Second, because H is a diagonal matrix with only positive values, it will always be positive definite, ensuring convexity of the problem and guaranteeing that the solution to the problem will be a global minimum. The major disadvantage of this method, however, is that the problem must be solved multiple times in order to explore all possible combinations of active chillers. This can be largely bypassed, however, by methodically testing specific active sets of chillers, beginning with the most efficient chillers in the system and gradually adding the less efficient chillers. This can greatly reduce the number of combinations tried. Upon solving the problem for these combinations, the best of these solutions can then be implemented. Because the QP problems being solved are fairly trivial, computation times for the static optimal chiller loading problem are not a major issue. The overriding concern is reaching a global solution, which is guaranteed by using this method but cannot necessarily be guaranteed by the MINLP formulation of the problem.

Dynamic Optimal Chiller Loading with Thermal Energy Storage

If the objective is to minimize total energy consumption over some time horizon by optimally placing the cooling load on certain chillers at suitable times of the day, the addition of thermal energy storage to a cooling network adds many more degrees of freedom. Using energy storage, cooling loads can be shifted, not only to the most efficient chillers, but to the times of the day when chillers operate most efficiently, typically when ambient wet bulb temperatures are lower. While the extra degrees of freedom by virtue of energy storage are very useful, they also make the problem much more difficult to solve. Typically, a dynamic optimization problem is discretized temporally into a certain number of time intervals, N_t , during which, it is assumed that inputs are held constant. For a system with N_C chillers, this creates a total of $N_t \times N_C$ degrees of freedom. If binary variables, δ , are used to represent the on/off states of the chillers, the total number of degrees of freedom becomes $2N_t \times N_C$. While solving problems of this size is certainly within the realm of some MINLP solvers, the problem of finding a global solution within a reasonable amount of time may be a limiting factor.

The high dimensionality may be mitigated, however, by re-formulating the problem. The number of degrees of freedom can be reduced by a factor of N_C if the set of chillers is considered to be a single optimal chiller, rather than N_C individual chillers. Essentially, this entails solving the static optimal chiller problem to determine the optimal total power consumption for a given load. Solutions to this problem are shown in Figure 7.3 for ambient wet bulb temperatures of 20°C and 25°C over a range of total chiller loads. As the figure shows, higher efficiencies are obtained at a lower wet bulb temperature. A general upward trend in $1/COP$ as load increases is also observed. However, the curves have some locations with sharp peaks. These non-smooth points indicate a change in the active set of chillers that is optimal for a given load. As load increases and crosses one of these points, it indicates that a new chiller would have to be turned on (and possibly another chiller turned off) in order for the system to optimally meet the given load.

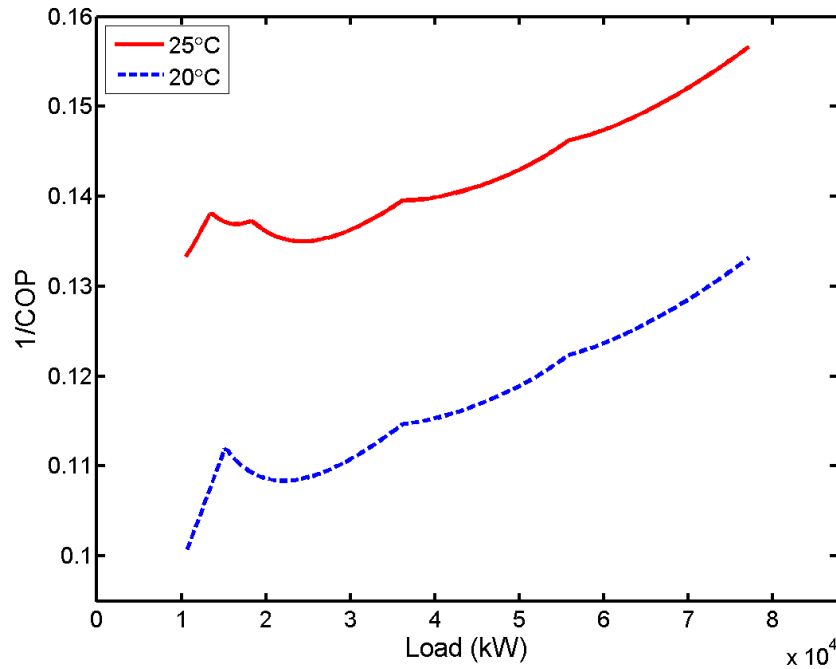


Figure 7.3: Solutions to the static problem vs. load.

As Figure 7.3 clearly indicates, it is generally more efficient to cool during times with lower ambient wet bulb temperature. Therefore, energy storage can be used to reduce energy usage by shifting the cooling load to times when lower wet bulb temperatures are expected. There are limits to the efficiency that can be gained by doing this, however, as increasing load at the lower temperature causes the system to be less efficient. With no constraints on energy storage rate or total capacity, the optimal solution for shifting load between these two temperatures would be achieved when the marginal decrease in power consumption per unit load at the less efficient time equals the marginal increase in power per unit load at the more efficient time.

Using the solution to the static optimal chiller loading problem, all chillers can be considered as a single, optimal chiller. This significantly reduces the combinatorial complexity of the dynamic problem. Rather than solving for loading on each chiller at each time interval, only the total load is needed at every time interval. The dynamic problem uses the total loads at each time interval as decision variables, with the loads placed on

individual chillers being determined by the static optimization sub-problem. This formulation is depicted graphically in Figure 7.4. As the figure illustrates, the dynamic problem uses the total load (Q_{tot}) at each time interval (j) as its decision variables. For a given $Q_{tot,j}$, the static problem is then solved to determine the optimal loading on each chiller ($Q_{i,j}$) required to meet $Q_{tot,j}$. The power consumed at each time interval under optimal loading (P_{tot}^*) is then communicated back to the dynamic problem. By solving the static optimal chiller loading problem at each time interval, the system of chillers, therefore, behaves essentially as a single chiller, operating at its most efficient point for a given load and given ambient conditions. While the system still has $N_t \times N_C$ degrees of freedom of which it can take advantage, the optimization problem is reduced to one with only N_C degrees of freedom with global optimality guaranteed at each time interval. One inherent disadvantage to this problem formulation is that it becomes more difficult to prevent chillers from switching on and off regularly. However, if a penalty on the change in total load from one time interval to the next is added, this will prevent excessive chiller switching, provided there are no dramatic swings in ambient conditions over the same interval.

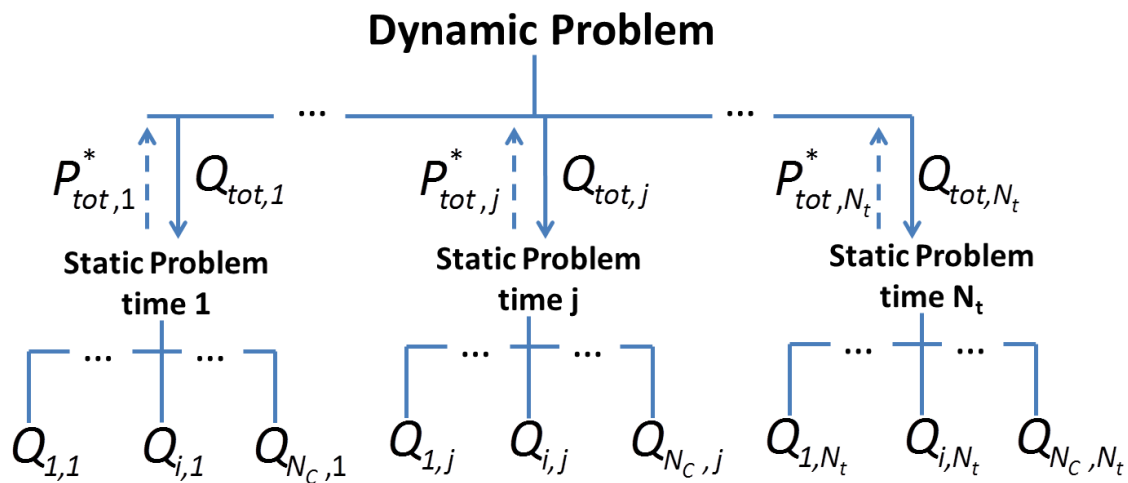


Figure 7.4: The hierarchical structure for the dynamic optimization problem.

A discrete-time version of the dynamic optimal chiller loading problem is described in (7.6). Here, a simple model (7.6b) is adopted for the energy stored (E), where the energy stored at time $j+1$ is equal to the difference in cooling delivered (Q_{tot}) minus the total cooling demand (Q_{demand}) at time j multiplied by the time interval Δt . The function Φ in (7.6a) refers to the composite chiller function at time j , as obtained from the solution of the static optimal chiller loading problem. The system is subject to inequality constraints on the amount of energy stored (7.6e) and the rate at which energy can be extracted or delivered to storage (7.6f). Here, a negative value of ΔE means that energy is being extracted from the storage system.

$$\min_{Q_{tot,j}} \sum_{j=1}^{N_t} \Phi(Q_{tot,j}, T_{c,j}^{in}, T_{e,j}^{out}) \Delta t \quad (7.6a)$$

subject to

$$E_{j+1} = E_j + \Delta E_j \quad (7.6b)$$

$$E_0 = E(0) \quad (7.6c)$$

$$\Delta E_j = (Q_{tot,j} - Q_{demand,j}) \Delta t \quad (7.6d)$$

$$0 \leq E_j \leq E_{max} \quad (7.6e)$$

$$\Delta E_{min} \leq \Delta E_j \leq \Delta E_{max} \quad (7.6f)$$

The system is subject to an initial condition on the amount of stored energy initially in the storage system (7.6c). With the objective to minimize total energy consumption over some time horizon, the optimal solution to this problem will generally be to finish with an empty storage tank. If this is undesirable, an additional constraint can be added that the energy stored at the final time must be equal to the energy stored initially ($E_{N_t} = E_0$).

Results

Dynamic optimal chiller loading using thermal energy storage is more effective when there is a larger swing in wet bulb temperature over the course of a day (giving the system a greater improvement in efficiency by shifting the cooling load to these times) and when there is a large swing in total cooling demand. Assuming a storage system that is initially uncharged ($E_0=0$), several days were simulated using actual wet bulb temperatures and cooling demands for a large campus in Austin, TX. One of these days is shown in Figure 7.5, where the total demand ranges from 39,600 to 65,300 kW of cooling, giving the system ample opportunity to shift the cooling load. The ambient wet bulb temperature ranges from 17.7°C to 23.3°C, which correlates fairly well with the cooling demand. The total storage capacity for this system is 136,800 kWh, meaning that the system has a little over 2 hours of full-load storage capacity in this case. However, because the storage can only be charged and discharged at a maximum rate of 21,100 MW, the storage lasts much longer as part-load storage.

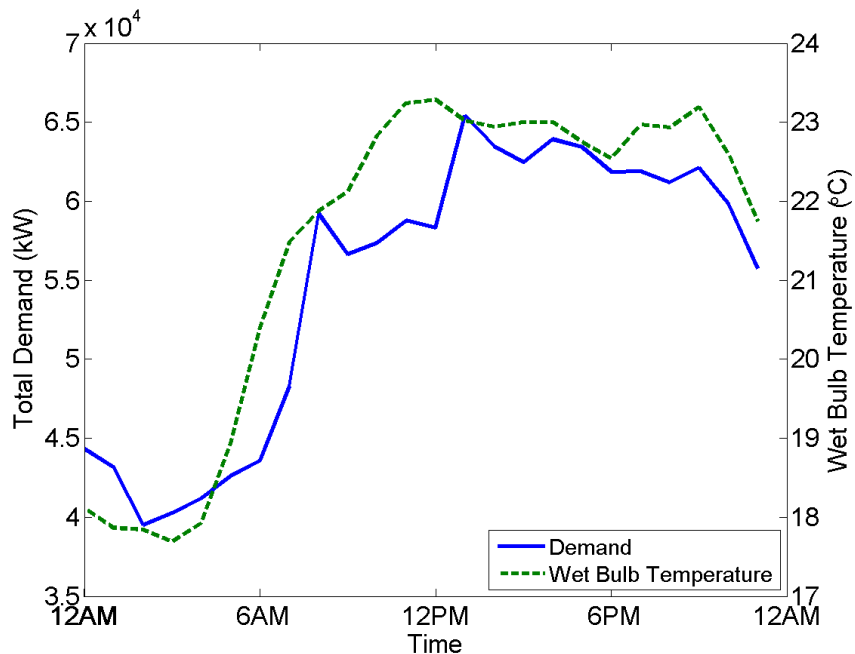


Figure 7.5: Total cooling demand and wet bulb temperature.

Three different chiller operating strategies are considered. An equal ratio loading operating strategy places the same proportional load (relative to the chiller maximum capacity) on each chiller. This operating scheme would represent a fairly naïve approach, given that it does not take advantage of the varying efficiencies of the chillers. The chiller loads vs. time that result from this strategy are shown in Figure 7.6 for the conditions given in Figure 7.5.

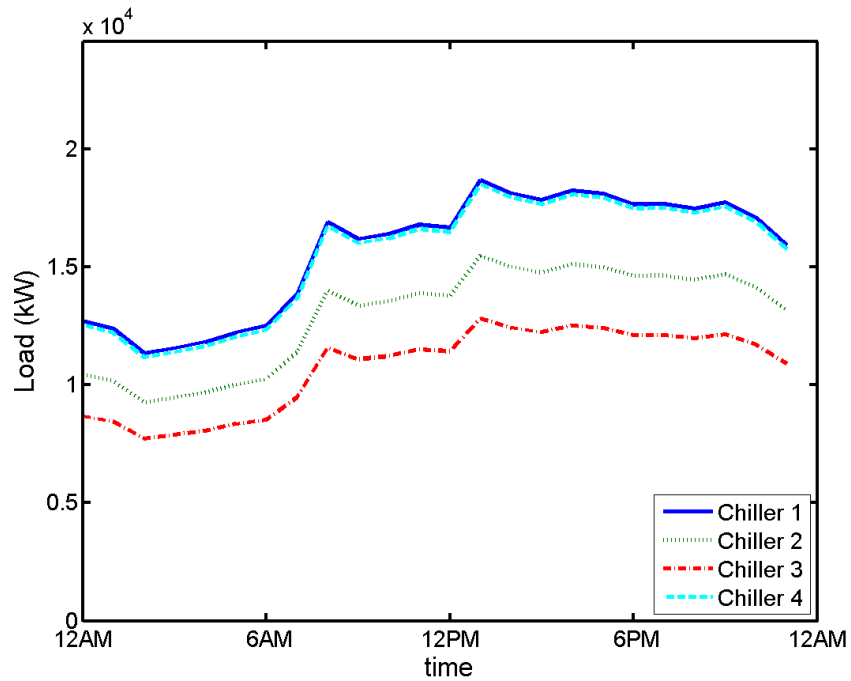


Figure 7.6: Chiller loads for equal chiller loading.

When static optimization is performed, the results show that, during peak times, Chiller 1 is used at full capacity. Peak loads require Chiller 3 (the least efficient chiller) to run for a total of 15 hours. Still, static optimal operation saves approximately 9% energy over an equal ratio loading strategy under these conditions. The chiller operation for static optimization is shown in Figure 7.7.

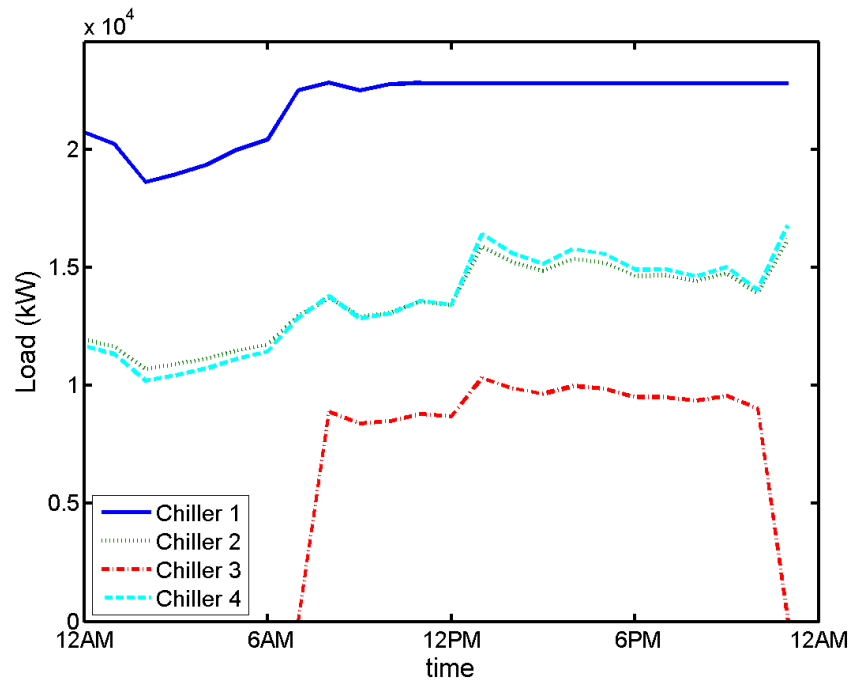


Figure 7.7: Chiller loads for static optimization.

Dynamic optimal chiller loading gives the system many more degrees of freedom. This allows the system to not only shift load to the more efficient chillers, but also to shift the load to the most efficient times of the day. Figure 7.8 and Figure 7.9 show the results of dynamic optimal chiller loading under the same conditions. As these results indicate, much of the load is shifted to the earlier parts of the day, under cooler conditions. Chiller 3 is still used; however, it is only required for a total of 7 hours as a larger percentage of the load is placed on the more efficient chillers in the system. Chiller 1 (the most efficient chiller at full load), for example, runs at full capacity the entire time, while Chillers 2 and 4 are kept near their optimal efficiency point. An added benefit of storage is that it allows the chillers to run at a more constant rate for the duration of the day, with only small fluctuations in the load on each chiller.

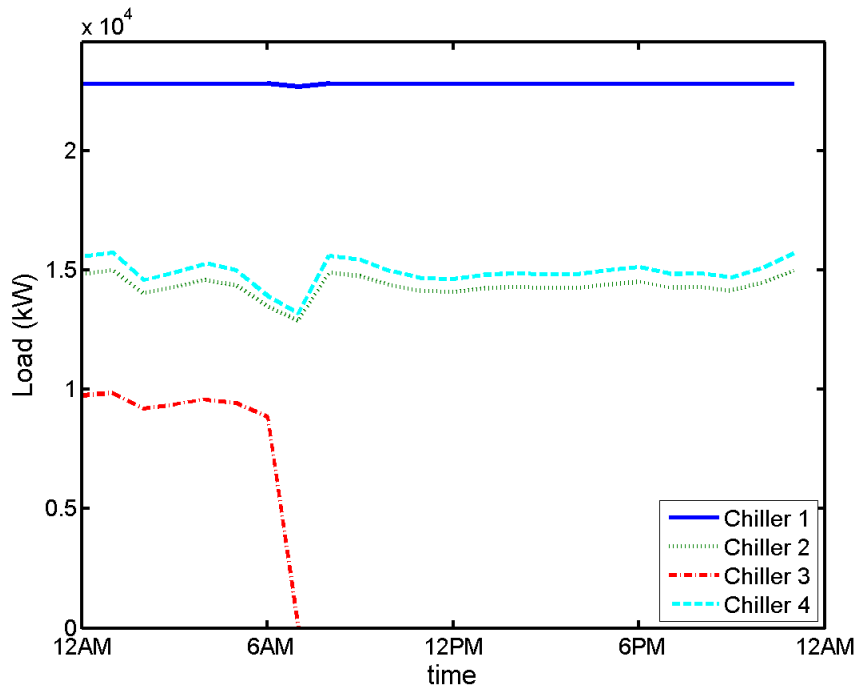


Figure 7.8: Chiller loads using dynamic optimization.

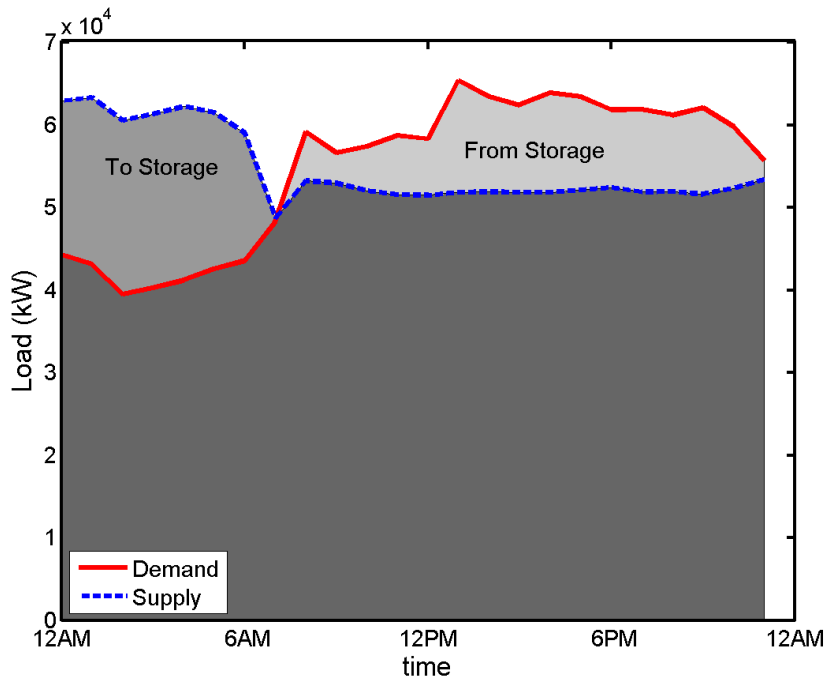


Figure 7.9: Storage using dynamic optimization.

Table 7.2, which summarizes the results of three different days used in this case study, shows that the total energy consumption is improved by a total of up to 9.4% in going from an equal ratio chiller loading strategy to a dynamic optimal chiller loading strategy with thermal energy storage. In Case 3, a day when there is little fluctuation (a range of only 0.9°C) in ambient wet bulb temperature, the savings are 6.8%. Therefore, the benefit of using thermal energy storage solely for shifting cooling loads to more efficient periods of the day depends on how much ambient conditions change during the day.

Table 7.2: A summary of results.

	Case 1	Case 2	Case 3
T_{WB} Range (°C)	6.4	5.6	0.9
Min Cooling Load (kW)	37,900	39,600	62,500
Max Cooling Load (kW)	55,400	65,300	76,400
Total Energy Consumption (MWh)			
Equal Ratio Chiller Loading	165.6	197.5	279.7
Static Optimal Chiller Loading	152.4	183.0	261.8
Dynamic Optimal Chiller Loading	150.0	179.7	260.8
Total Savings	9.4%	9.0%	6.8%

While thermal storage can shift cooling loads to periods where chillers can operate more efficiently, the major benefit of having thermal energy storage is its ability to shift electrical loads, not only cooling loads, temporally. Therefore, the true benefit of thermal energy storage must be quantified in terms of the savings achieved for the larger electrical system. The real-time value of electricity, for example, is often reflected in a time-of-use pricing structure, where electricity costs more during peak times of the day. If a simple time-of-use pricing structure is applied to this district cooling system, the savings change significantly. The price structure used in this case study is \$0.1/kWh during off peak times and \$0.2/kWh during peak times (12:00 PM to 8:00 PM). When this pricing structure is applied with an objective to minimize total cost, rather than total energy, the savings from

optimization and thermal energy storage increases to as much as 17.4%, as Table 7.3 indicates.

Table 7.3: Daily cost for the three cases.

	Case 1	Case 2	Case 3
Equal Ratio Chiller Loading	\$23,600	\$28,600	\$39,500
Static Optimal Chiller Loading	\$21,800	\$26,500	\$37,000
Dynamic Optimal Chiller Loading	\$19,500	\$23,900	\$34,500
Total Savings	17.4%	16.4%	12.7%

Conclusions

Optimization can be one of the most cost-effective methods to improve a utility network. For a cooling network with multiple chillers, several degrees of freedom exist, allowing an optimization scheme to dictate which chillers should be used and their corresponding cooling loads. The addition of thermal energy storage to a cooling network can also have a profound impact. While it does require some capital investment, a thermal energy storage tank is significantly less expensive than an industrial scale chiller, yet it can shift load to off-peak hours. Thermal energy storage also provides more degrees of freedom to a system, which can be exploited through optimization. Thermal storage allows for cooling loads to be shifted temporally, so that the system can take advantage of ambient conditions that are more amenable to efficient chiller operation. However, as this paper has shown, the true value of thermal storage comes by its ability to shift electrical loads, allowing the system to take advantage of less expensive off-peak rates. Thermal energy storage, therefore, can essentially be used as electrical storage, given that a significant portion of the electrical load in most climates is for HVAC purposes.

It has been shown that, for a quadratic chiller model, the power minimization problem of static optimal chiller loading can be easily solved by a series of QPs, assuming different sets of chillers to be active. The convexity of such problems guarantees a global solution for each active set assumed. This QP problem can be solved very quickly. The

dynamic optimal chiller loading problem is much more difficult to solve as it is inherently non-convex and has many degrees of freedom. However, it has been shown that the solution to the static optimal chiller loading problem can be used by the dynamic problem, significantly reducing the number of degrees of freedom and allowing for much faster solution times in addition to a better probability of converging to a global minimum for total energy consumption.

Nomenclature

Symbol	Description	Units
A	Horizontal N_{AC} vector of ones	-
B	Negative of the total cooling demand	kW
COP	Coefficient of performance	-
E	Energy stored	kWh
E_0	Initial energy stored in tank	kWh
E_{N_t}	Energy stored at the final time N_t	kWh
F	Vector containing the linear terms from each model	-
H	Diagonal matrix containing the quadratic terms for each chiller model	1/kW
i	Chiller number	-
j	Time interval number	-
M_c	Product of condenser heat exchanger coefficient and heat exchange surface area	kW/K
M_e	Product of evaporator heat exchanger coefficient and heat exchange surface area	kW/K
N_{AC}	Total number of chillers assumed to be active	-
N_c	Total number of chillers	-
N_t	Time intervals dynamic problem is discretized into	-
P	Electrical power input to chiller	kW
P^*_{opt}	Optimal power consumption for chilling network	kW
q_c	Rate of internal losses at the condenser	kW
Q_{demand}	Total cooling demand	kW
Q	Individual chiller cooling rate	kW
q_e	Rate of internal losses at the evaporator	kW
Q_{tot}	Sum of cooling rate at the evaporator for all chillers	kW
T_c^{in}	Condenser water inlet temperature	K
T_e^{out}	Evaporator water outlet temperature	K
T_{WB}	Wet-Bulb Temperature	°C
X	Vector containing the load placed on each chiller	kW
α	Grouped parameter with no dependence on Q_e	kW
β	Grouped parameter with linear dependence on Q_e	-
γ	Grouped parameter with quadratic dependence on Q_e	1/kW
δ	Binary decision variable	-
Δt	Time interval	Hr
Φ	Function predicting power consumption at the solution of static optimal chiller loading problem	-

CHAPTER 8 : DYNAMIC OPTIMIZATION OF A DISTRICT ENERGY SYSTEM WITH COMBINED HEAT AND POWER AND THERMAL ENERGY STORAGE

Introduction

Concern for energy scarcity and global climate change has been a driving force for the development of new energy technologies with an increasing emphasis on emissions reduction and improved efficiency. This has led to a diverse mix of energy resources and the growing technological challenge to integrate all of these resources into reliable systems. These systems must ensure that varying consumer demand for energy is met, while simultaneously managing transient and intermittent (in the case of solar and wind) energy supply. As more diverse energy technologies become connected to the grid, managing it becomes more difficult. These technological challenges have led to the implementation of the smart grid: an electric grid with enhanced flow of information, which enables intelligent, automated decisions to be made, ensuring robust and efficient energy distribution [173], [174]. The smart grid, where many different energy technologies interact and communicate with each other, introduces opportunities for system optimization [175], [176]. Optimization can improve overall system performance by allowing intelligent decisions to be made, so that a global objective is achieved from the individual components of the system [177].

The transient nature of both supply and demand of energy has also led to increased development and deployment of energy storage technologies, which help to alleviate supply and demand mismatch [73], [178]. In the context of the smart grid, energy storage technologies provide enhanced flexibility, which can be best exploited using optimization. Thermal energy storage (TES) is one of the few energy storage technologies that has proven to be an economically feasible large-scale storage solution [74], [179]. Unlike electrical energy storage, TES stores thermal energy, and must be located in close

proximity to the thermal loads which it services, such as in a district energy system, where electric or thermal power may be generated, distributed, and consumed in a small geographical area [79]. These energy systems are an excellent test bed for smart grid technologies. Unlike the smart grid, however, district energy systems may incorporate more than electrical distribution; they may include district heating and district cooling, where heating and cooling are generated at central locations and distributed to the surrounding area. These systems also extend the opportunities for optimization beyond electrical generation and distribution, creating the opportunity for a smart and diverse energy network which provides energy for electrical, heating, and cooling demands. While there is more opportunity for optimization in these systems, the optimization problems themselves are more complex and require models of a diverse range of systems. They also have additional constraints which must be adhered to, including meeting other (non-electrical) loads, such as heating and cooling.

District energy systems take advantage of economies of scale in order to efficiently and cost-effectively provide heating, cooling, or electricity for an immediate surrounding area. Many buildings can be supplied by large centrally-located generation equipment, rather than smaller individual units for each building [180], [181], [182]. Because of the large scales involved in these systems, optimization may be a valuable energy and cost saving tool [111], [183], [184]. In addition to the economies of scale available in central utility generation, a similar benefit is available for energy storage. Because the generation and distribution are already in place, large-scale TES can also be readily implemented in district heating and cooling systems [111], [185], [186]. The addition of TES provides low-cost energy storage, giving the system the ability to shift supply and demand of energy. TES can be used to avoid peak electricity rates by using electric chillers to generate cooling during off-peak hours, when electricity costs are lower [187]. This alleviates the cooling needs of the district during peak hours. The addition of TES to a district heating or cooling system also provides additional degrees of freedom, which can be exploited by optimization. This means the system can be optimized on a dynamic basis, and loads can

be shifted temporally so that cost or energy usage can be minimized over a finite time interval [79], [163].

District energy systems may also be equipped with combined heat and power (CHP), where electrical power is produced onsite. The waste heat from power production is then used in the district heating loop, making this setup very efficient [188], [189]. The opportunities for optimization in CHP systems is also tremendous. If power generation capacity exceeds demand, selling excess power (if regulations permit) can be a source of revenue to help offset operation and fuel costs. Optimization problems are often solved to determine the best CHP plant operation for economic dispatch [190], [191], [192], [193]. The addition of TES into a CHP district energy systems provides additional flexibility [83], [185]. TES can be used to shift loads and free up generation capacity during peak electrical hours, when prices are highest and maximum revenue can be generated.

System Overview

This district energy system, located at the University of Texas at Austin and detailed in this study, contains all the elements discussed above: CHP, district heating, district cooling, and TES. The CHP plant utilizes a gas turbine (43.1 MW_e capacity) for primary power generation. The exhaust gas from this turbine is fed to a heat recovery steam generator (HRSG), which converts the waste energy to superheated steam. The HRSG is also equipped with duct burners, where additional natural gas can be burned to ensure that the appropriate superheated steam temperatures are always reached. This high pressure superheated steam (at 30 bar) is then throttled to 11 bar for distribution to campus. During this process, additional power is generated using an extraction steam turbine, which generates power during steam expansion. In the turbine, enough medium pressure (11 bar) steam is extracted to meet heating demands. The rest is dropped to near ambient pressure at saturation conditions. With the combination of a gas and steam turbine, the power plant can effectively operate in combined cycle. The plant is thus a combined cycle and a tri-generation system, providing electricity, heating, and cooling.

The system is equipped with an auxiliary boiler, which burns natural gas and produces additional superheated steam at 30 bar. The steam output from the HRSG and the auxiliary boiler is combined in a high pressure header before steam is fed to the steam turbine. The auxiliary boiler is necessary during winter months when HRSG steam generation is insufficient to meet campus heating loads. The boiler can also be used to increase power production in the steam turbine.

In addition to providing electricity directly to campus, the CHP plant must also power nine electric chillers, which are used to produce chilled water to meet the campus's cooling needs. The chillers are each located in a central cooling station, which house three chillers each. Each station is equipped with a set of cooling towers, which provide cooling water for heat rejection in each chiller as well as multiple chilled and cooling water pumps. The combined electricity consumption from the cooling system can be significant, consuming up to half the total electricity output of the CHP plant.

In addition to the CHP plant providing power for the cooling system, the two are also linked by the turbine inlet cooling (TIC) system. The TIC system is used to pre-cool the ambient air before it is fed to the gas turbine. This increases the air density so that both the throughput and the efficiency of the gas turbine's compressor can be increased. The use of TIC allows the gas turbine to produce more power. However, it also consumes power because it requires additional cooling from the electrically-powered chillers. The chilled water from the cooling system is distributed via pipeline to the campus buildings, where it is used for space cooling. With the addition of chilled water TES, the cooling loads can be shifted, giving the system an important dynamic element.

Figure 8.1 shows that natural gas is used in three places: in the gas turbine, in the HRSG duct burners, and in the auxiliary boiler. The gas turbine feeds exhaust gas to the HRSG which, in conjunction with the auxiliary boiler, produces superheated steam that is fed to the steam turbine. The steam turbine produces additional power, while lowering the pressure of the superheated steam so that it can be distributed to the campus buildings. Electricity produced from both turbines powers the campus and the cooling system, which

of these models is included in the overall optimization problem and strongly interact with the other elements of the cooling system in nonlinear time-varying relationships.

With so many pieces of operating equipment, modeling the complete system proved to be a challenging undertaking. Although each component has dynamics, all but the TES system are assumed to operate at steady state. The TES dynamics do not significantly affect the optimization solution because of the much smaller time constants for other equipment in the system. The dynamic problems is solved in one-hour time increments, well beyond the settling time of any piece of equipment, which justifies this steady state assumption for all pieces of equipment except the TES, which has several hours of storage capacity.

For the chillers, the thermodynamic model of Gordon and Ng is used [194], [195]. This model expresses the inverse of the chiller coefficient of performance (COP) as a function of the compressor inlet temperature (T_{cond}^{in}), the evaporator inlet temperature (T_{evp}^{out}), the total cooling load on the chiller (Q), the heat loss in the evaporator (q_{evp}) and the condenser (q_{cond}), as well as the heat transfer coefficients in the evaporator (M_{evp}) and condenser (M_{cond}). This relationship is shown in (8.1).

$$\begin{aligned} \frac{1}{COP} = & -1 + \left(\frac{T_{cond}^{in}}{T_e^{out}} \right) + \left(\frac{1}{Q} \right) \left(\frac{q_{evp} T_{cond}^{in}}{T_{evp}^{out}} - q_{cond} \right) + \left(\frac{1}{Q} \right) \left(\frac{q_{evp}}{M_{cond} T_{evp}^{out}} \right) \left(\frac{q_{evp} T_{cond}^{in}}{T_{evp}^{out}} - q_{cond} \right) \\ & + \left(\frac{Q}{T_{evp}^{out}} \right) \left(\frac{T_{cond}^{in}}{T_{evp}^{out}} \right) \left(\frac{1}{M_{cond}} + \frac{1}{M_{evp}} \right) + \frac{\frac{q_{cond}}{M_{evp}} + \frac{q_{evp} T_{cond}^{in}}{T_{evp}^{out} M_{cond}} + \left(\frac{T_{cond}^{in} q_{evp}}{T_{evp}^{out}} - q_{cond} \right) \left(\frac{1}{M_{cond}} + \frac{1}{M_{evp}} \right)}{T_{evp}^{out}} \end{aligned} \quad (8.1)$$

Multiplying (8.1) through by the load (Q) yields the chiller power consumption (P_{ch}), given by (8.2):

$$\begin{aligned}
P_{ch} = \frac{Q}{COP} = & -Q + \left(\frac{T_{cond}^{in}}{T_{evp}^{out}} \right) Q + \left(\frac{q_e T_{cond}^{in}}{T_{evp}^{out}} - q_{cond} \right) \\
& + \left(\frac{q_{evp}}{M_{cond} T_{evp}^{out}} \right) \left(\frac{q_{evp} T_{cond}^{in}}{T_{evp}^{out}} - q_{cond} \right) + \left(\frac{Q^2}{T_{evp}^{out}} \right) \left(\frac{T_{cond}^{in}}{T_{evp}^{out}} \right) \left(\frac{1}{M_{cond}} + \frac{1}{M_{evp}} \right) \\
& + Q \frac{\frac{q_{cond}}{M_{evp}} + \frac{q_{evp} T_{cond}^{in}}{T_{evp}^{out} M_{cond}} + \left(\frac{T_{cond}^{in} q_{evp}}{T_{evp}^{out}} - q_{cond} \right) \left(\frac{1}{M_{cond}} + \frac{1}{M_{evp}} \right)}{T_{evp}^{out}}
\end{aligned} \tag{8.2}$$

The model terms are arranged so that the predictive model is linearly dependent on the unknown parameters and linear least squares can be used. The fit for Chiller 6.1 is shown in Figure 8.2 with an R^2 of 0.995, indicating that the model in (8.2) provides an excellent fit to the data.

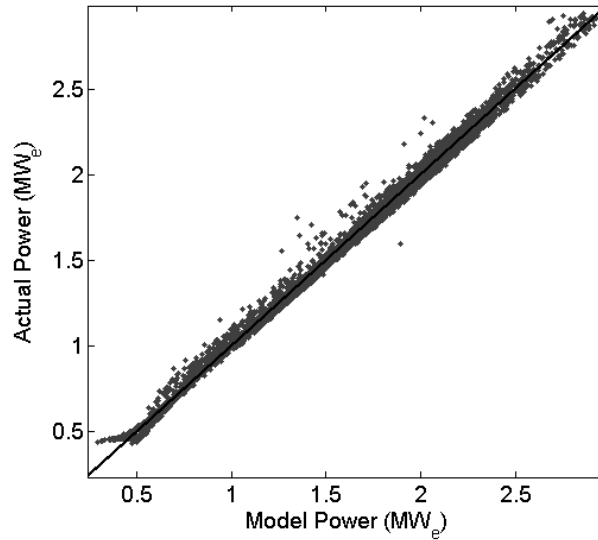


Figure 8.2: Parity plot illustrating the quality of the fit for Chiller 6.1.

Performance plots, shown in Figure 8.3, illustrate the differing efficiencies of the various chillers as $1/COP$ vs. chiller load using the models developed in Equation (8.1). Figure 8.4 shows the chiller power consumption as a function of chiller load as detailed in Equation (8.2). As these figures illustrate, there is a clear benefit to optimizing the system. Because some chillers perform so much more efficiently than others and at different loads,

it is beneficial to distribute the load optimally over the chillers. This optimal sequencing over time with chiller loading can be determined by minimizing the global cost of operation [79].

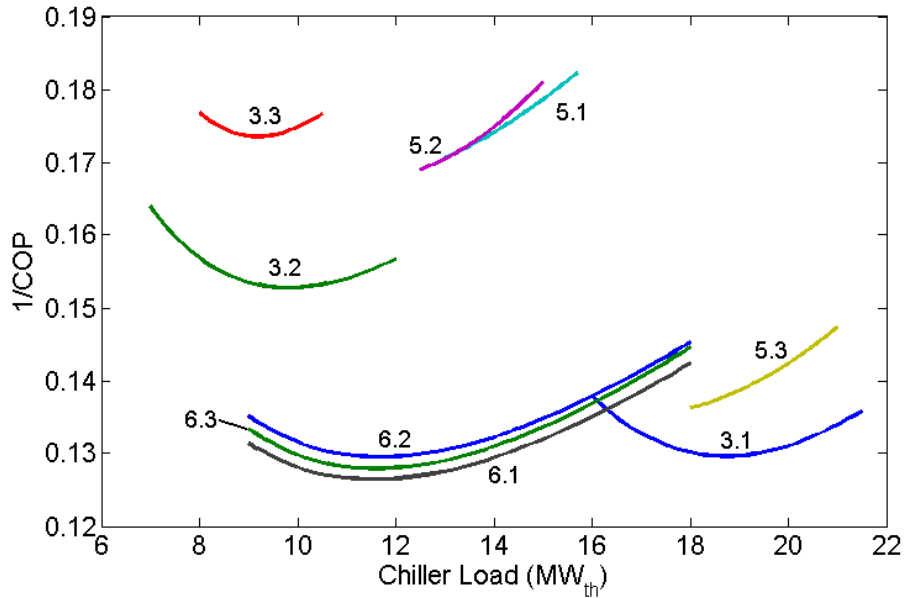


Figure 8.3: 1/COP vs. load for all chillers.

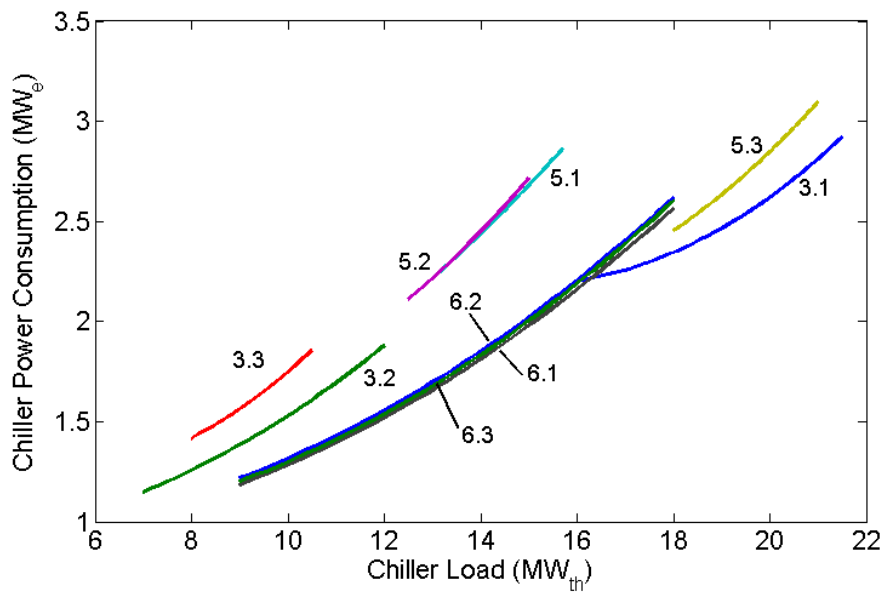


Figure 8.4: Chiller power consumption as a function of chiller load.

The cooling system auxiliaries (cooling towers and pumps) are challenging to model because of many different components (3 fans for each cooling tower and up to 18 pumps per station) and unmeasured individual flows for each pump. In order to simplify the modeling task, an empirical model is used to capture the total auxiliary power consumption for each station as a function of: the total cooling load for the station (Q_s), in addition to the ambient dry bulb temperature (T_{DB}), wet bulb temperature (T_{WB}), and relative humidity (R_H). A quadratic polynomial model is used for the multivariable empirical relationships. This model is shown in Equation 3, where X represents a vector of model inputs (Q_s , T_{DB} , T_{WB} , and R_H), and A (a matrix), B (a vector), and C (a scalar) represent model fitting parameters.

$$P_{aux} = X^T AX + BX + C \quad (8.3)$$

The fit for the Station 6 auxiliaries is shown in Figure 8.5. As the figure demonstrates, this simplified empirical model does not explain the data quite as well as the performance of the individual chiller models, indicating that the model form is imperfect or that there are measurement errors. However, the fit, with an R^2 value of 0.903, provides reasonable representation of auxiliary power consumption.

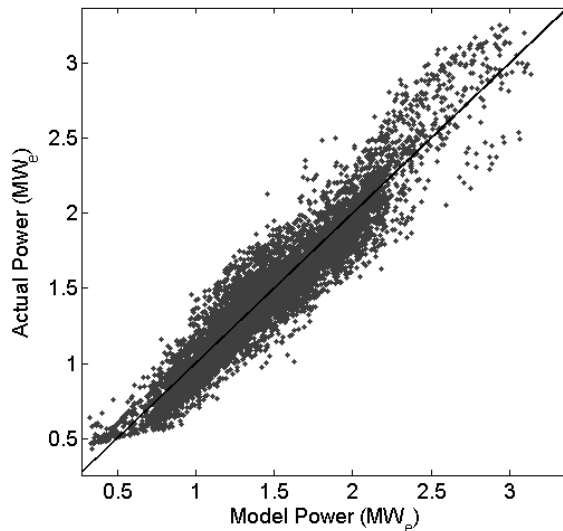


Figure 8.5: Parity plot for the auxiliary power consumption model.

The TIC system model is based on an energy balance between the chilled water and the air stream that the chilled water cools. For optimization purposes, the chiller loads are adjustable decision variables, so it is desirable to represent the TIC system in terms of cooling load as well. The TIC model then becomes:

$$Q_{TIC} = W_{air} C_{pc} (T_{DB} - T_i) \quad (8.4)$$

where Q_{TIC} is the cooling energy consumed by the turbine inlet air cooler, W_{air} is the air flow rate, C_{pc} is the average heat capacity of the air (with c in the subscript indicating lower temperature), and T_i is the temperature entering the gas turbine.

Because the optimization problem is solved on an hourly basis, a discrete-time dynamic model (8.5) that tracks the total energy stored (E_{TES}) at each hour i is used for the TES system. When the total cooling produced by the chillers at time i , exceeds the sum of the campus demand (L_C) and the TIC cooling load, the system charges. The TES system is also subjected to energy losses (E_{loss}) due to heat transfer and pumping, which are assessed during charging at 4% of the energy stored during that period. The charging rate ($Q_{TES,i}$) is the sum of all the chillers, minus the campus load and the TIC load at time i . The subscript j refers to the chiller index.

$$E_{TES,i} = E_{TES,i-1} + (Q_{TES,i} - E_{loss,i}) \Delta t \quad (8.5)$$

$$Q_{TES,i} = \sum_j Q_{i,j} - (L_{C,i} + Q_{TIC,i}) \quad (8.6)$$

The CHP system is mathematically modeled as a gas turbine, heat recovery steam generator, auxiliary boiler, and steam turbine. Details of each of these sub-models is given below.

The models for the CHP system are developed and fit by [196] using steady-state first principles models. Model parameters are identified using linear or nonlinear least squares, depending on the model. The power generated by the gas turbine (P_{GT}) is a function of the air flow, the fuel flow ($W_{f,GT}$), the inlet temperature, the temperature at the

exit of the compressor (T_d), the firing temperature (T_f), and the exhaust temperature (T_e). The various locations of the gas turbine are shown in Figure 8.6. The power output of the gas turbine is given by (8.7), where C_{ph} is the average high temperature heat capacity of the air and gas mixture.

$$P_{GT} = \left[(W_{air} + W_{f,GT}) C_{ph} (T_f - T_e) - W_{air} C_{pc} (T_d - T_i) \right] \quad (8.7)$$

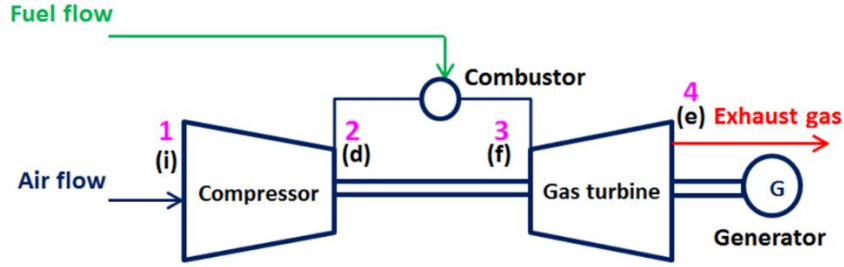


Figure 8.6: Schematic of the gas turbine configuration.

The compressor exit temperature is determined by the relationship in (8.8), where η_c is the compressor efficiency.

$$T_d = T_i \left(1 + \frac{x_c - 1}{\eta_c} \right) \quad (8.8)$$

where x_c is defined in (8.9), where PR is the compression ratio, γ_c is the cold-end ratio of specific heats, and $W_{air,n}$ is the air flow at nominal operating conditions (full load).

$$x_c = \left(PR \frac{W_{air}}{W_{air,n}} \right)^{\frac{\gamma_c - 1}{\gamma_c}} \quad (8.9)$$

The firing temperature is determined by an energy balance on the combustion chamber. The firing temperature is given in (8.10), where $W_{f,GT}$ is the fuel flow rate, $\eta_{comb,GT}$ is the combustor efficiency, and LHV is the lower heating value of the fuel.

$$T_f = T_d + \left(\frac{\eta_{comb,GT} LHV}{C_{ph}} \right) \left(\frac{W_{f,GT}}{W_{f,GT} + W_{air}} \right) \quad (8.10)$$

The exhaust temperature is given in (8.11).

$$T_e = T_f \left(1 - \left(1 - \frac{1}{x_h} \right) \eta_t \right) \quad (8.11)$$

where η_t is the turbine efficiency and x_h is defined as (8.12):

$$x_h = \left(PR \frac{W_{f,GT} + W_{air}}{W_{fn,GT} + W_n} \right)^{\frac{\gamma_h - 1}{\gamma_h}} \quad (8.12)$$

where γ_h is the ratio of specific heats.

The air flow is not determined directly, but rather is determined by adjusting the angle of the inlet guide vanes (θ_{IGV}), as shown in (8.13), where P_a is the ambient pressure, ΔP_{TIC} , is the pressure drop across the TIC, P_{a0} is the reference pressure, T_{a0} is the reference temperature, and θ_{max} and θ_0 are the maximum and reference guide vane angles, respectively.

$$W_{air} = \frac{P_a - \Delta P_{TIC}}{P_{a0}} \sqrt{\frac{T_{a0}}{T_{DB}}} \frac{\sin(\theta_{IGV} - \theta_0)}{\sin(\theta_{max} - \theta_0)} \quad (8.13)$$

Hourly data over a period of several days are plotted in Figure 8.7 illustrating the quality of the model fit compared to data. The R^2 value of 0.98 indicates a good model fit.

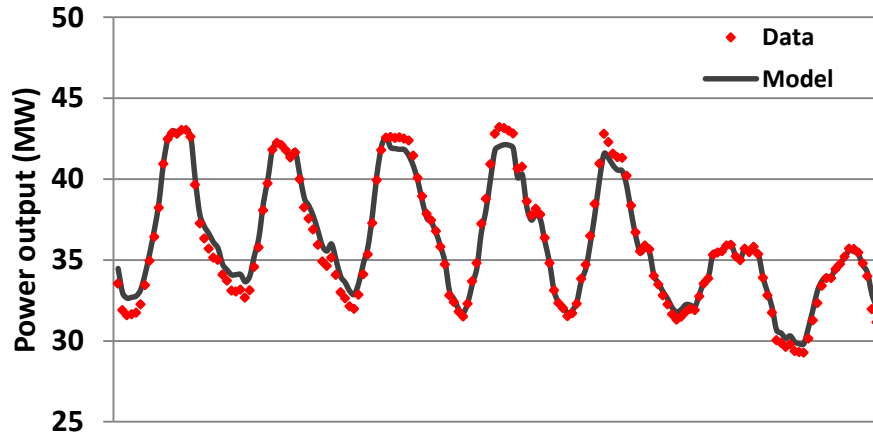


Figure 8.7: Model validation for the gas turbine model.

The HRSG is composed of several sections, where heat is transferred from the gas turbine exhaust gas to make superheated steam. When the gas turbine exhaust gas is not hot enough to produce the desired temperature of superheated steam or when additional superheated steam is desired from the HRSG, supplemental duct burners can be fired, providing more energy. The new exhaust gas temperature ($T_{e,HRSGi}$) is given by (8.14), where $\eta_{comb,HRSG}$ is the duct burner combustion efficiency, $W_{f,HRSG}$ is the duct burner fuel flow, and W_g is the gas turbine exhaust flow.

$$T_{e,HRSGi} = T_e + \frac{LHV\eta_{comb,HRSG}}{C_{ph}} \left(\frac{W_{f,HRSG}}{W_{f,HRSG} + W_g} \right) \quad (8.14)$$

The HRSG steam flow ($W_{SH,HRSG}$) exits the HRSG at 397 °C and 30 bar. This flow is computed by an overall energy balance on the HRSG, shown in (8.15), where η_{HRSG} is the HRSG efficiency, ΔH_{FW} is the feedwater heater heat duty, h_{SH} is the specific enthalpy of the superheated steam and h_{EC} is the specific enthalpy of the water entering the economizer.

$$W_{SH,HRSG} = \frac{C_{ph}\eta_{HRSG}(W_g + W_{f,HRSG})(T_{e,HRSGi} - T_{e,HRSGo}) - \Delta H_{FW}}{h_{SH} - h_{EC}} \quad (8.15)$$

A diagram of the HRSG is shown in Figure 8.8.

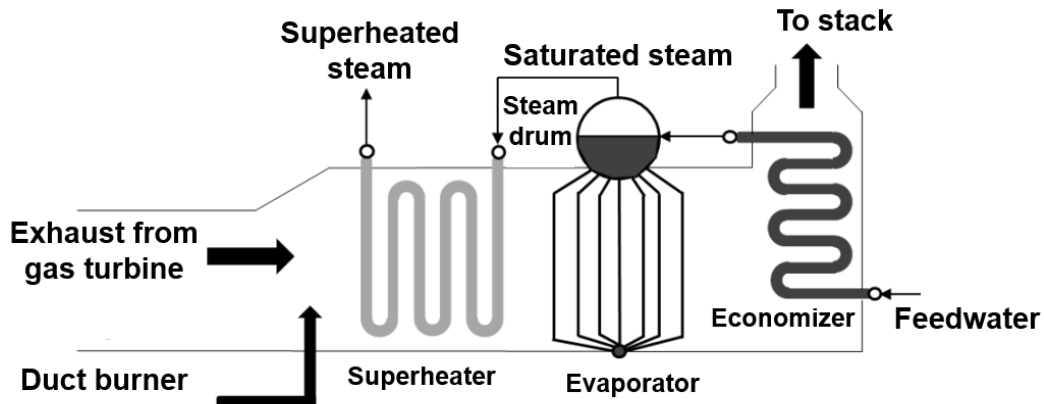


Figure 8.8: Diagram of the HRSG.

The auxiliary boiler generates additional superheated steam when it is needed. The steam output of the auxiliary boiler is computed by an energy balance, shown in (8.16), where $W_{SH, BR}$ is the superheated steam flow from the boiler, $W_{f, BR}$ is the fuel flow to the boiler, and η_{BR} is the overall boiler efficiency.

$$W_{SH, BR} = \frac{W_{f, BR} (\eta_{BR} LHV)}{h_{SH} - h_{EC}} \quad (8.16)$$

The steam turbine generates electrical power from the superheated steam that is fed from the HRSG and the auxiliary boiler. Because it is an extraction steam turbine, it can also extract medium pressure steam, which is removed and sent to campus to meet the heating demand. Any steam that is not removed by extraction passes through the full length of the turbine and comes out near saturated vapor conditions, enabling maximum energy to be removed from this stream. The steam turbine schematic is shown in Figure 8.9.

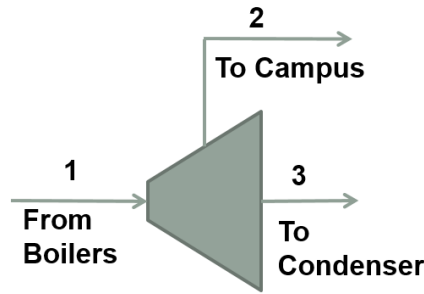


Figure 8.9: Diagram of the extraction steam turbine.

An energy balance is used on the steam turbine to calculate the power generation (P_{ST}) and is shown in (8.17), where $W_{S, EXT}$ is the extraction steam flow, $W_{ST, COND}$ is the condenser flow, and η_{ST} is the steam turbine efficiency.

$$P_{ST} = \eta_{ST} (W_{SH, tot} h_{SH} - W_{S, EXT} h_{S, EXT} - W_{S, COND} h_{S, COND}) \quad (8.17)$$

A mass balance on the superheated steam header yields the total steam flow entering the steam turbine (8.18).

$$W_{SH, tot} = W_{SH, HRSG} + W_{SH, BR} \quad (8.18)$$

Similarly, the flow sent to the condenser is determined by a mass balance on the steam turbine (8.19).

$$W_{SH,tot} = W_{s,EXT} + W_{s,COND} \quad (8.19)$$

The details of the sub-models pertaining to the CHP system can be explored in further detail in [196].

Static Optimization Problem Formulation

The optimization problem is formulated as a smaller static problem and as a larger dynamic problem with temporal resolution. The static problem is solved without the TES, allowing for a much smaller and simplified problem. The addition of dynamics through the TES allows energy loads to be shifted away from peak periods and dispatched on demand.

The objective for static optimization is to minimize the total cost by changing the decision variables, represented by u , subject to changing loads, prices, and ambient conditions. The objective function (8.20) is the total cost to operate the system including the fuel cost and the cost of buying and selling power from the grid, where C_f is the fuel cost, P_{net} is the net power exchange with the grid (positive when power is exported), and C_e is the electricity price. Operation and maintenance costs are assumed to be constant regardless of the operational strategy and do not affect the solution outcome. It is assumed that power is bought and sold at wholesale prices. Often, district energy systems must deal with a local utility, which may impose a different rate structure.

$$f = C_f \left(W_{f,GT} + W_{f,HRSG} + W_{f,BR} \right) - C_e P_{net} \quad (8.20)$$

The vector of decision variables (u) is given in (8.21), where δ are binary (0, 1) variables that determine whether a chiller is on (value of 1) or off (value of 0).

$$u = \left[Q_{3.1} \cdots Q_{6.3} \delta_{3.1} \cdots \delta_{6.3} Q_{TIC} \theta_{IGV} W_{f,GT} W_{f,HRSG} W_{f,BR} W_{s,EXT} P_{net} \right]^T \quad (8.21)$$

The models of each component in the system described by equations (8.2)-(8.19) are equality constraints in the optimization problem. The system is also subject to

inequality constraints. The chillers, if on, must be operated between fixed upper and lower bounds, given in Table 8.1. The binary variables are also incorporated into these constraints, not directly in the equality constraints or objective function, as this would lead to increased nonlinearity, making the optimization problem more difficult to solve. The constraints for each chiller (j) are shown in (8.22) with the binary constraints in (8.23).

$$\delta_j Q_{j,lo} \leq Q_j \leq \delta_j Q_{j,hi} \quad (8.22)$$

$$\delta_j \in [0,1] \quad (8.23)$$

Table 8.1: Lower and upper bounds on chiller loads.

Chiller	Lower Bound (MW_{th})	Upper Bound (MW_{th})
3.1	16	21.5
3.2	7	12
3.3	8	10.5
5.1	13	15.7
5.2	12.5	15
5.3	18	21
6.1	9	18
6.2	9	18
6.3	9	18

The other decision variables are also constrained with upper and lower bounds. These decision variables are purely continuous variables, so no binary variables are required.

$$u_{lo} \leq u \leq u_{hi} \quad (8.24)$$

The lower and upper bounds for the remaining decision variables are shown in Table 8.2. The heating load constraint is enforced directly on the decision variable, as the extraction steam flow must be greater than or equal to the heating load (L_H).

Table 8.2: Summary of constraints for other decision variables.

Decision Variable	Lower Bound	Upper Bound
Q_{TIC}	0 (MW _{th})	5 (MW _{th})
θ_{IGV}	52 (degrees)	88 degrees
$W_{f,GT}$	0.55 (kg/s)	3.44 (kg/s)
$W_{f,HRSG}$	0 (kg/s)	0.63 (kg/s)
$W_{f,BR}$.0028 (kg/s)	N/A
$W_{s,EXT}$	L_H (kg/s)	N/A
P_{net}	-40 (MW _e)	40 (MW _e)

In addition to the constraints on the decision variables, the system is also subject to several other inequality constraints. The system must produce enough electricity, heating, and cooling to meet each of these loads. The heating load constraint is handled in (8.24). The electrical load constraint is given in (8.25), which includes the net power exported. The campus (non-cooling) electric load ($L_{E,campus}$), combined with the power consumed by the cooling system comprise the total campus electric load. The cooling load (L_C), which includes TIC and storage, must also be met (8.26).

$$P_{GT} + P_{ST} - P_{net} \geq L_{E,campus} + \sum P_{ch} + \sum P_{aux} \quad (8.25)$$

$$\sum_i Q_{i,j} - Q_{TES} \geq L_C + Q_{TIC} \quad (8.26)$$

In addition to meeting the loads, the system is subject to other inequality constraints. The gas turbine firing (8.27) and exhaust temperatures (8.28) must remain below critical levels. The HRSG (8.29) and boiler (8.30) steam flows must remain below maximum limits. The HRSG gas temperature (after duct burning), must remain above the superheated steam temperature (8.31) by a minimum differential (ΔT_{min}) of 8 °C. The gas (8.32) and steam (8.33) turbines must also each remain within bounds.

$$T_f \leq 1107^\circ C \quad (8.27)$$

$$T_e \leq 522^\circ C \quad (8.28)$$

$$W_{SH,HRSG} \leq 36.4 \text{ kg / s} \quad (8.29)$$

$$W_{SH,BR} \leq 63.0 \text{ kg / s} \quad (8.30)$$

$$T_{SH,HRSG} + \Delta T_{min} \leq T_{e,HRSGi} \quad (8.31)$$

$$0 \leq P_{GT} \leq 44 \text{ MW}_e \quad (8.32)$$

$$0 \leq P_{ST} \leq 27 \text{ MW}_e \quad (8.33)$$

With all of the equality and inequality constraints determined, the static optimization problem is (8.34). Because the static problem does not include storing energy, equations (8.5) and (8.6) are omitted from the problem. Furthermore, for scenarios when power exchange from the grid is prohibited, P_{net} must be equal to zero indicating that the campus operates independently for power generation.

$$\min_u f(u, d) \quad (8.34)$$

s.t. (8.2)-(8.34), excluding (8.5)-(8.6)

The problem posed above is a mixed-integer nonlinear program (MINLP), due to the binary constraints in (8.23). These types of problems are typically more difficult to solve than standard NLPs. Special solution methods are required, such as branch and bound, where certain integer constraints are fixed while a relaxed NLP problem is solved. The binary variables represent which chillers are on and which are off. Because the chiller efficiencies are readily available from (8.1), pre-determined combinations of the binary variables are tried and the best solutions are kept. This removes much of the combinatorial

complexity of the full MINLP and enables much faster solution times. The NLP relaxations are solved using the sequential quadratic programming (SQP) algorithm in MATLAB.

Dynamic Optimization Problem Formulation

The dynamic optimization problem, where TES can be used to shift cooling loads (and subsequently, electrical loads), incorporates many more decision variables, where each of the decision variables defined above must be determined at every time step in the time horizon of the dynamic optimization problem. This makes the problem much larger in size and much more difficult to solve. The objective function for the dynamic problem is defined in (8.35), where the subscript, i , indicates the time. Hourly time steps are used in this case over a 24 hour period. A fixed fuel cost is used, while hourly (day-ahead market) electricity prices are used.

$$F = \sum_i \left[C_f (W_{f,GT,i} + W_{f,HRSG,i} + W_{f,BR,i}) - C_{e,i} P_{net,i} \right] (\Delta t) \quad (8.35)$$

Including the TES system in (8.5) and (8.6), the dynamic problem is also an MINLP, albeit a much larger one than the static problem. A total of 600 decision variables are determined and the constraints satisfied for every hour yielding an MINLP with 600 degrees of freedom (216 of them binary). A trial solution of the full, dynamic MINLP is solved in 27 CPU clock hours (on a 2.8 GHz processor) using the branch and bound solver BONMIN. This optimization problem is run on a single CPU while parallelization of the branch and bound technique would lead to a significant reduction in clock time. While the solution is valid, the excessive solve time is untenable. In order to resolve this, an alternative formulation is used. This formulation decouples the dynamic and static components of the problem. Because steady state models are used for all equipment except the TES, the TES charge rate at each hour can be used as the only decision variable. Given a charge rate for a specific hour, static sub-problems can then be solved so as to minimize cost (f) at each hour given the trial TES charging rate. The static sub-problems then report

back their optimal solutions to the dynamic problem so that its objective function (F) can be computed. This technique requires solving thousands of static problems, but it reduces the dynamic problem from a 600 variable problem to a 24 variable problem. Solution time is reduced to an average of 30-40 minutes.

Figure 8.10 illustrates how the decision variables for the dynamic problem (U_i) are fed to the static sub-problems (for each hour). When these problems are solved, they report back the value of their objective function at their optimal solutions (f_i^*) so that the objective function of the dynamic problem (F) can be computed. Numerical gradients and Hessians of the dynamic problem are generated at each iteration.

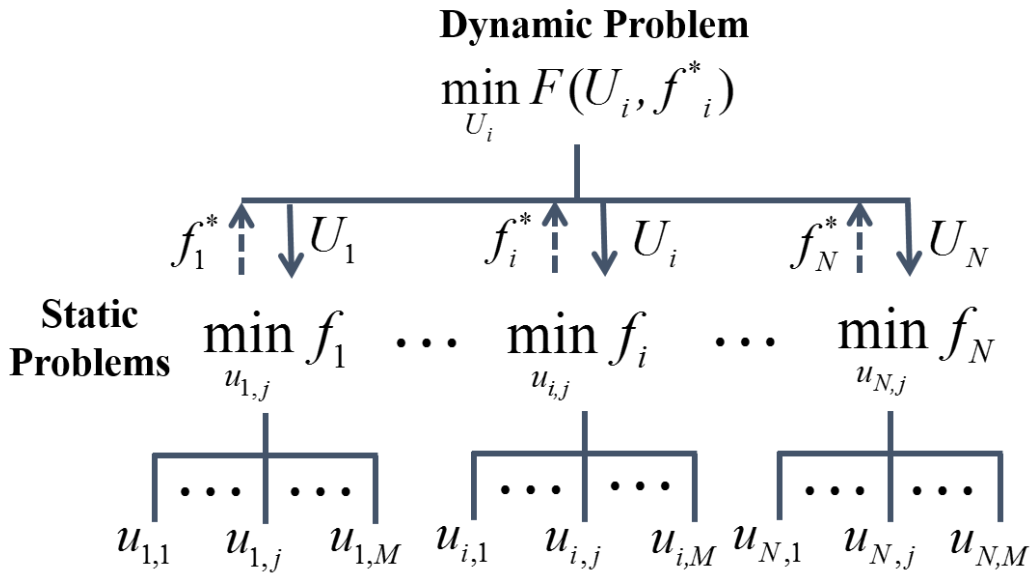


Figure 8.10: A diagram outlining the optimization problem decoupling.

In Figure 8.10, the decision variables to the dynamic problem (U_i) are the TES charge rates ($Q_{TES,i}$). These rates have upper and lower limits. Positive values indicate charging of the system, while negative values indicate discharging (8.36).

$$-36 MW_{th} \leq Q_{TES,i} \leq 25 MW_{th} \quad (8.36)$$

The total energy in the TES must also remain within its bounds (8.37).

$$0 \leq E_{TES,i} \leq 138 \text{ MWh}_{th} \quad (8.37)$$

With the new problem formulation, the dynamic problem is given in (8.38). The static constraints given must be satisfied for every time step i .

$$\min_{U_i} F \quad (8.38)$$

s.t. (8.2)-(8.37)

The dynamic problem is formulated and solved in MATLAB using the `fmincon` solver with the SQP algorithm for both the dynamic and the static optimization problems. The results are presented in the next section.

Results and Discussion

The dynamic (with storage) and static (without storage) optimization problems are solved under three scenarios: 1-minimizing fuel costs only, 2-minimizing costs, where revenue can be obtained by selling excess power to the grid, 3-minimizing costs where power can be both bought and sold to and from the grid. When power is exported and imported, the selling prices used are the day-ahead market prices for Austin, Texas from the corresponding hours. The study consists of a one year period from September 2011 through August 2012 using weather data from the national weather database for the Austin area [197].

The total power production for a one week period is shown in (a) of Figure 8.11 and Figure 8.12. These plots also show the net power exported to the grid in (b) and the selling price of the power in (c). The plots show the scenarios where power can be sold to the grid and compare it to the total electrical load. In Figure 8.11, the electricity prices remain relatively flat, except for a few peaks in the afternoon. On Sunday and Friday afternoon, excess power is sold, but price differentials are not steep enough to justify using the TES to free up more electric generation capacity to sell even more power. When the prices rise significantly higher, as is the case on Monday and Wednesday, the TES is

charged in the early morning. This frees up the capacity on the turbines so that more power can be sold later in the afternoon on those days. This is particularly important on Monday, when prices exceed \$200/MWh.

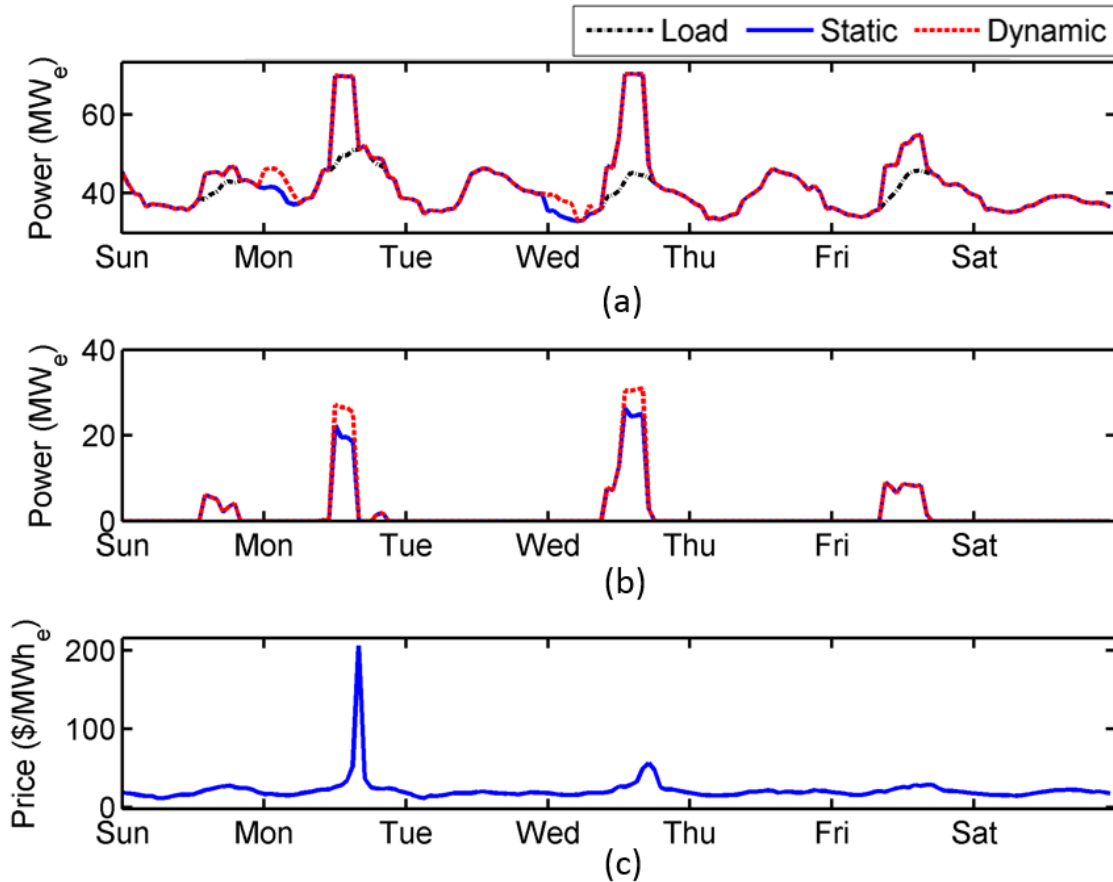


Figure 8.11: Total power production, net power sold, and electricity price.

When electricity prices fluctuate with more regularity, the storage is used much more frequently. In Figure 8.12, the storage is used every day of the week. While prices during this particular week do not reach the same levels as in the previous figure, they oscillate enough to justify charging the TES tank when prices are low so that the chiller electricity usage can be minimized during peak hours when the prices rise. In this figure, (a) is the total power production, (b) is the net power exported, and (c) is the electricity price.

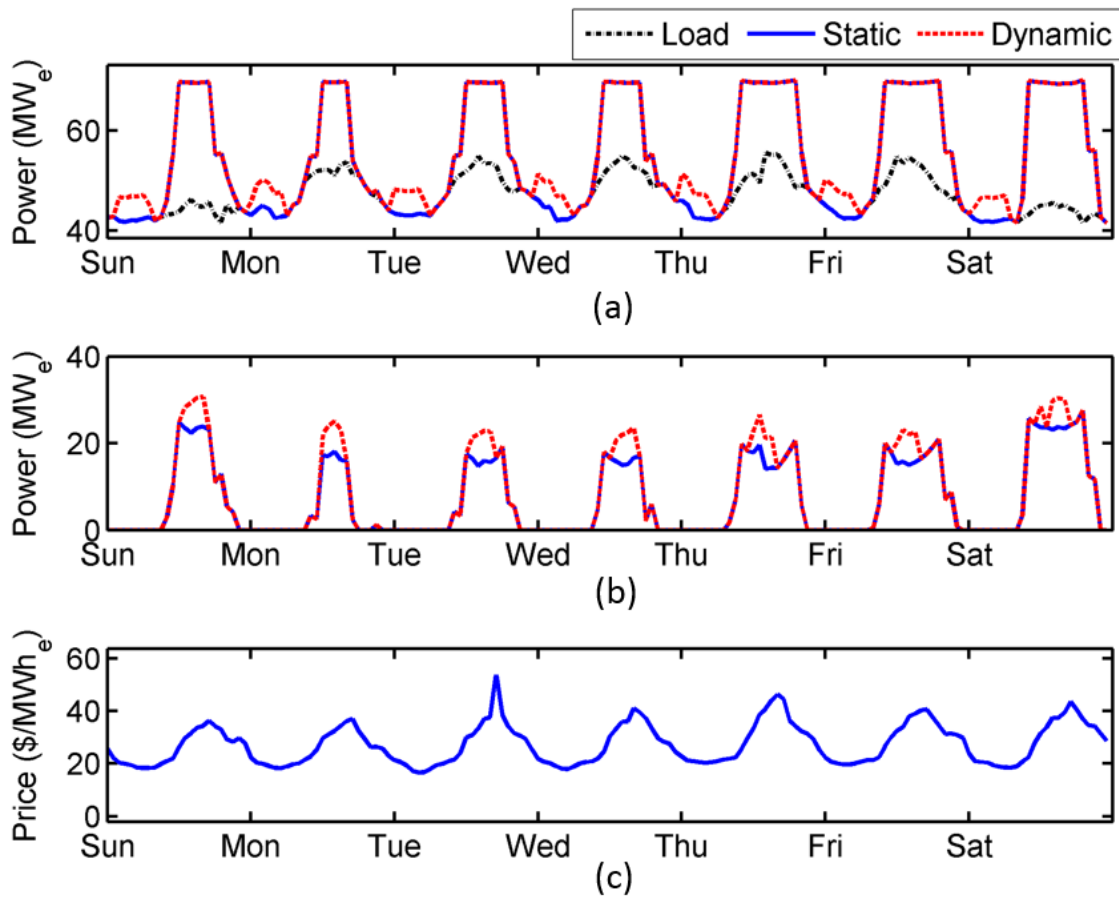


Figure 8.12: Total power production, net power sold, and electricity price.

The optimization problems, both static and dynamic, are non-convex. Therefore, the solvers have a tendency to converge at local optima, which is undesirable. It is critical, therefore, to use a good initial guess when solving the problem. The strategy for initializing the dynamic optimization problem in this study is to assume that the storage charges during times when electricity prices are low and discharges when the opposite is true.

The static and dynamic problems are solved for the entire year-long period for each scenario. The results, showing the total yearly cost for each scenario are shown in Figure 8.13. There is a savings of about \$250,000 for one year that can be obtained by optimizing the system. In terms of only minimizing fuel usage (the No Sell scenario), storage has only a marginal benefit. The efficiency that can be gained by shifting cooling loads from one

time to another is typically so small that it is offset by the storage losses. It is generally not beneficial to use storage only to improve efficiency for this particular system. In general, energy storage is only profitable when there is time of day pricing. For an isolated system that can meet peak demand and with constant fuel prices, there is little incentive to install energy storage.

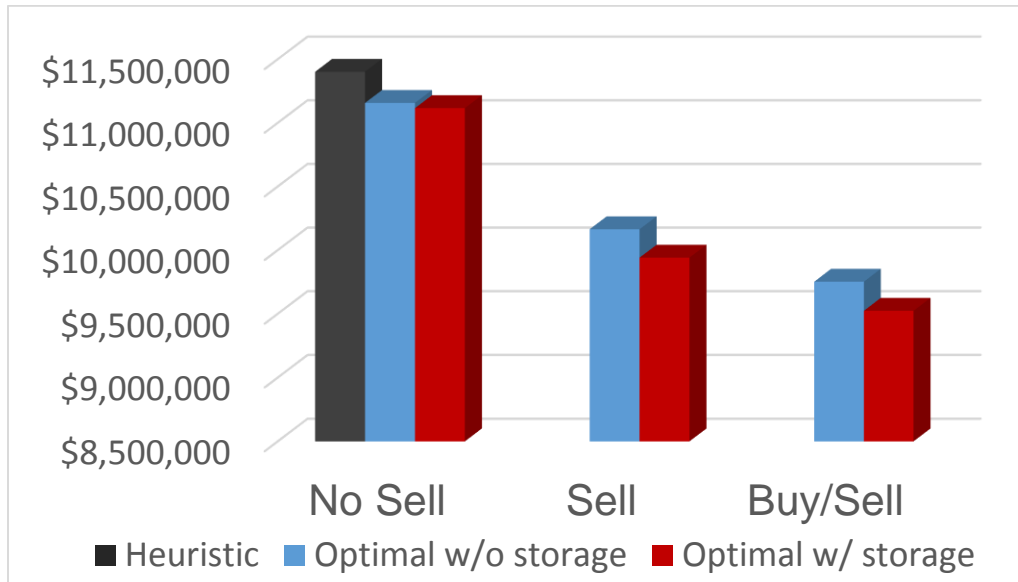


Figure 8.13: Summary of total operating costs for one year under various scenarios.

Revenue from selling excess power helps to significantly offset fuel costs. When power can be sold to the grid, the costs are reduced by \$1 million when going from the no selling/no storage to selling/no storage. Compared to the latter scenario, the incorporation of TES further reduces costs by 2.2%. The TES is particularly valuable when electricity prices are excessive, as it frees up electrical capacity by reducing the peak cooling load.

When power can be bought and sold from the grid, total costs are further reduced. As is sometimes the case, power can be imported at a lower cost than it can be generated. While the turbines must still be run to meet heating loads, their usage can be minimized by supplementing the electrical generation with imported power. When TES is used, arbitrage can be done. The TES can be charged when prices are low. When prices are high, the TES is discharged to reduce the campus electrical load. This provides excess electrical

generation capacity so that more power can be sold. The savings from using storage are 2.3% as compared to the buy/sell scenario without storage.

As expected, optimization is more effective when constraints are relaxed. While there may be regulatory constraints for district energy systems to freely buy and sell power from the grid, the ability to do so can significantly offset operating costs. From the worst case to the best case, a total savings of \$1.88 million (16.5%) is achieved. The results show that for this particular system, the benefit of TES is only fully realized when the system is allowed to participate in the electricity market.

It should be again noted that the costs discussed in this section are only fuel and electricity prices. No labor and other operational costs are included. The study also assumes the system can freely exchange electricity with the grid at wholesale market prices. This scenario is idealized as there may be other (non-technical) issues. For example, the system may be subject to the rates of the local utility, which would typically be higher than wholesale market rates, for buying electricity. When exporting power, there may be other regulatory hurdles to consider, which would likely increase costs. From a purely technical point of view, however, the benefits of using TES and participating in the open electricity market are clear.

Conclusions

District energy and CHP systems offer many advantages. Because of the proximity to a source of heat (the waste heat from power production), meeting electrical and heating demands can be done very efficiently. District cooling provides a unique opportunity to introduce low cost TES. Because the economy of scale benefit is already in place with centralized cooling, TES can be readily integrated. This gives the system flexibility and can alleviate the cost of additional cooling equipment, as much of the peak demand can be shifted to off-peak periods.

Systems with coupled heating, cooling, and power generation are quite complex as there are many inter-relations between the varying pieces of equipment. There are also

opportunities to optimize such systems. TES, while storing thermal energy, can be used to shift electrical loads, which can be integral if the system exchanges electricity with the grid. For this particular system, the benefits of TES from an efficiency standpoint are negligible. However, in terms of offsetting costs by participating in the electricity market, the benefit of TES can be significant.

The ability to buy or sell power from an outside source gives the district energy system additional degrees of freedom, allowing it to import power when electricity prices are low and to export when they are high. These degrees of freedom can be exploited through optimization, which finds the optimal values of decision variables so that some ideal objective is achieved. TES provides more degrees of freedom, giving the system the ability to shift loads temporally and take advantage of differences in efficiency or operating cost at different times. With the addition of TES, the problem becomes dynamic, and while the benefit of optimizing is greater, the difficulty also increases significantly. The dynamic problem can be simplified by breaking it into a series of static problems. This method allows the problem to be solved more efficiently so that real-time optimization can be performed.

With intermittent renewable technologies becoming more prevalent, the smart grid is being developed to enable efficient operation and two-way power flow. The smart grid provides new opportunities to optimize diverse energy systems. With district energy systems, the concept of the smart grid extends beyond electricity generation and can incorporate even more diverse types of equipment dealing with cooling or heating energy. These systems also provide ample opportunity to optimize cost and can be used to incorporate non-electrical energy storage (like TES), into a smart grid environment.

Nomenclature

Symbol	Description	Units
A	Matrix with coefficients for quadratic terms in cooling station auxiliary power model	-
B	Vector with coefficients for linear terms in cooling station auxiliary power model	-
C	Scalar with coefficients for constant terms in cooling station auxiliary power model	-
C_e	Electricity price	\$/MWh _e
C_f	Fuel price	\$/kg
COP	Coefficient of performance	-
C_{pc}	Average air heat capacity at lower temperatures at constant pressure	kJ/(kgK)
C_{ph}	Average air heat capacity at higher temperatures at constant pressure	kJ/(kgK)
E_{TES}	Energy stored in the TES	MWh
f	Objective function for static problem	\$/hr
F	Objective function for dynamic problem	\$
h_{EC}	Economizer water specific enthalpy	kJ/kg
$h_{S,COND}$	Steam turbine condenser steam specific enthalpy	kJ/kg
$h_{S,EXT}$	Extraction steam specific enthalpy	kJ/kg
h_{SH}	Superheated steam specific enthalpy	kJ/kg
i	Subscript indicating time interval	-
j	Subscript indicating chiller	-
L_C	Total campus cooling demand	MW _{th}
L_E	Total campus electrical demand	MW _e
L_H	Total campus heating demand	kg/s
LHV	Lower heating value of fuel	kJ/kg
M_{cond}	Product of condenser heat exchanger coefficient and heat exchange surface area	kW/K
M_{evp}	Product of evaporator heat exchanger coefficient and heat exchange surface area	kW/K
P_a	Ambient air pressure (absolute)	bar
P_{a0}	Reference ambient air pressure	bar
P_{aux}	Electrical power consumed by cooling system auxiliaries (cooling towers and pumps)	MW _e
P_{ch}	Electrical power consumed by chillers	MW _e
P_{GT}	Gas turbine power output	MW _e
P_{net}	Power exchange to/from grid	MW _e

PR	Gas turbine compression ratio	-
P_{ST}	Steam turbine power output	MW_e
Q	Individual chiller cooling load	MW_{th}
q_{cond}	Rate of internal losses at the condenser	MW_{th}
q_{evp}	Rate of internal losses at the evaporator	MW_{th}
Q_s	Total station cooling load	MW_{th}
Q_{TES}	TES charging rate	MW_{th}
Q_{TIC}	TIC cooling load	MW_{th}
R_H	Relative humidity'	%
T_{a0}	Inlet air reference temperature	K
T_{cond}^{in}	Condenser water inlet temperature	K
T_d	Pre-combustion temperature in gas turbine	K
T_{DB}	Dry Bulb Temperature	K
T_e	Turbine exhaust temperature	K
$T_{e,HRSGi}$	Post duct burner HRSG air temperature	K
T_{evp}^{out}	Evaporator water outlet temperature	K
T_f	Post combustion (firing) temperature in gas turbine	K
T_i	Turbine inlet temperature	K
T_{WB}	Wet Bulb Temperature	K
u	Vector of decision variables for static problem	-
U	Vector of decision variables for dynamic problem	-
W_{air}	Air mass flow rate (entering turbine)	kg/s
$W_{f,BR}$	Fuel mass flow rate (entering auxiliary boiler)	kg/s
$W_{f,GT}$	Fuel mass flow rate (entering turbine combustor)	kg/s
$W_{f,HRSG}$	Fuel mass flow rate (entering HRSG)	kg/s
W_g	Gas turbine exhaust mass flow rate	kg/s
W_n	Gas turbine air flow rate at nominal conditions	kg/s
$W_{S,COND}$	Steam turbine condenser flow rate	kg/s
$W_{S,EXT}$	Extraction steam flow rate	kg/s
$W_{SH,BR}$	Auxiliary boiler steam flow rate	kg/s
$W_{SH,HRSG}$	HRSG steam flow rate	kg/s
$W_{SH,tot}$	Total superheated steam flow rate	kg/s
X	Vector containing model inputs for cooling station power consumption models	-
x_c	Lumped variable	-
x_h	Superheated steam specific enthalpy	kJ/kg
γ_c	Low temperature ratio of specific heats	-
γ_h	High temperature ratio of specific heats	-

δ	Binary decision variable	-
ΔH_{FW}	HRSG feedwater heater heat duty	MW _{th}
ΔP_{TIC}	Pressure drop across TIC	bar
Δt	Time interval	hr
η_{BR}	Boiler efficiency	-
η_c	Compressor efficiency	-
$\eta_{comb,GT}$	Gas turbine combustor efficiency	-
$\eta_{comb,HRSG}$	HRSG combustor efficiency	-
η_{HRSG}	HRSG efficiency	-
η_t	Turbine efficiency	-
θ_0	Reference inlet guide vane angle	degrees
θ_{IGV}	Inlet guide vane angle	degrees
θ_{max}	Maximum inlet guide vane angle	degrees

CHAPTER 9 : CONCLUSIONS AND FUTURE WORK

Compared to some other energy storage methods, like batteries, TES is a somewhat simple technology. TES stores energy as heat or as cooling, which means that it can only be used in specific systems that can make use of energy in these forms. It is this simplicity, however, that makes TES a low-cost, but high-impact storage technology. Storing thermal energy requires only a tank filled with the appropriate storage medium. Although it is a simple technology, it can have a profound effect on an energy system. For solar thermal systems, TES is a cost-effective way to overcome the intermittency of solar energy. The availability of this low-cost storage technology is a considerable advantage that solar thermal systems have over photovoltaic systems, which require much more expensive battery storage. TES can also be used to shift cooling demand and is particularly cost-effective when used in a district energy system. TES can be very effective in reducing operating costs by helping the system to avoid and/or take advantage of peak energy prices.

This work has demonstrated that when TES is considered in the context of a complete energy system, it is a valuable component that can be used to make the other parts of the system perform better. Realizing this benefit requires optimizing the system on a dynamic basis, which yields substantial payback. Dynamic optimization requires taking into account prediction of the future ambient conditions as well as the supply and/or demand of energy over the time horizon. These forecasts will generally be imperfect, which means that deterministic optimization methods may not always produce the expected result. Because of the forecast uncertainty, stochastic optimization methods should be considered in the future. These methods can account for forecast uncertainty and optimize so that the objective is minimized, while also mitigating any risk that may be involved should the forecast prove to be inaccurate.

Another method for handling forecast uncertainty, in addition to modeling inaccuracies is to implement dynamic optimization on a rolling basis. If forecast inaccuracies exist, more up-to-date forecasts may be able to account for changes in the

conditions and produce a more accurate prediction. Because the forecast, ambient conditions, and plant states will change with time, real-time implementation should be done on a much smaller time scale than the optimization problem time horizon. For instance, while a 24 –hour time horizon is considered throughout this work, control moves should be implemented on the order of every hour. At the next time step, a new forecast, which incorporates the most recent data, can be generated, and the optimization problem can be solved again. Therefore, while the optimization problem solves for operation over the entire horizon, only the control move for the first time step is implemented. This methodology will help alleviate problems that may arise from forecast and modeling inaccuracies, by ensuring that the models are corrected by measured data frequently. This methodology is illustrated in Figure 9.1.

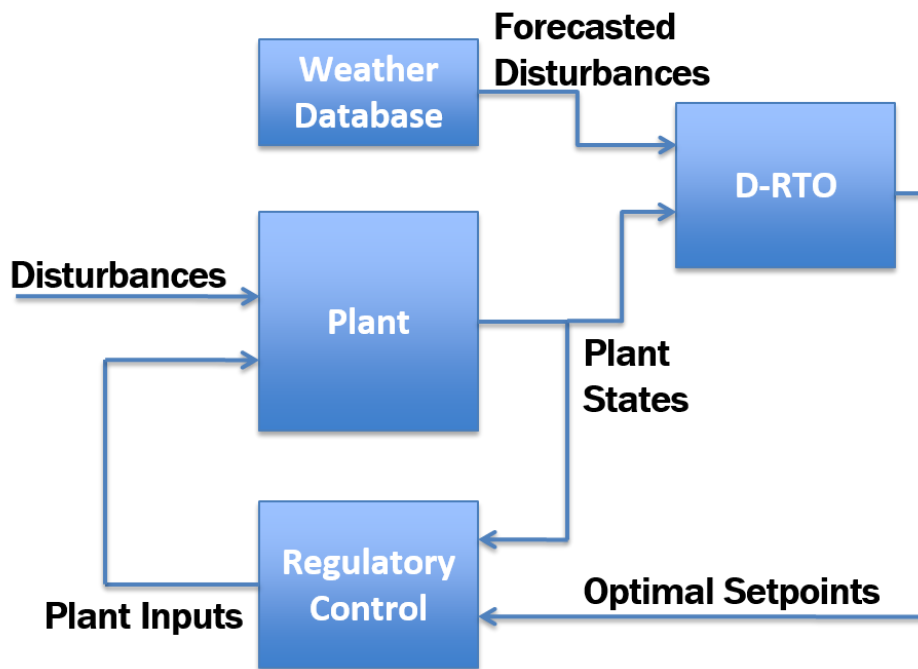


Figure 9.1: A block diagram for dynamic real-time optimization.

As the figure shows, the dynamic real-time optimization (D-RTO) block takes into account the most recent plant states and forecast information. The optimization problem is solved so that control moves can be implemented. It is recommended that the system be

designed so that lower-level regulatory controllers receive set points from the D-RTO and then implement the actual control action in the plant. In some cases, model predictive controllers (MPCs) may be necessary to ensure that the plant is effectively regulated. This should be the case for the solar system discussed in Chapter 2 and Chapter 3, where regulating the solar field temperature is a difficult nonlinear control problem in and of itself. While average solar irradiance may be predictable with reasonable accuracy, these 24-hour prediction models cannot account for sudden changes in available sunlight. Therefore, good measurement devices should be used to provide the MPCs with feedforward information so that proactive control moves can be made.

Because dynamic optimization of energy systems with TES has proven to be an effective cost and energy saving methodology, it is recommended that future work be focused on implementing these methods on real systems and in real-time. Real-time operation requires fast solution methods. Because the dynamic optimization problems in this work are non-convex, global solvers can be useful to ensure that optimality over the entire range of possible operation is achieved. However, because the problems are large MINLPs, using a global solver for real-time implementation may not be realistic. Another avenue for future work, therefore, is developing ways to overcome these challenges. Intelligent initialization routines, in addition to novel solution methods, are recommended.

TES has proven to be a valuable component to energy system with a thermal component because it provides new degrees of freedom. Dynamic optimization of these systems may significantly change the way they operate. With this in mind, another area for future work is designing novel energy systems that can best take advantage of the flexibility that storage provides. Solar thermal systems, for instance, can be designed to be more synergistic with fossil fuel systems. The TES can be a critical component by allowing solar energy to be collected, stored, and delivered at various temperatures, while the system relies on a fossil fuel source of energy to ensure that proper temperatures and power flows are achieved in the power block. Because hybrid operation represents a significant paradigm shift where solar energy and fossil fuels complement each other, the plant should

be designed with this in mind, so that the maximum amount of solar energy can be harvested.

While challenges still exist for implementation of these methods, this work has demonstrated the significant benefits of dynamic optimization of energy systems with TES. TES can alleviate supply/demand mismatch, enabling energy systems to deliver power on demand, or to shift loads to avoid peak. The degrees of freedom that TES provides can also be exploited to improve efficiency and reduce costs of the system using dynamic optimization to determine optimal operation.

WORKS CITED

- [1] R. M. Dell and D. A. J. Rand, “Energy storage -- a key technology for global energy sustainability,” *Journal of Power Sources*, vol. 100, no. 1–2, pp. 2–17, Nov. 2001.
- [2] I. Dincer and M. A. Rosen, *Thermal Energy Storage: Systems and Applications*. John Wiley & Sons, 2002.
- [3] A. Gil, M. Medrano, I. Martorell, A. Lázaro, P. Dolado, B. Zalba, and L. F. Cabeza, “State of the art on high temperature thermal energy storage for power generation. Part 1--Concepts, materials and modellization,” *Renewable and Sustainable Energy Reviews*, vol. 14, no. 1, pp. 31–55, Jan. 2010.
- [4] A. Fernández-García, E. Zarza, L. Valenzuela, and M. Pérez, “Parabolic-trough solar collectors and their applications,” *Renewable and Sustainable Energy Reviews*, vol. 14, no. 7, pp. 1695–1721, Sep. 2010.
- [5] T. Stuetzle, N. Blair, J. W. Mitchell, and W. A. Beckman, “Automatic control of a 30 MWe SEGS VI parabolic trough plant,” *Solar Energy*, vol. 76, no. 1–3, pp. 187–193, 2004.
- [6] M. Medrano, A. Gil, I. Martorell, X. Potau, and L. F. Cabeza, “State of the art on high-temperature thermal energy storage for power generation. Part 2—Case studies,” *Renewable and Sustainable Energy Reviews*, vol. 14, no. 1, pp. 56–72, Jan. 2010.
- [7] E. F. Camacho, F. R. Rubio, M. Berenguel, and L. Valenzuela, “A survey on control schemes for distributed solar collector fields. Part II: Advanced control approaches,” *Solar Energy*, vol. 81, no. 10, pp. 1252–1272, Oct. 2007.
- [8] R. N. Silva, L. M. Rato, J. M. Lemos, and F. Coito, “Cascade control of a distributed collector solar field,” *Journal of Process Control*, vol. 7, no. 2, pp. 111–117, 1997.
- [9] D. Mills, “Advances in solar thermal electricity technology,” *Solar Energy*, vol. 76, no. 1–3, pp. 19–31, Jan. 2004.
- [10] S. Kalogirou, *Solar Energy Engineering Processes and Systems*. Burlington, MA, 2009.
- [11] F. Incropera, D. DeWitt, T. Bergman, and A. Lavine, *Fundamentals of Heat and Mass Transfer*, 6th ed. Danvers, MA, 2007.
- [12] G. Gong, X. Huang, J. Wang, and M. Hao, “An optimized model and test of the China’s first high temperature parabolic trough solar receiver,” *Solar Energy*, vol. 84, no. 12, pp. 2230–2245, Dec. 2010.
- [13] M. J. Ahmad and G. N. Tiwari, “Solar radiation models—A review,” *Int. J. Energy Res.*, vol. 35, no. 4, pp. 271–290, Mar. 2011.
- [14] J. A. Duffie and W. A. Beckman, *Solar Engineering of Thermal Processes*, Third. Hoboken, NJ: John Wiley & Sons, 2006.
- [15] D. Seborg, T. Edgar, D. Mellichamp, and F. Doyle, *Process Dynamics and Control*, 3rd ed. Hoboken, NJ: Wiley, 2010.

- [16] H. L. Zhang, J. Baeyens, J. Degève, and G. Cacères, “Concentrated solar power plants: Review and design methodology,” *Renewable and Sustainable Energy Reviews*, vol. 22, no. 0, pp. 466–481, Jun. 2013.
- [17] D. Barlev, R. Vidu, and P. Stroeve, “Innovation in concentrated solar power,” *Solar Energy Materials and Solar Cells*, vol. 95, no. 10, pp. 2703–2725, Oct. 2011.
- [18] S. J. Wagner and E. S. Rubin, “Economic implications of thermal energy storage for concentrated solar thermal power,” *Renewable Energy*, no. 0, 2013.
- [19] S. Kuravi, J. Trahan, D. Y. Goswami, M. M. Rahman, and E. K. Stefanakos, “Thermal energy storage technologies and systems for concentrating solar power plants,” *Progress in Energy and Combustion Science*, vol. 39, no. 4, pp. 285–319, Aug. 2013.
- [20] J. H. Peterseim, S. White, A. Tadros, and U. Hellwig, “Concentrated solar power hybrid plants, which technologies are best suited for hybridisation?,” *Renewable Energy*, vol. 57, no. 0, pp. 520–532, Sep. 2013.
- [21] M. S. Jamel, A. Abd Rahman, and A. H. Shamsuddin, “Advances in the integration of solar thermal energy with conventional and non-conventional power plants,” *Renewable and Sustainable Energy Reviews*, vol. 20, no. 0, pp. 71–81, Apr. 2013.
- [22] G. Cau, D. Cocco, and V. Tola, “Performance and cost assessment of Integrated Solar Combined Cycle Systems (ISCCSs) using CO₂ as heat transfer fluid,” *Solar Energy*, vol. 86, no. 10, pp. 2975–2985, Oct. 2012.
- [23] G. Barigozzi, G. Bonetti, G. Franchini, A. Perdichizzi, and S. Ravelli, “Thermal performance prediction of a solar hybrid gas turbine,” *Solar Energy*, vol. 86, no. 7, pp. 2116–2127, Jul. 2012.
- [24] P. Schwarzbözl, R. Buck, C. Sugarmen, A. Ring, M. J. Marcos Crespo, P. Altwegg, and J. Enrile, “Solar gas turbine systems: Design, cost and perspectives,” *Solar Energy*, vol. 80, no. 10, pp. 1231–1240, Oct. 2006.
- [25] E. J. Sheu and A. Mitsos, “Optimization of a hybrid solar-fossil fuel plant: Solar steam reforming of methane in a combined cycle,” *Energy*, vol. 51, no. 0, pp. 193–202, Mar. 2013.
- [26] M. Jafarian, M. Arjomandi, and G. J. Nathan, “A hybrid solar and chemical looping combustion system for solar thermal energy storage,” *Applied Energy*, vol. 103, no. 0, pp. 671–678, Mar. 2013.
- [27] B. D. Vick and T. A. Moss, “Adding concentrated solar power plants to wind farms to achieve a good utility electrical load match,” *Solar Energy*, vol. 92, no. 0, pp. 298–312, Jun. 2013.
- [28] F. Manenti and Z. Ravaghi-Ardebili, “Dynamic simulation of concentrating solar power plant and two-tanks direct thermal energy storage,” *Energy*, vol. 55, no. 0, pp. 89–97, Jun. 2013.
- [29] K. M. Powell and T. F. Edgar, “Modeling and control of a solar thermal power plant with thermal energy storage,” *Chemical Engineering Science*, vol. 71, pp. 138–145, Mar. 2012.

- [30] A. H. Slocum, D. S. Codd, J. Buongiorno, C. Forsberg, T. McKrell, J.-C. Nave, C. N. Papanicolas, A. Ghobeity, C. J. Noone, S. Passerini, F. Rojas, and A. Mitsos, “Concentrated solar power on demand,” *Solar Energy*, vol. 85, no. 7, pp. 1519–1529, Jul. 2011.
- [31] E. Lizarraga-Garcia, A. Ghobeity, M. Totten, and A. Mitsos, “Optimal operation of a solar-thermal power plant with energy storage and electricity buy-back from grid,” *Energy*, vol. 51, no. 0, pp. 61–70, Mar. 2013.
- [32] M. Wittmann, M. Eck, R. Pitz-Paal, and H. Müller-Steinhagen, “Methodology for optimized operation strategies of solar thermal power plants with integrated heat storage,” *Solar Energy*, vol. 85, no. 4, pp. 653–659, Apr. 2011.
- [33] A. Giotri, M. Binotti, M. Astolfi, P. Silva, E. Macchi, and G. Manzolini, “Comparison of different solar plants based on parabolic trough technology,” *Solar Energy*, vol. 86, no. 5, pp. 1208–1221, May 2012.
- [34] L. Jianfeng, D. Jing, Y. Jianping, and Y. Xiaoxi, “Exergetic optimization for solar heat receiver with heat loss and viscous dissipation,” *Solar Energy*, vol. 86, no. 9, pp. 2273–2281, Sep. 2012.
- [35] E. F. Camacho, F. R. Rubio, M. Berenguel, and L. Valenzuela, “A survey on control schemes for distributed solar collector fields. Part I: Modeling and basic control approaches,” *Solar Energy*, vol. 81, no. 10, pp. 1240–1251, Oct. 2007.
- [36] A. J. Gallego and E. F. Camacho, “Adaptative state-space model predictive control of a parabolic-trough field,” *Control Engineering Practice*, vol. 20, no. 9, pp. 904–911, Sep. 2012.
- [37] M. Gálvez-Carrillo, R. De Keyser, and C. Ionescu, “Nonlinear predictive control with dead-time compensator: Application to a solar power plant,” *Solar Energy*, vol. 83, no. 5, pp. 743–752, May 2009.
- [38] V. M. Zavala, E. M. Constantinescu, T. Krause, and M. Anitescu, “On-line economic optimization of energy systems using weather forecast information,” *Journal of Process Control*, vol. 19, no. 10, pp. 1725–1736, Dec. 2009.
- [39] R. Marquez and C. F. M. Coimbra, “Intra-hour DNI forecasting based on cloud tracking image analysis,” *Solar Energy*, vol. 91, no. 0, pp. 327–336, May 2013.
- [40] R. Marquez and C. F. M. Coimbra, “Forecasting of global and direct solar irradiance using stochastic learning methods, ground experiments and the NWS database,” *Solar Energy*, vol. 85, no. 5, pp. 746–756, May 2011.
- [41] B. T. Baumrucker and L. T. Biegler, “MPEC strategies for optimization of a class of hybrid dynamic systems,” *Journal of Process Control*, vol. 19, no. 8, pp. 1248–1256, Sep. 2009.
- [42] B. T. Baumrucker, J. G. Renfro, and L. T. Biegler, “MPEC problem formulations and solution strategies with chemical engineering applications,” *Computers & Chemical Engineering*, vol. 32, no. 12, pp. 2903–2913, Dec. 2008.

- [43] A. U. Raghunathan and L. T. Biegler, "Mathematical programs with equilibrium constraints (MPECs) in process engineering," *Computers & Chemical Engineering*, vol. 27, no. 10, pp. 1381–1392, Oct. 2003.
- [44] L. T. Biegler, "An overview of simultaneous strategies for dynamic optimization," *Chemical Engineering and Processing: Process Intensification*, vol. 46, no. 11, pp. 1043–1053, Nov. 2007.
- [45] J. D. Hedengren, "APMonitor Modeling Language for Mixed-Integer Differential Algebraic Systems," in *Computing Society Sponsored Session on Optimization Modeling Software: Design and Applications*, 2012.
- [46] N. Movahedian and S. Nobakhtian, "Necessary and sufficient conditions for nonsmooth mathematical programs with equilibrium constraints," *Nonlinear Analysis: Theory, Methods & Applications*, vol. 72, no. 5, pp. 2694–2705, Mar. 2010.
- [47] H. Yin, F. Ding, and J. Zhang, "Active set algorithm for mathematical programs with linear complementarity constraints," *Applied Mathematics and Computation*, vol. 217, no. 21, pp. 8291–8302, Jul. 2011.
- [48] S. Tangaramvong and F. Tin-Loi, "An FE-MPEC approach for limit load evaluation in the presence of contact and displacement constraints," *International Journal of Solids and Structures*, vol. 49, no. 13, pp. 1753–1763, Jun. 2012.
- [49] S. Tangaramvong, F. Tin-Loi, and T. Senjuntichai, "An MPEC approach for the critical post-collapse behavior of rigid-plastic structures," *International Journal of Solids and Structures*, vol. 48, no. 19, pp. 2732–2742, Sep. 2011.
- [50] A. U. Raghunathan, M. Soledad Diaz, and L. T. Biegler, "An MPEC formulation for dynamic optimization of distillation operations," *Computers & Chemical Engineering*, vol. 28, no. 10, pp. 2037–2052, Sep. 2004.
- [51] S. A. Gabriel and F. U. Leuthold, "Solving discretely-constrained MPEC problems with applications in electric power markets," *Energy Economics*, vol. 32, no. 1, pp. 3–14, Jan. 2010.
- [52] B. T. Baumrucker and L. T. Biegler, "MPEC strategies for cost optimization of pipeline operations," *Computers & Chemical Engineering*, vol. 34, no. 6, pp. 900–913, Jun. 2010.
- [53] J. Björkqvist and T. Westerlund, "Automated reformulation of disjunctive constraints in MINLP optimization," *Computers & Chemical Engineering*, vol. 23, Supplement, pp. S11–S14, Jun. 1999.
- [54] I. E. Grossmann, "Review of Nonlinear Mixed-Integer and Disjunctive Programming Techniques," *Optimization and Engineering*, vol. 3, pp. 227–252, 2002.
- [55] I. E. Grossmann and M. Türkay, "Solution of algebraic systems of disjunctive equations," *Computers & Chemical Engineering*, vol. 20, Supplement 1, pp. S339–S344, 1996.
- [56] G. S. Liu and J. Z. Zhang, "A new branch and bound algorithm for solving quadratic programs with linear complementarity constraints," *Journal of Computational and Applied Mathematics*, vol. 146, no. 1, pp. 77–87, Sep. 2002.

- [57] N. W. Sawaya and I. E. Grossmann, "A cutting plane method for solving linear generalized disjunctive programming problems," *Computers & Chemical Engineering*, vol. 29, no. 9, pp. 1891–1913, Aug. 2005.
- [58] P. Tanarkeit and L. T. Biegler, "Stable Decomposition for Dynamic Optimization," *Industrial & Engineering Chemistry Research*, vol. 34, no. 4, pp. 1253–1266, Apr. 1995.
- [59] J. D. Hedengren, K. Allsford, and L. Ramlal, "Moving horizon estimation and control for an industrial gas phase polymerization reactor," *Proceedings of the American Control Conference*, pp. 1353–1358, 2007.
- [60] M. J. Leibman, T. F. Edgar, and L. S. Lasdon, "Efficient data reconciliation and estimation for dynamic processes using nonlinear programming techniques," *Computers & Chemical Engineering*, vol. 16, no. 10–11, pp. 963–986, Oct. 1992.
- [61] B. J. Spivey, J. D. Hedengren, and T. F. Edgar, "Constrained nonlinear estimation for industrial process fouling," *Industrial and Engineering Chemistry Research*, vol. 49, no. 17, pp. 7824–7831, 2010.
- [62] G. F. Carey and B. A. Finlayson, "Orthogonal collocation on finite elements," *Chemical Engineering Science*, vol. 30, no. 5–6, pp. 587–596, May 1975.
- [63] B. A. Finlayson, "Orthogonal collocation on finite elements—progress and potential," *Mathematics and Computers in Simulation*, vol. 22, no. 1, pp. 11–17, Mar. 1980.
- [64] B. W. Bequette, "Nonlinear control of chemical processes: a review," *Ind. Eng. Chem. Res.*, vol. 30, no. 7, pp. 1391–1413, Jul. 1991.
- [65] V. M. Zavala, "Computational Strategies for the Optimal Operation of Large-Scale Chemical Processes," PhD Dissertation, Carnegie Mellon University, Pittsburgh, PA, 2009.
- [66] L. T. Biegler, A. M. Cervantes, and A. Wächter, "Advances in simultaneous strategies for dynamic process optimization," *Chemical Engineering Science*, vol. 57, no. 4, pp. 575–593, Feb. 2002.
- [67] T. J. R. Hughes, A. Reali, and G. Sangalli, "Efficient quadrature for NURBS-based isogeometric analysis," *Computer Methods in Applied Mechanics and Engineering*, vol. 199, no. 5–8, pp. 301–313, 2010.
- [68] *MATLAB*. The MathWorks Inc., 2011.
- [69] R. Niemi, J. Mikkola, and P. D. Lund, "Urban energy systems with smart multi-carrier energy networks and renewable energy generation," *Renewable Energy*, vol. 48, pp. 524–536, Dec. 2012.
- [70] J. Wang, A. J. Conejo, C. Wang, and J. Yan, "Smart grids, renewable energy integration, and climate change mitigation – Future electric energy systems," *Applied Energy*, vol. 96, pp. 1–3, Aug. 2012.
- [71] M. Wissner, "The Smart Grid – A saucerful of secrets?," *Applied Energy*, vol. 88, no. 7, pp. 2509–2518, Jul. 2011.

- [72] A. Schroeder, "Modeling storage and demand management in power distribution grids," *Applied Energy*, vol. 88, no. 12, pp. 4700–4712, Dec. 2011.
- [73] N. S. Wade, P. C. Taylor, P. D. Lang, and P. R. Jones, "Evaluating the benefits of an electrical energy storage system in a future smart grid," *Energy Policy*, vol. 38, no. 11, pp. 7180–7188, Nov. 2010.
- [74] P. Arce, M. Medrano, A. Gil, E. Oró, and L. F. Cabeza, "Overview of thermal energy storage (TES) potential energy savings and climate change mitigation in Spain and Europe," *Applied Energy*, vol. 88, no. 8, pp. 2764–2774, Aug. 2011.
- [75] A. Arteconi, N. J. Hewitt, and F. Polonara, "State of the art of thermal storage for demand-side management," *Applied Energy*, vol. 93, pp. 371–389, May 2012.
- [76] F. G. F. Qin, X. Yang, Z. Ding, Y. Zuo, Y. Shao, R. Jiang, and X. Yang, "Thermocline stability criterions in single-tanks of molten salt thermal energy storage," *Applied Energy*, vol. 97, pp. 816–821, Sep. 2012.
- [77] D. L. Savicki, H. A. Vielmo, and A. Krenzinger, "Three-dimensional analysis and investigation of the thermal and hydrodynamic behaviors of cylindrical storage tanks," *Renewable Energy*, vol. 36, no. 5, pp. 1364–1373, May 2011.
- [78] S. Ievers and W. Lin, "Numerical simulation of three-dimensional flow dynamics in a hot water storage tank," *Applied Energy*, vol. 86, no. 12, pp. 2604–2614, Dec. 2009.
- [79] K. M. Powell, W. J. Cole, U. F. Ekarika, and T. F. Edgar, "Optimal chiller loading in a district cooling system with thermal energy storage," *Energy*, vol. 50, pp. 445–453, Feb. 2013.
- [80] W. Cole, K. Powell, and T. Edgar, "Optimization and advanced control of thermal energy storage systems," *Reviews in Chemical Engineering*, vol. 28, pp. 81–99, 2012.
- [81] Z. Ait Hammou and M. Lacroix, "A hybrid thermal energy storage system for managing simultaneously solar and electric energy," *Energy Conversion and Management*, vol. 47, no. 3, pp. 273–288, Feb. 2006.
- [82] K. M. Powell and T. F. Edgar, "Modeling and control of a solar thermal power plant with thermal energy storage," *Chemical Engineering Science*, vol. 71, pp. 138–145, Mar. 2012.
- [83] M. A. A. Majid, M. Nasir, and J. Waluyo, "Operation and Performance of a Thermal Energy Storage System: A Case Study of Campus Cooling using Cogeneration Plant," *Energy Procedia*, vol. 14, pp. 1280–1285, 2012.
- [84] D. Zhou, C. Y. Zhao, and Y. Tian, "Review on thermal energy storage with phase change materials (PCMs) in building applications," *Applied Energy*, vol. 92, pp. 593–605, Apr. 2012.
- [85] R. Marc A, "The exergy of stratified thermal energy storages," *Solar Energy*, vol. 71, no. 3, pp. 173–185, 2001.
- [86] P. Li, J. Van Lew, W. Karaki, C. Chan, J. Stephens, and Q. Wang, "Generalized charts of energy storage effectiveness for thermocline heat storage tank design and calibration," *Solar Energy*, vol. 85, no. 9, pp. 2130–2143, Sep. 2011.

- [87] Y. M. Han, R. Z. Wang, and Y. J. Dai, "Thermal stratification within the water tank," *Renewable and Sustainable Energy Reviews*, vol. 13, no. 5, pp. 1014–1026, Jun. 2009.
- [88] Y. H. Zurigat, P. R. Liche, and A. J. Ghajar, "Influence of inlet geometry on mixing in thermocline thermal energy storage," *International Journal of Heat and Mass Transfer*, vol. 34, no. 1, pp. 115–125, Jan. 1991.
- [89] W. P. Bahnfleth and J. Song, "Constant flow rate charging characteristics of a full-scale stratified chilled water storage tank with double-ring slotted pipe diffusers," *Applied Thermal Engineering*, vol. 25, no. 17–18, pp. 3067–3082, Dec. 2005.
- [90] J. D. Chung, S. H. Cho, C. S. Tae, and H. Yoo, "The effect of diffuser configuration on thermal stratification in a rectangular storage tank," *Renewable Energy*, vol. 33, no. 10, pp. 2236–2245, Oct. 2008.
- [91] M.-S. Shin, H.-S. Kim, D.-S. Jang, S.-N. Lee, Y.-S. Lee, and H.-G. Yoon, "Numerical and experimental study on the design of a stratified thermal storage system," *Applied Thermal Engineering*, vol. 24, no. 1, pp. 17–27, Jan. 2004.
- [92] M. G. Abu-Hamdan, Y. H. Zurigat, and A. J. Ghajar, "An experimental study of a stratified thermal storage under variable inlet temperature for different inlet designs," *International Journal of Heat and Mass Transfer*, vol. 35, no. 8, pp. 1927–1934, Aug. 1992.
- [93] A. Castell, M. Medrano, C. Solé, and L. F. Cabeza, "Dimensionless numbers used to characterize stratification in water tanks for discharging at low flow rates," *Renewable Energy*, vol. 35, no. 10, pp. 2192–2199, Oct. 2010.
- [94] P. F. Peterson, "Method for predicting and minimizing numerical diffusion," *Numerical Heat Transfer, Part B: Fundamentals*, vol. 21, no. 3, pp. 343–366, 1992.
- [95] A. Younes, M. Fahs, and P. Ackerer, "A new approach to avoid excessive numerical diffusion in Eulerian-Lagrangian methods," *Communications in Numerical Methods in Engineering*, vol. 24, no. 11, pp. 897–910, 2008.
- [96] D. A. Arias, A. C. McMahan, and S. A. Klein, "Sensitivity of long-term performance simulations of solar energy systems to the degree of stratification in the thermal storage unit," *Int. J. Energy Res.*, vol. 32, no. 3, pp. 242–254, 2008.
- [97] Y. Zurigat, K. Maloney, and A. Ghajar, "A comparison study of one-dimensional models for stratified thermal storage tanks," *Journal of Solar Energy Engineering*, vol. 111, pp. 204–210, Aug. 1989.
- [98] E. M. Kleinbach, W. A. Beckman, and S. A. Klein, "Performance study of one-dimensional models for stratified thermal storage tanks," *Solar Energy*, vol. 50, no. 2, pp. 155–166, Feb. 1993.
- [99] R. De Césaró Oliveski, A. Krenzinger, and H. A. Vielmo, "Comparison between models for the simulation of hot water storage tanks," *Solar Energy*, vol. 75, no. 2, pp. 121–134, Aug. 2003.
- [100] J. A. Duffie and W. A. Beckman, *Solar engineering of thermal processes*, 2nd ed. New York: Wiley Interscience, 1991.

- [101] R. Franke, "Object-oriented modeling of solar heating systems.," *Solar energy*, vol. 60, pp. 171–180, 1997.
- [102] R. A. Pate and W. F. Phillips, "Mass and energy transfer in a hot liquid energy storage system," in *Proceedings of the American Section of the International Solar Energy Society*, Orlando, FL, 1977.
- [103] C. K. Hsieh, "Exact solutions of Stefan problems for a heat front moving at constant velocity in a quasi-steady state," *International Journal of Heat and Mass Transfer*, vol. 38, no. 1, pp. 71–79, Jan. 1995.
- [104] S. I. Barry and J. Caunce, "Exact and numerical solutions to a Stefan problem with two moving boundaries," *Applied Mathematical Modelling*, vol. 32, no. 1, pp. 83–98, Jan. 2008.
- [105] J. Crank, *Free and Moving Boundary Problems*. New York: Clarendon Press, 1984.
- [106] Rajeev, K. N. Rai, and S. Das, "Numerical solution of a moving-boundary problem with variable latent heat," *International Journal of Heat and Mass Transfer*, vol. 52, no. 7–8, pp. 1913–1917, Mar. 2009.
- [107] Y. I. Lim, J. M. Le Lann, and X. Joulia, "Moving mesh generation for tracking a shock or steep moving front," *Computers & Chemical Engineering*, vol. 25, no. 4–6, pp. 653–663, May 2001.
- [108] B. Rezaie and M. A. Rosen, "District heating and cooling: Review of technology and potential enhancements," *Appl. Energy*, vol. 93, pp. 2–10, May 2012.
- [109] A. Thornton and C. Rodriguez Monroy, "Distributed power generation in the United States," *Renew. Sust. Energ. Rev.*, vol. 15, no. 9, pp. 4809–4817, Dec. 2011.
- [110] U. Persson and S. Werner, "District heating in sequential energy supply," *Appl. Energy*, vol. 95, pp. 123–131, Jul. 2012.
- [111] A. L. S. Chan, T.-T. Chow, S. K. F. Fong, and J. Z. Lin, "Performance evaluation of district cooling plant with ice storage," *Energy*, vol. 31, no. 14, pp. 2750–2762, Nov. 2006.
- [112] M. F. Akorede, H. Hizam, and E. Pouresmaeil, "Distributed energy resources and benefits to the environment," *Renew. Sust. Energ. Rev.*, vol. 14, no. 2, pp. 724–734, Feb. 2010.
- [113] K. Jonshagen and M. Genrup, "Improved load control for a steam cycle combined heat and power plant," *Energy*, vol. 35, no. 4, pp. 1694–1700, Apr. 2010.
- [114] J. Aghaei, T. Niknam, R. Azizipanah-Abarghooee, and J. M. Arroyo, "Scenario-based dynamic economic emission dispatch considering load and wind power uncertainties," *International Journal of Electrical Power & Energy Systems*, vol. 47, no. 0, pp. 351–367, May 2013.
- [115] M. Amina, V. S. Kodogiannis, I. Petrounias, and D. Tomtsis, "A hybrid intelligent approach for the prediction of electricity consumption," *Int. J. Electr. Power Energy Syst.*, vol. 43, no. 1, pp. 99–108, Dec. 2012.
- [116] D. W. Bunn, "Forecasting loads and prices in competitive power markets," *Proc. IEEE*, vol. 88, no. 2, pp. 163–169, Feb. 2000.

- [117] L. Hernandez, C. Baladron, J. M. Aguiar, B. Carro, A. J. Sanchez-Esguevillas, and J. Lloret, "Short-Term Load Forecasting for Microgrids Based on Artificial Neural Networks," *Energies*, vol. 6, no. 3, pp. 1385–1408, Mar. 2013.
- [118] Z. Hou, Z. Lian, Y. Yao, and X. Yuan, "Cooling-load prediction by the combination of rough set theory and an artificial neural-network based on data-fusion technique," *Applied Energy*, vol. 83, no. 9, pp. 1033–1046, Sep. 2006.
- [119] S. S. K. Kwok and E. W. M. Lee, "A study of the importance of occupancy to building cooling load in prediction by intelligent approach," *Energy Conv. Manag.*, vol. 52, no. 7, pp. 2555–2564, Jul. 2011.
- [120] Y.-Y. Lu, J. Chen, T.-C. Liu, and M.-H. Chien, "Using cooling load forecast as the optimal operation scheme for a large multi-chiller system," *Int. J. Refrig.-Rev. Int. Froid*, vol. 34, no. 8, pp. 2050–2062, Dec. 2011.
- [121] K. Marik, Z. Schindler, and P. Stluka, "Decision support tools for advanced energy management," *Energy*, vol. 33, no. 6, pp. 858–873, Jun. 2008.
- [122] E. Dotzauer, "Simple model for prediction of loads in district-heating systems," *Appl. Energy*, vol. 73, no. 3–4, pp. 277–284, Dec. 2002.
- [123] K. Powell, W. Cole, U. Ekarika, and T. Edgar, "Optimal chiller loading in a district cooling system with thermal energy storage," *Energy*, In press 2013.
- [124] A. Azadeh, S. F. Ghaderi, and S. Sohrabkhani, "Annual electricity consumption forecasting by neural network in high energy consuming industrial sectors," *Energy Conv. Manag.*, vol. 49, no. 8, pp. 2272–2278, Aug. 2008.
- [125] G. Q. Zhang, B. E. Patuwo, and M. Y. Hu, "Forecasting with artificial neural networks: The state of the art," *Int. J. Forecast.*, vol. 14, no. 1, pp. 35–62, Mar. 1998.
- [126] K. Lee, Y. Cha, J. Park, M. Kurzyn, D. Park, and O. Mohammed, "Short-Term Load Forecasting Using an Artificial Neural Network," *IEEE Trans. Power Syst.*, vol. 7, no. 1, pp. 124–132, Feb. 1992.
- [127] D. Park, M. Elsharkawi, R. Marks, L. Atlas, and M. Damborg, "Electric-Load Forecasting Using an Artificial Neural Network," *IEEE Trans. Power Syst.*, vol. 6, no. 2, pp. 442–449, May 1991.
- [128] A. Khotanzad, R. AfkhamiRohani, T. Lu, A. Abaye, M. Davis, and D. Maratukulam, "ANNSTLF - A neural-network-based electric load forecasting system," *IEEE Trans. Neural Netw.*, vol. 8, no. 4, pp. 835–846, May 1997.
- [129] T. Senjyu, H. Takara, K. Uezato, and T. Funabashi, "One-hour-ahead load forecasting using neural network," *IEEE Trans. Power Syst.*, vol. 17, no. 1, pp. 113–118, Feb. 2002.
- [130] P. F. Pai and W. C. Hong, "Forecasting regional electricity load based on recurrent support vector machines with genetic algorithms," *Electr. Power Syst. Res.*, vol. 74, no. 3, pp. 417–425, Jun. 2005.
- [131] S. H. Ling, F. H. F. Leung, H. K. Lam, Y. S. Lee, and P. K. S. Tam, "A novel genetic-algorithm-based neural network for short-term load forecasting," *IEEE Trans. Ind. Electron.*, vol. 50, no. 4, pp. 793–799, Aug. 2003.

- [132] H. S. Hippert, C. E. Pedreira, and R. C. Souza, "Neural networks for short-term load forecasting: A review and evaluation," *IEEE Trans. Power Syst.*, vol. 16, no. 1, pp. 44–55, Feb. 2001.
- [133] G. A. Darbellay and M. Slama, "Forecasting the short-term demand for electricity - Do neural networks stand a better chance?," *Int. J. Forecast.*, vol. 16, no. 1, pp. 71–83, Mar. 2000.
- [134] J. W. Taylor and P. E. McSharry, "Short-term load forecasting methods: An evaluation based on European data," *IEEE Trans. Power Syst.*, vol. 22, no. 4, pp. 2213–2219, Nov. 2007.
- [135] S. J. Huang and K. R. Shih, "Short-term load forecasting via ARMA model identification including non-Gaussian process considerations," *IEEE Trans. Power Syst.*, vol. 18, no. 2, pp. 673–679, May 2003.
- [136] S. S. Pappas, L. Ekonomou, D. C. Karamousantas, G. E. Chatzarakis, S. K. Katsikas, and P. Liatsis, "Electricity demand loads modeling using Autoregressive Moving Average (ARMA) models," *Energy*, vol. 33, no. 9, pp. 1353–1360, Sep. 2008.
- [137] J. Nowicka-Zagrajek and R. Weron, "Modeling electricity loads in California: ARMA models with hyperbolic noise," *Signal Process.*, vol. 82, no. 12, pp. 1903–1915, Dec. 2002.
- [138] T. W. S. Chow and C. T. Leung, "Nonlinear autoregressive integrated neural network model for short-term load forecasting," *IEE Proc.-Gener. Transm. Distrib.*, vol. 143, no. 5, pp. 500–506, Sep. 1996.
- [139] B. L. Zhang and Z. Y. Dong, "An adaptive neural-wavelet model for short term load forecasting," *Electr. Power Syst. Res.*, vol. 59, no. 2, pp. 121–129, Sep. 2001.
- [140] A. J. R. Reis and A. P. A. da Silva, "Feature extraction via multiresolution analysis for short-term load forecasting," *IEEE Trans. Power Syst.*, vol. 20, no. 1, pp. 189–198, Feb. 2005.
- [141] C. I. Kim, I. K. Yu, and Y. H. Song, "Kohonen neural network and wavelet transform based approach to short-term load forecasting," *Electr. Power Syst. Res.*, vol. 63, no. 3, pp. 169–176, Oct. 2002.
- [142] S. J. Yao, Y. H. Song, L. Z. Zhang, and X. Y. Cheng, "Wavelet transform and neural networks for short-term electrical load forecasting," *Energy Conv. Manag.*, vol. 41, no. 18, pp. 1975–1988, Dec. 2000.
- [143] A. Kusiak, M. Li, and Z. Zhang, "A data-driven approach for steam load prediction in buildings," *Applied Energy*, vol. 87, no. 3, pp. 925–933, Mar. 2010.
- [144] S. S. K. Kwok, R. K. K. Yuen, and E. W. M. Lee, "An intelligent approach to assessing the effect of building occupancy on building cooling load prediction," *Building and Environment*, vol. 46, no. 8, pp. 1681–1690, Aug. 2011.
- [145] A. E. Ben-Nakhi and M. A. Mahmoud, "Cooling load prediction for buildings using general regression neural networks," *Energy Conversion and Management*, vol. 45, no. 13–14, pp. 2127–2141, Aug. 2004.

- [146] Q. Li, Q. Meng, J. Cai, H. Yoshino, and A. Mochida, "Predicting hourly cooling load in the building: A comparison of support vector machine and different artificial neural networks," *Energy Conversion and Management*, vol. 50, no. 1, pp. 90–96, Jan. 2009.
- [147] L. Duanmu and Z. Wang, "A simplified method to predict hourly building cooling load for urban energy planning," *Energy and Buildings*, vol. 58, pp. 281–291, Nov. 2012.
- [148] S. Henchoz, F. Buchter, D. Favrat, M. Morandin, and M. Mercangöz, "Thermoeconomic analysis of a solar enhanced energy storage concept based on thermodynamic cycles," *Energy*, vol. 45, no. 1, pp. 358–365, Sep. 2012.
- [149] G. Kumaresan, R. Sridhar, and R. Velraj, "Performance studies of a solar parabolic trough collector with a thermal energy storage system," *Energy*, In Press.
- [150] A. Cavallo, "Controllable and affordable utility-scale electricity from intermittent wind resources and compressed air energy storage (CAES)," *Energy*, vol. 32, no. 2, pp. 120–127, Feb. 2007.
- [151] T. Niknam, F. Golestaneh, and A. Malekpour, "Probabilistic energy and operation management of a microgrid containing wind/photovoltaic/fuel cell generation and energy storage devices based on point estimate method and self-adaptive gravitational search algorithm," *Energy*, vol. 43, no. 1, pp. 427–437, Jul. 2012.
- [152] E. Hittinger, J. F. Whitacre, and J. Apt, "What properties of grid energy storage are most valuable?," *Journal of Power Sources*, vol. 206, pp. 436–449, May 2012.
- [153] S. M. Hasnain, "Review on sustainable thermal energy storage technologies, Part II: cool thermal storage," *Energy Conversion and Management*, vol. 39, no. 11, pp. 1139–1153, Aug. 1998.
- [154] B. Rismanchi, R. Saidur, H. H. Masjuki, and T. M. I. Mahlia, "Cost-benefit analysis of using cold thermal energy storage systems in building applications," *Energy Procedia*, vol. 14, pp. 493–498, 2012.
- [155] Y.-C. Chang, "A novel energy conservation method—optimal chiller loading," *Electric Power Systems Research*, vol. 69, no. 2–3, pp. 221–226, May 2004.
- [156] Z. W. Geem, "Solution quality improvement in chiller loading optimization," *Applied Thermal Engineering*, vol. 31, no. 10, pp. 1848–1851, Jul. 2011.
- [157] I. Dincer and M. A. Rosen, *Thermal Energy Storage: Systems and Applications*, 2nd ed. Chichester, West Sussex, UK: John Wiley & Sons, 2011.
- [158] Y.-C. Chang, J.-K. Lin, and M.-H. Chuang, "Optimal chiller loading by genetic algorithm for reducing energy consumption," *Energy and Buildings*, vol. 37, no. 2, pp. 147–155, Feb. 2005.
- [159] M. Sakawa, K. Kato, and S. Ushiro, "Operational planning of district heating and cooling plants through genetic algorithms for mixed 0–1 linear programming," *European Journal of Operational Research*, vol. 137, no. 3, pp. 677–687, Mar. 2002.

- [160] W.-S. Lee, Y.-T. Chen, and T.-H. Wu, "Optimization for ice-storage air-conditioning system using particle swarm algorithm," *Applied Energy*, vol. 86, no. 9, pp. 1589–1595, Sep. 2009.
- [161] Y.-C. Chang, F.-A. Lin, and C. H. Lin, "Optimal chiller sequencing by branch and bound method for saving energy," *Energy Conversion and Management*, vol. 46, no. 13–14, pp. 2158–2172, Aug. 2005.
- [162] H.-J. Chen, D. W. P. Wang, and S.-L. Chen, "Optimization of an ice-storage air conditioning system using dynamic programming method," *Applied Thermal Engineering*, vol. 25, no. 2–3, pp. 461–472, Feb. 2005.
- [163] G. P. Henze, B. Biffar, D. Kohn, and M. P. Becker, "Optimal design and operation of a thermal storage system for a chilled water plant serving pharmaceutical buildings," *Energy and Buildings*, vol. 40, no. 6, pp. 1004–1019, 2008.
- [164] P. B. Sáez and B. E. Rittmann, "Model-parameter estimation using least squares," *Water Research*, vol. 26, no. 6, pp. 789–796, Jun. 1992.
- [165] M. Hydeman, N. Webb, P. Sreedharan, and S. Blanc, "Development and testing of a reformulated regression-based electric chiller model," *ASHRAE Transactions*, vol. 108, no. 2, pp. 1118–1127, 2002.
- [166] T.-S. Lee, K.-Y. Liao, and W.-C. Lu, "Evaluation of the suitability of empirically-based models for predicting energy performance of centrifugal water chillers with variable chilled water flow," *Applied Energy*, vol. 93, pp. 583–595, May 2012.
- [167] T.-S. Lee and W.-C. Lu, "An evaluation of empirically-based models for predicting energy performance of vapor-compression water chillers," *Applied Energy*, vol. 87, no. 11, pp. 3486–3493, Nov. 2010.
- [168] D. J. Swider, "A comparison of empirically based steady-state models for vapor-compression liquid chillers," *Applied Thermal Engineering*, vol. 23, no. 5, pp. 539–556, Apr. 2003.
- [169] W. Jiang and T. A. Reddy, "Reevaluation of the Gordon-Ng performance models for water-cooled chillers," in *ASHRAE TRANSACTIONS TECHNICAL AND SYMPOSIUM PAPERS*, Kansas City, MO, United states, 2003, vol. 109 PART 2, pp. 272–287.
- [170] J. . Gordon, K. C. Ng, and H. T. Chua, "Centrifugal chillers: Thermodynamic modelling and a diagnostic case study," *International Journal of Refrigeration*, vol. 18, no. 4, pp. 253–257, May 1995.
- [171] Y.-C. Chang, W.-H. Chen, C.-Y. Lee, and C.-N. Huang, "Simulated annealing based optimal chiller loading for saving energy," *Energy Conversion and Management*, vol. 47, no. 15–16, pp. 2044–2058, Sep. 2006.
- [172] T. F. Edgar, D. M. Himmelblau, and L. S. Lasdon, *Optimization of chemical processes*, 2nd ed. New York, NY: McGraw-Hill, 2001.
- [173] J. Gao, Y. Xiao, J. Liu, W. Liang, and C. L. P. Chen, "A survey of communication/networking in Smart Grids," *Future Generation Computer Systems*, vol. 28, no. 2, pp. 391–404, Feb. 2012.

- [174] D. S. Markovic, D. Zivkovic, I. Branovic, R. Popovic, and D. Cvetkovic, "Smart power grid and cloud computing," *Renewable and Sustainable Energy Reviews*, vol. 24, no. 0, pp. 566–577, Aug. 2013.
- [175] M. Alonso, H. Amaris, and C. Alvarez-Ortega, "Integration of renewable energy sources in smart grids by means of evolutionary optimization algorithms," *Expert Systems with Applications*, vol. 39, no. 5, pp. 5513–5522, Apr. 2012.
- [176] "Muhittin Yilmaz and N. R. Dhansri", "'A Smart Grid Robust Optimization Framework'," *Procedia Computer Science*, vol. 12, no. 0, pp. 301–306, 2012.
- [177] F. G. Gonzalez, "An Intelligent Controller for the Smart Grid," *Procedia Computer Science*, vol. 16, no. 0, pp. 776–785, 2013.
- [178] S. Koochi-Kamali, V. V. Tyagi, N. A. Rahim, N. L. Panwar, and H. Mokhlis, "Emergence of energy storage technologies as the solution for reliable operation of smart power systems: A review," *Renewable and Sustainable Energy Reviews*, vol. 25, no. 0, pp. 135–165, Sep. 2013.
- [179] M. A. Ehyaei, A. Mozafari, A. Ahmadi, P. Esmaili, M. Shayesteh, M. Sarkhosh, and I. Dincer, "Potential use of cold thermal energy storage systems for better efficiency and cost effectiveness," *Energy and Buildings*, vol. 42, no. 12, pp. 2296–2303, Dec. 2010.
- [180] M. Pirouti, A. Bagdanavicius, J. Ekanayake, J. Wu, and N. Jenkins, "Energy consumption and economic analyses of a district heating network," *Energy*, no. 0.
- [181] S. M. Sanaei and T. Nakata, "Optimum design of district heating: Application of a novel methodology for improved design of community scale integrated energy systems," *Energy*, vol. 38, no. 1, pp. 190–204, Feb. 2012.
- [182] K. Sperling and B. Möller, "End-use energy savings and district heating expansion in a local renewable energy system – A short-term perspective," *Applied Energy*, vol. 92, no. 0, pp. 831–842, Apr. 2012.
- [183] R. S. Adhikari, N. Aste, and M. Manfren, "Optimization concepts in district energy design and management – A case study," *Energy Procedia*, vol. 14, no. 0, pp. 1386–1391, 2012.
- [184] D. Henning, S. Amiri, and K. Holmgren, "Modelling and optimisation of electricity, steam and district heating production for a local Swedish utility," *European Journal of Operational Research*, vol. 175, no. 2, pp. 1224–1247, Dec. 2006.
- [185] T. Nuytten, B. Claessens, K. Paredis, J. Van Bael, and D. Six, "Flexibility of a combined heat and power system with thermal energy storage for district heating," *Applied Energy*, vol. 104, no. 0, pp. 583–591, Apr. 2013.
- [186] V. Verda and F. Colella, "Primary energy savings through thermal storage in district heating networks," *Energy*, vol. 36, no. 7, pp. 4278–4286, Jul. 2011.
- [187] Y. Sun, S. Wang, F. Xiao, and D. Gao, "Peak load shifting control using different cold thermal energy storage facilities in commercial buildings: A review," *Energy Conversion and Management*, vol. 71, no. 0, pp. 101–114, Jul. 2013.

- [188] S. Harvey, C. Carcasci, and T. Berntsson, "Gas turbines in district heating combined heat and power systems: influence of performance on heating costs and emissions," *Applied Thermal Engineering*, vol. 20, no. 12, pp. 1075–1103, Aug. 2000.
- [189] B. Rolfsman, "Combined heat-and-power plants and district heating in a deregulated electricity market," *Applied Energy*, vol. 78, no. 1, pp. 37–52, May 2004.
- [190] M. Basu, "Artificial immune system for combined heat and power economic dispatch," *International Journal of Electrical Power & Energy Systems*, vol. 43, no. 1, pp. 1–5, Dec. 2012.
- [191] C.-L. Chen, T.-Y. Lee, R.-M. Jan, and C.-L. Lu, "A novel direct search approach for combined heat and power dispatch," *International Journal of Electrical Power & Energy Systems*, vol. 43, no. 1, pp. 766–773, Dec. 2012.
- [192] B. Mohammadi-Ivatloo, M. Moradi-Dalvand, and A. Rabiee, "Combined heat and power economic dispatch problem solution using particle swarm optimization with time varying acceleration coefficients," *Electric Power Systems Research*, vol. 95, no. 0, pp. 9–18, Feb. 2013.
- [193] A. Sashirekha, J. Pasupuleti, N. H. Moin, and C. S. Tan, "Combined heat and power (CHP) economic dispatch solved using Lagrangian relaxation with surrogate subgradient multiplier updates," *International Journal of Electrical Power & Energy Systems*, vol. 44, no. 1, pp. 421–430, Jan. 2013.
- [194] J. . Gordon, K. C. Ng, and H. T. Chua, "Centrifugal chillers: Thermodynamic modelling and a diagnostic case study," *International Journal of Refrigeration*, vol. 18, no. 4, pp. 253–257, May 1995.
- [195] J. M. Gordon and K. C. Ng, "A general thermodynamic model for absorption chillers: Theory and experiment," *Heat Recovery Systems and CHP*, vol. 15, no. 1, pp. 73–83, Jan. 1995.
- [196] J. S. Kim, "Economic dispatch of a combined heat and power plant," presented at the 3rd International Conference on Sustainable Chemical Product and Process Engineering, Dalian, China, 2013.
- [197] "NCDC," 2013. [Online]. Available: <http://www.ncdc.noaa.gov/>. [Accessed: 14-Jun-2013].